



HAL
open science

Cavity Quantum Electrodynamics with Carbon Nanotubes

Adrien Jeantet

► **To cite this version:**

Adrien Jeantet. Cavity Quantum Electrodynamics with Carbon Nanotubes. Materials Science [cond-mat.mtrl-sci]. Université Denis Diderot Paris 7, 2017. English. NNT: . tel-01523965

HAL Id: tel-01523965

<https://hal.science/tel-01523965>

Submitted on 17 May 2017

HAL is a multi-disciplinary open access archive for the deposit and dissemination of scientific research documents, whether they are published or not. The documents may come from teaching and research institutions in France or abroad, or from public or private research centers.

L'archive ouverte pluridisciplinaire **HAL**, est destinée au dépôt et à la diffusion de documents scientifiques de niveau recherche, publiés ou non, émanant des établissements d'enseignement et de recherche français ou étrangers, des laboratoires publics ou privés.



Distributed under a Creative Commons Attribution - NonCommercial - ShareAlike 4.0 International License

THÈSE de DOCTORAT
de l'Université Sorbonne Paris Cité
Préparée à l'Université Paris Diderot
École Doctorale 564: Physique en Île de France
Laboratoire Pierre Aigrain / Optique cohérente et non-linéaire

**Cavity Quantum Electrodynamics
with Carbon Nanotubes**

Par Adrien Jeantet

Présentée et soutenue publiquement à Paris, le 31 mars 2017

devant le jury composé de :

Agnès MAÎTRE	Professeure	Présidente	Université Paris 6
Ralph KRUPKE	Professeur	Rapporteur	Karlsruhe KIT
Jean-Michel GÉRARD	Directeur de Recherche	Rapporteur	CEA Grenoble
Sara DUCCI	Professeure	Examinateur	Université Paris 7
Alexia AUFFÈVES	Chargée de Recherche	Examinateur	Institut Néel
Jakob REICHEL	Professeur	Invité	Université Paris 6
Yannick CHASSAGNEUX	Chargé de Recherche	Invité	ENS Paris
Christophe VOISIN	Professeur	Directeur de thèse	Université Paris 7



Except otherwise noted, this worked is licensed under
<https://creativecommons.org/licenses/by-nc-nd/4.0/>



Laboratoire Pierre Aigrain
École Normale Supérieure / CNRS – UMR 8551
24, rue Lhomond
75005 Paris (France)



Abstract

Carbon nanotubes are extensively investigated for their amazing mechanical and electronic properties. Optically, they are excellent candidates for on-demand single-photon sources because they can be electrically excited and they can emit anti-bunched light at room temperature in the telecoms bands. However, their emission efficiency is low, its origins remain unclear and the spectral shape of their photoluminescence is complicated.

In this work, we build an original setup combining a confocal microscope and a fiber based micro-cavity which is both spatially and spectrally tunable. With this device, we observed the rise of cavity quantum electrodynamics effects by analyzing the evolution of the dipole-cavity coupling as a function of the cavity volume. We obtained a strong acceleration of the spontaneous emission rate, due to Purcell factors above 100. The associated effective efficiency of the source reaches up to 50%, leading to a brightness of up to 10%, while keeping excellent anti-bunching features.

We observe the effect of the cavity coupling as a function of the cavity detuning, and develop a model to account for emitters undergoing exciton-phonon coupling in the presence of a cavity. We show that our single-photon source is tunable on a range of frequencies more than a hundred times higher than the cavity spectral width, opening the way to extensive multiplexing.

Further strengthening of the coupling may open the way to the very rich physics of one-dimensional cavity polaritons. And conversely, cavity polaritons could be a tool to understand better the diffusion, and localization properties of excitons in carbon nanotubes. Finally, the original setup build here is extremely versatile and could be used to coupled other types of emitters, such as nano-diamonds or molecules.

Keywords : carbon nanotubes, micro-cavities, CQED, quantum physics, exciton, phonons

Résumé

Les nanotubes de carbone sont largement étudiés pour leurs propriétés mécaniques et électroniques étonnantes. Optiquement, ils sont d'excellents candidats pour les sources de photons uniques à la demande car ils peuvent être excités électriquement et peuvent émettre une lumière dégroupée à température ambiante dans les bandes de télécommunications. Cependant, leur efficacité d'émission est faible, les origines de l'émission restent peu claires et la forme spectrale de leur photoluminescence est complexe. Dans ce travail, nous construisons une configuration originale combinant un microscope confocal et une micro-cavité à base de fibres optiques qui est à la fois spatialement et spectralement ajustable. Avec ce dispositif, nous observons l'apparition des effets de l'électrodynamique quantique en cavité en analysant l'évolution du couplage dipôle-cavité en fonction du volume de la cavité. Nous obtenons une forte accélération du taux d'émission spontanée, grâce à des facteurs Purcell supérieurs à 100. L'efficacité effective associée de la source atteint jusqu'à 50%, conduisant à une brillance de 10%, tout en conservant d'excellentes caractéristiques de dégroupement. Nous observons l'effet du couplage de la cavité en fonction du désaccord de la cavité et développons un modèle pour tenir compte de l'effet du couplage exciton-phonon en présence d'une cavité. Nous montrons que notre source de photons uniques est accordable sur une gamme de fréquences plus de cent fois supérieure à la largeur spectrale de la cavité, ouvrant ainsi la voie à un multiplexage étendu. Un renforcement supplémentaire du couplage peut ouvrir la voie à la très riche physique des polaritons de cavité unidimensionnels. Inversement, les polaritons de cavité pourraient être un outil pour mieux comprendre la diffusion et les propriétés de localisation des excitons dans les nanotubes de carbone. Enfin, la configuration expérimentale est extrêmement polyvalente et pourrait être utilisée pour coupler d'autres types d'émetteurs, comme les nano-diamants ou les molécules.

Mots-clefs : nanotubes de carbone, micro-cavités, CQED, physique quantique, exciton, phonons

Acknowledgements

First of all I would like to thank Ralph Krupke and Jean-Michel Gérard, who have reviewed my thesis with attention. I am also most grateful to Agnès Maître for chairing the jury, as well as to my two examiners Alexia Auffèves and Sara Ducci. Thanks for all the questions, remarks and discussions which have helped to improve this work.

I hope the reader will accept my apologies for writing the following in French, which still feels more natural when it comes to acknowledgements.

Mon travail de recherche a été effectué au Laboratoire Pierre Aigrain de l'École Normale Supérieure, et je souhaite remercier ses directeurs Jean-Marc Berroir et Jérôme Tignon pour leur accueil et pour notre travail commun lorsque j'ai été membre du conseil de laboratoire.

Naturellement, mes remerciements s'adressent à Yannick et Christophe, mes encadrant et directeur de thèse. Parti de rien, c'est à dire d'une table vide et d'un étudiant de M2, vous avez su à travers un travail constant, patient, et énergique arriver à une expérience qui fera date, accompagnée d'un docteur qui vous est infiniment reconnaissant ! Dans cet encadrement qui se rapproche asymptotiquement de la perfection, j'aimerai souligner votre grande complémentarité, votre capacité à triompher d'expériences quasi-impossibles et de théories complexes, votre vision de long terme, mais aussi vos encouragements dans tous mes engagements parascientifiques. J'espère que je saurai me monter digne des qualités scientifiques que vous m'avez inculquées !

Ce travail a pu être réalisé grâce à une collaboration fructueuse avec l'équipe des Puces à Atomes du laboratoire Kastler-Brossel. Je tiens donc à remercier Jakob Reichel, membre invité de mon jury, pour avoir permis à ce projet d'exister, et pour m'avoir accueilli dans l'équipe le temps que je fabrique les fibres adaptées à mes expériences. Merci aussi pour l'enthousiasme et l'organisation d'un workshop rassemblant plusieurs projets autour de ces micro-cavités fibrées. Je souhaite également remercier Jean-Sébastien Lauret, pour sa collaboration avec Fabien, pour les discussions et pour notre travail commun sur les nanotubes. Je gage que nos deux équipes n'ont pas fini de travailler ensemble !

Je tiens aussi à remercier Philippe. Pour m'avoir accueilli dans ton équipe, pour ton humour, ton soutien, et toutes nos discussions politiques ! Je souhaite aussi remercier tous les membres permanents de l'équipe : Carole pour tes conseils et ton accueil à Singapour, Emmanuel pour ton enthousiasme débordant, Gabriel pour ton humour inimitable, Christos pour ton savoir et tes conseils, Claude parce que même si j'ai fait une ou deux remarques, j'aime bien ton humour :)

Une thèse n'est jamais possible sans tous les soutiens parfois discrets mais toujours efficaces qui viennent au quotidien. Je tiens à remercier l'implication toute particulière de Jack Olejnik, Nabil Garroum et Arnaud Leclercq. Au fil des années nous avons conçu les différentes versions de la plate-forme du cryostat, et tous ses petits détails techniques. Merci en particulier à Nabil et Arnaud pour le formidable boulot de

perçage des lentilles. Et bravo à Matthieu Sardin, Jean-Michel Isac et Allan Hourdry pour avoir transformé tous ces dessins en réalité. Un grand merci à Anne Matignon, Olga Hodges et Fabienne Rénia pour leur travail de fond, pour leur organisation et pour leur capacité à jongler avec toutes les commandes les plus complexes. Mes remerciements vont aussi à Olivier Andrieu, Florent Perrin et Aurélien Sabatie pour leur aide, leur sympathie et pour avoir toujours défendu les dewar d'azote. Une thèse sur des micro-cavités et des nano-émetteurs ne va pas sans des soudures minutieuses. Un immense merci à Anne Denis et Philippe Pace pour leur patience et pour m'avoir de nombreuses fois sauvé la mise! Merci à Mickael Rosticher et José Palomo pour m'avoir accueilli dans la salle blanche, et pour les superbes images SEM des fibres. Merci à Yann Colin qui règle tous les problèmes informatiques en un clin d'œil. Enfin, le laboratoire se serait sûrement écroulé sans les interventions multiples et extra-ordinaires de Didier Courtiade, Catherine Gripe et Célia Ruschinzik. Célia, merci aussi pour construire à côté du labo le monde d'asoiaf - tellement cool et nécessaire :D

Il est temps de remercier les docteurs et les thésards pour la bonne ambiance générale du groupe, de la R18 et du labo. Omblin, on a hanté ensemble pendant trois ans cette splendide pièce sans fenêtres, où l'on entendait pourtant parfois un chant de rossignol. J'espère qu'on pourra faire des phares à polaritons en nanotube à motifs de léopards. Mais en attendant, je suis sûr qu'on va révolutionner le monde de l'énergie tous les deux! Et comme on dit, jamais deux sans trois, merci Simon pour m'avoir accompagné avec humour depuis les excellents cours du mardi, jusqu'à la fin de la thèse.

Christophe merci beaucoup pour ton arrivée. Démarrer cette nouvelle manip' avec toi était un plaisir : je me suis senti utile, et j'ai trouvé qu'on interagissait et blaguait bien ensemble. Théo, tu as bien relevé le gant pour la suite, avec ton sérieux, et ton attention envers les autres. Je suis sûr que les cavités comme l'équipe sont entre de bonnes mains. Romaric, je suis sûr que tes hésitations entre chercheur et décorateur d'intérieur (de salle de manip) vont te mener loin! Tom, je suis fier d'avoir été aux côtés d'un combattant balafre capable de faire face à une famille de loups en toutes circonstances. Je suis sûr qu'avec Louis vous allez faire léviter de belles recherches. Assez parlé des p'tits jeunes : je remercie aussi les vieux qui m'ont accueilli dans "leur" mezza. Fabien, je te suis mille fois redevable pour m'avoir lancé sur la piste des animations 3D, Benjamin pour tous tes conseils relax sur le monde de la recherche et de l'enseignement. Maria c'était très chouette de pouvoir faire des discussions animées, pan-européennes en passant du français à l'anglais et à l'espagnol. Vous me manquez tous!

Je voudrais remercier tous les doctorants et post-doc du labo : les 4 Mat(t)hieu (plus ou moins un, j'ai perdu le compte;)), Feihu, Laure, Mohamed, Quentin, Holger, Armand, Danjelia, Thanya, Quentin, Andreas, Cécile, Sylvain, Romain, David, Rémi, Nathanaël, Tino, Loïc, Raphaël, Wei. Laurianne je savais que tu serais une formidable représentante, tu le montres déjà! Arthur, Sarah, merci pour tout ce chemin parcouru ensemble, on a bien réussi notre entrisme à Ulm;) J'ai hâte de vous appeler docteurs.

Au delà du LPA, je voudrais remercier tous les thésards de l'équipe Puce à Atomes, rien n'aurait été possible sans vous. Konstantin, je te souhaite de ne plus jamais voir une fibre optique de ta vie :p Sébastien, un grand merci pour ce setup tellement parfait que je n'ai eu qu'à mettre les pieds sous la table, ça roxxx! Francesco merci pour ta gentillesse et ta patience face à toutes mes questions. Merci Torben, Mohammed et Miles pour votre entourage, il faut se serrer les coudes dans la recherche :)

Pour finir je souhaite remercier ma famille pour son soutien indéfectible tout au long de mes études. Et bien sûr le mot de la fin est pour Claire. Un grand merci, en venant faire ta thèse à Paris, tu m'a mis sur la piste de ce labo et de ces quatre belles années. Je suis sûr qu'on va continuer à relever des défis ensemble avec enthousiasme!

CONTENTS

Introduction	1
1 Spontaneous Emission Control with a Cavity	5
1.1 Light - Matter Coupling	8
1.1.1 Atom in free-space	8
1.1.2 Cavity coupling: the Jaynes-Cummings model	10
1.2 Purcell effect	12
1.2.1 Purcell factor	13
1.2.2 High quality factor cavities	17
1.3 Purcell effect in condensed matter	19
1.3.1 Purcell factor for a condensed matter emitter	20
1.3.2 Light confinement in semi-conductor structures	24
1.3.3 The case of carbon nanotubes	29
2 Single Carbon Nanotube Properties	43
2.1 Structural and electronic properties	45
2.1.1 Structural properties	45
2.1.2 Electronic properties	49
2.2 Optical properties	52
2.2.1 Single electron model	52
2.2.2 Excitonic properties	57
2.3 Samples	62
2.3.1 Synthesis of Carbon Nanotubes	62
2.3.2 Micellar suspension	64
2.3.3 Spin coating	65
3 A Fiber Fabry-Perot Microcavity	67
3.1 Cavity Planar-Concave modes	69
3.1.1 Resonant condition	69
3.1.2 Spectrum of an empty cavity	72
3.2 Cavity mode volume	75
3.2.1 Manufacturing of fibered mirrors	75
3.2.2 Effective mode volume	80
3.3 Fiber - Cavity coupling	86
3.3.1 Single mode fibers	88
3.3.2 Beyond single mode fibers	90
3.4 Finesse and storage time	91

3.4.1	Losses	92
3.4.2	Measuring the finesse	94
4	Scanning confocal microscopy of carbon nanotubes	101
4.1	A scanning Confocal Microscope	103
4.1.1	Principle	103
4.1.2	Excitation	106
4.2	Low temperature single nanotube photoluminescence	110
4.2.1	Single carbon nanotube photoluminescence	110
4.2.2	Coupling to acoustic phonons	116
4.3	Spectral diffusion in Carbon Nanotubes	122
4.3.1	Spectral diffusion of the ZPL	122
4.3.2	Spectral diffusion of the Phonon Wings	123
5	A Purcell enhanced single-photon source	129
5.1	Coupling a tunable cavity to the confocal microscope	132
5.1.1	Cavity Setup	132
5.1.2	Lens-Fiber mounting principle	138
5.2	Measuring the Purcell Factor	141
5.2.1	Photon counts method	141
5.2.2	Time domain method	149
5.2.3	Experimental Results	154
5.3	Single-photon source	162
5.3.1	Statistics of a light source	166
5.3.2	Second order correlation function	168
5.3.3	Hanbury-Brown and Twiss setup	172
6	Efficiency of a cavity coupled nanotube	183
6.1	Cavity efficiency including the phonon wings : theoretical approach	185
6.1.1	Evolution of the populations	185
6.1.2	Cavity efficiency	188
6.2	Experimental derivation of the cavity efficiency	191
6.2.1	Experimental “reconstructed” spectra	192
6.2.2	Fit of the experimental data	197
6.2.3	Evolution with cavity volume	198
	Conclusion	205
	References	229
	Glossary	233

CONTENTS

Appendix A Derivations	235
A.1 A tunable fiber Fabry-Perot microcavity	235
A.1.1 Beam waist	235
A.1.2 Fiber mode	235
Appendix B Drilled objective	237
B.1 Numerical Aperture	237
B.2 Resolving power	239
Appendix C Effect of the vibrations	241
Appendix D Cavity efficiency with phonon coupling	245
D.1 Populations evolution of the system	245
D.1.1 Hamiltonian of the system	245
D.1.2 Master equation	247
D.2 Derivation of the coherence term	249
D.2.1 Trace splitting	249
D.2.2 Non-Interacting Blip Approximation	252
D.2.3 Trace over the phonon bath	252
D.3 Cavity efficiency	256
D.3.1 Emission and absorption spectra	256
D.3.2 Laplace transforms	256
French Summary	259

Introduction

In 1905, Albert Einstein addressed the challenge of explaining the photoelectric effect, which consisted in a discrete exchange of energy between a light field and a metal [1]. In order to do so, he made the hypothesis that the light was composed of quanta of energy, later to be called photons [2]. The success of his theory paved the way to the development of quantum mechanics, and definitely anchored the idea that light behavior was explainable only if considered both as a wave and as an ensemble of corpuscles.

In particular, a single-photon source can be defined as a source emitting a stream of individual photons. In such a stream, the delay between two consecutive photons has a vanishing probability to be zero. Such a property is typical of quantum mechanics and cannot be obtained or understood with classical tools. In the 1960s, the production of nearly single-photons was performed by attenuating a laser source until the probability of emitting two photons at a time became negligible. However, given the Poissonian statistics of the coherent light emitted by lasers, this probability could not drop to zero. The first experimental evidence for a truly anti-bunched light was obtained with sodium atoms in the late 1970s [3], and was followed a decade later by reliable single-photon sources [4, 5].

Since then, the field of single-photon generation has been ever developing, and several applications are considered. In particular, photons could be used as computing qubits, or bits of information for quantum cryptography [6, 7]. This cryptography technique consists in a highly secured means of transmitting information, which is protected from eavesdropping by the laws of quantum mechanics (especially the impossibility of measuring without changing the system, and the no-cloning theorem which states that copying quantum data is impossible). Nevertheless, in the presence of more than one photon, quantum cryptography becomes vulnerable [8], hence the importance of a truly single-photon source.

However, the emission of photons one by one is not the only requirement for such applications. It should also be on-demand, which means that the generation of photons could be triggered by optical or electric pulses ; its brightness, defined as the probability of obtaining a photon for each excitation pulse should ideally be one ; and the photons should be indistinguishable [9, 10], which means having the same wave packet. Furthermore, several practical properties are sought, such as the possibility of emitting in the telecoms bands (1.3 μm and 1.55 μm), the ability to work at room temperature and the ease of integration in devices.

The later requirement led researchers to investigate condensed-matter nano-scale emitters. Currently, the most advanced technology is based on quasi zero-dimensional emitters called quantum dots. Bright on-demand single-photon sources with a high degree of indistinguishability have now been achieved [11]. But they undergo three major downsides : the complicated extraction of photons from the source, the difficulty to emit at telecoms wavelengths [12], and at room temperature.

Carbon nanotubes, are an allotrope of carbon first synthesized in 1991 [13]. They

consist in a layer of atoms organized in a honeycomb lattice rolled up into a tube, having a diameter in the nanometer range and a micro-metric length. Research on these quasi one-dimensional structures have long been confined to their remarkable mechanical (light weight, high Young modulus) and electronic (metallic or semi-conducting, high mobility) properties [14, 15]. Until 2002, when O’Connell et al. [16] managed to isolate nanotubes from each other by means of micelle encapsulation, and thus to prevent the photoluminescence quenching.

The geometry of carbon nanotubes can be entirely characterized by its two chiral indices n and m . Most of the electronic and optical properties of carbon nanotubes can be predicted from them as well. In particular, some nanotubes are metallic while others have a direct gap, inversely proportional to their diameter. Synthesizing a carbon nanotube of a given species (i.e. with given chiral indices), to get a given transition energy, is a field of research of its own. Currently, most synthesis processes yield a distribution of species, but the post-selections can bring high purities [17]. However, the origin of the photoluminescence in carbon nanotubes is complex : the charge carriers are confined due to the the quasi one-dimensional geometry, leading to very stable excitons, dominating the emission up to room temperature [18]. The exciton wave-function spills out of the tube and hence is very sensitive to the dielectric permittivity of its surroundings [19]. As a consequence, the emission energy of a carbon nanotube cannot be completely predicted by its chiral indices, but strongly depends on its local environment. More over, Violla et al. [20] showed that the photoluminescence spectrum was significantly influenced by interactions between the exciton and the one-dimensional phonons propagating along the nanotube axis.

In 2008, Högele et al. [21] demonstrated that a single carbon nanotube could emit anti-bunched light at cryogenic temperature. However, the mechanism underlying this phenomenon remains unclear. It seems that multiple excitons annihilate at a fast rate by Auger processes [22, 23, 24] and that the remaining exciton is trapped by an electrostatic potential in the vicinity of the nanotube, or a defect in the nanotube lattice [25, 26]. As a matter of fact, the control of defects in nanotubes, by surface chemistry, led recently to the demonstration of anti-bunching both in the telecoms bands and at room temperature [27, 28].

A further asset of carbon nanotubes is their ability to be contacted and electrically excited, which opens the way to device integrated on-demand sources [29, 30]. Nonetheless, three major drawbacks hinder their development : the difficulty to obtain a nanotube emitting at a given wavelength (synthesis selectivity and sensitivity to the environment), their complicated optical spectrum and their limited quantum efficiency, i.e. their probability of emission per excitation pulse.

In this work, we couple a single carbon nanotube to a Fabry-Perot cavity. This coupling is a powerful tool to investigate the physics underlying carbon nanotubes photoluminescence, to address the challenge of driving the nanotube emission in the cavity quantum electrodynamics regime in a deterministic way, and to boost their characteristics as single-photon emitters. The so-called Purcell effect [31] consists in an increase of the spontaneous emission rate and thus directly translates in an increase

of the efficiency of the emitter. The smaller the volume of the cavity, the stronger the effect. However, coupling a cavity to a single emitter requires spatial matching - i.e. the cavity mode to be positioned on the emitter - and spectral matching - i.e. a same frequency for the nanotube emission and the cavity mode. The conventional monolithic cavities, mainly developed for quantum dots, are unsuited for carbon nanotubes because of the dependence of their emission energy on their nanoscale surroundings, with shifts largely overcoming the tuning range of such cavities. As a consequence, the coupling of a nanotube to such devices relies on random matching, with success rates irrelevant for applications [32].

By contrast, we adapted a flexible technology developed in the field of atomic physics [33]. It consists in an open micro-cavity formed between a mirror located at the apex of an optical fiber and a planar mirror on which carbon nanotubes are dispersed with a low density. In this way, a single carbon nanotube can be studied in free-space by confocal microscopy and the fiber Fabry-Perot cavity can be deterministically matched spatially (lateral motion of the fiber) and spectrally (distance between the mirrors) to the emitter.

The ability to study the same emitter without the cavity and for different cavity lengths (different couplings) gives an invaluable insight in the rise of Cavity Quantum Electro Dynamics effects. In the weak coupling regime, the cavity brings an increased brightening of the single-photon source via the Purcell effect. The tunability of the cavity also brings a mean to study the so-called cavity feeding effect [34, 35]. Atom like emitters have a linewidth narrower than the cavity in which they are embedded. On the contrary here, carbon nanotubes have a linewidth at least an order of magnitude larger. In this case, the cavity constrains to involve particular phonon modes in order to match the cavity frequency. Consequently, tuning of the cavity length brings a spectral tunability of the single-photon source.

The first chapter of this work explains the interest of coupling a single emitter to a resonator in order to obtain directional emission and accelerated spontaneous emission. It first covers the case of ideal two-level systems, such as atoms, in order to derive the conventional Purcell factor formula. However, this formula is no longer valid for realistic condensed matter emitters undergoing pure dephasing. The generalized Purcell factor is introduced to account for the pure dephasing [35]. Different experimental devices used in condensed matter such as micro-pillars, micro-rings or photonic cristal cavities are described and a review of the existing attempts to couple ensemble or single carbon nanotubes to resonators is given. Finally, the assets of a spatially and spectrally tunable micro-cavity are outlined.

The second chapter gives the theoretical background underlying the physics of carbon nanotubes. The structural and electronic properties are derived from the corresponding properties of graphene. The concept of excitons is introduced in the case of bulk materials and then investigated in the particular case of one-dimensional structures such as carbon nanotubes. The different synthesis methods available are briefly described, as well as the techniques used to separate individual nanotubes. Finally, the deposition process used in this work is explained.

The third chapter covers the properties of fiber Fabry-Perot cavities. In the first section, the resonant modes are derived theoretically and observed experimentally. The manufacturing of the fibers, done in the Laboratoire Kastler-Brossel, is described. The different parameters of this process are investigated to assess their impact on the mode volume of the cavity. The coupling of the fiber mode with the cavity mode is investigated, as well as the impact of the different losses on the finesse of the resonator.

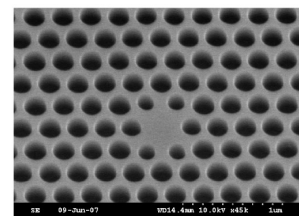
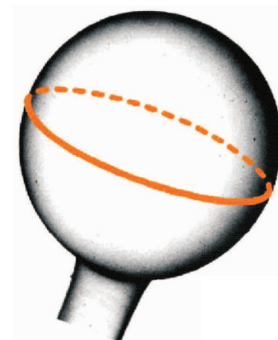
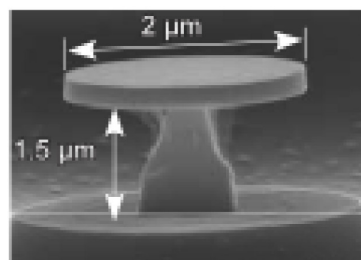
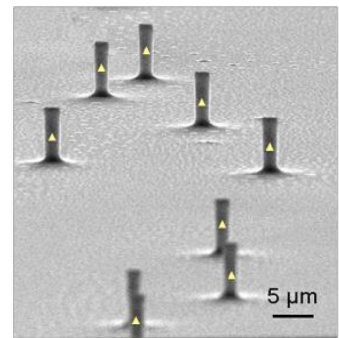
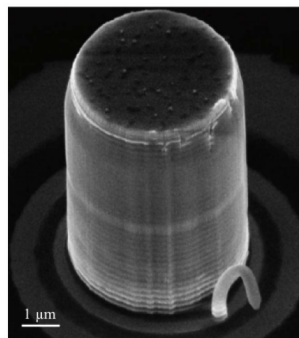
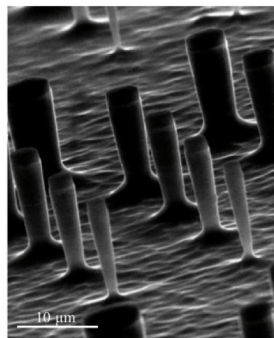
The fourth chapter describes the original scanning confocal microscopy setup developed to combine free-space and cavity experiments on the very same nano-emitter. Optical properties of single carbon nanotubes at cryogenic temperature are experimentally investigated. The emission from carbon nanotubes seems to arise from localized sites, which leads to a discussion of the possible trapping origin of excitons in carbon nanotubes and the likeliness of Auger annihilation processes. The model developed by Violla et al. [20] concerning exciton-phonon coupling model is introduced and compared to the experimental data recorded in this work. The effect of the residual spectral diffusion is investigated and compared to alternative models.

The fifth chapter covers the properties of the single-photon source made by a nanotube coupled to a fiber micro-cavity. The Purcell factor is experimentally measured by two independent methods. The first consists in comparing the count rates. Despite its apparent simplicity, it suffers from biases. Consequently, a more robust method relying on lifetime measurements is introduced. A reliable and reproducible change in the spontaneous emission rate is measured as a function of the cavity mode volume. Finally, the anti-bunching figure is measured with a Hanbury-Brown and Twiss experiment both in free-space and in cavity.

The sixth and last chapter explores how the original exciton-photon coupling brings a new handle to tune the source over an exceptional frequency range. A new model is developed to take into account the effect of the cavity on the full nanotube emission spectrum, including the non-Lorentzian features arising from interactions with phonons. The efficiency of the single-photon source is measured as a function of the cavity energy. A fit to the model brings an independent evaluation of the coupling factor between the dipole and the cavity. Finally, the impact of this coupling on the tunability is theoretically explored for comparatively higher couplings.

1

SPONTANEOUS EMISSION CONTROL WITH A CAVITY



Different optical cavities. Cf text for details and references

Contents

1.1	Light - Matter Coupling	8
1.1.1	Atom in free-space	8
	Emission and absorption	8
	Free-space spontaneous emission	9
1.1.2	Cavity coupling: the Jaynes-Cummings model	10
	Hamiltonian	10
	Rabi oscillations	12
1.2	Purcell effect	12
1.2.1	Purcell factor	13
	The lossy cavity	13
	Strong and weak coupling regimes	14
	The Fermi golden rule approach	16
1.2.2	High quality factor cavities	17
	The case of Rydberg Atoms	17
	The case of micro-sphere cavities	18
1.3	Purcell effect in condensed matter	19
1.3.1	Purcell factor for a condensed matter emitter	20
	Introducing the pure dephasing in the emitter - cavity coupling	20
	Generalized Purcell Factor	23
	Efficiency of the cavity coupled emitter	24
1.3.2	Light confinement in semi-conductor structures	24
	Micro-pillars	24
	Micro-rings	25
	Photonic crystals	26
	Plasmonic cavities	27
	Emitter - Cavity coupling	28
1.3.3	The case of carbon nanotubes	29
	Carbon nanotubes ensembles	29
	Individual carbon nanotubes	35
	A spatially and spectrally tunable cavity	39

Introduction

Developing a quantum computer, or implementing quantum cryptography, are goals highly sought by physicists. In this frame, photons are excellent candidates to be used as bits of information - the so called *flying qubits*. However, generating single, indistinguishable, entangled photons efficiently remains a challenge.

In particular, the spontaneous emission of an atom, occurring at an energy E and at a rate γ is non-directional, and thus difficult to use efficiently in applications. A way to tailor this emission resides in the coupling of the emitter with a resonator. In that case, the emission can be fully directional and, provided that the system remains in the so-called weak-coupling regime, the spontaneous emission rate is enhanced by a factor F_p , introduced by Purcell in 1946 [31]. Given their easy integrability in devices, solid-state emitters are intensively investigated for single-photon sources. In particular, increased spontaneous emission was demonstrated in quantum dots at the end of the twentieth century [36]. Since then, several other emitters and several geometries have arisen and improved the coupling between condensed matter emitters and optical cavities [37, 38, 39, 40].

In 2008, Högeler et al. [21] demonstrated for the first time that a carbon nanotube can behave as a single-photon source. Since then, several works have evidenced the assets of carbon nanotubes in view of applications : single-photon emission was demonstrated both at room temperature and at the telecoms wavelengths [27, 28]. More over, electrical excitation was investigated [29, 30], opening the way to on-demand electrically injected single-photon sources. However, carbon nanotubes have an disadvantage : their efficiency is low, meaning that for one excitation the probability of emission is well below 10% [41]. This drawback can be overcome if the nanotube is coupled to a cavity which enhances its probability of emission by accelerating its spontaneous emission rate.

However, matching a resonator to a carbon nanotube is more challenging than coupling it to quantum dots because the emission energy of the nanotube is difficult to control. Due to this difficulty, most groups work with ensemble of nanotubes up to now, thus losing the ability to make a single-photon source. More over, the few attempts to couple a single emitter to a cavity mostly relied on random matching, thus limiting the possibility for applications. On the contrary, this work offers a method to reproducibly couple a given nanotube to a tunable micro-cavity.

In this chapter, the coupling between light and matter is introduced and a focus is done on free-space spontaneous emission. The Jaynes-Cummings model, describing the coupling between a two-level system and a cavity is investigated and the two main regimes (strong and weak coupling) are defined. In the case of the later, the Purcell factor, giving the acceleration of the spontaneous emission, is derived. After a few examples in atomic physics, the case of solid-state emitters is discussed both theoretically and experimentally. The different existing cavity geometries are described. Then, the coupling of ensembles of CNT and individual nanotubes is

discussed as well as the device used in this work.

1.1 Light - Matter Coupling

An excited two-level system can release its energy towards its electromagnetic surrounding through a process called spontaneous emission : an electron decays from an upper to a lower energy level by emitting a photon with the corresponding energy. This process happens at a certain rate γ and yields an optical spectrum consisting in a Lorentzian line of width $\hbar\gamma$. However, these properties are not intrinsic to the emitter, they can be tuned if the electromagnetic surrounding of the emitter is modified, for example by the introduction of a resonant cavity. In the following, the case of an atom in free-space is described as well as the case in which it interacts with a cavity (Jaynes-Cummings model).

1.1.1 Atom in free-space

In free-space, meaning in the absence of a cavity, an atom and an electromagnetic field can interact. The three main processes are introduced and the spontaneous emission is investigated.

Emission and absorption

The energy of an atom can only take a series of discrete values (first quantization). For the sake of simplicity, the problem can be restricted to two levels of energy E_1 and $E_2 > E_1$. The electronic population of these two states are noted N_1 and N_2 . At thermal equilibrium, these two populations are related by a Boltzmann distribution :

$$\frac{N_2}{N_1} = e^{-\frac{\Delta E}{k_b T}} \quad (1.1)$$

where $\Delta E = E_2 - E_1$, k_b is the Boltzmann constant and T is the temperature. The interaction between the atom and an electromagnetic field corresponds to the exchange of energy ΔE in the form of a photon of frequency $\nu = \frac{\Delta E}{h}$ (where h is the Planck constant). Three kinds of interactions can occur : the spontaneous emission, the absorption and the stimulated emission.

In the spontaneous emission process, the atom decays spontaneously from the second level to the first level by emitting a photon of frequency ν . The photon is emitted in a random direction with a random phase.

If an electromagnetic wave at frequency ν impinges on the atom, a photon of energy ΔE can be absorbed by promoting one electron from state E_1 to state E_2 .

The third process is called stimulated emission : in that case the presence of a photon at energy $h\nu$ implies the decay of a electron from E_2 to E_1 , generating an

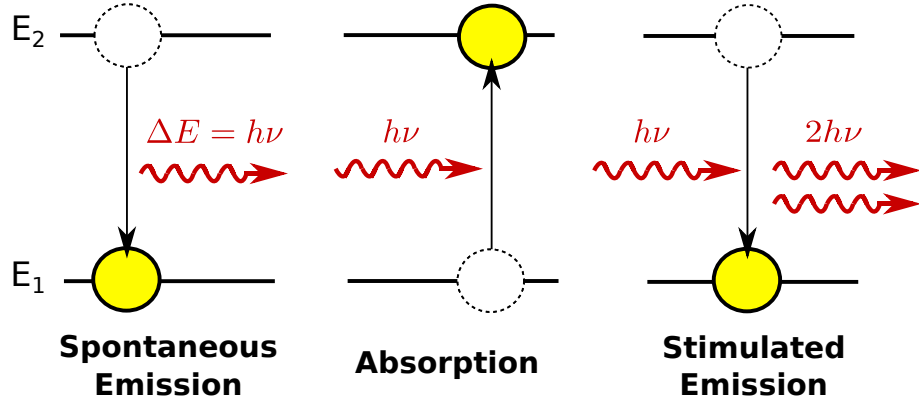


Figure 1.1 – Matter and light can interact through three processes depicted in this figure : the spontaneous emission for which a two-level system decays by generating a photon, the absorption and the stimulated emission for which the arrival of a photon on an excited two level system releases a second photon with the same characteristics.

additional photon at the same frequency, the same phase, same polarization and same direction than the first.

The work undertaken during this PhD focuses on spontaneous emission and how it is modified by the presence of a cavity.

Free-space spontaneous emission

Following [42, (ch. 10)] a lifetime limited emitter (i.e. : an emitter which spectral width is given by the Planck constant times the inverse of its lifetime) is studied in a large box of volume V (the volume will tend towards infinity, ie : the effect of the box on the emitter is negligible).

The spontaneous emission rate is defined as the transition from the excited atom in the empty box (state $|e, 0\rangle$ where e notes an excitation in the two-level system and 0 the absence of photons in the cavity) to the state where the atom is back to its ground level and the cavity contains one photon (state $|g, 1\rangle$ where g notes the ground state of the two-level system and 1 the presence of a photon in the cavity). If \vec{d} is the dipole moment of the emitter, \vec{E} is the electric field and $H = -\vec{d} \cdot \vec{E}$ is the interaction Hamiltonian, the transition rate in free-space is given by the Fermi golden rule :

$$\gamma = \frac{2\pi}{\hbar^2} |\langle e, 0 | -\vec{d} \cdot \vec{E} | g, 1 \rangle|^2 D_oS(\omega) \quad (1.2)$$

where $D_oS(\omega)$ is the density of states. Since the spontaneous emission is investigated, the field responsible for the transition is the vacuum field \vec{E} . The norm of the vacuum field can be obtained by equating the electromagnetic energy in the mode volume V with the zero-point energy $\frac{1}{2}\hbar\omega$. As the time-averaged contributions of the electric and magnetic field are equal, one gets :

$$2 \int \frac{1}{2} \epsilon_0 E_{vac}^2 dV = \frac{1}{2} \hbar \omega \quad (1.3)$$

It leads to an expression for the vacuum field :

$$E_{vac} = \left(\frac{\hbar \omega}{2 \epsilon_0 V} \right)^{1/2} \quad (1.4)$$

The matrix element is then obtained by averaging over all directions (which brings a factor $\frac{1}{3}$) :

$$| \langle e, 0 | - \vec{d} \cdot \vec{E} | g, 1 \rangle |^2 = \frac{1}{3} \mu^2 E_{vac}^2 = \frac{\mu^2 \hbar \omega}{6 \epsilon_0 V} \quad (1.5)$$

where μ is the electric moment of the transition :

$$\vec{\mu} = -e (\langle e, 0 | x | g, 1 \rangle \vec{e}_x + \langle e, 0 | y | g, 1 \rangle \vec{e}_y + \langle e, 0 | z | g, 1 \rangle \vec{e}_z) \quad (1.6)$$

The density of states for photon modes in free-space is given by :

$$DoS(\omega) = \frac{\omega^2 V}{\pi^2 c^3} \quad (1.7)$$

Finally, by injecting equations 1.5 and 1.7 in 1.2 one obtains the transition rate :

$$\gamma = \frac{\mu^2 \omega^3}{3 \pi \epsilon_0 \hbar c^3} \quad (1.8)$$

The spontaneous emission rate of an atom in free-space simply depends on its frequency and its transition moment.

1.1.2 Cavity coupling: the Jaynes-Cummings model

Now that the free-space spontaneous emission of an atom was introduced, the interaction with a perfect cavity is investigated. For that purpose, the Jaynes-Cummings model is presented.

Hamiltonian

The Jaynes-Cummings approach is a simplification of the emitter cavity-coupling in which the cavity is considered to be lossless. The emission comes from a two level system which couples to a single mode of the cavity. The Hamiltonian can be expressed as :

$$H = H_X + H_c + H_I \quad (1.9)$$

The emitter's part of the Hamiltonian simply reads $H_X = \hbar \omega_X |e\rangle \langle e|$ where \hbar is the reduced Planck constant, ω_{em} is the two-level emission frequency and $|e\rangle$ is the

excited state of the system. The cavity's Hamiltonian corresponds to the energy of a photon at the cavity frequency ω_c . It reads $H_c = \hbar\omega_c a^\dagger a$. Finally the interaction between the cavity and the two-level system is given by :

$$H_I = i\hbar g (\hat{a}^\dagger \hat{\sigma}_- - \hat{\sigma}_+ \hat{a}) \quad (1.10)$$

Where \hat{a}^\dagger and \hat{a} are the creation and annihilation operators for a photon in the cavity while $\hat{\sigma}_-$ and $\hat{\sigma}_+$ are the lowering and rising operators for the exciton. The coupling energy g is half the so-called Rabi splitting :

$$2\hbar g = \left(\frac{2\mu^2 \hbar \omega}{\epsilon_0 V} \right)^{1/2} \quad (1.11)$$

The H_I part of the Hamiltonian corresponds to the interaction : it links a state in which the cavity contains n photons and an excited emitter with a state in which the cavity contains $n + 1$ photons and the emitter is at its ground level :

$$\langle e, n | H_I | g, n + 1 \rangle = i\hbar g \sqrt{n + 1} \quad (1.12)$$

In this work, the focus is on single-photon emitters. For the sake of simplicity, the use of the Jaynes-Cummings model is restricted to the case where there is one and only one excitation, which can be either in the two-level system or in the cavity (in the form of a photon). In that case, the subspace becomes $(|g, 1\rangle, |e, 0\rangle)$ and the Hamiltonian can be rewritten as :

$$H = \hbar \begin{bmatrix} \omega_c & ig \\ -ig & \omega_X \end{bmatrix} \quad (1.13)$$

A diagonalization of the Hamiltonian yields the following eigenvalues :

$$E_{\pm} = \hbar \left(\omega_c - \frac{\delta}{2} \pm \frac{1}{2} \sqrt{4g^2 + \delta^2} \right) \quad (1.14)$$

Where $\delta = \omega_c - \omega_X$ is the detuning between the cavity frequency and the emitter's frequency. The energy splitting $\Delta E = E_+ - E_-$ between these two values reads :

$$\Delta E = \hbar \sqrt{4g^2 + \delta^2} \quad (1.15)$$

If one defines an angle θ such that $\tan \theta = \frac{2g}{\delta}$, the eigenvectors of the problem $|\Psi_{\pm}\rangle$ are given by :

$$|\Psi_+\rangle = \cos \theta |g, 1\rangle + \sin \theta |e, 0\rangle \quad (1.16)$$

$$|\Psi_-\rangle = \sin \theta |g, 1\rangle + \cos \theta |e, 0\rangle \quad (1.17)$$

Here, the two states are entangled (excitation in the matter and excitation in the

light). This entanglement is maximized if the cavity is resonant with the emitter ($\delta = 0$) :

$$|\Psi_{\pm}\rangle = \frac{1}{\sqrt{2}} (|g, 1\rangle \pm |e, 0\rangle) \quad (1.18)$$

Rabi oscillations

From this model, it is possible to predict the temporal evolution of the system. In this case, the system at $t = 0$ corresponds to a state where the two-level system is excited and the cavity empty : $|\Psi(t = 0)\rangle = |e, 0\rangle$ (It is assumed that the cavity and the emitter are resonant). In the eigenstate basis, this rewrites :

$$|\Psi(t = 0)\rangle = \frac{1}{\sqrt{2}} (|\Psi_{+}\rangle + |\Psi_{-}\rangle) \quad (1.19)$$

The evolution of the system is given by :

$$|\Psi(t)\rangle = \frac{1}{\sqrt{2}} (|\Psi_{+}\rangle e^{-iE_{+}t/\hbar} + |\Psi_{-}\rangle e^{-iE_{-}t/\hbar}) \quad (1.20)$$

$$= e^{i\omega t} (-i|g, 1\rangle \sin(gt) + |e, 0\rangle \cos(gt)) \quad (1.21)$$

The system oscillates between the two states : the one for which the energy is stored in the two-level system and the one for which the energy is stored in the form of a photon. At any time, the probability to find the excitation in the two-level system is given by :

$$P(t) = |\langle e, 0 | \Psi(t) \rangle|^2 = \cos^2(gt) \quad (1.22)$$

This coherent exchange of energy between the emitter and the cavity is called *vacuum Rabi oscillations*. However, the situation investigated here is idealized.

1.2 Purcell effect

In the previous section, it was shown that the spontaneous emission not only depends on the properties of the emitter but also on its environment. This phenomenon was stated by Purcell in 1946 [31]. In particular, the so-called Purcell effect describes the acceleration of the spontaneous emission when a resonant cavity surrounds the emitter in the weak-coupling regime.

In order to go further, the Jaynes-Cummings model introduced in the previous section is completed by the addition of losses in the cavity. An other approach, relying the Fermi golden rule is employed to investigate the weak-coupling regime and to derive the Purcell factor. Then, some experimental achievements are discussed.

1.2.1 Purcell factor

The Purcell effect is the acceleration of the spontaneous emission in the weak-coupling regime. This regime is defined and the expression of the Purcell factor derived.

The lossy cavity

In this section, two kinds of losses are considered. First, the emitter can couple to electromagnetic modes out of the Hilbert subspace under study, at a rate γ . Second, it is considered that the photons spend a finite amount of time τ_{cav} in the cavity. This phenomenon can be described by the decay rate of the cavity κ , which corresponds to the rate at which the photons are likely to leak out. The cavity can also be characterized by its mode linewidth $\hbar\kappa$ or by its quality factor :

$$Q = \frac{\omega_c}{\kappa} \quad (1.23)$$

If the space is still restricted to a maximum of one excitation, it can be restricted to the subspace $|e, 0\rangle, |g, 1\rangle, |g, 0\rangle$. Using the density matrix formalism, one can explore two quantities : the complex electric field in the cavity, which is proportional to $\langle g, 1|\rho|g, 0\rangle$ and the atomic dipole, which is proportional to $\langle e, 0|\rho|g, 0\rangle$. As state $|g, 1\rangle$ decays towards state $|g, 0\rangle$ at a rate κ , and state $|e, 0\rangle$ towards state $|g, 0\rangle$ at a rate γ , the density matrix evolution is given by [43] :

$$\begin{cases} \frac{d}{dt}\langle g, 1|\rho|g, 0\rangle &= g\langle e, 0|\rho|g, 0\rangle - (i\omega_X + \frac{\gamma}{2})\langle g, 1|\rho|g, 0\rangle \\ \frac{d}{dt}\langle e, 0|\rho|g, 0\rangle &= -g\langle g, 1|\rho|g, 0\rangle - (i\omega_c + \frac{\kappa}{2})\langle e, 0|\rho|g, 0\rangle \end{cases} \quad (1.24)$$

These two equations correspond to the evolution of two classical oscillators coupled and damped :

$$\frac{d^2x}{dt^2} + (2i\omega_X + \frac{\kappa + \gamma}{2})\frac{dx}{dt} + (\frac{\gamma}{2} + i\omega_X)(\frac{\kappa}{2} + i\omega_X) + g^2x = 0 \quad (1.25)$$

When the emitter is in resonance with the cavity ($\omega_c = \omega_X$), the complex values λ characterizing the system's evolution are solution of the equation :

$$\lambda^2 + (2i\omega_X + \frac{\kappa + \gamma}{2})\lambda + (\frac{\gamma}{2} + i\omega_X)(\frac{\kappa}{2} + i\omega_X) + g^2 = 0 \quad (1.26)$$

The spectrum $S(\omega)$ of the emission in the cavity is a function of the roots λ_{\pm} [44] :

$$S(\omega) \propto \left| \frac{\lambda_+ - \omega_X + i\frac{\kappa}{2}}{\omega - \lambda_+} - \frac{\lambda_- - \omega_X + i\frac{\kappa}{2}}{\omega - \lambda_-} \right|^2 \quad (1.27)$$

Depending on the sign of the discriminant $\Delta = \left(\frac{\kappa - \gamma}{2}\right)^2 - 4g^2$, two solutions can arise : the strong and the weak coupling regimes.

Strong and weak coupling regimes

The *strong coupling regime* is defined by $g > \frac{|\kappa - \gamma|}{4}$. This corresponds to the case for which the coupling between the cavity and the emitter is stronger than the losses of the system (the case treated in paragraph 1.1.2 falls in that category). In other words, the photon emitted by the relaxation of the two-level system stays in the cavity until it is reabsorbed. The solutions of equation 1.26 are given by [44] :

$$\lambda_{\pm} = \omega_X \pm \sqrt{g^2 - \frac{(\kappa - \gamma)^2}{16}} - \frac{i}{4}(\kappa + \gamma) \quad (1.28)$$

The Rabi oscillations are simply damped at a rate $\frac{\gamma + \kappa}{4}$ given by the imaginary part of λ_{\pm} . Spectrally, this strong coupling regime is characterized by the splitting around the resonant frequency, between two lines of width $\frac{|\kappa + \gamma|}{2}$ located at $\omega_X \pm \sqrt{g^2 - \frac{(\kappa - \gamma)^2}{16}}$ (real part of λ_{\pm}).

Conversely, the *weak coupling regime* is defined by $g < \frac{|\kappa - \gamma|}{4}$. In that case, the losses overcome the coupling between the cavity and the emitter. In other words, the photon emitted by the two-level system leaks out of the cavity too fast for Rabi oscillations to happen. The roots of eq. (1.26) are [44] :

$$\lambda_{\pm} = \omega_X \pm i\sqrt{\frac{(\kappa - \gamma)^2}{16} - g^2} - \frac{i}{4}(\kappa + \gamma) \quad (1.29)$$

This time, the real part is simply ω_X : there is only one oscillation frequency for the system, which is the frequency of the emitter. The degeneracy lift due to the coupling is entirely canceled by the losses. However the system has two relaxation rates γ_{\pm} . In the case for which $\kappa \gg \gamma$:

$$\gamma_+ \simeq \frac{\kappa}{2} \quad (1.30)$$

$$\gamma_- \simeq \frac{\gamma}{2} + \frac{2g^2}{\kappa} \quad (1.31)$$

Consequently, the spontaneous emission rate of the two-level system in cavity in the weak coupling regime γ_{weak} is given by [44] :

$$\gamma_{weak} = \gamma + \frac{4g^2}{\kappa} \quad (1.32)$$

This acceleration is the so-called Purcell effect. As this is the main focus of this work, this situation is investigated in more details in the following section.

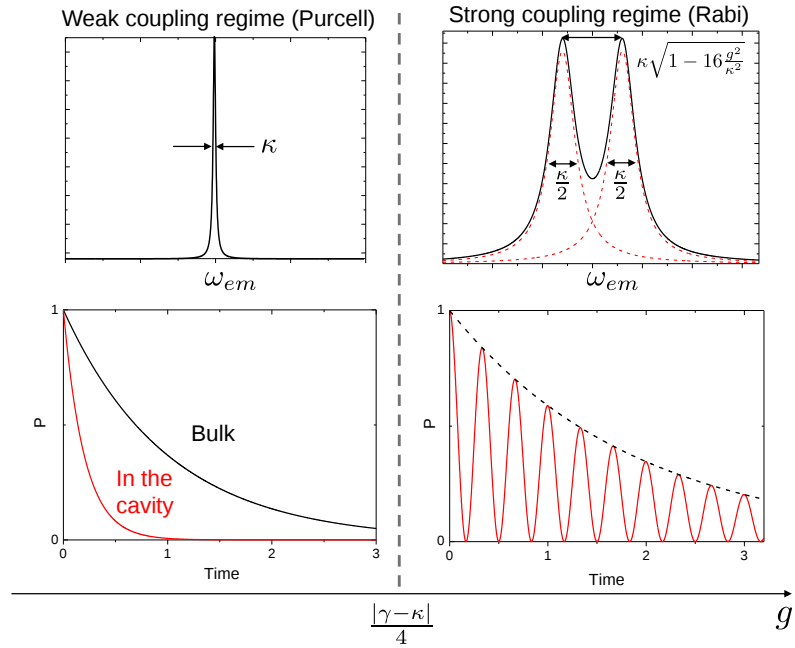


Figure 1.2 – Spectral (top) and temporal (bottom) characteristics of weak coupling (left) and strong coupling (right) regimes in the case where $\kappa \gg \gamma$. In the top left panel, the black line shows that the emission spectrum is Lorentzian. In the top right panel, the contribution of the two states is depicted in dashed red and the total spectrum is in black. In the bottom left, the black line shows the decay of the emitter and the red line its decay when coupled to the cavity. In the bottom right panel, the red line shows the damped Rabi oscillation while the dashed blacked line shows the damping envelope. Figure adapted from [45], with the author’s permission.

The Fermi golden rule approach

In order to calculate the Purcell factor with the Fermi golden rule, two assumptions are made : first, the cavity is single-mode, which means here that it has only one mode close to resonance with the emitter (the other modes are encompassed in γ). Second, the cavity mode is a Lorentzian of Full Width at Half Maximum (FWHM) $\kappa = \frac{\omega_c}{Q}$ where Q is the quality factor of the cavity and ω_c is the cavity resonant frequency.

The density of states in a cavity mode is given by [42, (ch. 10)] :

$$DoS(\omega) = \frac{2}{\pi\kappa} \frac{\kappa^2}{4(\omega - \omega_c)^2 + \kappa^2} \quad (1.33)$$

The density of states is normalized (assumption that there is only one resonant mode) :

$$\int_0^\infty DoS(\omega)d\omega = 1 \quad (1.34)$$

If one assumes that the two-level system transition is very narrow compared to κ and happens at a frequency ω_0 , the density to consider is simply $DoS(\omega_0)$. And the spontaneous emission rate in the cavity mode can be calculated from the Fermi golden rule :

$$\gamma_{TLS \rightarrow cav} = \frac{2\pi}{\hbar^2} |\langle e, 0 | -\vec{d} \cdot \vec{E}(\vec{r}) | g, 1 \rangle|^2 DoS(\omega_0) \quad (1.35)$$

As for the atom in free-space, \vec{d} is the dipole moment of the emitter, $\vec{E}(\vec{r})$ is the local electric field at the emitter location \vec{r} and $H = -\vec{d} \cdot \vec{E}(\vec{r})$ is the interaction Hamiltonian. Similarly to what was calculated in eq. (1.5), the matrix element can be expressed as :

$$|\langle e, 0 | -\vec{d} \cdot \vec{E}(\vec{r}) | g, 1 \rangle|^2 = \frac{\hbar\omega}{2\epsilon_0 V} |\vec{d} \cdot \vec{\epsilon}(\vec{r})|^2 \quad (1.36)$$

where V is the volume of the cavity, and $\vec{\epsilon}(\vec{r})$ is the normalized mode function. The Fermi golden rule rewrites as :

$$\gamma_{TLS \rightarrow cav} = \frac{2Q}{\hbar\epsilon_0 V} |\vec{d} \cdot \vec{\epsilon}(\vec{r})|^2 \frac{\kappa^2}{4\delta^2 + \kappa^2} \quad (1.37)$$

Where the detuning reads $\delta = \omega_c - \omega_X$. The ratio between the spontaneous emission rate in the cavity mode (eq. (1.8)) and the spontaneous emission rate in free-space (eq. (1.37)) reads :

$$\frac{\gamma_{TLS \rightarrow cav}}{\gamma} = \frac{3Q(\lambda/n)^3}{4\pi^2 V} \frac{|\vec{d} \cdot \vec{\epsilon}(\vec{r})|^2}{\mu^2} \frac{\kappa^2}{4\delta^2 + \kappa^2} \quad (1.38)$$

where λ is the wavelength, n the optical index of the material around the emitter

(c/ω is replaced by $(\lambda/n)/2\pi$). In eq. (1.38) one can already see that a strong acceleration of the radiative rate is submitted to two matching conditions :

- The *spatial matching* specifies that the emitter must be located in a maximum of the electric field of the cavity and the dipole must be oriented along the field (In that case $|\vec{d} \cdot \vec{\epsilon}(\vec{r})| = \mu^2$).
- The *spectral matching* specifies that the resonant energy of the cavity must match the optical transition of the emitter (detuning $\delta = 0$).

The Purcell factor F_p is defined in the case where both the spatial and spectral matching are obtained. It reads :

$$F_p = \frac{3Q(\lambda/n)^3}{4\pi^2V} \quad (1.39)$$

The total decay rate of the emitter in the cavity γ_{cav} is its emission in the cavity mode $\gamma_{TLS \rightarrow cav}$ plus its spontaneous emission towards all space γ , if the inhibition due to the cavity is neglected¹ :

$$\gamma_{cav} = \gamma + \gamma_{TLS \rightarrow cav} \quad (1.40)$$

$$= \gamma(1 + F_p) \quad (1.41)$$

The Purcell factor, as defined here, only depends on the cavity and quantifies the acceleration it can provide to an atom's spontaneous emission rate. This factor increases linearly with the quality factor of the cavity and the inverse of its volume. However this ideal case holds only when the emitter's linewidth is much sharper than the one of the cavity, which is generally not the case for condensed matter emitters.

1.2.2 High quality factor cavities

In eq. (1.39), it is visible that the Purcell factor depends mostly on two parameters : it increases with the inverse of the mode volume and with the quality factor. Now, two experimental implementations of this Purcell factor is introduced.

The case of Rydberg Atoms

The first experimental proof of emitter-cavity coupling was done with Rydberg atoms in 1983 in the group of S. Haroche [47]. A circular Rydberg state, is a state with a high principal quantum number n^2 and with maximal orbital and magnetic quantum number (l and m_l). Such Rydberg atoms have a large size, proportional to n^2 . Consequently, they exhibit strong interactions with electric and magnetic fields.

¹If the cavity blocks the emission towards a portion α of the space, one must consider that the non-directional emission in the cavity becomes $(1-\alpha)\gamma$ and the total emission $\gamma(1-\alpha+F_p)$. In most case, α is negligible and in any case, for a sizable Purcell effect $F_p \gg 1$, one has : $\gamma_{cav} \approx \gamma_{cav mode}$. See ref [46] for details.

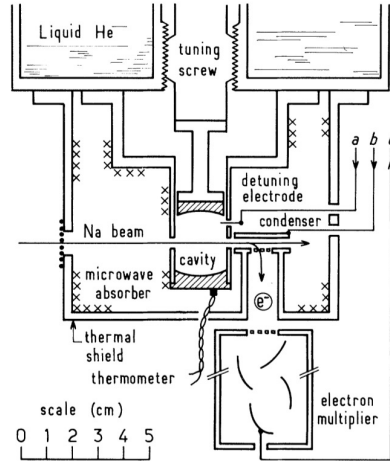


Figure 1.3 – Experimental schema of the setup built by Haroche et al. for the first demonstration of the Purcell factor, on Rydberg atoms. Reprinted figure with permission from *Goy, Raimond, Gross, and Haroche, S, Physical review letters 50, 24 (1983) [47]*. Copyright 1983 by the American Physical Society.

Experimentally, Haroche et al. used Na atoms for which the transition frequency between the two states of interest is $\nu_0 = 340$ GHz. It corresponds to a wavelength $\lambda_0 = 0.8$ mm. Given that large wavelength, obtaining a low ratio $\frac{V}{\lambda_0^3} \approx 1$ is achievable even with a macroscopic cavity (about a millimeter cube). However, the main difficulty resides in obtaining a significant quality factor.

The cavity used in this experiment is a Fabry-Perot resonator. It consists in two mirrors facing each other. The interferences lead to stationary modes. The volume of the mode depends mostly on the curvature of the mirrors while the quality factor increases with their reflectivity. However, this quality factor is limited by the scattering at the surface of the mirrors and their finite size (a small part of the mode is lost at each reflection on the edges). The quality factor obtained in the experiment mentioned above was $7.5 \cdot 10^5$ (since then quality factors three orders of magnitude higher were observed [48]). As a consequence, a rough estimation of the Purcell factor from eq. (1.39), yields $F_p = 5 \cdot 10^4$ for a mode volume equal to λ_0^3 . With an effective² mode volume of $V_{eff} = 70$ mm³, the change observed in the emission rate of the atoms led to an experimentally estimated Purcell factor of $F_p = 5 \cdot 10^2$.

The case of micro-sphere cavities

The Fabry-Perot cavities described above enable to observe high Purcell factor due to their high quality factor. However, reaching lower mode volumes helps to increase the Purcell factor, or to obtain an equivalent Purcell factor for lower wavelengths. In

²The effective mode volume is calculated from the electric field and may be different than the geometrical volume. This topic is discussed in section 3.2.

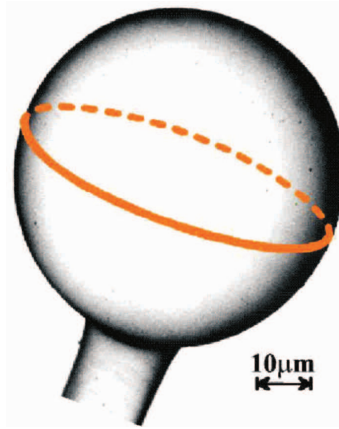


Figure 1.4 – Scanning electronic microscope image of a fused-silica micro-sphere, 56 μm microns in diameter. Reprinted figure from [49] under CC BY-NC-SA 3.0 license.

this view, some researchers investigated the coupling of cooled atoms to micro-sphere which can have both a small mode volume and very high quality factor.

Such cavities consist in a dielectric micro-sphere, as depicted in fig. 1.4, with a refractive index higher than the one of the surrounding medium. The light is trapped by total internal reflection around the equator of the sphere, in the so-called whispering gallery modes (WGM). Typically, in the case of silica micro-spheres, diameters such as 40 μm can be reached, leading to mode volume of $V_{eff} = 100 \mu\text{m}^3$ [49]. At the same time, the quality factors obtained can reach up to 10^{10} [50].

With such low mode volumes, it is possible to observe Purcell effect for atomic transitions in the visible range or the infrared. However, the difficulty with this technique arises in the coupling of light with the WGM. The coupling process is done by frustrated total internal reflection : a material of high refractive index is brought close to the sphere and some of the light tunnels into it. With this technique, the typical coupling reaches 30% [49].

1.3 Purcell effect in condensed matter

Though coupling atoms to cavities led to an interesting tuning of their emission properties, applications remained hindered by the difficulty of integrating them into devices. In this frame, a strong interest developed for condensed matter emitters.

However, in such a case the quality factor of the cavity is no longer the limiting factor : due to interactions with its environment, the emitter can have a quality factor lower than the one of an atom. Consequently, for a given emitter, the strategy for obtaining a sizable Purcell factor relies mostly on lowering the mode volume of the cavity.

In this section, the generalized Purcell Factor for a solid state emitter coupled to

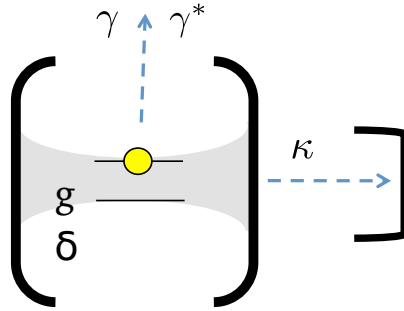


Figure 1.5 – An emitter with relaxation rate γ , undergoing pure dephasing modeled by a rate γ^* is coupled with a factor g to a cavity of linewidth κ and detuned of δ . Adapted figure with permission from Auffèves, Gerace, Gérard, França Santos and Andreani, *Phys. Rev. B* 81, 24 (2010) [35]. Copyright 2010 by the American Physical Society.

a cavity is derived and several examples of micro-cavities are described. Finally, the case of carbon nanotubes is discussed.

1.3.1 Purcell factor for a condensed matter emitter

In condensed matter *artificial atoms*, the coupling to the environment can include phonon assisted mechanisms [51, 20] or spectral diffusion at different time scales [52, 53]. Pure dephasing phenomena lead to a decoherent broadening of the transition line, which can overcome the cavity’s linewidth. Indeed, in our experiment, the typical width of the cavity is $30 \mu\text{eV}$ while the nanotube’s FWHM ranges from $300 \mu\text{eV}$ to 2meV (while the lifetime limit of the transition is around a few μeV).

Introducing the pure dephasing in the emitter - cavity coupling

The case of the phonon assisted transitions is left for chapter 6. Following the work of Auffèves et al. [34, 35] this section restricts to a condensed-matter emitter undergoing pure dephasing. Its emission is described by a Lorentzian³ of width $\gamma + \gamma^*$ where $\gamma = \frac{1}{\tau_{FS}}$ is its relaxation rate, inversely proportional to its free-space lifetime τ_{FS} . γ^* is an additional relaxation term that takes into account pure dephasing [35, 54]. All the parameters are summed up in figure 1.5.

The cavity itself keeps the parameters defined in the previous sections : its frequency ω_c , its FWHM κ , its quality factor $Q = \frac{\omega_c}{\kappa}$ and the detuning δ with the emitter of frequency ω_X : $\delta = \omega_c - \omega_X$.

The Hamiltonian of the system can be written [35] :

³Let’s underline once again that the model developed here holds only for a Lorentzian emitter. A more general description is given in chapter 6

$$H = \hbar\omega_X \hat{\sigma}_+ \hat{\sigma}_- + \hbar\omega_c \hat{a}^\dagger \hat{a} + i\hbar g (\hat{a}^\dagger \hat{\sigma}_- - \hat{\sigma}_+ \hat{a}) \quad (1.42)$$

Where \hat{a}^\dagger and \hat{a} are the creation and annihilation operators for a photon in the cavity while $\hat{\sigma}_-$ and $\hat{\sigma}_+$ are the lowering and rising operators for the exciton. The quantum evolution of the system is governed by a master equation containing damping and dephasing terms :

$$\dot{\rho} = i\hbar[\rho, H] + \mathcal{L}_{damp}^{cav} + \mathcal{L}_{damp}^X + \mathcal{L}_{deph} \quad (1.43)$$

The first damping Lindblad operators is here to take into account the losses of the cavity and reads :

$$\mathcal{L}_{damp}^{cav} = \frac{\hbar\kappa}{2} (2\hat{a}\rho\hat{a}^\dagger - \hat{a}^\dagger\hat{a}\rho - \rho\hat{a}^\dagger\hat{a}) \quad (1.44)$$

The decay rate of the emitter is described by \mathcal{L}_{damp}^X :

$$\mathcal{L}_{damp}^X = \frac{\hbar\gamma}{2} (2\hat{\sigma}_-\rho\hat{\sigma}_+ - \hat{\sigma}_+\hat{\sigma}_-\rho - \rho\hat{\sigma}_+\hat{\sigma}_-) \quad (1.45)$$

The third Lindblad operator takes into account the pure dephasing channel :

$$\mathcal{L}_{deph} = \frac{\hbar\gamma^*}{4} (\hat{\sigma}_z \rho \hat{\sigma}_z - \rho) \quad (1.46)$$

where $\hat{\sigma}_z$ is the Pauli matrix. The Lindblad operators are noted $\mathcal{L} = \mathcal{L}_{damp}^{cav} + \mathcal{L}_{damp}^X + \mathcal{L}_{deph}$.

The population evolutions for an operator A (such as $\hat{\sigma}_+\hat{\sigma}_-$) can be derived by writing :

$$\frac{d\langle A \rangle}{dt} = \frac{dTr(\rho A)}{dt} = Tr(\dot{\rho} A) \quad (1.47)$$

$$= Tr((i\hbar[\rho, H] + \mathcal{L}) A) \quad (1.48)$$

$$= Tr(i\hbar\rho[H, A]) + Tr(\mathcal{L} A) \quad (1.49)$$

$$= i\hbar\langle[H, A]\rangle + Tr(\mathcal{L} A) \quad (1.50)$$

The four operators expectation values are related by :

$$\frac{d}{dt} \begin{pmatrix} \langle \hat{\sigma}_+ \hat{\sigma}_- \rangle \\ \langle \hat{a}^\dagger \hat{a} \rangle \\ \langle \hat{a}^\dagger \hat{\sigma}_- \rangle \\ \langle \hat{\sigma}_+ \hat{a} \rangle \end{pmatrix} = M \begin{pmatrix} \langle \hat{\sigma}_+ \hat{\sigma}_- \rangle \\ \langle \hat{a}^\dagger \hat{a} \rangle \\ \langle \hat{a}^\dagger \hat{\sigma}_- \rangle \\ \langle \hat{\sigma}_+ \hat{a} \rangle \end{pmatrix} \quad (1.51)$$

Where

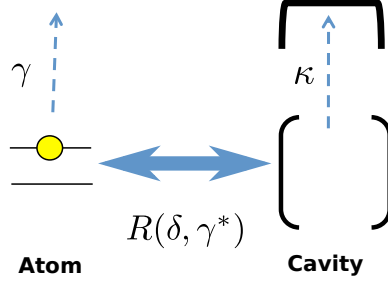


Figure 1.6 – The cavity coupled to the condensed matter emitter is formally equivalent to a two boxes system. One box represents an ideal two-level system (atom) decays at a rate γ while the other box represents the cavity, decaying at a rate κ . The two boxes are coupled by an exchange rate R which depends on the detuning δ and the pure dephasing γ^* . Adapted figure with permission from *Auffeves, Gerace, Gérard, França Santos and Andreani, Phys. Rev. B 81, 24 (2010)* [35]. Copyright 2010 by the American Physical Society.

$$M = \hbar \begin{pmatrix} -\gamma & 0 & -g & -g \\ 0 & -\kappa & g & g \\ g & -g & -i\delta - \frac{\gamma_{all}}{2} & 0 \\ g & -g & 0 & -\frac{\gamma_{all}}{2} + i\delta \end{pmatrix} \quad (1.52)$$

And the total dephasing term is :

$$\gamma_{all} \equiv \kappa + \gamma + \gamma^* \quad (1.53)$$

One can diagonalize the matrix M in order to find its eigenvalues. In a simple picture, one can consider that the first two, λ_1 and λ_2 , describe what happens for the evolution of an excitation in the matter $\langle \hat{\sigma}_+ \hat{\sigma}_- \rangle$ and what happens for the evolution of an excitation in the cavity $\langle \hat{a}^\dagger \hat{a} \rangle$. They read :

$$\begin{cases} \lambda_1 & = -(\gamma + R) \\ \lambda_2 & = -(\kappa + R) \end{cases} \quad (1.54)$$

The parameter R describes an effective coupling rate between the cavity and the emitter [35] :

$$R = \frac{4g^2}{\gamma_{all} \left(1 + \left(\frac{2\delta}{\gamma_{all}} \right)^2 \right)} \quad (1.55)$$

The system can be viewed as the coupling between two boxes : an ideal two-level system box is initially launched with a quantum of energy (excitation in the emitter). It can escape in the environment with a rate γ or in the cavity box at a rate R . Once the excitation is in the cavity box, it can be reabsorbed by the emitter with a probability per unit of time R or leak out of the cavity at a rate κ . This view is

depicted in figure 1.6.

Generalized Purcell Factor

The evolution of $\langle \hat{\sigma}_+ \hat{\sigma}_- \rangle$ is a mono-exponential decay with a characteristic time $1/\lambda_1$: $e^{-(\gamma+R)t}$. In other words, the emission rate in the cavity is $\gamma + R = \gamma(1 + R/\gamma)$. The generalized Purcell factor F_p^* is defined as the additional emission rate in the cavity mode at zero detuning :

$$F_p^* = \frac{R(\delta = 0)}{\gamma} \quad (1.56)$$

$$F_p^* = \frac{4g^2}{\gamma\gamma_{all}} \quad (1.57)$$

In order to compare this generalized Purcell factor to the usual one, the later has to be rewritten. The decay rate of the emitter in the cavity mode $\gamma_{TLS \rightarrow cav}$ is given at resonance by (eq. (1.31)) :

$$\gamma_{TLS \rightarrow cav} = \frac{4g^2 Q}{\omega_c} \quad (1.58)$$

which means that the (not generalized) Purcell factor at resonance can be written :

$$F_p = \frac{\gamma_{TLS \rightarrow cav}}{\gamma} = \frac{4g^2}{\gamma\kappa} \quad (1.59)$$

The generalized Purcell factor is similar to the usual Purcell factor, provided that the decay rate of the cavity is replaced by the sum of κ and the total emitter's linewidth $\gamma + \gamma^*$. In order to rewrite the generalized Purcell factor in a form similar to equation (1.39), the emitter's quality factor is introduced :

$$Q_{em} = \frac{\omega_x}{\gamma + \gamma^*} \quad (1.60)$$

and the effective quality factor of the cavity-emitter system Q_{eff} :

$$\frac{1}{Q_{eff}} = \frac{1}{Q} + \frac{1}{Q_{em}} \quad (1.61)$$

Finally, the generalized Purcell factor at resonance reads :

$$F_p^* = \frac{3Q_{eff}(\lambda/n)^3}{4\pi^2 V} \quad (1.62)$$

In this expression the cavity's and the emitter's quality factors play a symmetrical role. In fact, for our experiment, the quality factor of the cavity exceeds by two orders of magnitude the one of the emitter, which means that the Purcell effect

is mainly limited by the linewidth of the carbon nanotube. As in the case of the two-level system, the generalized Purcell factor depends on the quality factor and the inverse of the volume. However, this time the quality factor is the one of the emitter and only sample engineering can improve it. On the cavity side, reducing the volume is the only way to increase the spontaneous emission rate.

Efficiency of the cavity coupled emitter

When the emitter is excited, it behaves as if it had two options : one being a decay in the environment at a rate γ , just as in free-space ; the other being a decay into the cavity mode, at a rate R . The energy in the cavity mode itself leaks out into the environment at a rate κ . The losses γ are non-directional, and thus complicated to collect. On the contrary, the cavity mode losses κ can be considered as the useful ones. The effective efficiency β of the cavity coupled emitter, is defined as the percentage of useful losses. It is thus given by :

$$\beta = \frac{\frac{R\kappa}{R+\kappa}}{\gamma + \frac{R\kappa}{R+\kappa}} \quad (1.63)$$

where $\frac{R\kappa}{R+\kappa}$ is the rate at which the emitters relaxes towards the cavity mode and then towards the environment .

If $R > \kappa$, it means that the energy is transferred quicker from the emitter to the cavity than from the cavity to the environment. In other words, a photon emitted spends a finite time in the cavity mode before it leaks out. This regime, called *good cavity regime*, does not necessarily imply a coherent interaction between the emitter and the cavity: the photon can remain in the cavity without being reabsorbed by the emitter.

If $R < \kappa$, it means that the cavity empties out as soon as it gets a photon from the emitter. This *bad cavity regime* is the one used throughout this work. In this regime, the cavity can be considered, in the point of view of the atom, as an additional source of losses.

1.3.2 Light confinement in semi-conductor structures

In the previous sections, the generalized Purcell factor was introduced : it gives the acceleration of the spontaneous emission that can be obtained by tailoring the electromagnetic surroundings of an emitter. Such a modification can be obtained by several means, such as plasmonic or dielectric cavities. In the following paragraphs, different solutions available in condensed matter are discussed.

Micro-pillars

A micro-pillar cavity is a special type of Fabry-Perot cavity which is now widely used with quantum dots. It consists in a cylinder of semi-conductor, as shown in fig. 1.7,

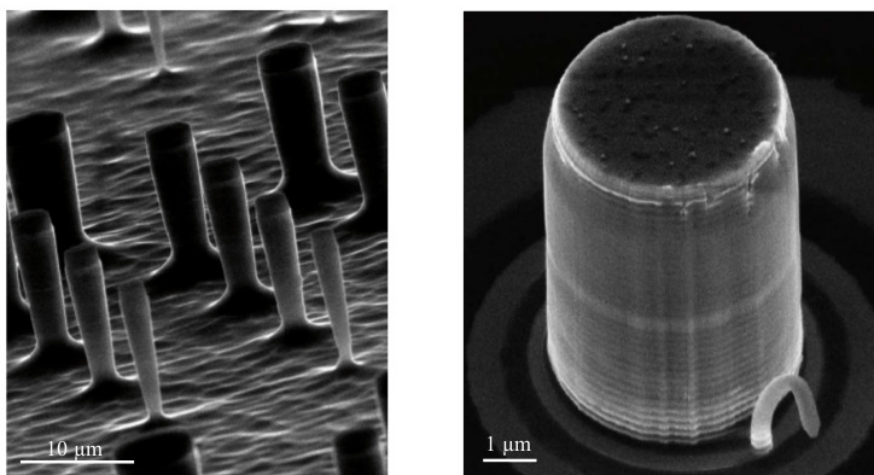


Figure 1.7 – MEB image of micro-pillars. Reprinted figure from [55], with the author’s permission.

which can be roughly divided in three main parts : the bottom mirror, the top mirror, and in between the cavity space in which the emitter is embedded. The two mirrors are Distributed Bragg Reflectors (DBR), which means alternate layers of two materials with a large optical index difference⁴, leading to constructive interferences for a given range of wavelengths.

These cylindrical cavities, typical etched out from a planar cavity, are usually a few micrometers in diameter and 10 μm high. The lowest mode volumes obtained are $0.3 \mu\text{m}^3$ [38], about $10(\lambda/n)^3$, and the usual quality factors are 10^3 and can reach several 10^4 . The photons are emitted along the axis of the pillar. A slight difference in the reflectivity of the two mirrors can induce a suppressed emission towards the bottom, and thus a fully directional emission towards the top of the pillar.

It is this kind of cavities that was used to demonstrate the first acceleration of the spontaneous emission of a QD ensemble in 1998, with a Purcell factor of up to 5 [36]. Since then, the strong coupling regime was reached with InAs QD [38], and more recently, an improvement in the fabrication technique (discussed in section 1.3.2) made such cavities easier to adapt to quantum dot emitters, leading to demonstration of high brightness entangled source [56] or photon indistinguishability [57].

Micro-rings

Micro-rings or micros-disks do not rely on two mirrors to confine light. In that case the structure is a disk with a diameter of a few microns and a thickness low enough to allow a single stable mode λ/n (where n is the optical index). Due to the difference of optical index between the micro-disk material and the air, the light is

⁴A very common structure is the so-called Bragg mirror for which each layer has a thickness $\lambda/4n$ where n is the optical index.

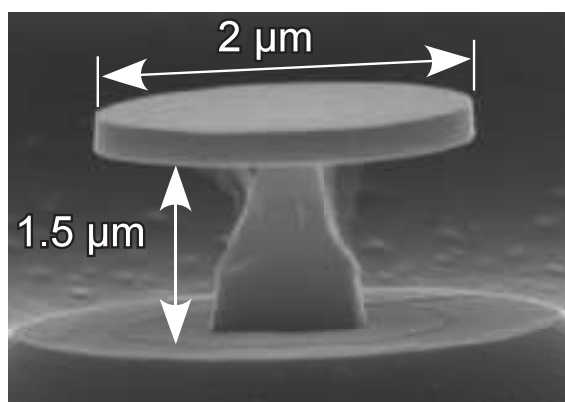


Figure 1.8 – Scanning electron microscopy side view of a $2\ \mu\text{m}$ diameter micro-disk. Reprinted figure with permission from *Peter, Senellart, Martrou, Lemaître, Hours and Gérard, Physical review letters 95, 6 (2005) [58]*. Copyright 2005 by the American Physical Society.

totally reflected at the interface, leading to a three-dimensional confinement in the structure. This kind of modes is close to the one seen for micro-sphere cavities.

Such structures can have mode volumes as low as a few $(\lambda/n)^3$ and quality factors as high as 10^4 , leading to Purcell factors above a 100 [59]. However, the emission of photon is done in the 2D plane of the disk, which means that it is more difficult to extract light than in the case of micro-pillars for example. The strong coupling was reached in 2005 with a quantum dot by E. Peter et al. [58]. And more recently, two teams successfully coupled multiple or ensembles of nanotubes to such microrings (section 1.3.3).

Photonic crystals

A Distributed Bragg Reflector, already introduced in the paragraph about micro-pillars, can be considered as a 1D photonic crystal cavity : it is a periodical sequence of alternate layers of dielectric materials that confines light in one direction of space.

The 2D photonic crystals are obtained from a membrane of a semi-conductor material where holes are periodically created. The light propagating in the membrane faces a lattice of holes with an index $n = 1$ differing strongly from the one of the material. This lattice creates a forbidden band for photons just as a periodic lattice of atoms creates a forbidden band for electrons. A cavity can then be created by omitting one or several holes, as shown in figure 1.9. Vertically, the confinement is obtained by total internal reflection.

Amongst dielectric resonators, photonic crystals are the systems with which one can obtain the lowest optical mode volumes. It can drop down below the diffraction limit $(\frac{\lambda}{2})^3$ (and as low as $0.05\ \mu\text{m}^3$) while keeping quality factors such as $5 \cdot 10^4$ [61]. The photons extracted come from the losses of the cavity that go in a direction perpendicular to the membrane. The emission angular aperture is a function of the

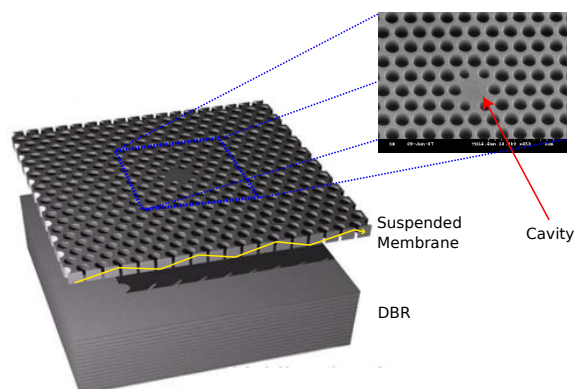


Figure 1.9 – 2D Photonic crystal cavity : the light is confined in the membrane by internal reflection (yellow line). The cavity is obtained by omitting a hole in the lattice. Reprinted figure with permission from *Kim, Kim and Lee, Physical Review B 73, 23 (2006) [60]*. Copyright 2006 by the American Physical Society.

inverse of the contrast of indices between the membrane and its surroundings. The emission can be collected by a high numerical aperture objective.

The coupling of QD to such cavities was demonstrated in 2005, with a Purcell factor of 8 [62]. Indistinguishability [63] and strong coupling [64] were also demonstrated.

Plasmonic cavities

The three different kinds of cavities described above face a limitation in the reduction of their mode volume. In order to go further, it is possible to use Surface Plasmon (SP) modes. A surface plasmon is a coherent delocalized electron oscillation wave propagating along the interface between a metal (typically gold or silver) and a dielectric [65], as shown in fig. 1.10.

Even though plasmonic cavities have a strong asset in their volume, they have three drawbacks. First, they undergo the so-called ohmic losses : their non-radiative decay rate increases strongly when the emitter is close to the surface [67]. As a consequence, a trade-off must be found between increasing the Purcell factor of the emitter (reducing its distance to the interface) and keeping reasonably low ohmic losses (increasing its distance to the surface). This requires a positioning with a nanometric accuracy. The second issue is a consequence of the first : as long as the quality factor is low, it means that the spectral purity of the source is low (ie : the spectrum of the cavity is large). Finally, the emission in surface plasmon cavities remains non-directional [68], which would limit the brightness of devices.

A number of different geometries exist for plasmonic enhancement of a solid state emitter : metallic nano-disks [69], metallic grating [70], metallic nano-wires [37] or metallic antennas [71]. Whatever the geometry, the surface plasmons are confined

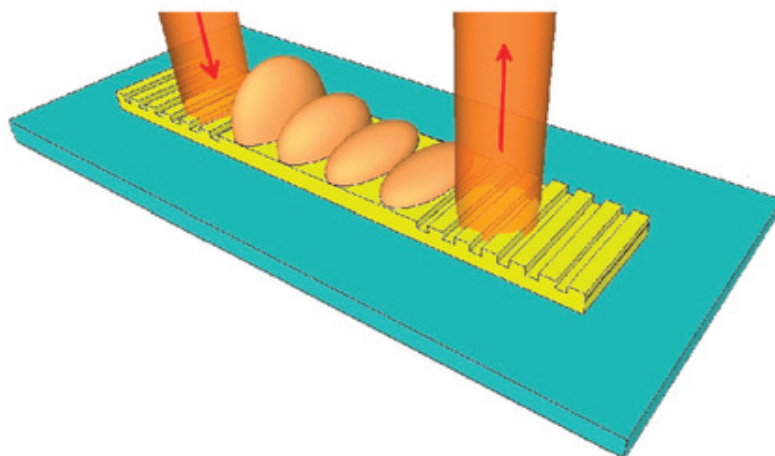


Figure 1.10 – Single SPPs excited in a metallic stripe waveguide by single photons from parametric down conversion. Reprinted figure with permission from *Di Martino, Sonnefraud, Kéna-Cohen, Tame, Özdemir, and Kim, Nano Letters 12, 5 (2012) [66]*. Copyright 2012 by the American Chemical Society.

close to the interface. Consequently, the density of states is strongly increased locally for the emitter, and the effective mode volumes can be well below the diffraction limit. For example, De Leon et al. [72] demonstrated a Purcell factor of 75 with silver nano-wires. In their case, the mode volume is $0.04(\lambda/n)^3$ with a quality factor of 100.

Emitter - Cavity coupling

The previous section described different kind of cavities to which a solid-state emitter - such as a quantum dot - can be coupled. These cavities can be classified by their two parameters of interest : the quality factor Q and the effective mode volume V_{eff} . However the dependence of the Purcell factor on the ratio $\frac{(\lambda/n)^3 Q}{V_{eff}}$ holds only if the cavity is matched to the emitter.

Until 2005, the matching of quantum dots to cavities was randomly achieved. The group of Imamoglu showed for the first time a deterministic coupling with photonic crystal cavities [73]. The method was to grow quantum dots, to locate a given one with an AFM and to measure its spectral characteristics. A photonic crystal cavity was then centered on the quantum dot and its resonant energy adjusted by modifying the size of the holes.

As this method was difficult to achieve, other paths were explored, in particular the control of the growth position of the quantum dots and the use of tunable cavities. However, the most successful method to date to deterministically couple a quantum dot to a cavity is in-situ lithography. This technique was developed in the team of P. Senellart [74]. The first step consists in the growth of a planar cavity with a layer

of quantum dots in between the mirrors. The quantum dots are then located by means of confocal microscope and their optical characteristics are probed. Once a target quantum dot is defined, the planar cavity is etched so as to leave a micro-pillar precisely at the right location. The spectral matching is obtained by tuning the diameter of the micro-pillar created. With this technique, the spatial localization is better than 50 nm and the spectral matching is better than the linewidth of the cavity.

1.3.3 The case of carbon nanotubes

A complete discussion of the properties of carbon nanotubes, and in particular their optical characteristics is given in chapter 2. However, a few trends can already be introduced.

Carbon nanotubes are often obtained, after synthesis, in powders or dilute solutions. In such cases, the deposition of a carbon nanotube at a precise location is difficult. Consequently, the location of a cavity must be adapted to the location of the emitter and not the opposite. In the beginning of the 2000 the growth of carbon nanotubes between two pillars, or over a trench was demonstrated [75].

However these improvements, which can ease spatial matching, do not solve the second issue encountered with CNT : spectral matching. Indeed, it is still difficult to grow carbon nanotubes selectively. Usually, the output of a synthesis is composed of several nanotube species with emission wavelengths varying by hundreds of meV. Furthermore, the emission energy of an individual CNT depends strongly on its immediate surroundings, which means that CNT of the same species, coming from the same production process, can have emission energies varying by tens of meV. As a consequence, the spectral matching of a monolithic cavity to an individual CNT is challenging.

Up to now, two approaches have been investigated to succeed in coupling nanotubes to cavities : the use of nanotube ensembles and random matching. The aim of this project is to move to a deterministic approach and to keep enough flexibility to perform a thorough investigation of the nanotube-cavity coupling in the CQED regime.

Carbon nanotubes ensembles

The first study showing the coupling of an ensemble of carbon nanotubes with a cavity was done by Gaufres et al. [76] in 2010. In that setup, a layer of carbon nanotubes was placed between two dielectric mirrors forming a Fabry-Perot cavity with a quality factor of 160. The thickness of the nanotubes layer was adjusted so that the energy of the cavity mode could roughly match the maximum of the nanotubes emission energy distribution. With the cavity, the photoluminescence was increased by a factor of 30 compared to a film of nanotubes in free-space, the emission was directive in a cone of 6° and the spectral width was 5.5 meV.

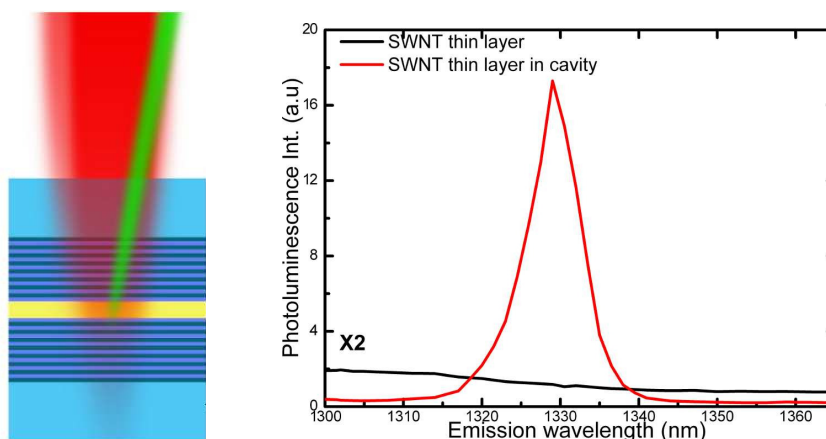


Figure 1.11 – Left : sketch of the optical cavity : a layer of nanotubes is in-between two dielectric mirrors. Right : photoluminescence of a thin layer of nanotubes with and without a cavity. Adapted from *Gaufrès, Izard, Le Roux, Kazaoui, Marris-Morini and Cassan, Optics express 18, 6 (2010) [76]* with permission from OSA Publishing.

Very similarly, in 2013, Legrand et al. [77] coupled a film of nanotubes with a monolithic cavity. In that case, nanotubes were dispersed in a solution with Poly(methyl methacrylate) (PMMA). The cavity was formed by a dielectric mirror on which a nanotubes-PMMA layer was deposited, as shown in fig. 1.12. It was closed by a silver mirror. The cavity was spectrally tuned in resonance with a particular nanotube species by choosing the thickness of the nanotubes-PMMA layer (a thickness of 340 nm was used to obtain a transmission at 1.192 eV). The quality factor of the cavity was about 30. With this monolithic cavity setup, the authors demonstrated their ability to select the emission of a particular CNT species and to obtain a photoluminescence spectral width of 30 meV, mainly limited by the inhomogeneities in the layer's thickness.

The coupling of an ensemble of nanotubes to a Fabry-Perot Cavity was also done by Fujiwara et al. [78]. In that case, a film of CNTs was deposited in a cavity composed either of two gold mirrors (quality factor of 50) or of two dielectric mirrors (quality factors of 180). With this setup, they showed a blackbody emission with a linewidth as narrow as 30 meV arising from their ensemble, around 1.5 μm .

In 2012, Gaufrès et al. [79] coupled an ensemble of carbon nanotubes to a silicon waveguide. The waveguide was made of a 220 nm thick layer of silicon on a 1 μm layer of silica, as shown in fig. 1.13. It had a sub-micrometer width, with a shrinkage in the region of interaction with carbon nanotubes. A film of PFO-wrapped nanotubes was deposited on the waveguide, resulting in a stable emission at the telecoms wavelengths at room temperature and above. The spectral width obtained was 20 meV.

Continuing their work on photonic devices, the same team investigated in 2014 (Noury et al. [80]) the coupling of an ensemble of CNTs to micro-rings having a

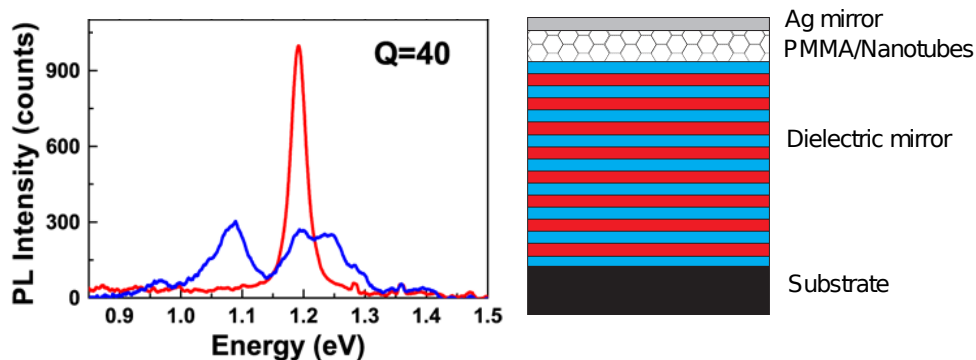


Figure 1.12 – Left, Photoluminescence spectrum of the nanotubes-PMMA layer (blue) and of the cavity excited at 2.331 eV and detected at normal incidence (red). Right : sketch of the optical cavity composed of a dielectric mirror, a layer of nanotubes-PMMA and a silver mirror. Adapted from *Legrand, Roquelet, Lanty, Roussignol, Lafosse, Bouchoule, Deleporte, Voisin and Lauret, Applied Physics Letters 102, 15 (2013)*. [77], with the permission of AIP Publishing.

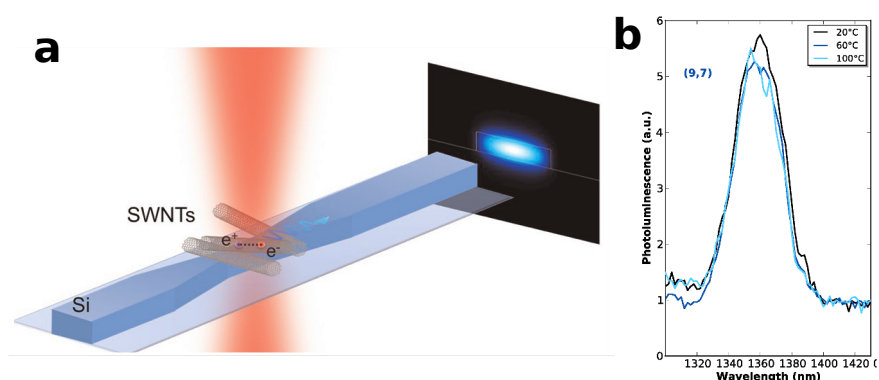


Figure 1.13 – a) Integration scheme of carbon nanotube thin layer composite with silicon waveguide. b) Photoluminescence generated from the (9,7) nanotube under excitation by a 800 nm pump laser, coupled in the silicon waveguide for three temperatures (20, 60, and 100 °C). No wavelength shift or signal reduction are observed. Adapted with permission from *Gaufrès, Izard, Noury, Le Roux, Rasigade, Gilles and Beck, and Vivien, ACS Nano 6, 5 (2012)* [79]. Copyright 2012 American Chemical Society.

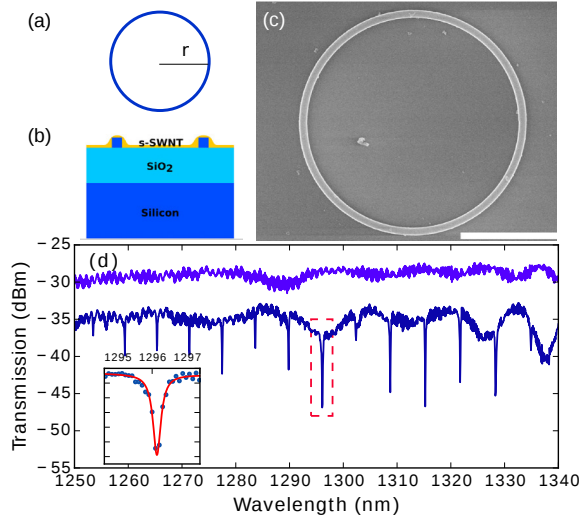


Figure 1.14 – (a) Top view of a micro-ring resonator of radius r . (b) Cross-section of the micro-ring, with polyfluorene-wrapped s-SWNT top layer (not to scale). (c) Scanning electron micrograph of as-fabricated micro-ring, with a radius r of $5\ \mu\text{m}$. The scale bar is $5\ \mu\text{m}$. (d) Transmission spectra of a typical $10\ \mu\text{m}$ radius micro-ring resonator coupled to a strip waveguide (dark blue) and a reference strip waveguide (light blue). The reference was up-shifted by 5 dBm for clarity. The nanotube absorption corresponds to the thin Lorentzian lines. Inset depicts a close view of one of the resonance, fitted with a Lorentzian lineshape (solid line). Courtesy of N. Izzard, corresponding to the data published in [80].

diameters of $5\ \mu\text{m}$ or $10\ \mu\text{m}$ and a quality factor of up to 4000. A layer of PFO-wrapped nanotubes was deposited on the micro-ring, as depicted in figure 1.14. In that case, a significant number of nanotubes were deposited on the cavity so that each of the resonant modes were coupled to several emitters. The authors showed that the coupling led to a spectrum composed of regularly spaced peaks, with a spectral width as low as $250\ \mu\text{eV}$ and a spacing defined by the diameter of the micro-ring.

Very recently, Zakharko et al. [81] coupled a film of nanotubes to a periodic array of gold nano-disks, as shown in fig. 1.15. These nanostructures give rise to hybrid photonic-plasmonic modes referred to as Surface Lattice Resonances (SLRs). The gold nanodisks had a diameter of $160 - 180\ \text{nm}$. They formed a square lattice, which pitch defined the resonant frequency. Nanotubes were sorted to obtain a single species and dispersed randomly over the structure in a $100\ \text{nm}$ film covered by a $150\ \text{nm}$ layer PMMA. The authors demonstrated that with their device, a film of nanotubes emitting around $1000\ \text{nm}$ transforms into a source that can reach the telecoms bands if the pitch is chosen accordingly, with an intensity enhancement of up to 15 and a spectral width of $20\ \text{meV}$. Furthermore, the emission was polarized and directed in a cone as narrow as 1.5° .

Besides carbon nanotubes films, for which a high numbers of emitters couple to

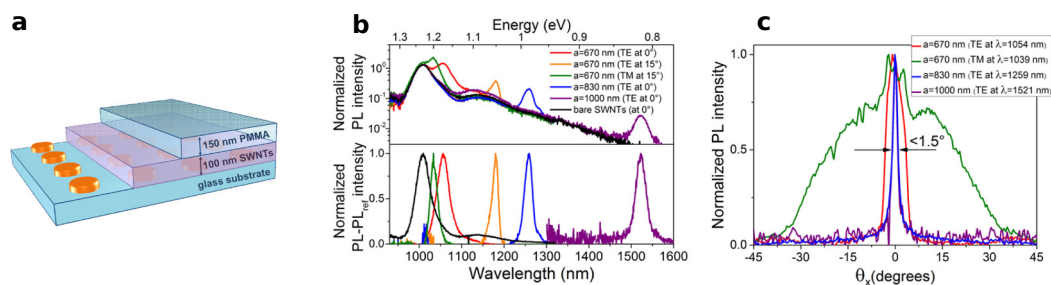


Figure 1.15 – a) Schematic illustration of a sample consisting of a glass substrate, gold nanodisks array, a 100 nm layer of random (6,5) SWNTs and a 150 nm PMMA layer on top. b) Normalized (to E 11 transition, top) and normalized differential (bottom) PL spectra of pure SWNTs (black) and TE-polarized emission normal to the sample surface with pitch 670, 830, and 1000 nm, TE and TM polarizations at $\pm 15^\circ$ for pitch 670 nm. c) Angle dependence of normalized PL for TM-polarized emission for pitch 670 nm (at 1039 nm, green) compared to TE-polarized light at peak positions 1054 (red), 1259 (blue), and 1521 nm (purple) corresponding to the three samples with pitch 670, 830, and 1000 nm. Reprinted with permission from *Zakharko, Graf, Schießl, Hähnlein, Pezoldt, Gather, Malte and Zaumseil, Nano Lett. 16, 5 (2016) [81]*. Published under ACS AuthorChoice License 2016.

the cavity, it is possible to couple a limited number of emitters to a photonic structure. Pyatkov et al. [29] made a photonic crystal nanobeam cavity (PCNBC) by etching a photonic waveguide (width 0.6 μeV) out of a layer of Si_3N_4 suspended over SiO_2 [82], and etching holes in the waveguide, as shown in fig. 1.16. The quality factor of the cavity obtained was about 700 for the fundamental mode. A difference in the lengths of the photonic crystal parts on each side of the nanobeam brought directional emission (exactly as an asymmetry in the reflectivity of two mirrors composing a Fabry-Perot would direct the emission in the direction of lower reflectivity). The nanotubes were sitting either on a hole or on the dielectric part between two holes of the cavity. They were electrically excited by means of two Au/Cr electrodes. With this device, the authors showed an enhanced electroluminescence (by up to a factor 5), with a linewidth limited by the cavity's one (slightly below 2 meV) and a coupling efficiency of 75%.

Pursuing this work, the same group showed that electrically driven CNTs coupled to a waveguide circuit could emit anti-bunched light. In the paper of Khasminskaya et al. [30], semi-conducting nanotubes were deposited on the center of a waveguide. The spectral width of the emitters at room temperature was about 20 meV. Two superconducting nano-wire single-photon detectors (SNSPD) were placed on each side of the waveguide, in order to allow on-site correlation function measurements. With this device, at cryogenic temperature, the autocorrelation function obtained

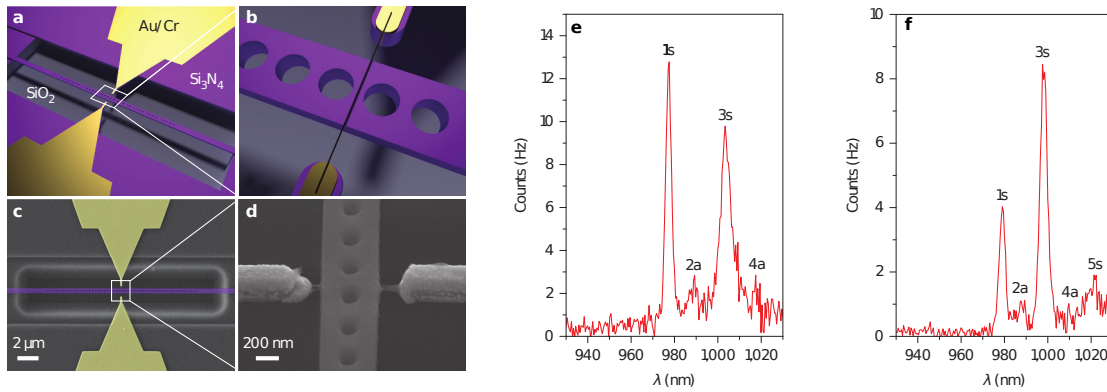


Figure 1.16 – a) Schematic view of the multilayer device structure consisting of two Au/Cr electrodes (yellow) and a photonic waveguide (purple) that is etched into the Si_3N_4 layer. Its central part is underetched into the SiO_2 layer and holes are formed. b) Close-up of the PCNBC illustrating the CNT (black line) in contact with the electrodes on top of the waveguide. c) False-colored SEM image of the PCNBC structure between two electrodes. The cavity center is precisely aligned with the midpoint between the tips of the two electrodes. d) SEM image of the cavity center with the waveguide and two electrodes, bridged by several SWNT. The suspended parts of the CNTs are clearly visible, whereas the material contrast on the waveguide top is too low to resolve the CNTs. e) f) Spectra of electrically driven CNT coupled to the cavity for two devices. Reprinted by permission from Macmillan Publishers Ltd: Nature Photonics *Pyatkov, Futterling, Khasminskaya, Flavel, Hennrich, Kappes, Krupke and Pernice, Nature Photon 10, 6 (2016) [29]*, copyright 2016.

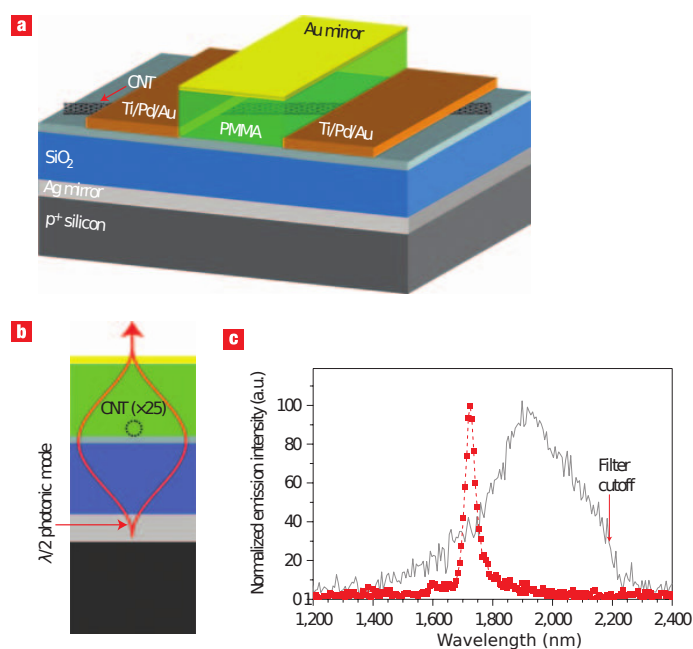


Figure 1.17 – a) 3D schematic representation of the microcavity-controlled infrared nano-light source comprising a field effect transistor integrated with a planar microcavity. b) Schematic photonic mode profile showing the geometrical overlap of the nanotube and the spatial intensity distribution. The microcavity is formed by the Au and Ag mirrors and the light is emitted through the top Au mirror. c) Electroluminescence spectra with (dashed red) and without (solid gray) top gold cavity mirrors under electrical excitation. Reprinted by permission from Macmillan Publishers Ltd: Nature Nanotechnology Xia, Steiner, Lin, and Avouris, *Nature nanotechnology* 3, 10 (2008) [85], copyright 2008.

reached down to $g_2(0) = 0.5^5$ for a lifetime of about a hundred picoseconds. The efficiency of the full device was estimated to 10^{-4} photons per carrier, which is extremely high for electrically driven nanotubes [84].

Individual carbon nanotubes

In cases where a great number of nanotubes are coupled to a cavity, the particular feature of an individual emitter are lost. In order to investigate them, it is necessary to couple a single emitter to a resonant mode of a cavity. The carbon nanotubes

The first work concerning the coupling of an individual nanotube with a cavity was published in 2008 by Xia et al. [85]. The Fabry-Perot cavity was made with a silver and a gold mirror, with a quality factor of 40. In between the mirrors, three

⁵It is unclear here whether there is a non-perfectly anti-bunched single emitter or whether there are two emitters. In section (5.3.2), we will choose $g_2(0) < 0.5$ as our single-photon source criterion. A thorough discussion is given in ref. [83].

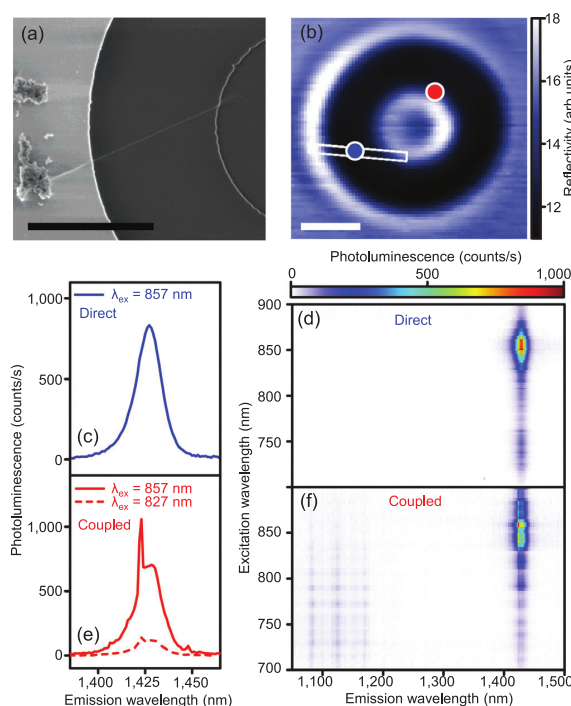


Figure 1.18 – (a) SEM image of a suspended nanotube attached to a micro-disk. (b) Reflectivity image of a device measured in (c)–(f). The disk diameter is 3 μm . Blue and red dots indicate the positions at which the data in (c),(d) and (e),(f) are taken, respectively. The white box shows the position of the suspended nanotube. The scale bars in (a) and (b) are 2 μm . (c) Directly measured PL spectrum of the suspended nanotube. (d) PLE map obtained by direct measurement of the suspended nanotube. (e) PL spectrum of nanotube emission coupled to the micro-disk. (f) PLE map of nanotube emission coupled to the micro-disk. Reprinted from *Imamura, Watahiki, Miura, Shimada, and Kato, Applied Physics Letters 102, 16 (2013) [87]*, with the permission of AIP Publishing.

stacks of dielectric were placed : PMMA, aluminum oxide and silicon oxide. By means of this configuration, the nanotube was placed close to a field maximum and oriented along the mirrors, to secure spatial matching, as can be seen in figure 1.17. The carbon nanotube was electrically excited. As the resulting emission spectrum was much larger than the cavity spectral width, the resonant matching condition was not stringent. The authors observed that while the free-space electroluminescence was spectrally broad (tens of meV), non-directional, and inefficient, the presence of the cavity increased the directionality (10° to 15°) and yielded an enhancement of the collection rate by a factor of 4, with a spectral width of 17 meV. A very similar design was used in 2016 by Liang et al. [86] to make photo-detectors with carbon nanotubes. With it, the authors showed a six-fold enhancement of the photoelectric conversion efficiency, leading to a suppression of the noise and thus to a better detection and recognition of specific signals.

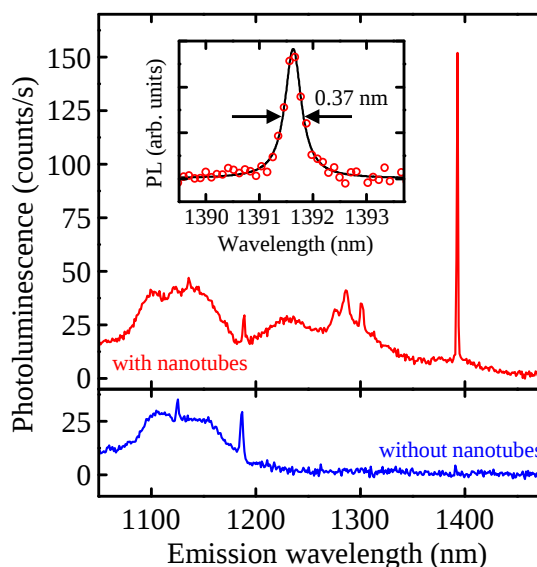


Figure 1.19 – Scanning electron micrographs of as-fabricated crystal photonic cavities. The top left panel shows a plan view, and the middle left panel is an enlarged view of the cavity. The bottom left panel shows a cross section of the slab structure. The scale bars are $2\ \mu\text{m}$, $0.5\ \mu\text{m}$, and $1\ \mu\text{m}$ for the top, middle, and bottom panels, respectively.

The Top and bottom right panels show PL spectra of the cavity with and without nanotubes. Inset shows a higher resolution spectrum of the fundamental mode. Circles are data and the solid line is a Lorentzian fit. Reprinted from *Watahiki, Shimada, Zhao, Chiashi, Iwamoto, Arakawa, Maruyama, and Kato, Applied Physics Letters 101, 14 (2012) [88]*, with the permission of AIP Publishing.

A random matching was obtained by Imamura et. al [87], who grew nanotubes directly on micro-rings. For that they used chemical vapor deposition and were able, with a success rate of 10%, to grow a single nanotube suspended over a trench separating the micro-ring from the bulk material. With a quality factor of 3000 for their WGM, they observed a modification of the PL of their tube due to the cavity. However, as shown in figure 1.18, the spectral purity of their source was limited.

In 2012, Watahiki et al. [88] tackled the challenge of coupling a single nanotube to a photonic crystal cavity. In that case, the cavity was made in a silicon layer with etched holes on an oxide layer. The cavity itself consisted in three missing holes in a line, as can be seen in figure 1.19. Micelles-encapsulated CNT were deposited on the silicon layers leading to the coupling of a few nanotubes with the modes of the cavity. Interestingly, this random matching enabled them to obtain the coupling of a single nanotube to a particular cavity mode, as shown in figure 1.19. In that case, the quality factor was 3800 (limited by the deposition of nanotubes on the device), the spectral width was $230\ \mu\text{eV}$ and the emission enhancement was estimated to at least a factor of 50.

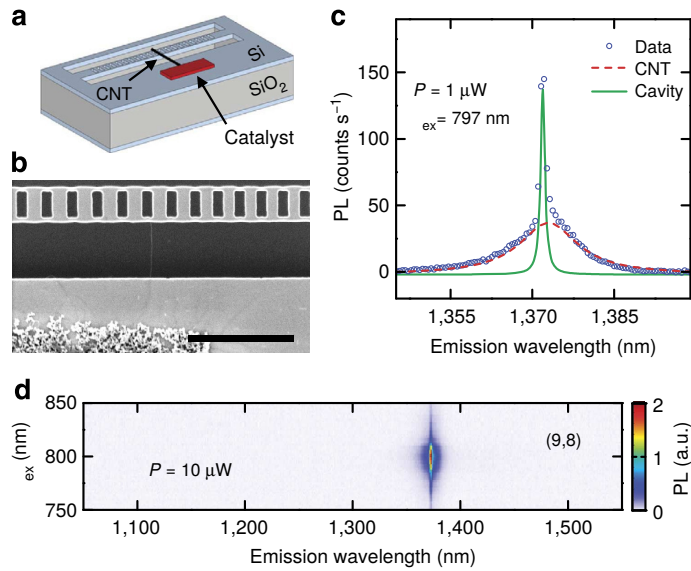


Figure 1.20 – An individual carbon nanotube coupled to a nanobeam cavity. (a) A schematic of a device. (b) Scanning electron microscope image of a device with a suspended nanotube. Scale bar is 2 μm . (c) Typical PL spectrum of an air-mode device coupled to a nanotube. The dots are data and the lines are Lorentzian fits. (d) PL excitation map of the device shown in c taken with the laser polarization perpendicular to the nanobeam. Reprinted from [32], published under the Creative Commons CC-BY licence.

The coupling of a single nanotube to a photonic crystal cavity was also investigated by Miura et al. [32]. Their silicon nanobeam photonic crystal cavity had an extremely small volume (obtained from FDTD calculations) of $0.02(\lambda/n)^3$, a quality factor of 3500 and the quality factor of other emitter was around 100. With this they estimated the maximum reachable Purcell factor for a perfect coupling to be above 300. The spectral width obtained was 420 μeV . However, the typical success rate of the random matching was “one in thousands”...

A spatially and spectrally tunable cavity

In the two previous sections two main ways of overcoming the coupling issues between nanotubes and resonators were explored : the first consists in using an ensemble of nanotubes. Statistically, a great number of emitters couple to the cavity modes, but the downsides of this technique are that the features of a single emitter are lost and the emission of single photons is impossible. The second method consists in the random coupling of a single emitter with a cavity. It overcomes the two drawbacks above mentioned but has the disadvantage of having extremely low success rate.

In this work, a completely different approach is offered : a large number of carbon nanotubes are spin-casted on a flat dielectric mirror with a density low enough to address a single emitter with a diffraction limited optical spot. The emitters are investigated in free-space with a home built confocal microscope described in chapter 4. Once an emitter is selected, a second dielectric mirror is brought above it in order to form the cavity, as shown in fig. 1.21a. The second mirror has a concave shape - which characteristics define the lateral confinement of the cavity - and is located at the end face of an optical fiber, as described in chapter 3. As the fibered mirror is located on a movable fiber, the spatial tunability is a built-in feature of these cavities. In addition, a fine tuning of the distance between the two mirrors brings the spectral tunability.

A similar kind of cavities, formed by two fibered mirrors, was used in 2013 by Stapfner et al. [90] to detect the Brownian motion of a suspended carbon nanotube. Furthermore, such fibered cavities were used by Hümmer et al. [89] to investigate the Raman features of a single nanotube at room temperature, as shown in figure 1.21. With a quality factor as high as 10^5 and a mode volume of $15\lambda^3$, they showed a Purcell enhancement factor of 6 for the Raman spectrum.

The results obtained during this work are summarized in chapters 5 and 6, however a few advantages of the Fabry-Perot cavities can already be announced. Compared to the other photonic structures already described, they combine a very reasonable mode volume (as low as $2\lambda^3$) with very high quality factors (up to 10^5), largely overcoming the intrinsic quality factors of the nanotubes currently available. As previously stated, these cavities can be spatially and spectrally matched to a given emitter. Besides, their length can be increased by steps of $\lambda/2$. It yields a tuning of the cavity volume, helpful to explore the dependence of the Purcell enhancement over the volume. Last but not least, the cavity can be altogether

1.3. PURCELL EFFECT IN CONDENSED MATTER

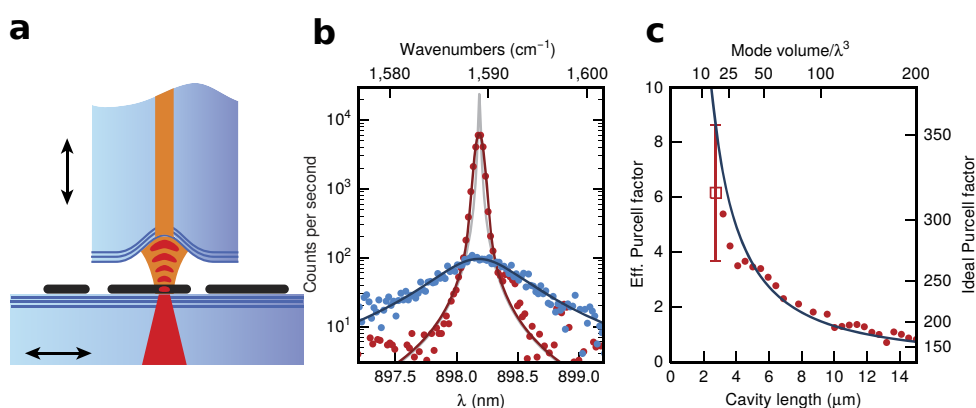


Figure 1.21 – a) Schematic of the cavity formed by the end-facet of an optical fiber (top) and a macroscopic mirror (bottom). CNTs (black lines) are deposited on the macroscopic mirror and interact strongly with the light field when inside the cavity. The large mirror can be positioned laterally by a nanopositioner and the cavity length can be tuned by a piezo actuator (see black arrows). b) Raman spectra taken with a confocal microscope (blue data points with Lorentzian fit) and the cavity, normalized to the same intensity at the nanotube. The gray line shows the intrinsic cavity resonance. c) Scaling of the integrated cavity-enhanced Raman intensity (red data points) as a function of the effective length of the cavity. The red square is evaluated from the measurement shown in b, and the solid line is the theoretically predicted ideal and effective Purcell factor. Reprinted from [89], published under the Creative Commons CC-BY licence.

removed in a non-destructive way. This enables to compare directly the very same single emitter in free-space and coupled to the cavity, a feature unreachable with monolithic resonators.

Conclusion

In this chapter, the concept of spontaneous emission was introduced : it consists in the emission of photons at an energy E and with a rate γ . It is possible to tailor this rate, as well as the directionality of the emission by coupling the emitter to a micro-cavity. In that case, the spontaneous rate in the cavity becomes $\gamma(1 + F_p)$ where F_p is the so-called Purcell factor.

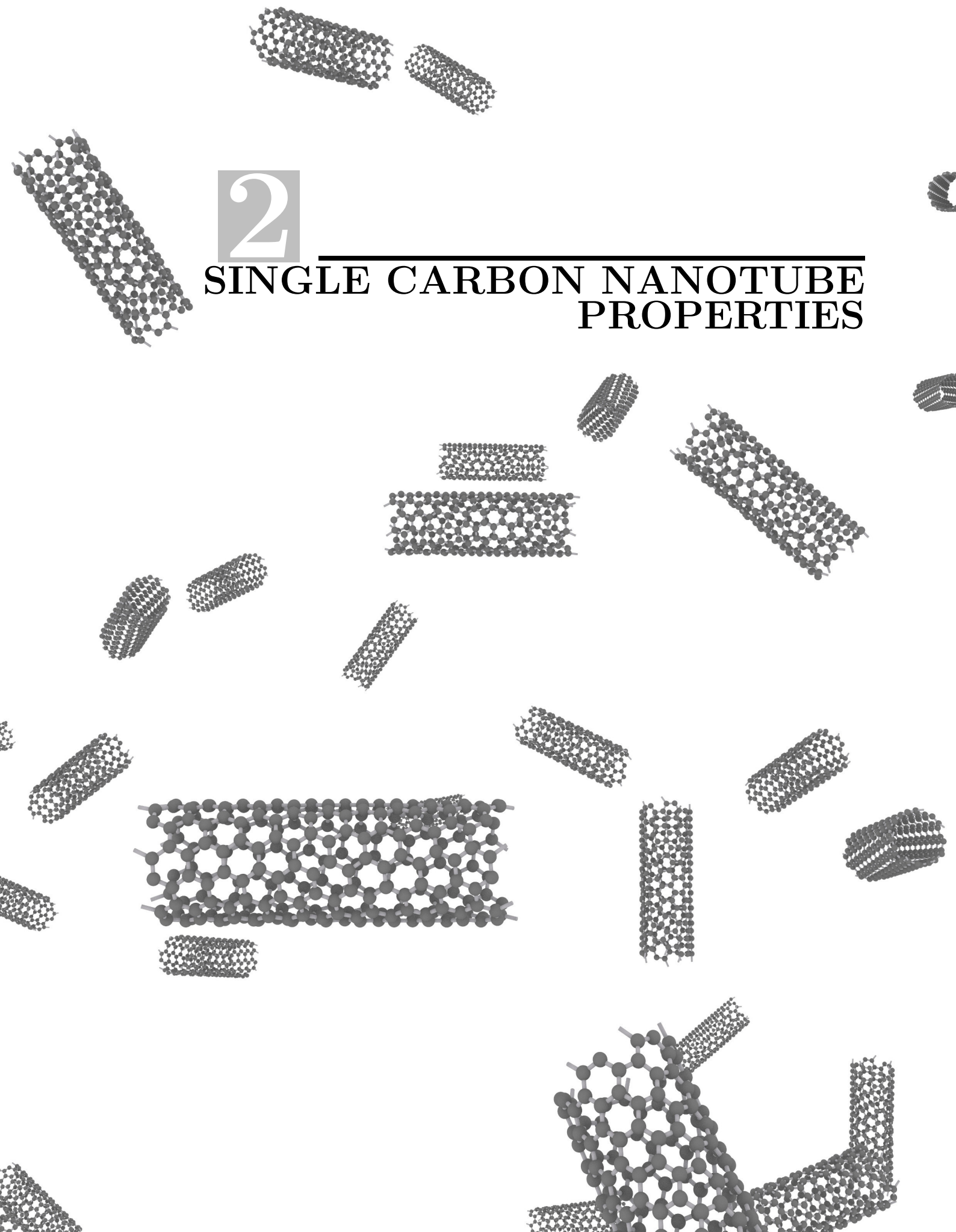
For a ideal two-level system, this Purcell factors simply depends on the quality factor of the cavity and the ratio between its volume and $(\lambda/n)^3$. In atomic physics, Fabry-Perot cavities and micro-sphere cavities were developed because of their extremely high quality factors. However, in condensed matter, the spectral width of the emitter can exceed the one of the cavity and a generalized Purcell factor has to be defined to take it into account. The two parameters that can be tuned to increase the Purcell factor become the volume of the cavity and the sample itself.

Different solid state cavities were presented : micro-pillars, microdisks, photonic crystals. All these cavities have strong assets and have now been well developed for emitters such as quantum dots. Their use in the case of carbon nanotube is sometimes possible but with strong difficulties arising from their lack of tunability. The coupling of nanotubes with resonators has relied, up to now, either on ensembles (with a loss in the intrinsic features) or on random matching (low production efficiency). In this work, a novel geometry of cavity is presented. It enables to localize a single carbon nanotube with confocal microscopy and then to adapt a fibered Fabry-Perot cavity to its position and spectral characteristics.



2

SINGLE CARBON NANOTUBE PROPERTIES



Contents

2.1	Structural and electronic properties	45
2.1.1	Structural properties	45
	Bravais Lattice	45
	Reciprocal Lattice	48
2.1.2	Electronic properties	49
	Band structure of carbon nanotubes	49
	Metallic or semi-conducting character	51
	Density of state and Van-Hove singularity	52
2.2	Optical properties	52
2.2.1	Single electron model	52
	Optical transition	52
	Selection rules and depolarizing effect	53
	Trigonal warping	55
2.2.2	Excitonic properties	57
	Exciton in a bulk semiconductor	57
	Excitons in Carbon Nanotubes	59
	Dark excitons	61
2.3	Samples	62
2.3.1	Synthesis of Carbon Nanotubes	62
2.3.2	Micellar suspension	64
2.3.3	Spin coating	65

Introduction

Carbon nanotubes are an allotrope of carbon, like graphene or diamond. Single-wall nanotubes (SWNT) consist in a atomic monolayer wrapped into the form of a tube, with a diameter ranging from 0.4 nm to 10 nm and a length comprised between a few hundreds of nanometers and a millimeter. Multi-wall nanotubes can be considered as multi-layers of graphene warped around themselves. The optical properties of such tubes depend on the contribution of each layer and their interactions. This study is restricted to SWNT¹.

The goal of this work is to investigate how the coupling of a nanotube to a cavity can enhance the optical properties of the former. Currently, it is complicated to synthesize an ensemble of nanotubes with identical optical properties. Consequently,

¹We also use the acronym CNT, without mentioning every time that they are single walled

the study of an ensemble blurs out the intrinsic properties of each emitter. To overcome this issue, the present work focuses on individual SWNT, referred to as *single carbon nanotubes* in the text.

This chapter starts with a derivation of the structural and electronic properties of SWNT from those of graphene. In particular metallic and semi-conducting nanotubes are distinguished. After that, the basics of single nanotubes optical transitions are introduced. Due to the quasi one-dimensional character of these emitters, the charge carriers interactions are stronger compared to three-dimensional bulk materials. Consequently, the single electron model is completed by a discussion taking into account excitonic effects. Finally, a description of the samples used in this work is given.

2.1 Structural and electronic properties

Single Wall Carbon Nanotubes (SWNT) are hollow cylinders that can be considered as graphene sheets wrapped around themselves. Graphene is an allotrope of carbon consisting in a single layer of atoms organized in a hexagonal pattern. First, some information are given about the properties of this material and then the properties of carbon nanotubes are derived from them.

2.1.1 Structural properties

Bravais Lattice

In a graphene sheet, the atoms are bound to their nearest neighbors by covalent sp^2 bonds, with a distance $a_{C-C} = 1.42 \text{ \AA}$. They are on the nodes of a 2-dimensional triangular Bravais lattice, defined with respect to the orthonormal basis (\vec{e}_x, \vec{e}_y) by the vectors :

$$\vec{a}_1 = \frac{\sqrt{3}}{2}a_0 \vec{e}_x - \frac{a_0}{2} \vec{e}_y, \quad \vec{a}_2 = \frac{\sqrt{3}}{2}a_0 \vec{e}_x + \frac{a_0}{2} \vec{e}_y \quad (2.1)$$

where the norm of the vectors is $a_0 = \sqrt{3}a_{C-C} = 2.46 \text{ \AA}$. The pattern associated with this lattice is made of two carbon atoms located in $(0, 0)$ and $(\frac{1}{2}, \frac{1}{2\sqrt{3}})$ (in the (\vec{e}_x, \vec{e}_y) basis), forming the so-called *honeycomb* lattice, as depicted in figure 2.1. The crystal obtained has a six-fold symmetry, and belongs to the hexagonal Bravais family.

A single wall carbon nanotube consists in a graphene sheet wrapped around itself along a vector which is perpendicular to the nanotube's axis, as shown in fig. 2.1. This vector, which entirely characterizes the geometrical properties of the nanotube, is called *chiral vector* and is defined as :

$$\vec{C}_h = n \cdot \vec{a}_1 + m \cdot \vec{a}_2 \quad n, m \text{ integers} \quad (2.2)$$

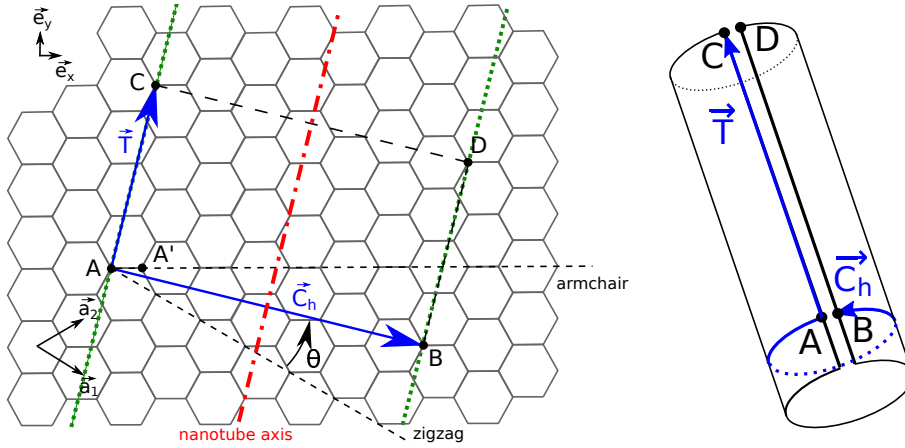


Figure 2.1 – Graphene is composed of carbon atoms organized as a 2-dimensionnal *honeycomb* lattice. Its basis vectors \vec{a}_1 and \vec{a}_2 are depicted in black. A carbon nanotube can be considered as a graphene sheet wrapped around its chiral vectors \vec{C}_h . The basis vectors of the primitive cell of a CNT are \vec{C}_h and \vec{T} , where \vec{T} is along the axis of the tube. The dashed green line depicts the full zone along which the nanotube is wrapped. All the figures in this chapter are, unless otherwise mentioned, inspired to some extent from [91, 92, 93], with the authors permission.

The primitive cell of a carbon nanotube is defined by the chiral vector and the smallest perpendicular vector belonging to the graphene lattice. This *translation vector* is given by:

$$\vec{T} = t_1 \cdot \vec{a}_1 + t_2 \cdot \vec{a}_2 \quad (2.3)$$

$$t_1 = \frac{2m + n}{d_R} \quad \text{and} \quad t_2 = -\frac{2n + m}{d_R} \quad (2.4)$$

Where d_R is the greatest common divisor of $2n + m$ and $2m + n$. The number of carbon atoms in the primitive cell is twice the number of hexagons N , given by :

$$N = \frac{\|\vec{C}_h \wedge \vec{T}\|}{\|\vec{a}_1 \wedge \vec{a}_2\|} = \frac{2(n^2 + nm + m^2)}{d_R} \quad (2.5)$$

Every pair of indices (n, m) defines a unique carbon nanotube, with a diameter, expressed as :

$$d_t = \frac{|\vec{C}_h|}{\pi} = \frac{a_0}{\pi} \sqrt{n^2 + m^2 + m \cdot n} \quad (2.6)$$

Usual carbon nanotubes have a diameter varying from 0.5 nm to 3 nm, while their length ranges from a few hundreds of nanometers to several hundreds of microns.

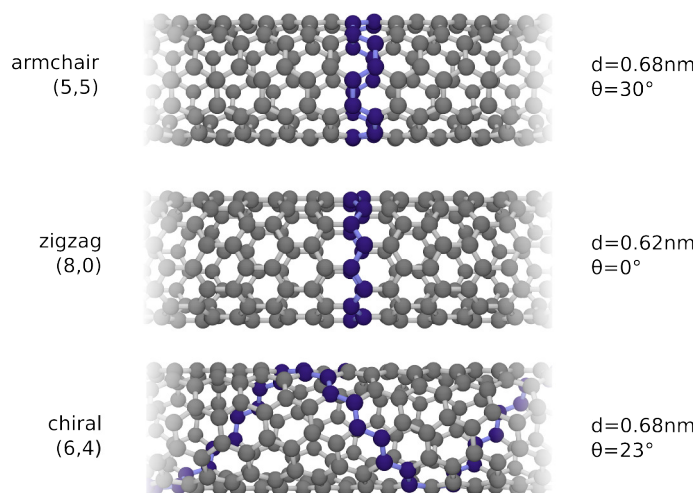


Figure 2.2 – Three different carbon nanotubes. The bonds of a section perpendicular to the tube axis are highlighted in blue. **a)** A (5, 5) armchair nanotube). **b)** A (9, 0) zigzag nanotube. **c)** A (6, 4) chiral nanotube

Finally, the wrapping angle θ , between \vec{C}_h and \vec{a}_1 , is called *chiral angle* and characterizes uniquely many properties of a nanotube. It is given by:

$$\cos \theta = \frac{2n + m}{2\sqrt{n^2 + nm + m^2}} \quad (2.7)$$

Due to the six-fold symmetry of the crystal, θ is in the range $[0, \pi/3]$. The nanotubes can be categorized with respect to their chiral angle. In particular, two families correspond to non-chiral objects (they are not distinguishable from their image in a mirror). The first family, defined by the indices (n, n) (or $\theta = \pi/6$), has *Cis* bonds perpendicular to the tube axis, as shown in figure 2.2. Due to their form, they are called armchair, while the second family $(n, 0)$ ($\theta = 0$ or $\theta = \pi/3$) is called zigzag due to its *Trans* bonds perpendicular to the tube axis.

All the other carbon nanotubes are chiral (they can't be superimposed to their image in a mirror). It is worth noting that for $0 < m < n$, the carbon nanotube (n, m) with a chiral angle $\theta \in [0, \pi/6]$ is the mirror image of its enantiomer (m, n) which has a chiral angle $\theta \in [\pi/6, \pi/3]$. In the literature, the distinction between enantiomers is usually left aside, and it is conventional to use (n, m) with $n > m$ for both. Nevertheless, it must be remembered that this approximation has limits. For example, Dukovic et al. [94] showed the presence of circular dichroism in racemic SWNT solutions.

Reciprocal Lattice

In the reciprocal space, the First Brillouin Zone (FBZ) of graphene is hexagonal. The basis vectors (\vec{b}_1, \vec{b}_2) of the primitive cell are given by :

$$\vec{b}_1 = \frac{2\pi}{\sqrt{3}a_0}(\vec{e}_x - \sqrt{3}\vec{e}_y), \quad \vec{b}_2 = \frac{2\pi}{\sqrt{3}a_0}(\vec{e}_x + \sqrt{3}\vec{e}_y) \quad (2.8)$$

The first Brillouin zone is hexagonal and contains several points of high symmetry, called Γ , M, K and K', that have special properties concerning the band structure of graphene. The location of these points is given by :

$$\vec{k}_\Gamma = \vec{0} \quad \vec{k}_M = \frac{\vec{b}_1 + \vec{b}_2}{2} \quad (2.9)$$

$$\vec{k}_K = \frac{\vec{b}_1 + 2\vec{b}_2}{3} \quad \vec{k}_{K'} = \frac{2\vec{b}_1 + \vec{b}_2}{3} \quad (2.10)$$

The basis vector of the reciprocal space for carbon nanotubes (\vec{K}_1, \vec{K}_2) are defined with respect to the chiral vector : \vec{K}_1 is collinear to \vec{C}_h , while \vec{K}_2 is collinear to \vec{T} :

$$\vec{C}_h \cdot \vec{K}_1 = 2\pi, \quad \vec{T} \cdot \vec{K}_1 = 0, \quad \vec{C}_h \cdot \vec{K}_2 = 0, \quad \vec{T} \cdot \vec{K}_2 = 2\pi \quad (2.11)$$

These two vectors can also be expressed with the basis vectors of graphene's reciprocal space :

$$\vec{K}_1 = \frac{1}{N}(t_2\vec{b}_1 - t_1\vec{b}_2), \quad \vec{K}_2 = \frac{1}{N}(-m\vec{b}_1 + n\vec{b}_2) \quad (2.12)$$

Any vector of the reciprocal space \vec{k} can be expressed as a function of (\vec{K}_1, \vec{K}_2) :

$$\vec{k} = k_\perp \vec{K}_1 / \|\vec{K}_1\| + k_\parallel \vec{K}_2 / \|\vec{K}_2\| \quad (2.13)$$

Along the carbon nanotube axis, the periodicity is given by the translation vector \vec{T} . If one considers the carbon nanotube as infinitely long, k_\parallel is continuous and the first Brillouin zone along the carbon nanotube is given by $k_\parallel \in [-\frac{\pi}{\|\vec{T}\|}, \frac{\pi}{\|\vec{T}\|}]$.

However, along the nanotube's circumference, a translation of a vector \vec{C}_h in the real space brings one back to its starting point. This boundary condition implies that k_\perp are discrete and satisfy the relation $\vec{k} \cdot \vec{C}_h = 2\pi\mu$ with $\mu \in \llbracket 1, \dots, N-1 \rrbracket$. This means that $k_\perp = \mu \|\vec{K}_1\|$.

The first Brillouin zone is thus made of N segments of length $\frac{2\pi}{\|\vec{T}\|} = \|\vec{K}_2\|$, parallel to the Carbon nanotube axis, as depicted in figure 2.3.

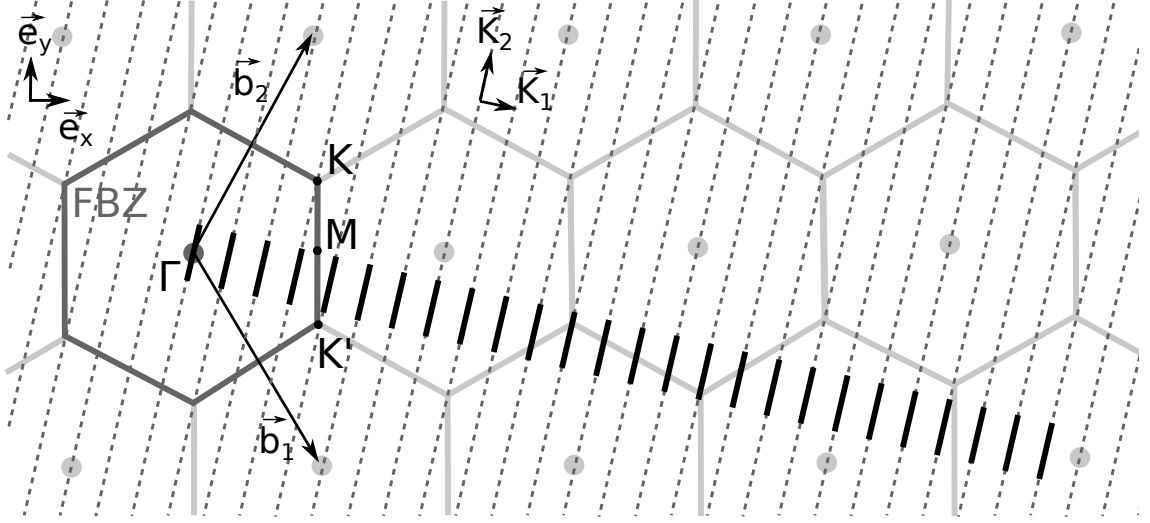


Figure 2.3 – Reciprocal lattice of graphene (solid gray lines), and its first Brillouin zone (FBZ, dark gray). The reciprocal lattice of a (5, 2) CNT is depicted (dashed lines) as well as its first Brillouin zone (solid black). The high symmetry points Γ , M, K and K' are indicated.

2.1.2 Electronic properties

In this section, the geometrical description of carbon nanotubes is used to explore their electronic properties. First the band structure of graphene is derived and then the Van Hove singularities are introduced.

Band structure of carbon nanotubes

In the frame of the tight binding approximation, a derivation taking into account up to the second nearest neighbors yields the following band structure for graphene [95] :

$$E_g(\vec{k}) = \pm t \sqrt{3 + f(\vec{k})} - t' f(\vec{k}) \quad (2.14)$$

$$f(\vec{k}) = 4 \cos\left(\frac{\sqrt{3}}{2} k_x a_0\right) \cos\left(\frac{1}{2} k_y a_0\right) + 2 \cos(k_y a_0) \quad (2.15)$$

where $\vec{k} = (k_x, k_y)$ is a vector from the reciprocal space, $t \simeq 2.7$ eV is the nearest neighbor hopping energy and $t' \simeq 0.2t$ is the next nearest neighbor hopping energy. The \pm sign indicates that there are two bands on either side of the $E = 0$ plan : the conduction and valence bands. These bands are almost symmetrical compared to this plan as only the second nearest neighbor contribution creates a deviation to this symmetry. The bands around the first Brillouin zone are shown in figure 2.4.

At the absolute zero, without doping, the lower band is full (valence band) while the upper one is empty (conduction band). These two bands join at the Fermi level

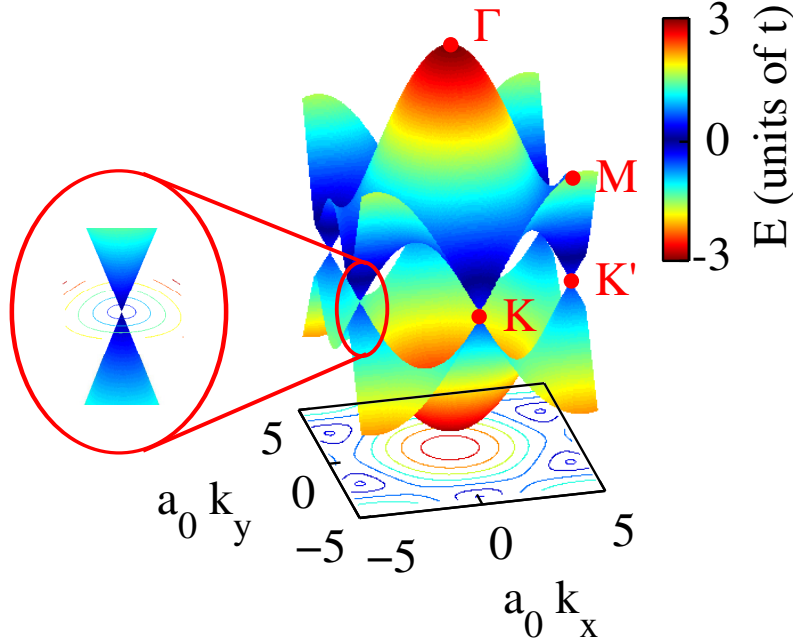


Figure 2.4 – Band structure of graphene around the first Brillouin zone. The gap between the valence and the conduction band is zero in K and K' points, and the dispersion is linear and isotropic immediately around these points. The inset shows a Dirac cone

($E = 0$) in K and K' . Graphene is thus a zero gap semiconductor. Around these points, the dispersion can be approximated as linear, giving rise to the so-called *Dirac cones*.

As a first approximation, the dispersion relations of carbon nanotubes can be derived from the one of graphene. Indeed, the wave-vector remains continuous along the tube axis but is quantized along \vec{C}_h , as detailed in paragraph 2.1.1. Consequently, the dispersion relation of a carbon nanotube is composed of N linear cuts in the band-structure of graphene. These are given by the N lines of the nanotube's First Brillouin Zone [96] :

$$E_\mu = E_g(\vec{k} = \mu\vec{K}_1 + k_\parallel \frac{\vec{K}_2}{\|\vec{K}_2\|}) \quad (2.16)$$

$$\text{with } \mu \in \llbracket 1, \dots, N-1 \rrbracket \quad \text{and} \quad k_\parallel \in [-\pi/\|\vec{T}\|, \pi/\|\vec{T}\|]$$

Each cut defines two bands : a valence band below the Fermi level and a conduction band above it. As already mentioned, graphene is a zero-band gap semi-conductor, so if one of the cuts passes by either a K or a K' point, the two bands join, as shown in figure 2.5. Then, the density of state is non-zero at the Fermi energy, and the nanotube is metallic. Otherwise, there is a non-zero gap between

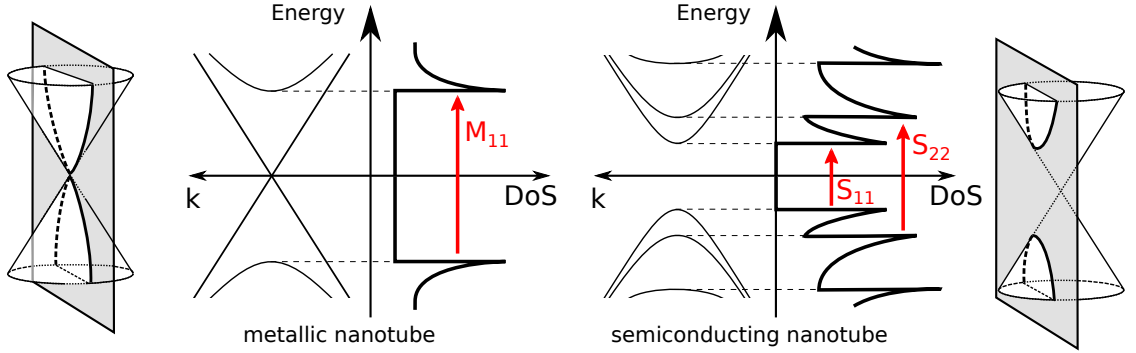


Figure 2.5 – Band structure and density of state of a metallic nanotube (left) and a semi-conducting one (right).

highest valence band and the lowest conduction band. The density of state at the Fermi level is zero and the nanotube is semi-conducting.

Metallic or semi-conducting character

In order to determine whether a carbon nanotube is semi-conducting or metallic, one can focus on the bands closest to the Fermi level, which are the bands closest to the K (or K') points. As long as the linear approximation around such a point holds, the dispersion relation of a carbon nanotube is given by [97] :

$$E_{\mu}(\vec{k}) = \pm \sqrt{\left(\frac{\sqrt{3}a_0t}{2}\delta k_{\parallel}\right)^2 + E_{\mu}^2}, \quad \text{where} \quad E_{\mu} = \frac{a_0t}{\sqrt{3}d}|3\mu - n + m| \quad (2.17)$$

where $\delta k_{\parallel} = (\vec{k} - \vec{k}_K) \cdot \vec{K}_2 / \|\vec{K}_2\|$ is the distance to K point (along the cut). At its lowest point the energy is given by E_{μ} , and is a function of $|3\mu - n + m|$. Depending on the indices, two cases arise :

$$\begin{aligned} n - m = 0 \pmod{3} &\Rightarrow |3\mu - n + m| = 0, 3, 6, 9, \dots \\ n - m \neq 0 \pmod{3} &\Rightarrow |3\mu - n + m| = 1, 2, 4, 5, 7, 8, \dots \end{aligned} \quad (2.18)$$

From there it is clear that if $n - m$ is a multiple of 3, there is a number μ for which $|3\mu - n + m|$ is zero, and the nanotube is metallic. in that case, $E_{\mu} = 0$ and the dispersion is linear around $k = 0$, as can be seen in figure 2.5. While if $n - m$ is not a multiple of 3, $|3\mu - n + m|$ never cancels out and the nanotube is semi-conducting. The dispersion around $k = 0$ is hyperbolic. Statistically, about one third of the carbon nanotubes are metallic. Nevertheless, in this study the samples used are enriched in semi-conducting nanotubes (see section 2.3).

Density of state and Van-Hove singularity

The density of state (DoS) of carbon nanotubes is characteristic of their unidimensional nature. In order to derive it, one has to take into account the contribution DoS_μ of each band μ , given by [96] :

$$DoS_\mu(\epsilon) = \frac{2}{\ell|k_z|} \int dk_z \delta(\epsilon - E_\mu(k_z)) \left| \frac{\partial E_\mu}{\partial k_z} \right|^{-1} \quad (2.19)$$

where ℓ is the First Brillouin Zone length and the factor of 2 arises from spin degeneracy.

After a quick derivation, one gets the full density of states DoS [97] :

$$DoS(E) = \frac{2a_0}{\pi^2 \gamma_0 d_t} \sum_\mu g(E, E_\mu) \quad (2.20)$$

$$DoS(\epsilon, E_\mu) = \begin{cases} |\epsilon|/\sqrt{\epsilon^2 - E_\mu^2} & \text{if } |\epsilon| > E_\mu \\ 0 & \text{if } |\epsilon| < E_\mu \\ 1 & \text{if } E_\mu = 0 \end{cases} \quad (2.21)$$

The density of state is thus diverging for carbon nanotubes, giving rise to the so called Van Hove singularities (see figure 2.5). This phenomenon is characteristic of ideal one-dimensional structures [98].

2.2 Optical properties

In the previous paragraphs, the structural and electronic properties of carbon nanotubes were described. From there on, a derivation of their optical properties should be accessible by using the Fermi golden rule. However the low dimensionality of the nanotubes induces specific properties : indeed, the Coulombic interactions are enhanced compared to bulk materials and excitons are very stable (the binding energy is around 400 meV). In this section, a single electron model is introduced and a description of the excitonic effects is given.

2.2.1 Single electron model

Optical transition

In general, the optical properties are directly linked to the electronic properties, and in particular the density of states. Two quantities are commonly used in optics : the probability for an electron to relax towards a lower state $W_\downarrow(\hbar\omega)$, by releasing a photon, and the probability for an electron to be promoted to a higher state by the absorption of a photon, $W_\uparrow(\hbar\omega)$. By using Fermi Golden rule, one can evaluate these coefficients :

$$\begin{aligned}
 W_{\uparrow}(\hbar\omega) &= \frac{2\pi}{\hbar} \sum_{\mu,\mu'} \sum_{k,k'} |M_{\mu\mu'}(k, k')|^2 \delta(E_{\mu'}(k') - E_{\mu}(k) - \hbar\omega) \cdot (1 - f(E_{\mu'}(k'))) \cdot f(E_{\mu}(k)) \\
 W_{\downarrow}(\hbar\omega) &= \frac{2\pi}{\hbar} \sum_{\mu,\mu'} \sum_{k,k'} |M_{\mu\mu'}(k, k')|^2 \delta(E_{\mu'}(k') - E_{\mu}(k) - \hbar\omega) \cdot (1 - f(E_{\mu}(k))) \cdot f(E_{\mu'}(k))
 \end{aligned}
 \tag{2.22}$$

Where the sum is made over all the transitions between a state with wave-vector k in a subband with index μ , and a state with vector k' in a subband with index μ' (as written here $E_{\mu'}(k') > E_{\mu}(k)$). The Dirac delta ensures the conservation of energy. The variable $f(E_{\mu}(k))$ gives the electronic occupation number and $(1 - f(E_{\mu}(k)))$ the hole occupation number of the μ band at energy $E(k)$ (at thermal equilibrium, it is the Fermi-Dirac distribution). The $M_{\mu\mu'}$ are the matrix elements between these states, and their derivation is beyond the scope of this work (see [99] for details)

In this manuscript, the focus is on transitions in the range of 1.3 eV to 1.5 eV, thus lower than $t \sim 3 \text{ eV}^2$. This implies that the states involved in the optical transition are close to the K and K' points. It was shown that in this region, the matrix elements element do not vary significantly with the wavevector [100]. The emission and absorption characteristics are mostly defined by the electronic density of states, and thus by the Van Hove singularities.

Selection rules and depolarizing effect

This work focuses on interband absorption and luminescence of carbon nanotubes. In the formalism just introduced, absorption is the promotion of an electron from a valence band $|v, \mu, k\rangle$ to an empty state in a conduction band $|c, \mu', k'\rangle$, while luminescence is the opposite phenomenon. The selection rules discussed here are the links between μ and μ' , as well as between k and k' .

Let's start with the later. As already stated, the transitions of interest have an energy close to 1 eV, which means a wavelength close to 1 μm . This is well higher than the characteristic size of the lattice $a_0 = 2.46 \text{ \AA}$. In other words, the momentum of the photon is negligible with respect to the size of the First Brillouin Zone of the nanotube. Hence the first selection rule : only vertical transitions are allowed [101] :

$$\Delta\vec{k} = \vec{k}' - \vec{k} = 0
 \tag{2.23}$$

The transitions appear vertical on a dispersion graph, such as the one of figure 2.5.

Because of the symmetries of the initial and final states, the matrix element $M_{\mu\mu'}(k, k')$ is zero for most combinations between bands. Actually, the selection rules than arise from this depend on the orientation of the electric field with respect

²We recall that t is the first neighbor hopping energy

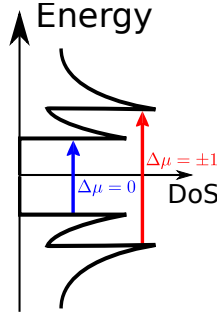


Figure 2.6 – Orientation of the electric field with respect to the nanotube axis for the two lowest energy transitions.

to the carbon nanotube's axis (along \vec{T}) [102] :

$$\begin{cases} \Delta\mu = 0 & \text{if } \vec{E} \parallel \vec{T} \\ \Delta\mu = \pm 1 & \text{if } \vec{E} \perp \vec{T} \end{cases} \quad (2.24)$$

Even if a transition is allowed, it does not mean that it is experimentally visible. Indeed one has to take into account the oscillator strength, a non-dimensional parameter proportional to the square of the interaction matrix element [103]. As shown in fig. 2.6, the lowest energy transition happens when the electric field is along the nanotube axis ($\Delta\mu = 0$) and is responsible for the photoluminescence signal observed throughout this work. For $\Delta\mu = \pm 1$, when the field polarization is perpendicular to the tube axis, the oscillator strength is lower, as was confirmed experimentally [104].

In the samples used in this work, the nanotubes have a typical aspect ratio of 1000. If an electric field \vec{E} is parallel to the tube, the charges created at both ends have a limited impact and the external field felt by the tube (and all the more so by a localized exciton) is \vec{E} . The nanotube's absorption is then governed by the imaginary part of its electric polarizability $\alpha(\omega)$. Now, let's consider a field \vec{E} perpendicular to the nanotube's axis. It leads to a separation of charges along the nanotubes. This implies a screened polarizability $\tilde{\alpha}(\omega)$ depending on the tube's length L and radius R [105] :

$$\tilde{\alpha}(\omega) = \left(\alpha(\omega)^{-1} + \frac{2}{LR^2} \right)^{-1} \quad (2.25)$$

Due to the very low diameter (below 1 nm in this work), this screening is high and reduces the effective field felt by the nanotube (see also section 4.2.1).

Eventually, the optical transitions favored in carbon nanotubes correspond to the transition between two n^{th} Van Hove singularities, with a polarization along the carbon nanotube axis. These transitions are noted S_{nm} for the semi-conducting

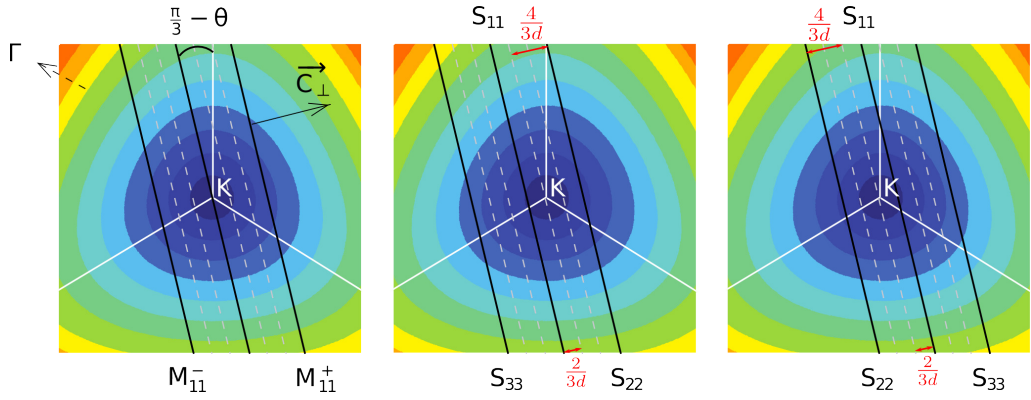


Figure 2.7 – Graphene FBZ, with isoenergetic zones in colors. The solid black lines are the nanotube FBZ, the dashed gray lines are separated by $\frac{1}{d_t}$. To the left, a metallic nanotube for which there is a degeneracy lift (M_{11}^+ and M_{11}^- do not have the same energy). In the center, a Type II nanotube (S_{11} energy is lower than predicted with $\frac{1}{d}$ rule). To the right, a Type I nanotube for which the reverse happens.

nanotubes and M_{nn} for the metallic ones. In the conical approximation, their energies are given by :

$$S_{nn} = \frac{2a_0t}{\sqrt{3}d_t} p_n \quad \text{avec } p = 1, 2, 4, 5, 7, 8, \dots \quad (2.26)$$

$$M_{nn} = \frac{2a_0t}{\sqrt{3}d_t} 3n \quad \text{avec } n \in \mathbb{N}^* \quad (2.27)$$

From these formulas one can see that the transition energy is inversely proportional to the nanotube's diameter, as shown in figure 2.8. And for a given diameter, a simple rule applies : $S_{22} = 2S_{11}$, $M_{11} = 3S_{11}$, $S_{33} = 4S_{11}$, etc..

Trigonal warping

In the previous section, only an isotropic and linear dispersion around K and K' points was considered. This is a valid approximation for optical transitions verifying $\hbar\omega \ll 2t$. This approximation is quite good for the carbon nanotubes considered in this work, with a diameter close to 1 nm, but it is questionable for optical transitions in the visible range, due to an effect called *trigonal warping*.

In order to understand what trigonal warping is, the First Brillouin Zone (FBZ) of graphene is plotted around K points in figure 2.7. The colors indicate isoenergetic contours, and the black lines depict the lines of the nanotubes FBZ, parallel to vector \vec{T} and spaced by $\frac{2}{d_t}$. Among the black segments, let's consider the three closest to the K points, they are the one giving rise to the lowest energy Van Hove

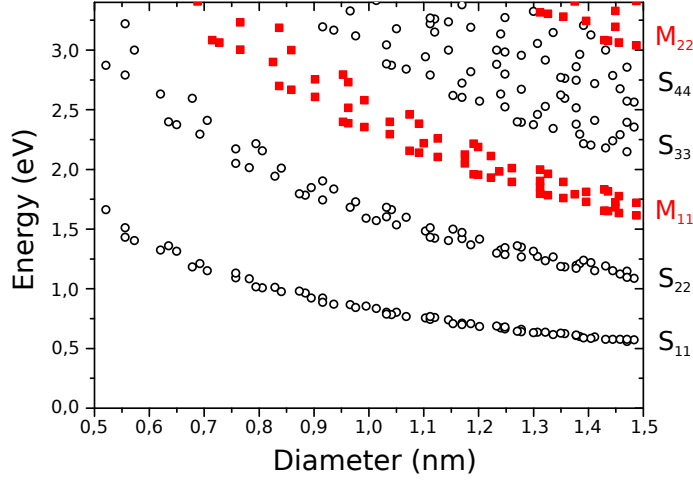


Figure 2.8 – Nanotubes transition energies as a function of their diameter. Reprinted figure from [91], with author’s permission.

singularities (meaning S_{11} , S_{22} and S_{33} for a semi-conducting nanotube). If one considers a metallic nanotube, one of the segments passes by K point. If the nanotube is semi-conducting, one finds that in any case the distance between K and the closest line is $\frac{2}{3d_t}$ while the distance to the second closest is $\frac{4}{3d_t}$. In fact, the black lines position is given by the chiral angle of the nanotube, and the projection of $\vec{\Gamma K}$ over the chiral vector \vec{C}_h is a multiple of $\frac{2}{3d_t}$:

$$\vec{\Gamma K} \cdot \frac{\vec{C}_h}{C_h} = \frac{2}{3d_t}(2n + m) \quad (2.28)$$

The isoenergetic lines around K point have a non-isotropic shape. consequently, a cut done for a given chiral angle θ , at a given distance of K , does not have exactly the same energy whether it is on the side of Γ or on the other side. The consequences depend on the nanotube type :

- For metallic nanotubes, there is a degeneracy lift of the M_{11} transition into two transitions noted M_{11}^+ and M_{11}^- , as confirmed experimentally [106].
- For semi-conducting nanotubes, one distinguishes Type I, for which $2n + m = 1 \pmod{3}$ and Type II for which $2n + m = -1 \pmod{3}$. For a given diameter d , in the later case, the cut happens on the Γ point side while in the former it is on the other side, and the energy is thus lower. In fact, the energy is lower for all odd transitions, and higher for all even transitions. This asymmetry grows larger with the chiral angle θ and increases with decreasing diameters.

It was noted previously that the optical gap in carbon nanotubes is proportional

to $\frac{1}{d}$. The modifications, compared to the linear dispersion approximation discussed in this paragraph, imply that this law is slightly modified : a Type II carbon nanotube has its odd transition energies increased compared to the $\frac{1}{d}$ law, and its even transition decreased while the opposite happens for a Type I nanotube. The transition energies as a function of the diameter, taking into account trigonal warping, are plotted in figure 2.8.

2.2.2 Excitonic properties

The optical properties discussed in the previous section were derived from a tight binding model, considering that the electrons are independent from each other. This model is relevant to describe some simple properties, such as whether a nanotube is metallic or semi-conductor. However, it is no longer valid when one wants to derive accurately the energy of the first optical transition. Indeed, in low dimensional objects, the interactions between charge carriers are enhanced, leading to two main effects : a renormalization of the gap due to the repulsive interactions between electrons, and excitonic features. In this section, the properties of excitons in a bulk material are introduced. Then, more details are given about the case of carbon nanotubes.

Exciton in a bulk semiconductor

Let's consider a bulk semiconductor with a direct gap ϵ_g . The valence and conduction bands have a parabolic dispersion characterized by the effective masses m_c^* and m_v^* , and centered in $\vec{k} = 0$. In the fundamental state, the valence band (below the Fermi level) is full and the conduction band (above the Fermi level) is empty. If one considers that there are no interactions between charge carriers (between electron and hole), the first excited state is the one for which an electron is promoted from the valence to the conduction band, and the energy to provide for such an event is equal to ϵ_g . However, in a simple picture, one may expect the electron and the hole left behind in the valence band - which are of opposite charge - to interact via Coulombic force. This interaction leads to bound states called excitons, with an energy lower than the energy of the gap.

Let's consider a very simple model for the exciton, taking into account only the electron-hole interactions. In the barycentric frame, the problem can be replaced by the one of a fictive particle in a central force motion [98]. This pseudo-particle has an effective mass $M = m_c^* + m_h^*$ (where the effective mass of the hole is $m_h^* = -m_v^*$). By analogy with the hydrogen atom, the total energy of the exciton (indexed by quantum number $\alpha \in \mathbb{N}$) is given by :

$$\epsilon_\alpha(\vec{K}) = \epsilon_g^{renorm} + \frac{\hbar^2 K^2}{2M} - \frac{R^*}{\alpha^2} \quad (2.29)$$

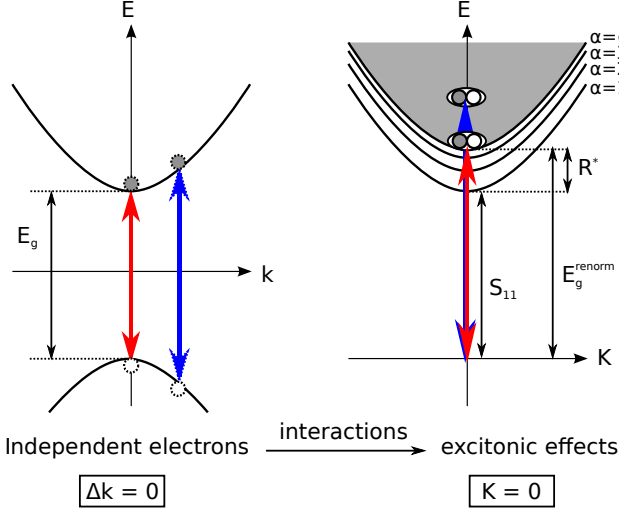


Figure 2.9 – Dispersion for a bulk semiconductor. On the left, the independent electron model. On the right, excitonic levels labeled by α . The electronic transitions at $\Delta k = 0$ correspond to excitonic transitions at $K = 0$.

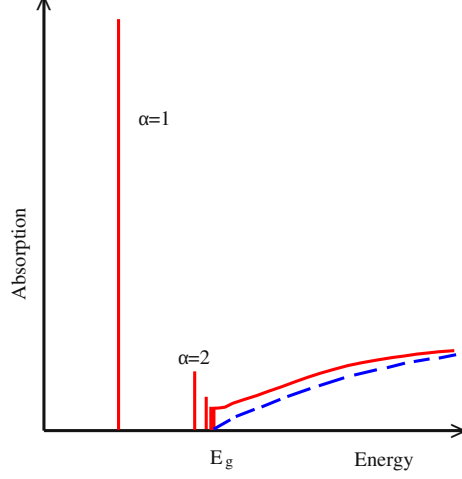


Figure 2.10 – Absorption coefficient of a bulk material. In blue, the independent electron case. In red, the excitonic features are present as single absorption lines below the energy of the gap.

where ϵ_g^{renorm} is the renormalized gap energy ($\epsilon_g^{renorm} > \epsilon_g$), \vec{K} is the wave-vector of the exciton's center of mass. The energy between to lowest energy exciton ($\alpha = 1$, called *1s* by analogy with hydrogen) and the energy of the continuum of unbound states (which minimum is given by $\alpha = \infty$.) is called *binding energy*, or Rydberg energy of the exciton $R^* = \frac{\mu e^4}{2\hbar^2(4\pi\epsilon)^2}$. This is depicted in figure 2.9. The binding energy can be re-written to let appear the Bohr radius of the exciton r_B (i.e. the mean distance between the electron and the hole):

$$R^* = \frac{\hbar^2}{2\mu r_B^2} \quad (2.30)$$

$$r_B = \frac{4\pi\epsilon\hbar^2}{\mu e^2} \quad (2.31)$$

It has already been stated, in the section concerning the selection rules 2.2.1, that the optical transitions happen for $\Delta \vec{k} \simeq 0$. Rewriting this as a function of the wavevectors of the electron \vec{k}_e and the hole \vec{k}_h , one gets $\vec{k}_e \simeq -\vec{k}_h$. This immediately leads to a relation for the wave-vector of the exciton $\vec{K} = \vec{k}_e + \vec{k}_h \simeq 0$. In other words, the transition happens for an excitonic wave-vector equal to zero, and as long as α is finite, the absorption (or the emission) spectrum is composed of single lines below the renormalized energy of the gap (cf. figure 2.10).

The influence of the bulk material on the excitons is contained in its permittivity ϵ and in the effective masses. For most materials, the binding energy is low compared to the gap, for example in gallium arsenide $\epsilon_g = 1.424$ eV [107], $R^* = 5$ meV and the Bohr radius of the exciton is bigger than the size of the primitive cell $r_b = 10$ nm [108]. The excitonic effects, in this case, are hardly visible at room temperature as the thermal energy $kT \simeq 26$ meV is higher than the binding energy R^* .

Excitons in Carbon Nanotubes

Several features of the excitonic description given above change when one goes from a bulk material to a low-dimensional material. Indeed, excitonic effects arise from Coulombic interactions, thus the confinement of charge carriers in a small volume induces an enhancement of these interactions. This means that the binding energy increases, as well as the oscillator strength of the transition due to the first exciton $\alpha = 1$ [108].

Actually, in an ideal one-dimensional system, the excitonic binding energy diverges [109]. Obviously in the case of carbon nanotubes the confinement is not strictly one dimensional, as their lateral extension is non-zero. In order to evaluate quantitatively this phenomenon, two different methods were used. One way consisted in starting from a 3D model in which the confinement was taken into account by setting a small (but finite) width to the system. Semi-conducting quantum-wires were successfully modeled by this process [110]. A second method consisted in a regularization of the Coulombic potential [111, 112]. In that case, the description remained one-dimensional but introduced new parameters that were determined to fit experimental data.

In fact, excitonic effects in one-dimensional structures were first investigated in the case of quantum wires. The binding energies found for the thinnest GaAs wires ($r_b = 4.5$ nm) were higher than in bulk materials but of the same order of magnitude than those found for GaAs quantum wells [113], failing to bring evidence of the specific 1D confinement. On the contrary, the nanotubes are particularly interesting to show these effects as their diameter can be smaller than 1 nm (about 0.7 nm in this work), and thus can display a stronger confinement than quantum-wires. Experimentally, two-photons measurements gave the evidence that the optical transitions in nanotubes arise from excitons [18, 114]. And the binding energy found was about one third of the gap energy (400 meV for a 1.2 eV gap [114]), or even a little larger for suspended nanotubes [115]. Given this large binding energy, interactions giving rise to excitonic effects in carbon nanotubes cannot be treated as perturbations. The binding energy is greater than k_bT , making the exciton stable against thermal agitation, even at room temperature. These features make the study of excitonic effects easier in nanotubes than in other 2D or 1D semi-conducting nanostructures.

The nanotubes excitons are extremely sensitive to their local environment. Indeed, a nanotube is an extreme case as each of its atoms is at its surface and the Bohr radius of the exciton is of the order of the diameter, about 1 nm [116, 117, 118]. The

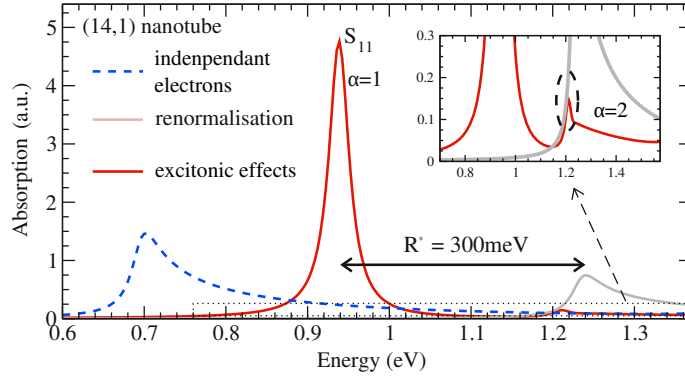


Figure 2.11 – The optical absorption of a carbon nanotube is computed with an independent electron model (dashed blue line). The Coulombic self-energy leads to a gap renormalization (gray solid line) and the excitonic effects drastically change the spectrum (solid red line). The spectrum is dominated by the transition to the first exciton, the transition to the second is plot in the inset. Adapted from [119].

excitonic wave function spills out of the tube and makes it very sensitive to the dielectric permittivity of its surroundings (an increase of the external permittivity induces screening and a decrease in the transitions energies) [19]. In particular, the presence of molecules inside or outside the walls of the nanotube partially screens the Coulombic interactions between the nanotube’s charges.

Now, a theoretical calculation can be done to illustrate the effect of excitonic interactions in carbon nanotubes : figure 2.11 shows the absorption spectrum of a nanotube calculated by Malic et al [119]. If the Coulombic interactions are neglected, the absorption spectrum is simply reduced to a Van Hove singularity in the range of energies considered. However, the interaction between electrons of the valence band implies a renormalization of the gap towards higher energies (blue shift). The excitonic effects induce the existence of a series of lines at lower energies. The lowest, corresponding to $\alpha = 1$, is dominant in the absorption spectrum, but an inset lets appear the second line ($\alpha = 2$). One can note that the renormalization of the gap and the stabilization of the exciton by Coulombic interactions do not compensate exactly : a slight increase of the transition energy happens compared to the independent electron model.

An estimation of the direction of the energy shift with the modification of the environment is also possible from that figure. An increase in the dielectric constant of the nanotube’s surroundings increases the screening of the interactions, which leads to a decrease in the gap’s renormalization energy as well as in the excitonic binding energy. As the former is larger than the later, the optical transition energy is shifted towards the lower energies. This phenomenon explains the red shifts observed in functionalized nanotubes [92, 93].

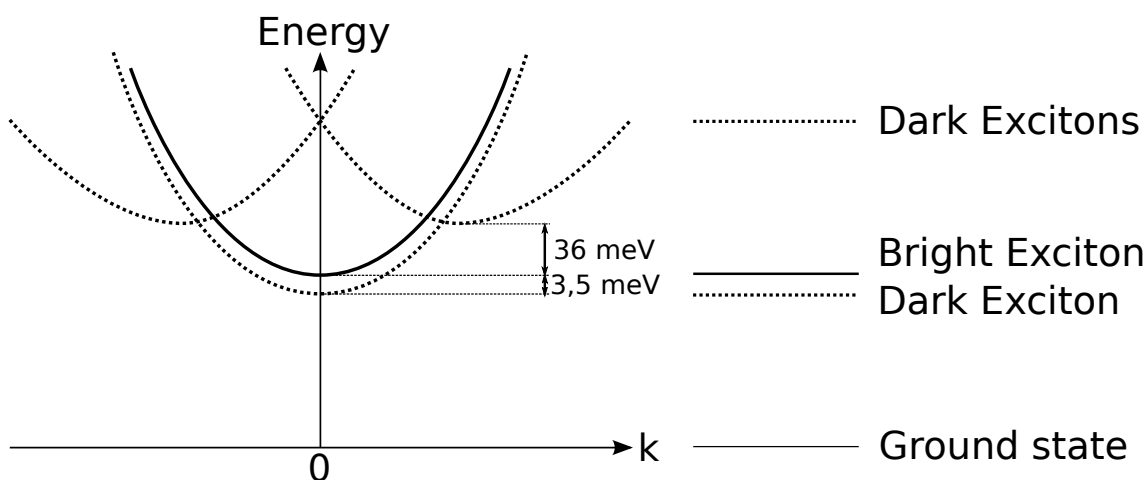


Figure 2.12 – Example of the band structure of the excitonic state $\alpha = 1$ for a chiral nanotube. One state is optically active while the three others are dark. The values indicated are for (6, 5) nanotubes and come from [121, 124].

Dark excitons

In order to reproduce the experimental absorption and emission spectra, the description given for the excitonic effects has to be completed : the inter-valley degeneracy leads to a more complex excitonic structure [120, 121, 122]. Each hydrogenoid state α , associated with each Van Hove singularity pair is built from four bands (a valence and a conduction band for each valley), which leads to the existence of four excitonic bands [123].

In figure 2.12 the four bands associated with the lowest energy hydrogenoid state for a chiral nanotube are depicted. Two bands have their minimum for a non-zero wavevector. They correspond to a non-zero angular momentum and thus cannot be involved in optical transitions [123]. Such states are called *dark* because of their optical inactivity. These two are specifically referred to as Dark K-momentum in the literature. The two other bands have their minimum for a zero wavevector, however one of these exciton is dark (while the other is optically active). Their relative energy depends on the symmetry of the hydrogenoid state : when α is odd, the dark exciton is lower while it is the reverse when α is even. This dark exciton can be activated by the application of a magnetic field [125].

Even though the Dark K-momentum excitons cannot be directly involved in optical interactions, they can play a part in second order processes involving a photon and a phonon. In figure 2.13 two processes are considered : the absorption of a photon and the emission of a longitudinal optical (LO) phonon, which implies the creation of a dark exciton with a non zero wavevector. The relaxation of this exciton involves the emission of a photon and a LO phonon. In that case, an absorption band can be observed above the energy of the bright excitonic state and an emission band can be observed below. These absorption and emission bands are called phonon

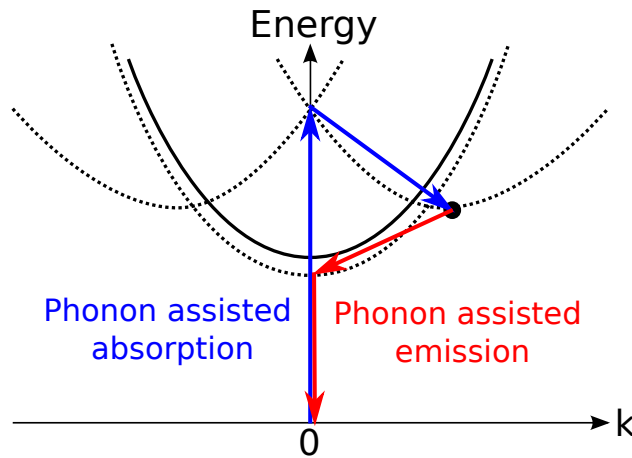


Figure 2.13 – Two phonon assisted processes involving dark excitons (depicted with a black dot). This implies the existence of an absorption band with an energy above the one of the bright state (blue arrows) and an emission band below (red arrows).

side bands and were experimentally observed [120, 121, 122].

To conclude on the excitonic effect, let's emphasize that the nanotubes are an excellent system to investigate them because of their one-dimensional characteristic. The binding energy amounts to a few tenths of eV, which is an order of magnitude higher than in other nanostructures. Finally, the majority of the oscillator strength is concentrated in the lowest energy bright exciton. This transition is thus simply referred to as S_{11} for semi-conducting nanotubes.

2.3 Samples

In this section, the different methods used to grow carbon nanotubes are introduced. Afterwards, the interest of micellar suspension are described, and an explanation of how the nanotubes are deposited by spin-coating on mirrors is given.

2.3.1 Synthesis of Carbon Nanotubes

Carbon nanotube are scarce in the natural environment, but probably exist in common fires [126]. Their first artificial synthesis was made in the group of Ijima in 1991 [13], using an arc-discharge evaporation method, with graphite electrodes under high temperature and low pressure. This first method, which had previously been established for the production of fullerene had the disadvantage of creating many different carbon allotropes, including amorphous ones. Carbon nanotubes rapidly drew the interest of researchers, as well as industrials, due to their amazing physical properties. This gave birth to a entire field of research, still very active now, on their synthesis. The efforts are taking two directions : first a high purity is sought (this means reducing the presence of amorphous carbon, limiting crystalline defects).

Second, a control of the geometrical properties of carbon nanotubes (their diameter, or chiral angle) is the aim of many researcher. The selectivity (meaning to capacity to choose the (n, m) indices of the nanotubes grown) remains limited, and is often based on post-selection. All the synthesis methods have their pros and cons. They are all briefly introduced, though the nanotubes used during this PhD all came from the same commercial sources.

The most common synthesis method is called Chemical Vapor Deposition (CVD) [127] and was applied for carbon nanotubes since 1993. It consists in a clean substrate in a temperature and pressure controlled chamber. On this substrate, metallic catalysts (such as nickel, cobalt or iron nanoparticles) are deposited, and the growth is started by the introduction of two gases : a process gas (such as ammonia) and a gas containing carbon (such as methane). The carbon nanotubes start growing on the metallic particles and their size is related to the size of the catalysts. Several types of CVD are currently employed :

- In the *High Pressure Carbon Monoxide* (HiPCo) method, the reaction happens in gas phase : the carbon monoxide (CO) provides for carbon atoms while an iron pentacarbonyl ($Fe(CO)_5$) is used to produce iron nanoparticles on which the growth starts [128]. This method is designed to produce single-wall carbon nanotubes, with diameters in the 0.7 nm to 1.2 nm range and lengths spanning from 100 nm to 1000 nm³.
- An other method is called *Cobalt Molybden Catalyst* (CoMoCat). In this case, carbon monoxide is also used as the source of carbon atoms, but the catalysts are Cobalt nanoparticles. The specificity lies in the fact that the Cobalt forms a non-metallic dual oxide with Molybdenum oxide (MoO_3) [129]. After interaction with CO , it produces highly dispersed small metallic cobalt clusters. This results in a higher selectivity of the nanotube chiral species grown compared to the HiPCo method, with a majority of (6, 5) nanotubes and other species having a nearby diameter⁴.

In the previous sections the properties of carbon nanotubes were introduced, and it showed clearly that some of these properties depend critically on the nanotubes (n, m) indices, in particular their transition energy (see section 2.2). The synthesis processes described above are never perfectly selective, which means that several nanotube species, with different optical transitions, cohabit. This issue is dramatic for applications because the integration of a particular species, with given characteristics, in not possible. However, very recently, some methods reached a success rate above 99% for a given species [17].

As for laboratory experiments, it is always possible to isolate a single carbon nanotube after the synthesis and then study it thoroughly. In order to ease that process, some techniques were developed to obtain nanotubes with a low density. It

³<http://www.nanointegris.com/en/hipco>

⁴<http://www.sigmaaldrich.com/catalog/product/aldrich/773735>

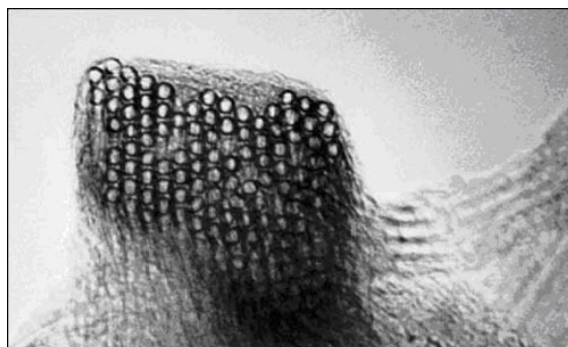


Figure 2.14 – TEM image of a rope made of about a hundred carbon nanotubes. From *Thess, Lee, Nikolaev, and Dai, Science 273, 5274 (1996)* [131]. Reprinted with permission from AAAS.

is also possible to control accurately where the growth happens and thus to select the environment of the nanotube (substrate or suspended). In our laboratory, the CVD is optimized for bigger carbon nanotube diameters than the one this study focuses on. Consequently, commercial solutions were employed. The micellar suspensions used to separate nanotubes from each other are introduced in the next section.

2.3.2 Micellar suspension

Though carbon nanotubes were synthesized since 1991, their photoluminescence was observed for the first time at the beginning of the 21st century. The reason is that they were produced as a powder in which the nanotubes formed small bundles (a specific case can be seen in figure 2.14). These aggregates hold by Van der Waals bonds. Though the forces involved are low, their integration over the full nanotubes length leads to very strong binding energies, typically over a few $\text{eV } \mu\text{m}^{-1}$, which means over thermal agitation, even at room temperature. The issue is that bundles lead to interactions between semi-conducting and metallic nanotubes, which in turn lead to a quenching of the fluorescence of the formers [130].

In 2002, O’Connell et al. proposed a way to break these bundles in order to individualize carbon nanotubes [16]. For that, an aqueous dispersion of raw single wall carbon nanotubes was diluted in sodium dodecyl sulfate (SDS) and ultrasonic agitation was performed. Afterwards, they used centrifugation to remove the remaining bundles. The nanotubes left were encapsulated in cylindrical micelles, as depicted in figure 2.15. In these micelles, the hydrophobic part of the SDS molecules is against the tube, and the hydrophilic one is towards the outside, which eases the solubilization.

This method provides for homogeneous and stable individualized nanotubes for which an optical study is possible. Though SDS is still widely used in the production of micelle encapsulated carbon nanotubes, the ones studied in this work were processed with an other molecule called polyfluorene (PFO). The idea of using

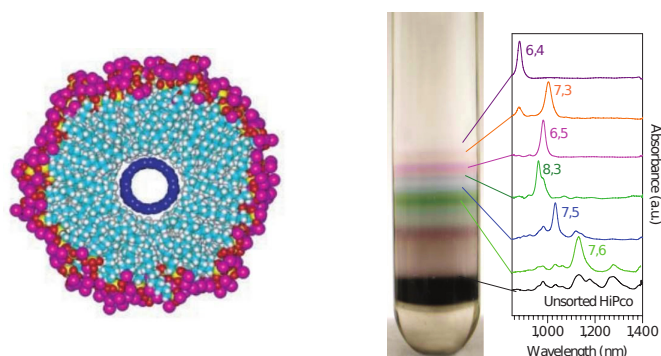


Figure 2.15 – A micelle encapsulated single carbon nanotube. Separating the different carbon nanotube species by centrifugation. From *O’connell et al, Science 297, 5581 (2002)* [16]. Reprinted with permission from AAAS.

aromatic polymers arose in 2007 [132], with the aim of getting a better selectivity for some species and thus an enhancement of the percentage of photoluminescing nanotubes in a given sample.

The sample used in this work consisted in PFO-wrapped CoMoCat nanotubes, diluted in toluene, prepared at LPS Orsay by Nicolas Izard, with a technique described in [133]. These nanotubes-PFO co-polymers were then ultracentrifugated to eliminate bundles. In the end, the metallic nanotubes are scarce, and the semi-conducting ones have emission wavelengths in the near infrared ($\lambda \simeq 900$ nm).

2.3.3 Spin coating

In this section, the way carbon nanotubes are spatially individualized is presented. A density of nanotubes low enough to obtain a single object per optical spot is sought. This step is particularly important to make an optical study of individual objects possible.

For that, a technique called *spin coating* is used. It consists in putting a drop of the liquid containing the carbon nanotubes on a substrate and spin this substrate quickly (1500 spins per minute). The drop splashes and the content spreads homogeneously, forming a thin film, with a good thickness reproducibility. After a few seconds, the liquid (toluene here) evaporates and one gets an homogeneous layer of carbon nanotubes on the substrate. The speed of the spinning and the concentration of the solution are the two parameters that one can adjust to tune the density of objects. For the optical study of single carbon nanotubes, it is mandatory that the emitters are separated from each other, in average, by a distance higher than the typical size of a focused beam (here $\lambda/2 \lesssim 500$ nm).

After optimization of the process, a density of emitters of $0.1 \mu\text{m}^{-2}$ was obtained, which is a good compromise between well separated emitters and a density high enough for convenience. But the emitters detected from photoluminescence do not compose the whole sample. Indeed some semi-conducting nanotube do not

display photoluminescence, others emit out of our detection range, and some metallic nanotubes may be present, even with PFO samples. All together, absorption measurements [134] show that the density of nanotubes is about an order of magnitude higher than the *effective* density of emitters (i.e. the ones detected by photoluminescence).

Carbon nanotubes are usually subject to several kinds of disruption in their photoluminescence signal, which are discussed in section (4.3). These effects are most likely due to their interactions with the substrate [135, 26], and in particular their sensitivity to local charge fluctuations [53]. An experimental optimization led us to choose to embed them in a polystyrene matrix in order to reduce these perturbations, as well as aging.

The details about the cavities used in this work are given in chapter 3, however it is already important to mention that the substrate on which the carbon nanotubes are deposited, in a layer of polystyrene, is a mirror (distributed Bragg reflector, described in 3.2.2). In this scope, polystyrene is diluted in toluene and then mixed with PFO-wrapped carbon nanotubes also diluted in toluene. The concentration of polystyrene is experimentally optimized to obtain the desired layer thickness and the nanotube concentration is adapted to keep the density of emitters equal to $0.1 \mu\text{m}^{-2}$. The thickness of the layer is chosen to let carbon nanotubes be in a field maximum of the cavity. Typically, the thickness used is $120 \pm 5 \text{ nm}$.

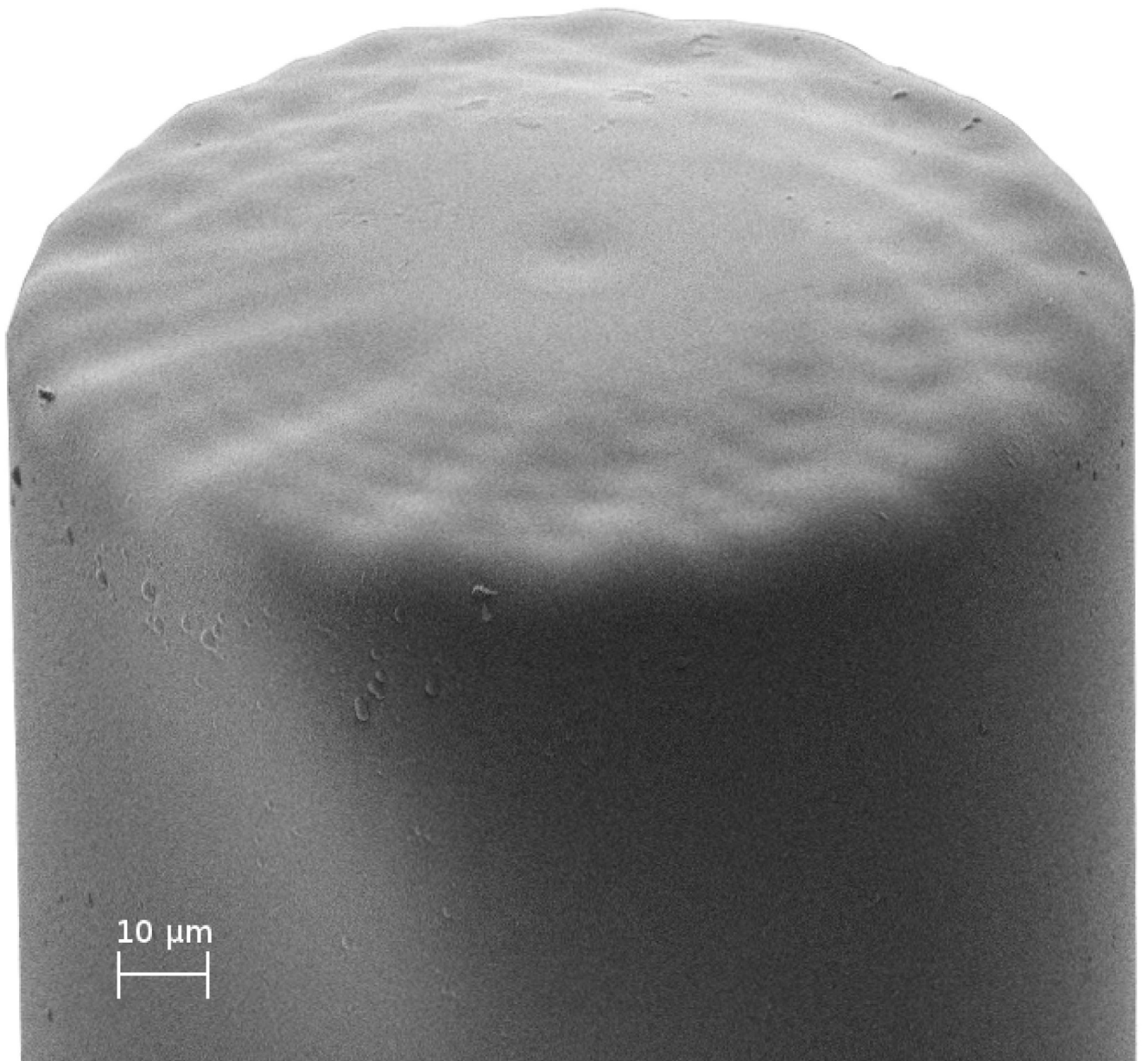
Conclusion

In this chapter, the structural and electronic properties of carbon nanotubes were introduced. Their optical properties depend strongly on their geometry. In particular, the emission wavelength for semi-conducting nanotubes depends on the inverse of their diameter. More over the confinement induced by the one-dimensional geometry implies a strong interaction between the charge carriers, leading to stable excitons which govern the optical properties up to room temperature.

Though progresses are constant, a completely selective synthesis is still not available for carbon nanotubes. More over, the strong dependence of their optical properties on their environment implies that their transition energy varies even between two emitters of the same species. Given that, spin coating is used to make nanotubes samples with a density optimized to allow single emitters to be coupled with fiber Fabry-Perot microcavities.

3

A FIBER FABRY-PEROT
MICROCAVITY



Contents

3.1	Cavity Planar-Concave modes	69
3.1.1	Resonant condition	69
	Hermite-Gauss modes	70
	Resonant frequency	71
3.1.2	Spectrum of an empty cavity	72
	White field measurement	72
	Transverse field distribution	74
3.2	Cavity mode volume	75
3.2.1	Manufacturing of fibered mirrors	75
	Laser ablation principle	76
	Fiber preparation	77
	Shooting setup	77
3.2.2	Effective mode volume	80
	Field penetration in dielectric mirrors	81
	Incidence of the fiber shape	82
3.3	Fiber - Cavity coupling	86
3.3.1	Single mode fibers	88
	Mismatch between fiber and cavity modes	88
	Structure centering and angle between the mirrors	88
3.3.2	Beyond single mode fibers	90
	Multimode Fibers	90
	Using the planar output of the cavity	91
3.4	Finesse and storage time	91
3.4.1	Losses	92
	Absorption losses	92
	Scattering losses	92
	Clipping losses	93
3.4.2	Measuring the finesse	94
	Varying the cavity Length	94
	Cavity ring down spectroscopy - photon storage time	95
	Vibrations and “effective finesse”	97

Introduction

Fiber Fabry-Perot cavities were designed for cold atoms physics. The technology was developed by Jakob Reichel, from the Atom Chips team of the Laboratoire Kastler Brossel (LKB) and the group of David Hunger, from the Ludwig-Maximilians-Universität München. Their first goal was to obtain a small volume and very a high finesse in order to miniaturize a Bose-Einstein Condensation setup [136], but the technology is more versatile.

Such characteristics can be reached with laser ablation, which enables to create a concave depression at the apex of an optical fiber, with a very low surface roughness [33]. This optical fiber is then coated with a high-reflectivity dielectric stack. A cavity can be formed with two such mirrors or with a fibered mirror and a planar one. The former geometry is more suited to cold atoms experiments, but the later is more convenient to study nano-emitters, which can easily be deposited on the planar surface.

Though the technology had been developed for cold atoms, the LKB team extended it to the field of condensed matter to study quantum wells and quantum dots [137]. And more recently Albrecht et al. [138, 139], as well as [140], used fibered cavities to couple single nitrogen or silicium vacancies in nanodiamonds.

In this chapter, the modes for planar-concave cavities are described and characterized. Afterwards, a description of the fiber manufacturing procedure is given. Further considerations about the field penetration in the mirrors lead to introduce an expression of the effective cavity volume. Finally, the fiber-cavity coupling issue is addressed and the finesse is defined. How the cavity is embedded into the global setup is kept for chapter 5.

3.1 Cavity Planar-Concave modes

The Fabry-Perot interferometer is a textbooks classics : if two mirrors face each other, some stationary modes are established in between. These modes depend on the curvature of the mirrors, their reflectivity and the distance between them. A discussion of the longitudinal resonant condition is given, as well as a description of the spatial properties of these modes.

3.1.1 Resonant condition

Let's consider two planar mirrors with reflection coefficients $R_{1,2}$, separated by a geometrical distance L . It is easy to show that the constructive interferences lead to stationary modes of wavelength λ_n , given by the condition :

$$L = n \cdot \frac{\lambda_n}{2} \text{ with } n \in \mathbb{N}^* \text{ or } L = n \cdot \frac{c}{2\nu_n} \text{ in term of frequency} \quad (3.1)$$

The spectral gap between two modes is called Free Spectral Range (FSR), and is given by :

$$FSR_\lambda = \lambda_{n+1} - \lambda_n \text{ or } FSR_\nu = \frac{c}{2L} \text{ in term of frequency} \quad (3.2)$$

and the finesse of the cavity, defined by the ratio between the FSR and the spectral width $\delta\nu$ of a peak $\mathcal{F} = \frac{FSR_\nu}{\delta\nu}$, is given by :

$$\mathcal{F} = \frac{\pi}{2 \arcsin\left(\frac{1}{\sqrt{F}}\right)} \quad (3.3)$$

$$F = \frac{4\sqrt{R_1 R_2}}{(1 - \sqrt{R_1 R_2})^2} \quad (3.4)$$

For high reflectivity mirrors this formula is commonly approximated by :

$$\mathcal{F} \simeq \frac{\pi(R_1 R_2)^{1/4}}{1 - (R_1 R_2)^{1/2}} \quad (3.5)$$

In this work, one mirror is planar while the other has a concave shape. In the same way than the field is labeled along the cavity axis by a number n , two other indices (l, m) are introduced to take into account the lateral confinement of the mode induced by the mirror's curvature.

Hermite-Gauss modes

Gaussian beams are a solution to the paraxial Helmholtz equation [141, (ch. 16.4)] that describes the field established in the Fabry-Perot cavity in the paraxial approximation for a spherical mirror. The field is written as follows :

$$\begin{cases} E_{n,l,m}(x, y, z) &= E_l(x, z)E_m(y, z)Z_n(z) \\ E_l(x, z) &= \mathcal{H}_l\left(\frac{\sqrt{2}x}{w(z)}\right) \exp\left(-\frac{x^2}{w^2(z)}\right) \exp\left(-i\frac{kx^2}{2R(z)}\right) \exp(i\psi_l(z)) \\ E_m(y, z) &= \mathcal{H}_m\left(\frac{\sqrt{2}y}{w(z)}\right) \exp\left(-\frac{y^2}{w^2(z)}\right) \exp\left(-i\frac{ky^2}{2R(z)}\right) \exp(i\psi_m(z)) \\ Z_n(z) &= E_0 \frac{w_0}{w(z)} \exp(-ikz) \end{cases} \quad (3.6)$$

where $k = \frac{2\pi}{\lambda}$, \mathcal{H}_i is the i^{th} Hermite polynomial¹ and the other parameters characterizing the beam are :

¹It is defined as : $\mathcal{H}_i(X) \equiv (-1)^m \exp X^2 \frac{\partial^i}{\partial X^i} \exp(-X^2)$

- The beam transversal width :

$$w(z) = w_0 \sqrt{1 + \left(\frac{z - z_0}{z_R}\right)^2} \quad (3.7)$$

- The curvature of the wavefront :

$$R(z) = (z - z_0) \left(1 + \left(\frac{z_R}{z - z_0}\right)^2\right) \quad (3.8)$$

- The Gouy phase :

$$\psi_l(z) = \left(l + \frac{1}{2}\right) \arctan\left(\frac{z - z_0}{z_R}\right) \quad (3.9)$$

- The Rayleigh length :

$$z_R = \frac{\pi w_0^2}{\lambda} \quad (3.10)$$

Where z_0 is the position of the waist. The cavity mode is stable only if its curvature corresponds to the one of the mirrors in $z = 0$ and $z = L$. This implies that the beam waist is on the planar mirror, taken as the origin $z_0 = 0$, and that $R_n(L) = \mathcal{R}$, the radius of curvature of the fibered mirror. This is depicted in figure 3.1. From these relations, one gets the mode waist in the cavity (derivation in appendix A.1.1) :

$$w_0^2 = \frac{L\lambda}{\pi} \sqrt{\frac{\mathcal{R}}{L} - 1} \quad (3.11)$$

In general, one can consider that the cavity is stable as long as $L < \mathcal{R}$, which is of limited importance as this work focuses on very short cavities.

Resonant frequency

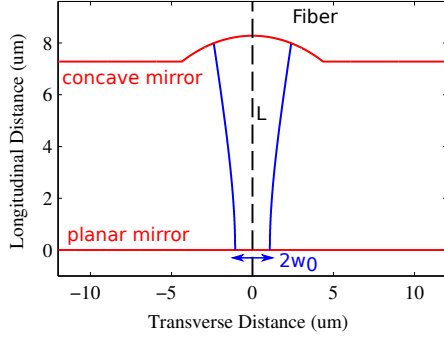
After a round trip in the cavity, the phase acquired by the wave must be zero :

$$\Delta\phi = 2\pi n, \text{ with } n \in \mathbb{Z} \quad (3.12)$$

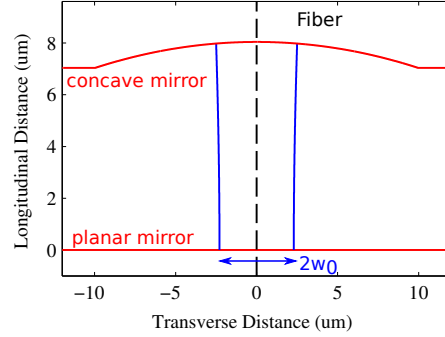
The resonant condition is thus given by [141, (p.761)] :

$$\nu_{l,m,n} = \frac{c}{2\pi L} \left(\pi n + (m + l + 1) \arccos\left(\pm \sqrt{1 - \frac{L}{\mathcal{R}}}\right) \right) \quad (3.13)$$

The second term, arises from the Gouy phase. For $m = l = 0$, one finds the fundamental gaussian modes, separated by the FSR defined in eq. (3.2). The other modes come in between, with a separation depending on the cavity length and the radius of curvature of the concave mirror. These higher order modes are characterized by a different transversal repartition of the field, with $m + l + 1$ lobes (see section 3.1.2



(a) The concave mirror has a radius of curvature $\mathcal{R} = 10 \mu\text{m}$, the cavity length is $L = 8 \mu\text{m}$ and the waist is $w_0 = 1.1 \mu\text{m}$



(b) The concave mirror has a radius of curvature $\mathcal{R} = 50 \mu\text{m}$, the cavity length is $L = 8 \mu\text{m}$ and the waist is $w_0 = 2.3 \mu\text{m}$

Figure 3.1 – The cavity is composed of a planar mirror on a flat substrate and a concave mirror laser machined at the apex of an optical fiber. The curvature of the later mirror and the cavity length define the waist, which is located on the planar mirror.

for more details). It is noteworthy that the modes having the same $m + l$ value are degenerate.

3.1.2 Spectrum of an empty cavity

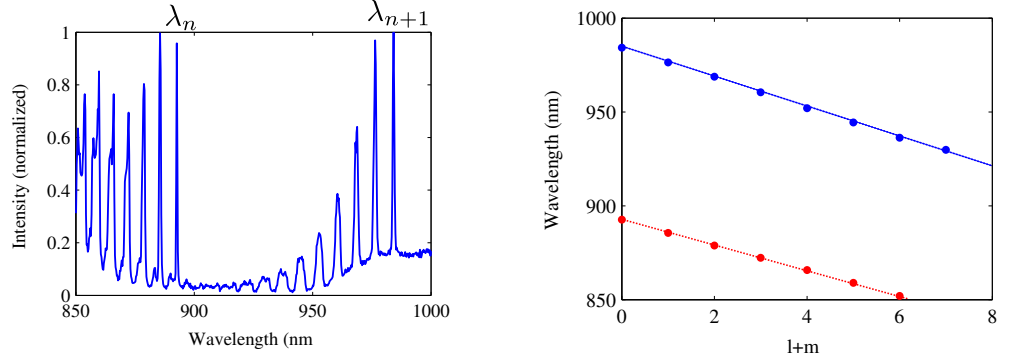
Now that the (n, l, m) modes of the cavity are defined, the optical spectrum of such a cavity is considered in order to get informations about its geometry. In this setup, the cavity is formed between a fixed planar mirror and a movable concave mirror manufactured at the apex of an optical fiber. The cavity length is controlled with a nanometric precision by means of a “slip-stick” technology piezoelectric². The other end of the fiber is used to couple the input light, and the transmission of the cavity can be recorded with a spectrometer and a Charged Coupled Device (CCD).

White field measurement

The spectrum of the empty planar-concave fibered micro-cavity can be obtained by measuring the transmission of a white field (within the reflectivity range of the mirrors) through the cavity. The typical spectrum of such an experiment is given in figure 3.2. One can clearly see two sets of modes, corresponding to two different longitudinal modes n . Each set is composed, from right to left, of transversal modes with increasing $m + l$ indices.

By measuring the distance between the two fundamental modes, one gets the cavity length from eq. (3.2) :

²Attocubes ANC350



(a) Dispersion with 150 lines/cm grating. Two sets of peaks are visible, corresponding to two families of longitudinal modes $n = 10$ and $n = 11$. The spectral range between the two main peaks is 91 nm. The non-zero background on the edges is due to the variation in the reflectivity of the mirrors with respect to the wavelength.

(b) Wavelengths of the two series of modes visible in a) labeled by increasing $l + m$. In blue, the $n + 1$ series and in red the n series. The dotted lines correspond to linear fits.

Figure 3.2 – A white field is sent into the cavity and the transmission is dispersed by a spectrometer before being recorded by a Charge Coupled Device.

$$L = \frac{\lambda_n \lambda_{n+1}}{2FSR_\lambda} \quad (3.14)$$

where the FSR is in units of wavelength. From equation 3.13, one finds that the frequency gap $\Delta\nu$ between the transverse modes depends only on the ratio $\frac{L}{\mathcal{R}}$. For a given cavity length, measuring this gap is thus a way of measuring the radius of curvature of the concave mirror, and a way to estimate the waist of the mode w_0 :

$$\Delta\nu = \nu_{l,m+1} - \nu_{l,m} = \frac{c}{2\pi L} \left(\arccos \left(\pm \sqrt{1 - \frac{L}{\mathcal{R}}} \right) \right) \quad (3.15)$$

$$\mathcal{R} = L \sin \left(2\pi \Delta\nu \frac{L}{c} \right)^{-2} \quad (3.16)$$

$$w_0^2 = \frac{L\lambda}{\pi} \tan \left(2\pi \Delta\nu \frac{L}{c} \right)^{-1} \quad (3.17)$$

In the end, such a white field measurement yields both the length and the waist of the cavity mode, which ultimately lead to the mode volume, as discussed in section 3.2. It is also visible in figure 3.3 that there is a lifting of the degeneracy of the high order transverse modes, for example TEM_{n01} and TEM_{n10} . This can be explained by the ellipticity of the fibered mirror which can typically reach 10% for the

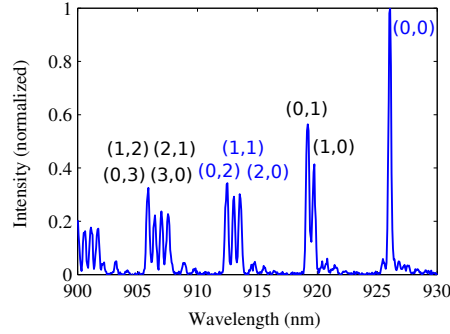


Figure 3.3 – Compared to figure 3.2, the dispersion grating has 600 lines/cm. The splitting between mode TEM_{n01} and TEM_{n10} is clearly visible, as well as the splitting in higher order constant $l + m$ modes. The (l, m) indices are noted above each peak.

smallest structures. In order to illustrate this phenomenon, the formula 3.13 can be used to compute the resonant mode TEM_{n10} and TEM_{n01} of the same longitudinal series $n = 6$. If one considers that the first is reflected in a direction where the radius of curvature is $10 \mu\text{m}$ while the second is reflected in a direction where the radius of curvature is $11 \mu\text{m}$, the wavelengths obtained for a cavity length $L = 3 \mu\text{m}$ are 942 nm and 945 nm . This discrepancy of $L = 3 \text{ nm}$ corresponds well to the range of values measured with the cavities used in this work.

Transverse field distribution

The previous paragraph focused on the spectral characteristics of the cavity modes. But it is also possible to get informations about the spatial characteristics. Indeed, from formula 3.6, one gets the transverse intensity profile associated with the (l, m) Hermite-Gauss mode :

$$I_{lm} \propto E_{lm} E_{lm}^* \propto \mathcal{H}_l \left(\frac{\sqrt{2}x}{w} \right)^2 \mathcal{H}_m \left(\frac{\sqrt{2}y}{w} \right)^2 \exp \left(-2 \frac{x^2 + y^2}{w^2} \right) \quad (3.18)$$

The fundamental mode has a gaussian profile while the higher order modes are characterized by l nodes in the x direction and m nodes in the y direction.

As in the previous section, the cavity is created by bringing a planar mirror close to the concave mirror at the tip of the fiber and a monochromatic laser beam is sent through the cavity. Its far-field output is directly recorded with a camera³. As the cavity length is tuned, several modes come to resonance with the laser. By this method, all the peaks of figure 3.3 can be assigned to a transverse electromagnetic mode. Some examples are given in figure 3.4.

³Thorlabs DCC1645C

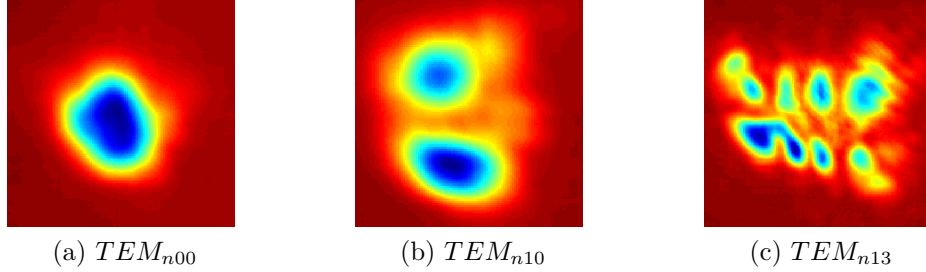


Figure 3.4 – Transverse modes observed on a camera at the output of the cavity. The distorted shapes are due to the ellipticity of the concave mirror and to a non optimized imaging system.

3.2 Cavity mode volume

One of the most important parameters of these cavities is the volume of their modes. Considering as a first approximation that the TEM_{n00} mode is a cylinder of radius w_0 and of length L (a valid approximation as long as L is lower than the Rayleigh length defined in eq. (3.10)), one gets the following expression for the volume :

$$V \simeq \frac{\pi}{4} w_0^2 L \simeq \frac{\lambda}{4} L^{3/2} \sqrt{\mathcal{R} - L} \quad (3.19)$$

In order to obtain the lowest mode volume cavity, two parameters can be reduced : the cavity length and its radius of curvature. Given the dependency on these parameters in the volume's formula, letting the length tend towards zero may seem the most efficient way to decrease the volume, even at the cost of letting the radius of curvature increase. However, as explained in section 3.2.2, the cavity's minimum length is limited by the field penetration in the mirrors. Consequently, a compromise is needed between reducing \mathcal{R} and L .

In this section details are given about how the concave mirrors are produced, in order to explain within which limits \mathcal{R} is chosen. Then the field penetration into the mirrors is described in order to sketch the limits of L and derive an effective mode volume.

3.2.1 Manufacturing of fibered mirrors

The cavities in this work are composed of a planar dielectric mirror and a second mirror laser-machined at the apex of an optical fiber. This technology has been developed in the past years in the Atom Chips team of the Laboratoire Kastler Brossel, under the supervision of Jakob Reichel. The goal of their work was to get micro-mirrors, with controlled radii of curvature and smooth surfaces.

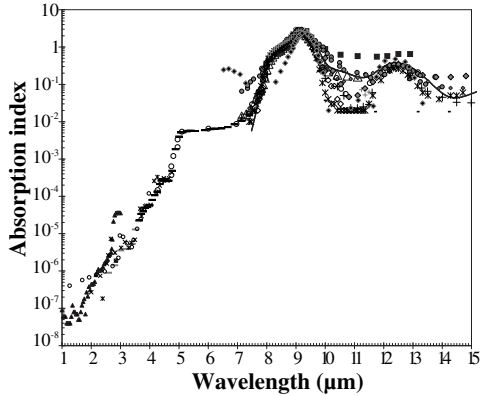


Figure 3.5 – Optical absorption (imaginary part of the optical index) of silica. Reprinted from [147], with permission from OSA Publishing.



Figure 3.6 – Principle of laser ablation : a CO₂ laser is highly absorbed in the first tens of microns of silica.

Laser ablation principle

In this work, the aim was to go towards very small mode volume cavities (typically lower than $10\lambda^3$) while retaining a finesse over a few thousand. Thus the goal was to create a concave spherical mirror, at the tip of an optical fiber, with a radius of curvature lower than $50\ \mu\text{m}$ and with a low surface roughness.

Optical fibers are usually made of melted silica, an amorphous form of SiO₂. In order to create a concave shape at their tip, one can consider mechanical machining [142] but it is limited by the size of the instruments; chemical dissolution in HF acid, but the shape is difficult to control [143]; or focused ion beam (FIB) which is very accurate but for which the surface roughness is too high compared to the requirements of the experiments considered [144, 145].

Silica is transparent in the visible and near infrared, thus laser ablation is very hard to implement at these wavelengths and requires pulsed excitation and very high intensities in order to take advantage of the non-linear processes. With this kind of methods, the surface roughness obtained does not fit the requirements [146].

Nevertheless, vibration modes of Si-O-Si have a resonance around $9\ \mu\text{m}$ [147] as shown in figure 3.5. This is why a CO₂ laser operating at $10.6\ \mu\text{m}$ is used. When the laser is focalised at the tip of the fiber, as depicted in figure 3.6, it is highly absorbed in the first tens of microns of silica. Then two phenomena happen : the surface of the fiber sublimates, creating the depression, while a little bit deeper the silica melts, and the surface tension of the liquid obtained smooths the surface, leading to a surface roughness of about $\sigma = 0.2\ \text{nm}$ [33].

This technique is now well mastered and was used to obtain micro-lenses, as well as concave depressions. The Atom Chips team even developed a standard way of

shooting the fibers, so that they can use multiple shots to tailor the shape of their fibers. Their specialty is to create micro-mirrors with a large radius of curvature (up to 1 mm) [148]. On the contrary, this work focuses on radii of curvature as small as possible, which lead to slight modifications of their setup.

Fiber preparation

The fibers used in this work were intended to go into ultra high vacuum for multilayer dielectric deposition, which forbids the use of standard acrylate coatings. This is why copper coated fibers⁴, operating in the 800 nm – 1000 nm range were used. Their diameter was 125 μm without the coating; with a mode field diameter of 6 μm for the single mode fibers and a core of 50 μm for the multimode fibers.

The coating was removed over a few millimeters by sonication in a ClFeIII solution⁵ during 20 minutes. They were cleaned with distilled water and isopropanol. The fibers were then cleaved using a commercial setup⁶ which applies a tension to the fiber and breaks it with a diamond blade. The cleave angle is critical for the laser ablation and must be within 0.5° of the perpendicular direction to the fiber axis.

Once the fibers were cleaved they were placed in home-made mounts (see fig. 3.8) which can hold up to 42 fibers in rows, at 2 mm from each others. Using these mounts, the shooting can easily be processed repeatedly.

Shooting setup

The fiber shooting setup, described in figure 3.7, has two main devices : in the upper position the fibers are imaged with an interferometer to measure the shape of their surface. Once it is done, the plate which holds them (see fig. 3.8) is moved to a second position, where an aspherical lens focuses the CO_2 laser beam to process with the ablation.

The interferometer is a Mirau objective working at 515 nm with a numerical aperture of 0.4 and a working distance of 4 mm, enabling to image fully a 125 μm diameter fiber. The interferences between the surface under study and the reference mirror lead to fringes. Their phase depends linearly on the distance between the two reflective surfaces :

$$I(x, y) = I_0 \left(1 + \cos \left(\frac{4\pi}{\lambda} z(x, y) \right) \right) \quad (3.20)$$

Where $z(x, y)$ is the depth of the surface under study. The translation stage has an accuracy of about a nanometer. Hence, it is possible to change the distance of the surface under study (typically by steps of $\lambda/8 = 64 \text{ nm}$) and to record the interferences. After a few steps, one can reconstruct the shape of the surface with an accuracy of the order of 1 nm in depth and 1 μm radially [149].

⁴IVG Fibers Cu800 (single mode) and Cu50-125 (multimode)

⁵Concentration : 336 g/l

⁶NYFORS Auto-cleaver

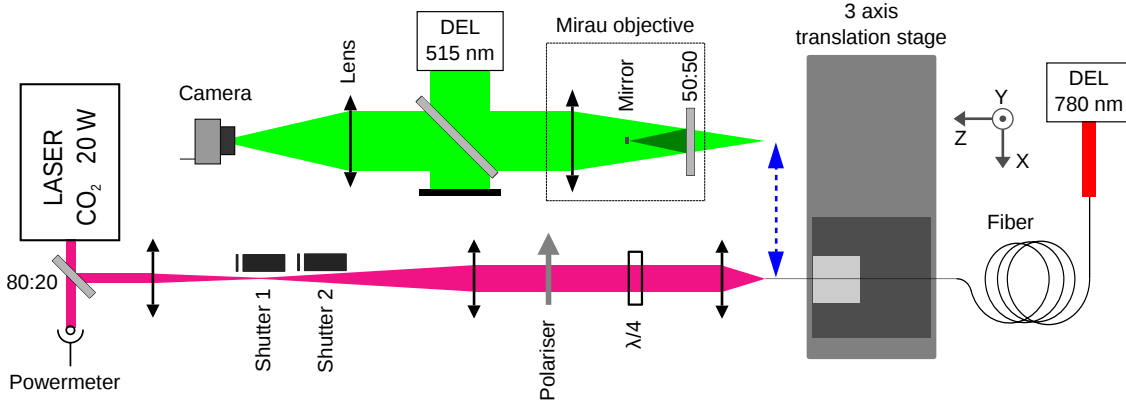


Figure 3.7 – Schema of the shooting setup : the fiber is on a translation stage, which can switch between two positions. The shooting position is in the lower part of the schema. In the upper part, a Mirau objective is present to analyze the surface of the fiber before and after the shoot. Adapted from [149], with the author’s permission.

Once the surface is investigated, the fiber is shifted to the shooting position with micrometer stages. The lateral shift simply corresponds to the distance between the interferometer’s optical axis and the CO₂ beam axis, but the longitudinal displacement is of major importance : it controls how far the fiber surface is from the CO₂ beam waist.

As a matter of fact, the shape of the depression obtained depends mostly on three parameters : the impulsion duration, its energy and the beam width, given by (see eq. (3.7)) :

$$w(z) = w_0 \sqrt{1 + \frac{\lambda_{CO_2}}{\pi w_0^2} (z - z_0)} \quad (3.21)$$

where w_0 is the CO₂ beam waist and z_0 its position compared to the surface of the fiber.

The depression created can be approximated by a gaussian over a large range of shooting parameters. However, the link between the Gaussian parameters and the CO₂ beam parameters is complex (see reference [150] for details). Because of this shape, the local radius of curvature changes along the transverse coordinate, but fortunately the variation is small close to the center. In this region the depression can be approximated by a portion of sphere. This sphere has a radius of curvature \mathcal{R} , taken as the radius of curvature of the future mirror, a depth z_t and a diameter D , defined as the full width at $1/e$ of the gaussian profile, which is considered as the effective diameter of the mirror, as can be seen in figure 3.9.

By use of the gaussian approximation, these parameters can be linked together with the formula [33] :

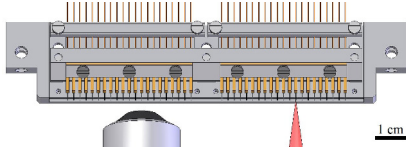


Figure 3.8 – Shooting setup : on the left a Mirau objective enables a measurement of the surface, on the right, a CO₂ laser is focused by an aspherical lens. The fibers are rowed in a metallic holder, to be shot in series. Reprinted from [149], with the author’s permission.

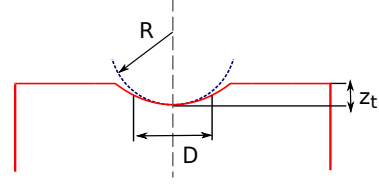


Figure 3.9 – Depression profile and parameters : In red the shot fiber, in blue the spherical approximation (with a radius of curvature R). z_t is the depth of the structure, and D its diameter, as defined in the text.

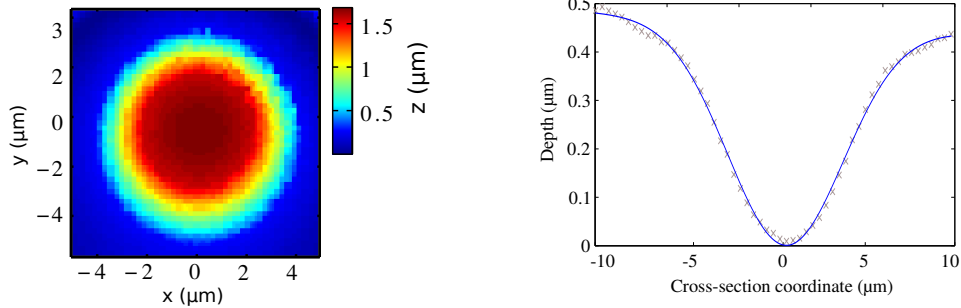
$$z_t \approx \frac{D^2}{8\mathcal{R}} \quad (3.22)$$

Consequently, these three parameters cannot be controlled independently. For a given radius of curvature, a reduction of the depth (sought for a decrease in the cavity length), implies a decrease of the mirror diameter, which has a cost in terms of stability (see section 3.4.1 and [151]).

The shooting parameters (impulsion duration, energy and beam width) are not independent. Nor are the parameters of the created structure parameters (RoC, depth and diameter). The dependence of the later on the former and on the CO₂ beam waist is quite complex. Roughly, one can state that for a given power and impulsion length, shooting closer to the CO₂ beam waist creates smaller and deeper structures. For a given position, increasing the power or the impulsion length has a similar impact : it makes deeper and larger structures. One seeking very small radii of curvature should use comparatively shorter and more powerful impulsions while one seeking shallow structure should decrease the power and increase the impulsion length.

The Atom Chips team specialty is to create large radii of curvature (from a hundred microns to over a millimeter), either with single or multi-shoots. For that, the aspherical lens used has a focal $f = 25.4$ mm and the shots are performed several hundreds of microns away from the beam waist.

For this work, smaller structures are sought. Consequently, an $f = 12.7$ mm aspherical lens is used to focus the CO₂ beam to a waist lower than $10 \mu\text{m}$ and the fibers are shot directly at the waist of the beam. With this modification, the fibers obtained have a radius of curvature $\mathcal{R} = 50 \mu\text{m}$ and a depth $z_t = 0.3 \mu\text{m}$ for the



(a) Surface imaged with the Mirau interferometer, as described in the text. The color axis indicates the depth.

(b) A cross-section in the surface profile.

Figure 3.10 – Surface of a typical fiber manufactured by laser ablation. Here the diameter is $D \simeq 10 \mu\text{m}$, the depth is $z_t = 1.5 \mu\text{m}$ and the radius of curvature is $RoC = 12 \mu\text{m}$.

largest and shallowest structures. An a radius of curvature $\mathcal{R} = 8.5 \mu\text{m}$ and a depth $Z = 1.5 \mu\text{m}$ for the smallest, as displayed in figure 3.10.

Once the fibers are shot, they are sent, as well as planar mirrors, to a company⁷ which deposits dielectric mirrors by low loss ion beam sputtering. As they control tightly the deposition, the surface roughness of the mirrors obtained remain equal to the one of the surface below the coatings.

3.2.2 Effective mode volume

The cavity mode volume is more complex than the cylinder approximation introduced in eq. (3.19). The effective mode volume felt by an emitter in the cavity is defined with respect to the energy density as the integrated square of the field over its maximum⁸ [44] :

$$V_{eff} = \frac{\int d\vec{r} \epsilon_r(\vec{r}) |\vec{E}(\vec{r})|^2}{\max(\epsilon_r(\vec{r}) |\vec{E}(\vec{r})|^2)} \quad (3.23)$$

In the following paragraphs, the effect of the field penetration in the mirrors is investigated and the impact of the fiber shape is discussed.

⁷Laseroptik, Garbsen

⁸Here, the integral in the numerator can be understood from the normalization in eq. (1.3). The maximum function in the denominator arises from the fact that the Purcell factor is defined for the case where the emitter is in a maximum of the cavity field.

Field penetration in dielectric mirrors

In order to have high reflectivities and low losses, mirrors composed of multiple thin layers of materials with a very large optical index contrast are used. By choosing appropriately the thickness of these layers, one can reach very high reflectivities for a given wavelength λ . The simplest structure for such dielectric mirrors is called a Distributed Bragg Reflector (DBR) composed of m layers of the two media, each of which has a thickness $\lambda/4n$.

In this case, the materials are silica (SiO_2 , $n = 1.468$) and tantala (Ta_2O_5 , $n = 2.076$) because they have a very low absorption in the visible and near infrared. Moreover, the top layer is the one with the highest index because it limits the field penetration into the mirror [152].

Let's recall that the cavities used in this work are composed of a fibered mirror and a planar mirror on which the emitters are deposited. The field simulation corresponding to the coating of the fiber is presented in figure 3.11a.

As described in section 2.3.3, an extra layer containing the emitters is added on the top of DBR. It is composed of polystyrene ($n = 1.6$) in which the emitters are embedded. As the position of the emitters inside this layer is not controlled, its thickness must ensure that at least part of them are located in the field maximum. The modified field simulation in the case where an extra polystyrene layer of 400 nm is added, as shown in figure 3.11b.

In fact, most of the experiments done during this work were carried out with a different planar mirror. This commercial mirror⁹ had the advantage of being easily available, and of having a reflectivity a bit lower than the fibered mirror (see section 3.3.2). This mirror was characterized with reflectivity and transmission measurements. The structure deduced is displayed in figure 3.12a. For this mirror, the lower index was on top, which meant that a thinner polystyrene layer was necessary to ensure that the nanotubes could be in the field maximum. The structure experimentally used, with a 120 nm thick layer, is shown in figure 3.12b. Unless otherwise mentioned, all the further experiments are done with this mirror.

Due to this penetration length, three different “lengths” need to be defined for the cavity :

- L_g is the geometrical length, meaning the distance between the surface of the planar mirror and the surface of the bottom of the concave depression.
- L_{FSR} is the length deduced from the measure of the Free Spectral Range. It takes into account the penetration depth L_p into the Bragg mirror. The relation to the geometrical length L_g is given by :

$$L_{FSR} \simeq L_g + L_p \quad (3.24)$$

⁹Edmund 47587

The penetration length estimated for a typical cavity is 1.1 μm . In order to obtain this value, the two mirrors are simulated (as in fig. see figure 3.11) and the resonances are computed. The penetration length is obtained from the difference between the geometrical length and the length defined by the FSR obtained from these resonances.

- L_{en} is the energetic length which measures the spatial extension of the mode. Its definition is directly obtained from the definition of the mode volume :

$$L_{en} = \frac{\int dz \epsilon_r(z) e^2(z)}{\max(\epsilon_r(z) e^2(z))} \quad (3.25)$$

where the mode is considered as almost cylindrical : $E(\vec{r}) \approx \exp(-r^2/w_0^2)e(z)$. From the above mentioned simulations, one gets (at $\lambda = 900 \text{ nm}$) :

$$L_{en} \simeq 0.425 L_{FSR} \quad (3.26)$$

This length is about half the geometrical length because it measures the spatial extension of the energy of the mode, which is mostly located close to its center (factor 1/2 coming from the mean of a cosine square).

The effective mode volume can be estimated from the product of the energetic length (axial length of the cylinder) and the waist (lateral extension). It is given by :

$$V_{eff} \approx \frac{\pi w_0^2}{2} L_{en} \quad (3.27)$$

The waist itself is given by eq. (3.17). In this formula, the FSR length comes in reference with the transverse mode spacing $\Delta\omega$, while the geometrical length is introduced in the ratio with the radius of curvature. Finally, one gets :

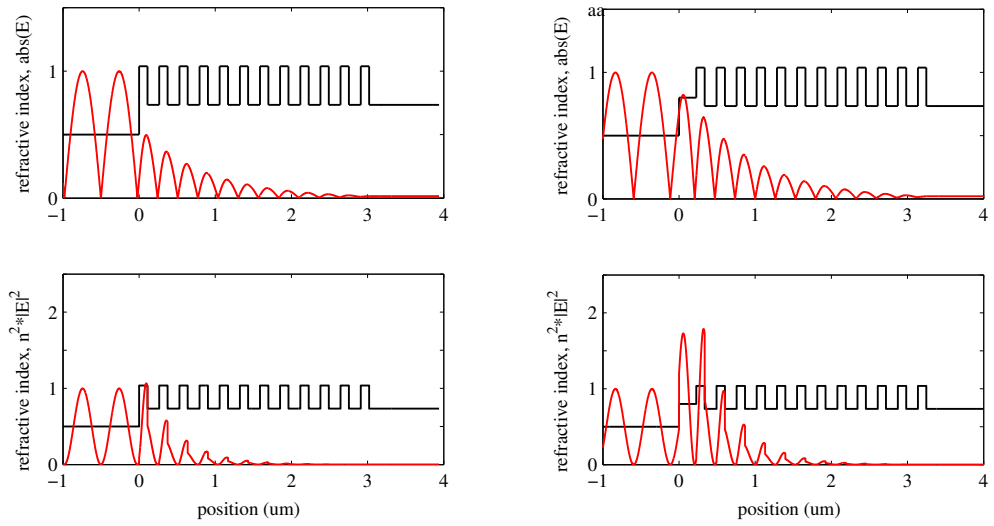
$$w_0^2 = \frac{L_{FSR}\lambda}{\pi} \tan\left(2\pi\Delta\nu\frac{L_g}{c}\right)^{-1} \quad (3.28)$$

$$V_{eff} \approx \frac{L_{FSR}L_{en}\lambda}{2 \tan(2\pi L_g \Delta\omega/c)} \quad (3.29)$$

The volume depends on the three lengths defined above, and cannot be arbitrarily reduced because the field penetration into the dielectrics mirror implies finite FSR and energetic lengths.

Incidence of the fiber shape

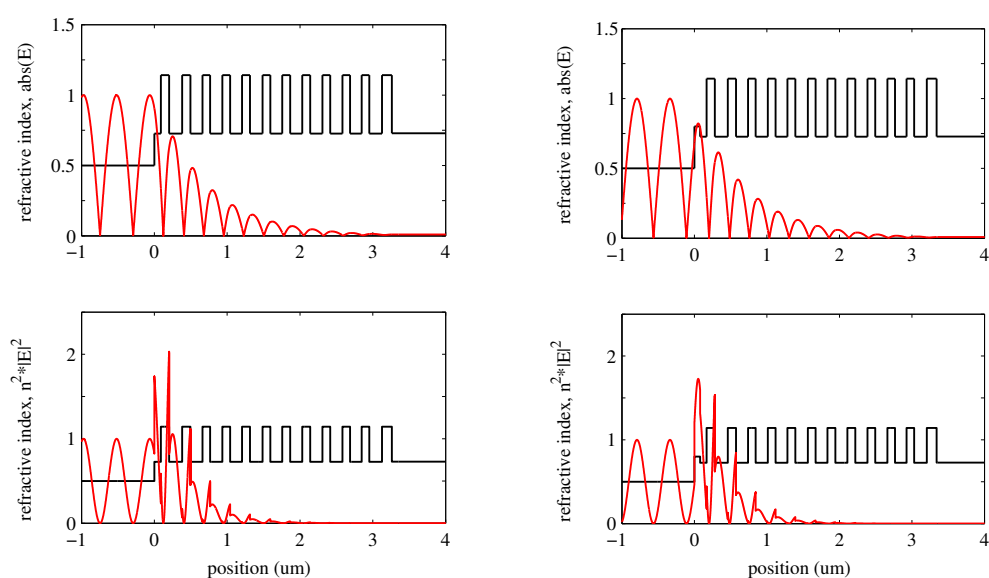
The first generation of fibers used during this PhD had been made by Benjamin Besga during his work on quantum wells [137]. These were multimode fibers, shot a single time, with a radius of curvature, $\mathcal{R} = 50 \mu\text{m}$ and depth $z_t = 0.5 \mu\text{m}$. With



(a) Bragg mirror composed of 12 layers of tantalum ($n = 2.076$) and silica ($n = 1.468$), centered at 910 nm, with the high index on top.

(b) The same Bragg mirror with a layer (400 nm thick) of polystyrene ($n = 1.6$), containing the nanotubes, on top.

Figure 3.11 – Simulation of the electrical field penetration in a Bragg mirror. In black, the optical index. On the top figures $|\vec{E}|$ is plotted in red while in the bottom figures $\epsilon|\vec{E}|^2$, the quantity directly involved in the cavity mode volume, is displayed in red. Both are normalized to a maximum of 1 before reaching the mirror.



(a) Bragg mirror composed of 11 layers of materials with indices $n = 2.284$ and $n = 1.456$, centered at 970 nm, with the lower index on top.

(b) The same DBR mirror with a layer (120 nm thick) of polystyrene ($n = 1.6$), containing the nanotubes, on top.

Figure 3.12 – Simulation of the electrical field penetration in the planar commercial mirror used for CNT deposition. In black, the optical index. On the top figures $|\vec{E}|$ is plotted in red while in the bottom figures $\epsilon|\vec{E}|^2$, the quantity directly involved in the cavity mode volume, is displayed in red. Both are normalized to a maximum of 1 before reaching the mirror.

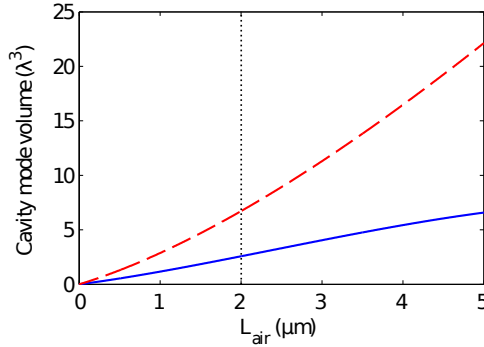


Figure 3.13 – Cavity mode volume as a function of the cavity geometrical length L_{air} , for a $\mathcal{R} = 10 \mu\text{m}$ in solid blue and $\mathcal{R} = 50 \mu\text{m}$ in dashed red. The vertical dashed black line indicates the typical minimum geometrical length obtained for “pencil shape” cavities.

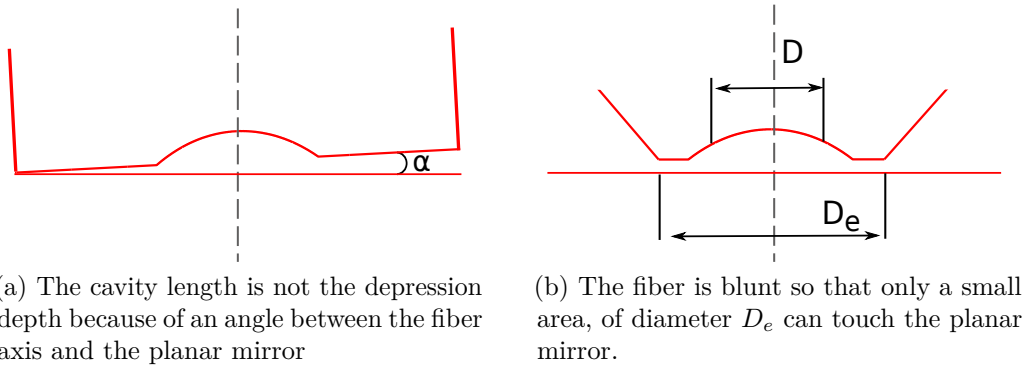


Figure 3.14 – The principle of “pencil” shape fibers

these fibers, the minimum length obtained, estimated from FSR measurements, was $L_{FSR} = 3.5 \mu\text{m}$, with a mode waist estimated to $w_0 = 2.5 \mu\text{m}$. The associated mode volume was $V_{eff} = 20\lambda^3$ at $\lambda = 900 \text{ nm}$.

As a reduction of this mode volume was sought, two strategies were followed : the first and most obvious was to reduce the radius of curvature of the concave depression, see figure 3.13. This leads to a decrease of the cavity mode’s waist and thus to a decrease of its volume. There are two prices to pay : first the cavity’s stability range, limited to $L < \mathcal{R}$, is reduced [151]. Second, in the case of single mode fibers, the coupling between the fiber mode and the cavity mode is reduced as well (see section 3.3.1 for details). Several fibers were made with radii of curvature ranging from $\mathcal{R} = 8.5 \mu\text{m}$ to $\mathcal{R} = 50 \mu\text{m}$ in order to investigate. Concave depressions with a radius of curvature below $\mathcal{R} = 8 \mu\text{m}$ were not studied because mirror deposition implies distortions in such cases [153].

The second strategy is linked to the fact that the effective minimum length

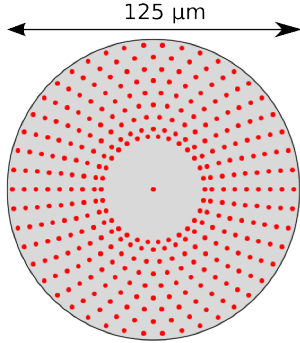


Figure 3.15 – Shooting array. Each dot represents one shoot. The first is the one in the center, afterwards the shots are done in concentric circles from the outer towards the center of the fiber.

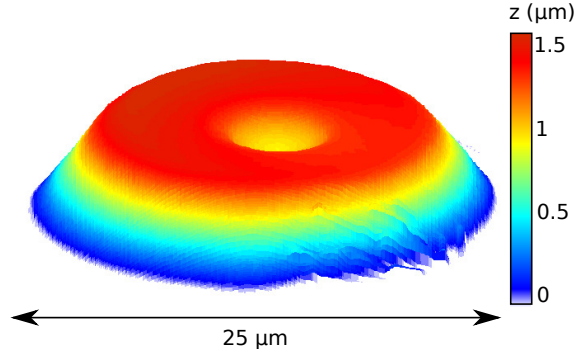


Figure 3.16 – A typical “pencil” shape fiber, with $\mathcal{R} = 10 \mu\text{m}$ measured by profilometry. The “flat” area around the concave depression has a diameter smaller than $20 \mu\text{m}$. The z scale is magnified three times compared to the x and y scales.

obtained with the first generation of cavities was well larger than the depression depth. This was interpreted as the sign that the fiber axis was not perfectly perpendicular to the planar mirror, leading to an angle, as depicted in figure 3.14. Consequently, the fibers were blunt in order to give them a “pencil” shape.

For this process, the fibers are first shot once to create the concave depression at their center. Afterwards, they are shot about 300 hundred times between the the concave depression and the edge (shooting pattern in figure 3.15). These supplementary shots are done concentrically from the outer towards the inner of the fiber. A gradient of power is set, to ensure a rather smooth “pencil” shape. In the end, only a small area of the fiber remains at its initial height, as shown in figures 3.16 and 3.17. A TEM image of such a fiber is displayed on the front page of this chapter.

By means of this method, the minimum length obtained is much closer to the depression depth. It was applied to fibers with a typical radius of curvature of $\mathcal{R} = 10 \mu\text{m}$ and with a depression depth of $z_t = 1.5 \mu\text{m}$, leading to mode volumes about an order of magnitude smaller than with the first generation of fibers : $V_{eff} \approx 2\lambda^3$. The parameters of the fibers mostly used in this work are summed up in table 3.1.

3.3 Fiber - Cavity coupling

In this section, the fiber-cavity mode coupling is investigated. First, the coupling for single mode fibers is expressed analytically and then the advantages of going beyond single mode fibers is described.



Figure 3.17 – A “pencil” shape fibers observed with a microscope. the rough surface far from the mirror reflects the shooting pattern .The diameter of the fiber is $125\ \mu\text{m}$, the concave depression RoC is $10\ \mu\text{m}$. SEM image of such a fiber is displayed on the front page of this chapter.

Fiber	\mathcal{R}	z_t	D	w_0	$L_{FSR,min}$	V_{eff}	Mode
Unit	μm	μm	μm	μm	μm	λ^3	
A	50	0.5	30	2.5	3.5	20	multi
B	16	1.8	10	1.3	2.5	5	single
C	10	1.5	10	0.9	2.5	2	single

Table 3.1 – Parameters of the three fibers mostly used in this work. They are referred to as fibers A, B or C throughout this document.

3.3.1 Single mode fibers

Using a single mode fiber has an advantage : the output mode of the fiber is well defined and can be used to align spatially the cavity. A description of how the fiber and cavity modes couple, and how this depends on the parameters of the concave depression is given, as well as the effects of misalignment.

Mismatch between fiber and cavity modes

Concerning the coupling between the fiber mode (considered gaussian [154]) and the cavity mode of waist w_0 , one can consider that for a fiber mode of transverse width w_f , the curvature of the wavefront after the mirror is given by [33] : $R_f = \frac{\mathcal{R}}{n_f - 1}$, where \mathcal{R} is the radius of curvature of the mirror and n_f is the optical index of the fiber. From this, one can find the position $z_{0,f}$ of the fiber mode's waist $w_{0,f}$ (details in appendix A.1.2). Assuming that the modes are aligned transversally, the coupling efficiency ϵ is then given by [155] :

$$\epsilon = 4 \left(\left(\frac{w_{0,f}}{w_0} + \frac{w_0}{w_{0,f}} \right)^2 + \left(\frac{\lambda}{\pi} w_0 w_{0,f} z_{0,f} \right)^2 \right)^{-1} \quad (3.30)$$

A schema of the cavity and fiber mode mismatch is given in fig. 3.18 and the efficiency is plotted as a function of the cavity length in fig. 3.19. This coupling efficiency has a maximum plateau, which value depends on the radius of curvature of the mirror. When the cavity length decreases below a few micrometers, or when it is within a few micrometers of its stability bound, the coupling collapses.

Structure centering and angle between the mirrors

Let's first consider that the fiber axis is transversally shifted with respect to the cavity mode axis of a distance d (this can happen if the laser ablation is not perfectly centered), as shown in figure 3.20. The coupling is then given by [155] :

$$\epsilon_d = \epsilon e^{-(d/d_e)^2} \quad \text{with} \quad d_e^2 = \frac{2}{\epsilon \left(\frac{1}{w_f^2} + \frac{1}{w_0^2} \right)} \quad (3.31)$$

Typically, d_e is of the order of $3 \mu\text{m}$ with the cavities of interest, as shown in figure 3.21. If one considers that d is lower than $1 \mu\text{m}$ (typical accuracy of the shooting setup), this centering defect may decrease the coupling efficiency by up to 25%.

In addition to a centering inadequacy one has to consider that the two mirrors forming the cavity are not perfectly perpendicular to each other, as depicted in figure 3.22. If the angle between them is θ the coupling changes as follows [155] :

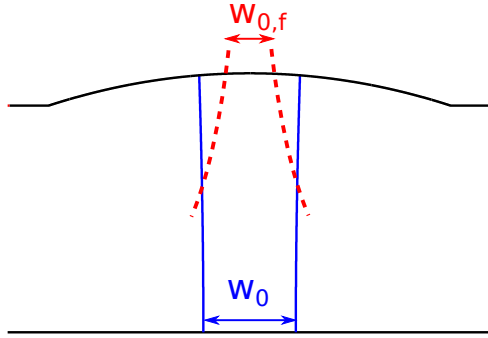


Figure 3.18 – Schematic view of the fiber-cavity mode mismatch : the cavity mode has a waist w_0 located on the planar mirror while the fiber mode has a waist $w_{0,f}$ located on the concave mirror.

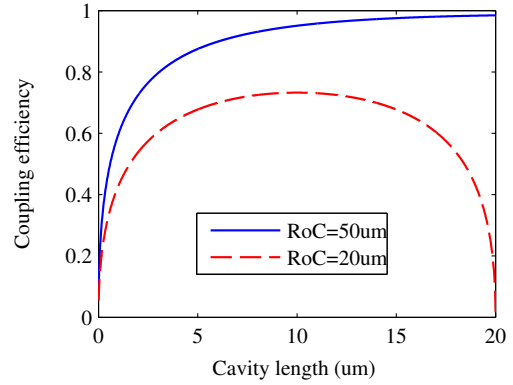


Figure 3.19 – Coupling efficiency between the fiber mode and the cavity mode, for $n_f = 1.54$, $w_f = 3 \mu\text{m}$ and radii of curvature $\text{RoC} = 50 \mu\text{m}$ in solid blue and $\text{RoC} = 20 \mu\text{m}$ in dashed red.

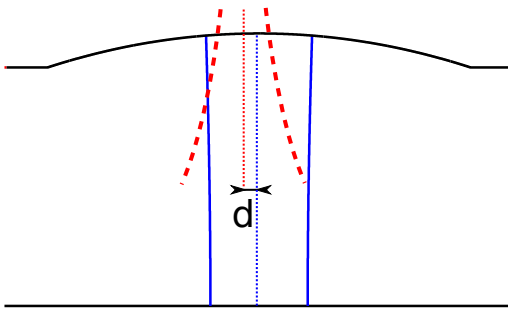


Figure 3.20 – Schematic view of the fiber-cavity mode centering mismatch : if the laser ablation is not properly centered the two modes are transversally shifted of a distance d .

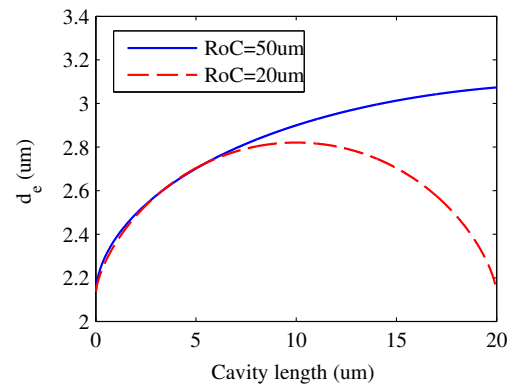


Figure 3.21 – Critical size for the distance between cavity axis and fiber axis. Fiber mode $w_f = 3 \mu\text{m}$ and radii of curvature $\text{RoC} = 50 \mu\text{m}$ in solid blue and $\text{RoC} = 20 \mu\text{m}$ in dashed red.

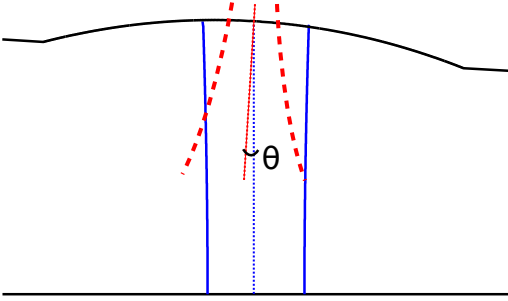


Figure 3.22 – Schematic view of the fiber-cavity mode angular mismatch : if the two mirrors are not parallels, the mismatch depends on the angle θ between their axes.

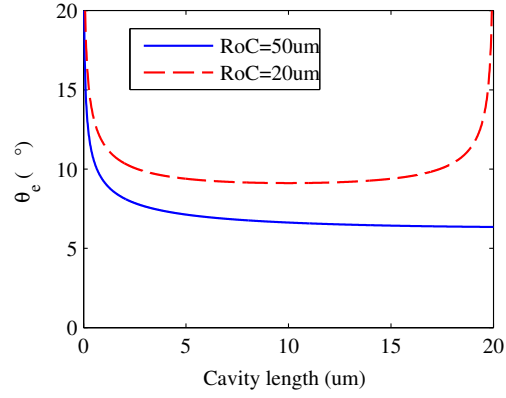


Figure 3.23 – Critical angle between planar and concave mirrors. Fiber mode $w_f = 3 \mu\text{m}$ and radii of curvature $\text{RoC} = 50 \mu\text{m}$ in solid blue and $\text{RoC} = 20 \mu\text{m}$ in dashed red.

$$\epsilon_\theta = \epsilon_d e^{-(\theta/\theta_e)^2} \quad \text{with} \quad \theta_e^2 = \frac{2}{\pi^2 \epsilon \left(\left(\frac{w_f}{\lambda} \right)^2 + \left(\frac{w_0}{\lambda} \right)^2 \right)} \quad (3.32)$$

Concerning the angular mismatch, the loss of coupling is less important for short cavities and for small radii of curvatures. With the cavities considered θ_e is always greater than 5° as shown in figure 3.23, increasing to about 15° for the smallest cavities. As the angle θ can be considered lower than 1° (cleave angle of the fibers), this factor can be considered small or negligible.

3.3.2 Beyond single mode fibers

It was explained that the coupling between a single mode fiber and the cavity mode can drop below 50% if the parameters of the cavity are not optimized or if the cavity is misaligned. This drawback can be overcome by using a multimode fiber or by using the planar end of the cavity as the output.

Multimode Fibers

The first generation of cavities considered in this work was made at the tip of multimode (MM) fibers (fiber A in table 3.1), having a core of $50 \mu\text{m}$. With such fibers the output spectrum of the cavity was a random superposition of a great number of modes [156]. Typically, the transverse electromagnetic modes in the cavity were observed up to $l + m \sim 15$, with decaying amplitude, as was shown in figure 3.2.

This could appear as a disadvantage because the output of the fiber is large and

is a mix of several modes, but it brings two benefits : first the concave depression centering is of lesser importance with such a large core : an inaccuracy of about $1\ \mu\text{m}$ is insignificant. Second, what limits the output coupling of the cavity to the fiber is the numerical aperture of the later, given by $NA = \sin \theta_{acc} = 0.22$, where θ_{acc} is the acceptance angle of the fiber. The coupling between the output mode of the cavity and all the modes supported by the fiber remains close to unity as long as the divergence of the cavity mode $\theta_0 = \frac{\lambda}{\pi w_0}$ remains smaller than θ_{acc} . This leads to the following condition :

$$w_0 \geq \frac{\lambda}{\pi \theta_{acc}} \gtrsim 1.9\ \mu\text{m} \quad (3.33)$$

Fiber A reasonably fits this condition, but fibers B and C have lower waists.

Using the planar output of the cavity

Nevertheless, there is an other way to overcome the coupling issue between the fiber mode and the cavity mode : using the planar mirror as the output of the cavity. Indeed, the output on that side of the cavity is a cone, with a half angle θ_{out} given by the divergence of the associated gaussian beam :

$$\theta_{out} = \frac{\lambda}{\pi w_0} \quad (3.34)$$

where λ is the wavelength of the cavity mode and w_0 is the mode's waist (located on the planar mirror). For the cavities used, this angle is in the range $7^\circ < \theta_{out} < 16^\circ$ (see section 5.2.1 for a measurement). It is then easy to collimate the output of the cavity with a lens, placed a few millimeters away from the planar mirror (in this experiment, a lens with effective focal length 18.5 mm, with a numerical aperture $NA = 0.5$ is used).

This method applies indifferently whether the fiber is single or multimode. Moreover, in order to increase the extraction through the planar side, it is possible to choose two mirrors with different reflectivities so that the cavity mode preferentially leaks out from the chosen side. Typically with a reflectivity of 99.97% on the planar side and 99.99% on the fiber side, about 90% of the intensity goes out through the planar mirror. Though further applications need the fibered output, all the experiments in this work are done using the planar output of the cavity for the sake of simplicity.

3.4 Finesse and storage time

The cavities were described in term of volume and the coupling between cavity mode and fiber mode was expressed. In the following, the finesse of these cavities is defined and its measurement is explained.

The finesse of an empty cavity is intrinsic to its mirrors and depends weakly on its length. It is given by :

$$\mathcal{F} = \frac{\pi}{\mathcal{T}_1 + \mathcal{T}_2 + \mathcal{L}}. \quad (3.35)$$

where \mathcal{T}_1 and \mathcal{T}_2 are the transmissions of the two mirrors, and \mathcal{L} accounts for all the losses. The transmissions \mathcal{T} can be tuned by changing the number of layers of the corresponding Bragg mirror. It depends on the wavelength, but typically goes down to 300 ppm¹⁰, at its minimum for the mirrors used in this work. Such a transmission gives a finesse of about 10 000, if the losses are zero.

3.4.1 Losses

In order to have a good extraction of the cavity mode, it is crucial to keep the losses \mathcal{L} significantly lower than the transmission. A description of the different mechanisms involving losses is thus given.

Absorption losses

An electromagnetic field that is reflected at an interface partly enters the material (it can be transmitted or there can simply be an evanescent wave). In any case, this field penetration leads to a partial absorption by the medium. In usual metallic mirrors this absorption is around 1%, several orders of magnitude too high for the requirements of the experiments considered in this work.

The firm which produces the mirrors specifies absorption losses of a few ppm for pristine Bragg mirrors. In the planar-concave cavities, the absorption losses are more important on the planar mirror, which has an extra polystyrene layer. However no finesse drop was observed after such a deposition. Thus, one can consider that the losses introduced are at least an order of magnitude lower than the transmission ($\mathcal{L}_A \sim 20$ ppm). For a higher finesse cavity, an improvement of the polystyrene deposition and a better control of the induced losses may be necessary.

Scattering losses

In addition to the absorption losses, the surface roughness of the mirrors leads to scattering losses, expressed by [157, 158] :

$$\mathcal{L}_S \simeq \left(\frac{4\pi\sigma}{\lambda} \right)^2 \quad (3.36)$$

where σ is the quadratic mean roughness given by :

¹⁰ppm reads part per million and is a common unit for high reflectivity mirrors.

$$\sigma = \sqrt{\frac{1}{L_x L_y} \int_0^{L_x} \int_0^{L_y} (z(x, y) - \bar{z}(x, y))^2 dx dy} \quad (3.37)$$

where L_x and L_y are the lateral dimensions of the surface, z is the surface height and \bar{z} is its mean. As the mirrors deposition is well controlled it does not increase the surface roughness, which remains the one of the substrate. In the case of the fiber, it was estimated to $\sigma = 0.2$ nm, so the scattering losses amount to $\mathcal{L}_S \sim 10$ ppm.

Clipping losses

Until now, it was considered that mirrors reflect the entire cavity mode into the cavity. This is a valid approximation as long as the mirror diameter is much larger than the mode diameter. In this work, this condition is not always fulfilled, in particular for fibers B and C. Thus, one has to consider the finite size of the mirror, which leads to “spillover” losses upon reflection on the edges of the cavity. For a single reflection at the fiber, the losses read [33] :

$$\mathcal{L}_{C,1} = \exp\left(-2\left(\frac{D}{2w(L)}\right)^2\right) \quad (3.38)$$

where D is the diameter of the concave mirror and $w(L)$ is the waist of the cavity mode upon impact (as defined in eq. (3.7)). As the planar mirror has a diameter two orders of magnitudes larger than D , it is considered that there are no losses upon that reflection, so that the losses are given by the number of round trips (i.e. the finesse) times the losses on the fibered mirror :

$$\mathcal{L}_C = \mathcal{F} \cdot \mathcal{L}_{C,1} \quad (3.39)$$

As a conclusion, one can consider that the cavities have a transmission of 300 ppm, absorption and scattering losses of 30 ppm, and clipping losses as defined by eq. (3.38). In the case of mirror with $D = 10$ μm and $\mathcal{R} = 10$ μm , the clipping loss remain below 100 ppm for a cavity length below 5 μm . In the case of a larger mirror, with $D = 20$ μm , the losses remain completely negligible in the range of lengths used in this study. The corresponding finesse as a function of the cavity length is given in figure 3.24. One must note that Benediketer et al. [151] explored more thoroughly the dependence of the finesse on the cavity length for fibered Fabry-Perot cavities. It comes out that the finesse can collapse much more quickly than expected - typically by a factor of two before the length reaches half the radius of curvature - due to the non-ideal shape of the mirrors, in particular ellipticity.

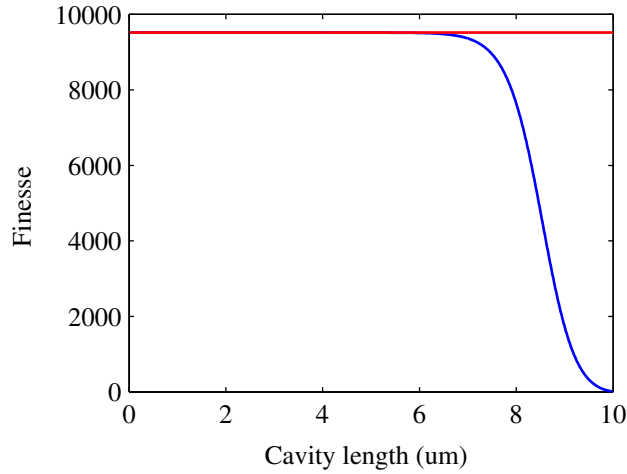


Figure 3.24 – Finesse as a function of cavity length. In blue $\mathcal{R} = 10 \mu\text{m}$ and $D = 10 \mu\text{m}$, while in red $D = 20 \mu\text{m}$ and $\mathcal{R} = 50 \mu\text{m}$. The remaining parameters are $\lambda = 900 \text{ nm}$, and other losses of 330 ppm for each mirror.

3.4.2 Measuring the finesse

The theoretical background underlying the concept of finesse was given in section 3.4.1. In this section, the experimental measurement is presented and the effect of longitudinal vibrations is discussed.

Varying the cavity Length

The finesse of a Fabry-Perot is defined by :

$$\mathcal{F} = \frac{FSR_\lambda}{\delta\lambda} \quad (3.40)$$

where $\delta\lambda$ is the spectral width of a longitudinal mode. Theoretically, the finesse could be extracted directly from figure 3.2. Unfortunately, the cavity is easily affected by vibrations, and these vibrations increase the effective spectral width of the cavity peaks measured with a spectrometer (details follow in paragraph 3.4.2). For this reason, it is useful to monitor on a photodiode the output of the cavity at a fixed wavelength while varying its length.

The length variation must be quicker than the typical timescale of the vibrations (of the order of 1 kHz). For that, the fiber is moved with piezoelectrics slip-stick at room temperature. A single step, of sufficient amplitude to cover at least two longitudinal modes, is operated in a few milliseconds. The result is presented in figure 3.25.

From this figure one can immediately deduce the finesse as the ratio of the distance between two longitudinal peaks by the width of a peak. As long as a linear

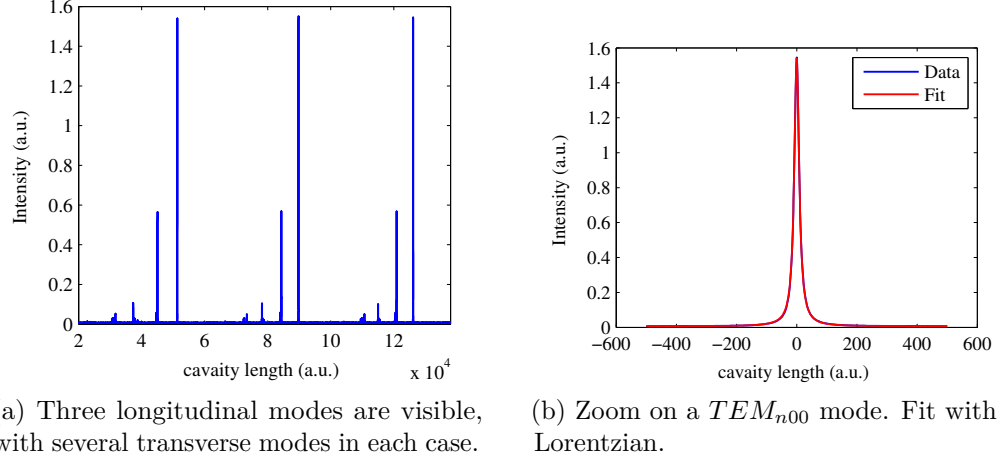


Figure 3.25 – The wavelength is fixed and the cavity length is swept fast while its output is recorded with a photodiode. The ratio of the distance between two longitudinal peaks and the width of a peak gives the finesse of the cavity.

displacement is assumed¹¹, it requires no scale in abscissa.

Though this method is convenient, it cannot be used at cryogenic temperature because the displacement range of our piezoelectric translation stages is not enough to cover two modes quickly. A way to overcome this issue is to measure the finesse as a function of the wavelength once and for all at room temperature, and to use these values afterwards. Unfortunately the finesse is not homogeneous over the whole planar mirror because of the nanotubes and polystyrene deposition on its surface. Given that, an other method to measure the finesse locally at cryogenic temperature was developed.

Cavity ring down spectroscopy - photon storage time

A light entering in the cavity is either transmitted or lost. In the low loss limit, if some light is stored inside the cavity, its intensity decreases exponentially with a characteristic time τ_{stor} :

$$\tau_{stor} = \frac{2L}{c(\mathcal{L} + \mathcal{T})} = \frac{L\mathcal{F}}{\pi c} \quad (3.41)$$

where L is the effective cavity length and c the velocity of light. This characteristic time is sometimes called the lifetime of the cavity, or the photon *storage time* in the cavity. The later term is used in this work in order to avoid any confusion with the solid state emitters lifetime.

In order to measure the storage time, one can perform cavity ring-down spectroscopy [159]. It consists in sending an input light resonant with one of the modes of

¹¹the symmetry of the transmission peaks is a good indication of the validity of this approximation.

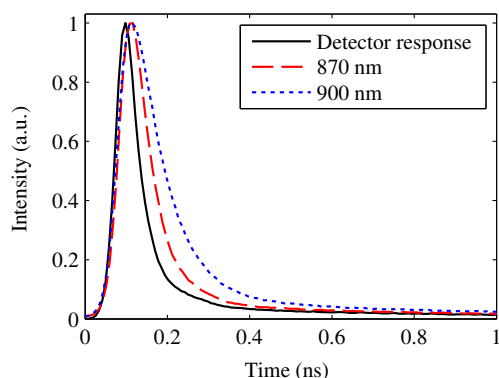


Figure 3.26 – Cavity ring-down spectroscopy. Black solid line : detector response. Red dashed line : cavity transient at 870 nm. Blue dotted line : cavity transient at 900 nm.

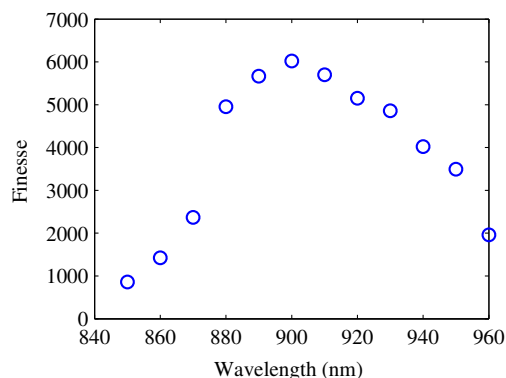


Figure 3.27 – Finesse of the cavity as a function of the wavelengths, measured by ringdown spectroscopy (see eq. (3.41)).

the cavity and recording the transmission with an avalanche photodiode. When the incident light is shut down, one observes a mono-exponential decay of the intensity of the output. In order to repeat the process many times conveniently a pulsed excitation (described in 4.1.2) is used.

The typical storage time of the cavities investigated is between 15 ps and 80 ps, unfortunately our fastest detectors¹² have a characteristic time of about 40 ps, so the recorded signal had to be deconvolved by the measured response time of the instrument in order to retrieve the storage time. Finally, the finesse was obtained with equation (3.41) : $\mathcal{F} = \frac{\pi\tau_{stor}c}{L}$ (the cavity effective length was obtained from FSR measurements).

Interestingly, the finesse (or the storage time) can also be interpreted as a measure of the mean number of round trips N before a photon goes out of the cavity :

$$N = \frac{\mathcal{F}}{2\pi} = \frac{c\tau}{2L} \quad (3.42)$$

An other figure of merit of the cavities, directly linked to the finesse, is the quality factor Q . It has already been introduced in section 1.3.1 and quantifies the ratio between the resonant frequency ω_n over the spectral width of the cavity κ :

$$Q = \frac{\omega_n}{\kappa} = \omega_n\tau = \frac{2L}{\lambda_n}\mathcal{F} \quad (3.43)$$

Contrarily to the finesse, the quality factor does not depend only on the reflectivity of the mirrors, but also on the cavity length. One can keep in mind that our cavities

¹²IDQ 100

have a typical quality factor $Q \sim 10^5$.

Vibrations and “effective finesse”

For fibered cavities, the planar mirror is fixed and the fibered mirror position can be controlled with a nanometric precision. Nevertheless, the fiber position can vibrate slightly, especially if it is used at low temperature (due the cryostat vibrations).

These vibrations can be decomposed into axial and lateral vibrations. The waist of the cavity mode has a value above $1 \mu\text{m}$, while the spectral matching of the cavity with the emitter requires a nanometric precision. For this reason, the effect the lateral vibrations are considered as second order compared to the axial ones, and are neglected in this study. From equations 3.1 and 3.2, one can link a small variation of the cavity length δL to a small variation of its resonant frequency $\delta \lambda$:

$$\delta L = \frac{\lambda \delta \lambda}{2FSR_\lambda} \quad (3.44)$$

where the Free Spectral Range is in units of wavelength. To give a rough idea, it means that for a typical cavity, at a wavelength $\lambda = 900 \text{ nm}$ with a $FSR_\lambda = 100 \text{ nm}$ and a spectral width of $\delta \lambda = 30 \text{ pm}$, a change $\delta L = 130 \text{ pm}$ corresponds to a spectral shift greater than the spectral width.

A continuous laser light, at a given wavelength λ_0 , is sent in the cavity and the transmitted intensity I is recorded on a photodiode. The cavity length is swept to cover at least two transmission modes in a slow, reproducible way, so that the width Γ of a TEM_{n00} peak and the distance between two peaks in arbitrary units ΔX can be extracted. This distance is proportional to the FSR, so that a constant of proportionality α can be introduced : $\alpha \Delta X = FSR_\lambda = \lambda_0/2$.

Once this calibration is done, the cavity length is tuned so that the resonant frequency is at mid-slope of one of the broader peaks (close to the edge of the stop band). At this point, the local slope is $1/\Gamma$, assuming that the peak is Lorentzian. So :

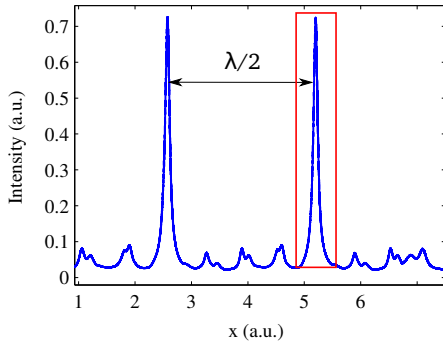
$$\frac{dI}{dx} = \alpha \frac{dI}{dL} = \frac{1}{\Gamma} \quad (3.45)$$

Using the definition of α :

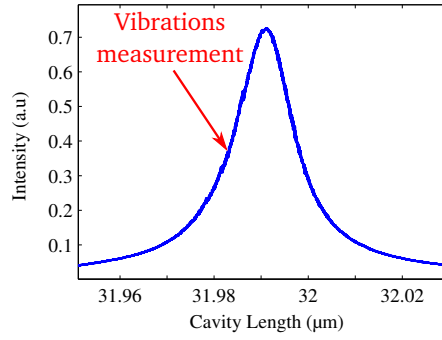
$$dL = \frac{\lambda_0 \Gamma}{2\Delta X} dI \quad (3.46)$$

The cavity is let free and the intensity variations over time at this point are recorded with a fast photodiode. These are converted in term of length with eq. (3.46) and finally δL , which is twice the standard deviation of this quantity : $\delta L = 2\text{std}(dL)$ is retrieved. The typical longitudinal vibrations amount to 5 nm . At best, vibrations as low as 1 nm are obtained (at room temperature), as shown in fig. 3.28.

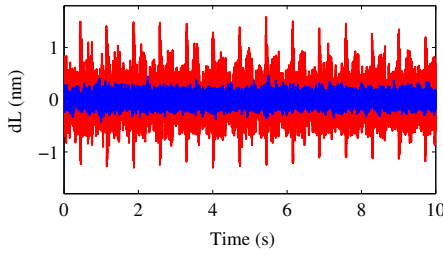
Most of the vibrations take place on a time scale (milliseconds) much shorter than the usual timescale of our measurements (seconds). This means that the cavity



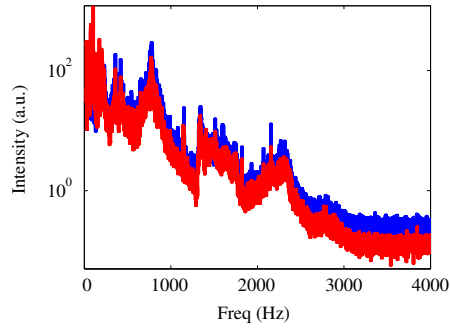
(a) The input wavelength λ_0 is fixed and the transmission is monitored on a photodiode while the cavity is swept over a spectral range sufficient to measure an FSR. Two TEM_{n00} peaks are visible, separated by $\lambda_0/2$.



(b) Zoom on the red square in figure (a). The length is chosen so that the transmission is at mid-slope of the Lorentzian peak. The abscissa is calibrated with figure (a).



(c) Longitudinal vibrations versus time, extracted from the intensity variations on the photodiode, from eq. (3.46). In blue the cryostat is off, in red it is on and the regular peaks correspond to its cycles.



(d) Vibration spectrum obtained by a Fourier transform of figure (c). In blue the cryostat is off, in red it is on.

Figure 3.28 – Estimation of the longitudinal vibrations of the cavity.

peaks recorded with a CCD do not reflect the real cavity spectral width, but the cavity spectral width modulated by the vibrations. To give an example, for a cavity of finesse 6000, with a length of 5 μm , the spectral width of the cavity peak is about 20 pm, or 8 GHz, but the width of the peak measured by white field transmission is 200 pm, or 80 GHz, due to the vibrations.

It is crucial to understand that for the solid state emitters under study this is NOT an “effective finesse”. Indeed, the typical lifetime of nanotubes is 100 ps, and the cavity storage time is in the same order of magnitude. At these time scales, the cavity length can be considered as constant, as well as the mode’s energy and spectral width. As a consequence, the vibrations do not directly affect the Purcell effect and the intrinsic spectral width of the cavity is the relevant parameter. For a more complete discussion of the effect of the vibrations on the experimental measurement of the Purcell effect, refer to appendix C.

Conclusion

The cavities introduced in this work consist in a planar dielectric mirror and a concave one laser machined at the tip of an optical fiber. The resonant Hermite-Gaussian modes were described and measured from white-field transmission. A description of how the characteristics of the dip created on the fiber by laser ablation can be tuned were given, as well as their incidence on the cavity mode volume. After discussing how the field in the cavity could be extracted, either on the fiber side or on the planar mirror side, the finesse was described, as well as the quality factor and storage time of these cavities.

A few numbers should be kept in mind for what follows : in the first generation of fibers used during this PhD (fiber A), the radius of curvature was $\mathcal{R} = 50 \mu\text{m}$, the length was limited to $L_{min} \approx 3.5 \mu\text{m}$, leading to a cavity mode volume $V_{eff} \approx 20\lambda^3$. The finesse was about 6000 at 900 nm, leading to typical lifetimes of about 50 ps and quality factors of about 10^5 .

The second generation of fibers (fiber B and C) have a lower radius of curvature, $\mathcal{R} = 10 \mu\text{m}$ and are blunt to reach lower length $L_{min} \approx 1.5 \mu\text{m}$, leading to mode volumes as low as $V_{eff} \approx 2\lambda^3$, while the finesse and quality factor remain similar.

It is now clear that these micro-cavities combine the advantages of having an extremely high finesse¹³, very small mode volume and efficient extraction. In the chapter 5 a description is given of how the flexibility obtained from the ability to move the fiber is used to make the cavity tunable spatially and spectrally.

¹³Here it is willingly limited to 10 000 to match the spectral width of the emitter, but it can reach 150 000 [149]

4

SCANNING CONFOCAL MICROSCOPY OF CARBON NANOTUBES



Contents

4.1	A scanning Confocal Microscope	103
4.1.1	Principle	103
	Collection	104
	Steering mirror	105
4.1.2	Excitation	106
	Continuous Wave Source	106
	Pulsed Wave Source	108
	Excitation side	108
4.2	Low temperature single nanotube photoluminescence .	110
4.2.1	Single carbon nanotube photoluminescence	110
	Shape of the PL spectrum	110
	Spatial localization	111
	Polarization and anisotropy	113
	Saturation of the emission	114
	Exciton trapping	114
4.2.2	Coupling to acoustic phonons	116
	Hamiltonian of the system	116
	Confinement of the acoustic phonons	118
4.3	Spectral diffusion in Carbon Nanotubes	122
4.3.1	Spectral diffusion of the ZPL	122
4.3.2	Spectral diffusion of the Phonon Wings	123

Introduction

The exciton relaxation mechanisms can be understood by the study the photoluminescence spectrum of single carbon nanotubes. Nevertheless, as nanotubes are entirely made of atoms at their surface, they are extremely sensitive to their environment. This interaction creates a great number of non-radiative decay processes, and hence a decrease in the intensity of the photoluminescence (PL). Actually, more than ten years passed between the synthesis of CNT in 1991 and the first observation of their PL, made available by physical isolation in micelles [16]. Even today, nanotubes are low quantum yield emitters and their study needs a high sensitivity confocal setup. Furthermore, the thermal broadening of the transitions blurs out the intrinsic characteristics, which is why the experiments in this section are carried out at cryogenic temperatures.

This chapter describes the home-made confocal microscope used in this work and present a few general characteristics of carbon nanotubes photoluminescence. Namely the anisotropy, the saturation of the emission and the spatial localization. Beyond that, a particular interest is taken in the shape of the nanotubes optical spectrum. Even though this shape depends strongly on the emitters environment, a complete model unifying the optical spectrum of CNT at low temperature was developed in the group a few years back [20]. This model is presented shortly, and the focus remains on the narrow-width emitters which are relevant for cavity experiments. Finally, this chapter is concluded by studies on the time evolution of these optical spectra. In particular, it is shown how the experiments on spectral diffusion support the above mentioned model.

4.1 A scanning Confocal Microscope

The work presented here aims at studying the optical response of a single carbon nanotube, which means an object with a diameter below 1 nm and in this case a length of about 500 nm. For that, a laser beam focused to the diffraction limit is used as the excitation source, and the photoluminescence of the object under study is collected with a high numerical aperture lens. The setup built is a home-made confocal microscope, which principle is introduced in this section. A description of how the sample is raster scanned is also given. Finally the different excitation sources are described.

4.1.1 Principle

The principle of confocal microscopy is that the excitation and the detection pass through the same focal lens. Indeed, an excitation laser beam is focused close to its diffraction limit ($\lambda/2$) on the sample, using an aspherical lens of numerical aperture 0.68, focal length 3.1 mm, and working distance 1.76 mm¹. If a carbon nanotube is at the focal point, its photoluminescence is collected by the same aspherical lens and then separated from the excitation beam with a dichroic mirror² (see figure 4.1). As the excitation wavelength is typically 760 nm, while the emission is typically 900 nm, the dichroic mirror is chosen to transmit fully wavelengths below 850 nm and reflect totally the wavelengths above it.

As an aspherical lens is used, the focal length is not exactly the same for the excitation than for the emission. One can choose to find a compromise between the excitation spot diameter and the collection collimation. Otherwise, it is possible to tune the lens position to the emission focal length and make the excitation beam slightly divergent to compensate.

¹Thorlabs C330TME-B or C330TMD-B

²Edmund Optics 69-209

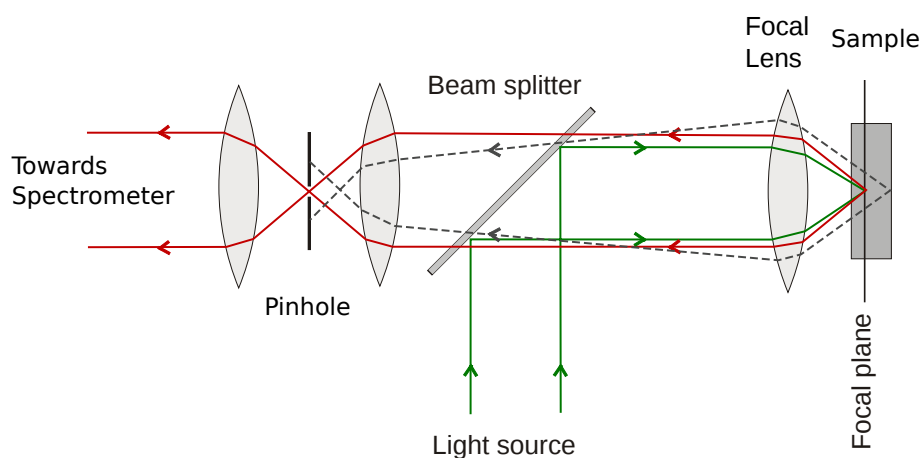


Figure 4.1 – Principle of confocal microscopy : the excitation (solid green line) and the collection (solid red line) pass through the same focal lens. They are separated with a dichroic beam splitter. The collection is then filtered with a pinhole in order to eliminate out-of-plane emission (dashed gray line).

Collection

The emission is dispersed with a 500 mm spectrometer³ and recorded with a silicon charged coupled device⁴. However, before the emission beam reaches the spectrometer with which the emission spectrum is analyzed, it passes through a pinhole. Two lenses⁵ with a focal length of 100 mm are placed in a telescope configuration. The plane in between is the conjugate image of the sample plane. A hole of 100 μm is placed in this plan to filter the volume observed. To be accurate, it limits the lateral zone of the sample observed to 1 μm and it reduces the depth of field as well. This is particularly useful to increase the signal-to-noise ratio by eliminating the photoluminescence (or elastic diffusion) of the substrate. This configuration is widely used in physics as well as in biology for the spectroscopy of molecules or nano-objects [160]. In the setup described here, the signal-to-noise ratio is seldom an issue, so the pinhole part of the confocal setup is built on a removable platform. Most of the time, it is removed and the slits of the spectrometer are used for filtration. The emission beam is focused with a 40 mm achromatic lens on the slits (which width can be tuned down to 10 μm). By using this configuration, single nanotubes belonging to the following species (8, 3), (7, 5), (6, 5), (6, 4), (5, 4), (9, 1) are efficiently detected.

Finally, it is worth noting that all the experiments carried out during this work are done at cryogenic temperature. Consequently, the sample as well as the confocal lens are embedded into a pulsed tube cryostat. The detailed organization inside the cryostat is given in paragraph 5.1.1.

³Princeton Instruments SP2500i, with three gratings (150, 600 and 1200 lines per millimeter)

⁴Princeton Instruments Pylon

⁵Thorlabs AC254-100-B

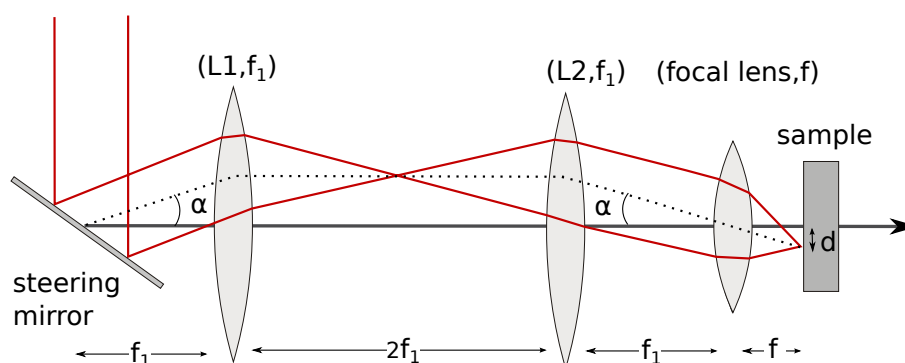


Figure 4.2 – Principle of the steering mirror : the beam has a deviation α from the optical axis. The two lenses $L1$ and $L2$, center it on the focal lens. it is then focused on a distance $d = \alpha f$ from the image focal point of this last lens.

Steering mirror

The density of carbon nanotubes was already discussed in 2.3.3 : it is a compromise between having a sufficient number of nanotubes and having a low probability of getting two of them in the excitation spot. Though it is rather simple to find a nanotube manually, it is interesting to be able to raster scan quickly the sample in order to compare the different emitters, and to select the ones having the best features for cavity experiments.

One ways of scanning the sample is to move the focusing lens. But in our case this lens is inside the cryostat, and held on piezoelectrics slip-stick which movements are not perfectly reproducible on large scales (over $1\ \mu\text{m}$). Thus, a steering mirror⁶ is used to implement the raster scan, as shown in figure 4.2.

Indeed, if a collimated beam arrives on the focal lens (of focal length f) with an angle α , the beam spot is simply shifted by $d = \alpha f$ (as long as it remains in the Gauss conditions at least). The angle of the steering mirror can be tuned precisely and repeatedly by the application of a voltage, with a conversion factor of $26\ \text{mrad}/\text{V}$ ⁷ and a maximum of $10\ \text{V}$, which means a distance of about $100\ \mu\text{m}$.

Technically, applying an angle to the steering mirror quickly leads the beam to fall out of the focal lens (which clear aperture is only $5\ \text{mm}$), so two 2 inches lenses⁸ of focal length $f_1 = 200\ \text{mm}$ are used to redirect the beam. The first lens is at a distance f_1 from the steering mirror, the second one is at a distance $2f_1$ from the first and a distance f_1 separates it from the focal length. As depicted in figure 4.2, this setup has the advantage that whatever the angle α of the steering mirror, the beam arrives centered on the focal lens with the same angle α .

The collection beam passes through the same setup and the dichroïc beam splitter is placed just after the steering mirror. This way the emission beam path does

⁶Newport FSM-300

⁷The repeatability is $3\ \mu\text{rad}$

⁸Thorlabs AC508-200-B

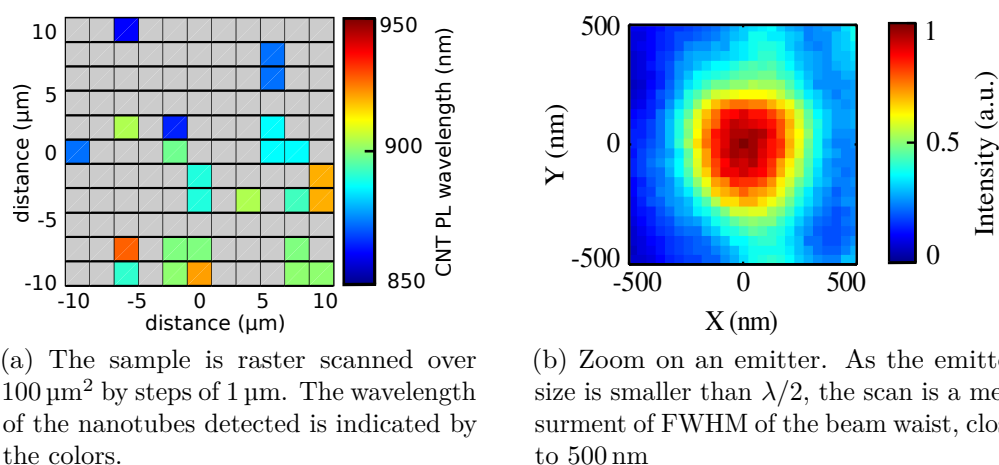


Figure 4.3 – Photoluminescence maps of a typical sample

not depend on the angle α after being reflected by the dichroic beam splitter, in particular for the pinhole part or the coupling into the spectrometer.

With this steering mirror, photoluminescence maps of the sample can be done, with a typical size of $25 \mu\text{m} \times 25 \mu\text{m}$ in order to find and compare carbon nanotubes. A more tightened map can also be done to assess that the emitter is localized. Two such maps are showed in figure 4.3.

4.1.2 Excitation

In the experiments carried out here, two sources are used : a tunable continuous wave Ti:Sa, and a pulsed Ti:Sa working at 800 nm . Let's note that the sources were always filtered⁹ to make sure that no spurious light would hinder the PL measurements. In this section, these sources are described, as well as the setup used to get a tunable pulsed beam. Some details about the optical path are also given.

Continuous Wave Source

In this experiment, the main source is a continuous mode Titanium-Sapphire laser¹⁰ tunable between 700 nm and $1 \mu\text{m}$, with a line-width of 50 kHz . This laser, is driven from a computer and can scan this range of wavelengths without any manual operation. The only limitation, with the version used, is that a continuous scan over more than 0.5 nm without mode hopping is not available.

Indeed, one of the features of a laser is an optical gain medium, which range is very broad. Within this range, many longitudinal modes of the laser cavity are available. In order to get narrower features, a Birefringent Filter (BRF) is added to

⁹Typically with short-pass filters such as FES 800 or FES 850 from Thorlabs

¹⁰M Squared, SolsTiS

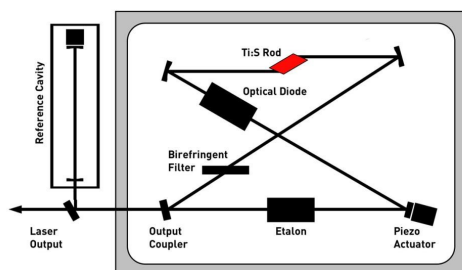


Figure 4.4 – Schema of our commercial continuous wave laser. The gain medium is Titanium:Sapphire. The cavity modes are filtered by a birefringent filter (BRF) and a Fabry-Perot called Etalon.

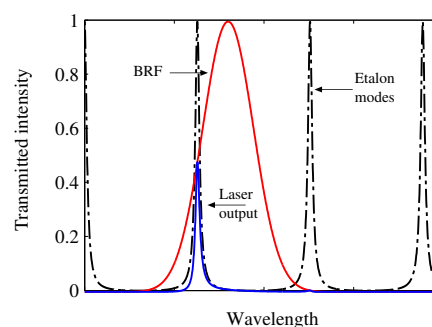


Figure 4.5 – Principle of the wavelength tuning : a wavelength range is selected by the birefringent filter in red. A finer selection comes from the etalon filter in dashed black. The output arises from the convolution of the two, in blue, with the laser cavity modes. Tuning the etalon spacing changes the output wavelength, but once the full BRF line-width is traveled, one has to make the BRF jump farther away to continue tuning the output wavelength.

introduce a wavelength-dependent loss into the cavity (see laser schema on figure 4.4). Wavelength tuning is then accomplished by rotating the BRF. As the BRF tuning is coarse, a Fabry-Perot filter called *etalon* is added. The spectral filtering features are depicted on figure 4.5. The spacing of the etalon can be electronically adjusted to tune the wavelength finely. Finally, the output wavelength of the laser can be locked on the external cavity by tuning the laser cavity length with a piezo actuator.

It is possible to tune the etalon without moving the BRF, but it limits the scan to the line-width of the BRF. For experiments where the precision required on the wavelength is within the accuracy of the spectrometer, this limitation can be easily overcome. One can move in a coordinated way the BRF and the etalon so that after each jump of the BRF, the wavelength comes back to its value before the jump. The laser wavelength is monitored with the spectrometer all along the experiment and the results are computationally “stitched” together. This easy wavelength tunability enables us to perform detailed Photoluminescence Excitation (Photoluminescence spectrum as a function of the excitation wavelength) of single carbon nanotubes to identify the wavelengths at which they preferentially absorb light.

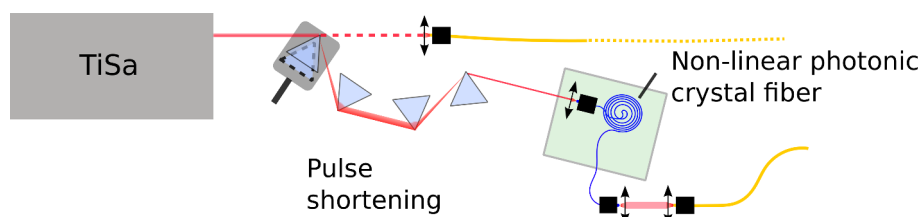


Figure 4.6 – The pulsed Ti:Sa source can be directly coupled to a fiber. Otherwise, the beam is intercepted by a prism. It passes through four prisms to shorten the impulsions and then through a non-linear photonic crystal fiber to generate wavelengths from the visible to the near infrared. Courtesy of C. Raynaud.

Pulsed Wave Source

In addition to this continuous-wave laser, a pulsed Titanium:Sapphire laser¹¹ operating at 800 nm is used. The pulses last 100 fs and the repetition rate is 80 MHz. Pulsed excitation is particularly useful for experiments in the time domain detailed in section 5.2.2.

As some measurements (see sections 3.4.2 and 5.2.3) require pulsed excitation at different wavelengths, a setup was built¹² to generate ultrashort tunable pulses with this fixed wavelength Titanium-Sapphire laser, as depicted in figure 4.6. Its pulses are sent through four prisms so that the shorter wavelengths travel along a longer path, as shown in figure 4.7. This negative dispersion index medium ($\frac{\partial n}{\partial \lambda} < 0$) compresses the impulsions, which are then sent through a non-linear photonic crystal fiber. Thanks to a non-negligible third order susceptibility, it is possible to generate any wavelength between the blue and the infrared (an example is given in figure 4.8) with the ultrashort input impulsions, while keeping pulses in the 100 fs range.

Excitation side

Until now, a standard confocal microscope was considered, with the addition of a steering mirror to raster-scan the sample. This setup aims at a comparison of the photoluminescence in free-space (i.e. in confocal microscopy) with the photoluminescence in cavity (see section 5.2.1). In a confocal microscope, the excitation and the collection pass through the very same lens. In such a case the excitation in free-space and in cavity cannot be the same (the cavity would block it), which is why a second way of exciting the sample in free-space is available.

Once the sample is raster scanned, a nano-object selected and placed at the focal point of the lens, the excitation beam is switched, as shown in figure 4.9. The laser is then focused with an other lens¹³ (of focal 12.5 mm and numerical aperture 0.5)

¹¹Coherent Vitesse

¹²This setup was built by Christophe Raynaud as a part of his master project, under the supervision of Yannick Chassagneux.

¹³Edmund Optics 69-863

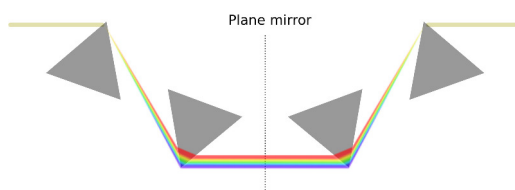


Figure 4.7 – Principle of impulsion shortening with four prisms. Alternatively, two prisms and a plane mirror (dashed line) can be used. Courtesy of C. Raynaud.

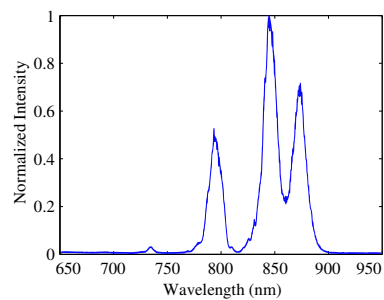


Figure 4.8 – Typical spectrum of the output of the non-linear photonic crystal fiber. The spectrum can be tuned by tuning the injection in the fiber.

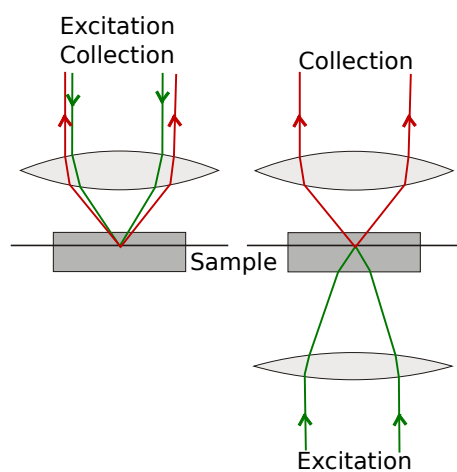


Figure 4.9 – On the left, a standard confocal setup, on the right the excitation is switch to the back.

and passes through the flat mirror on which the carbon nanotubes are deposited. The excitation spot is much larger (about $50\ \mu\text{m}^2$), but the zone collected remains the same.

4.2 Low temperature single nanotube photoluminescence

From the description given in chapter 2, one should expect a single nanotube photoluminescence spectrum to consist in strong lines, corresponding to the different excitonic levels, with an energy depending on the nanotube's chiral indices. In fact, the optical spectrum of a single carbon nanotube is more complicated, first because it depends strongly on its surroundings and second because the transitions can be phonon-assisted. In this section, a brief introduction of the usual photoluminescence spectrum of carbon nanotube is given and a phonon model is introduced to account for it.

4.2.1 Single carbon nanotube photoluminescence

A complete study of the PL characteristics of CNTs was done in the team by Fabien Violla [20] before this work. Compared to the former PL setup, the one described in section 4.1, as well as the samples improvements, gave a twenty times higher signal-to-noise ratio and an increased number of spectrally narrow emitters. Thanks to these improvements, the measures taken during this work confirmed the previous observations. Here, the typical features of nanotubes photoluminescence are reported.

Shape of the PL spectrum

The PL spectrum of a CNT, excited non-resonantly, can vary sensibly from one specimen to the other due to its environment. It generally consists of a main line, with a Lorentzian shape and a Full Width at Half Maximum (FWHM) ranging from $40\ \mu\text{eV}$ in [161] to a few meV. This main line is accompanied on both sides by features of lesser intensity. The ratio between the integrated intensity of the main line and the integrated intensity of the whole spectrum is called Branching Ratio BR . It typically ranges between 0.4 and 0.9 for the nanotubes investigated.

A detailed account of the different shapes of CNT spectra is given in [92, chap. 2]. In this work the focus is on narrow FWHM nanotubes because of their strong interest for cavity coupling (see section 1.3.1). Such a nanotube's photoluminescence spectrum is shown in figure 4.10.

The shape of the emission spectrum can be explained by the interactions between the exciton and the carbon nanotube's phonons, as already noted by Htoon et al in 2005 [162]. The central line is accounted for by the relaxation of the exciton, and by elastic exchanges with phonons. This Lorentzian line has a width related to the

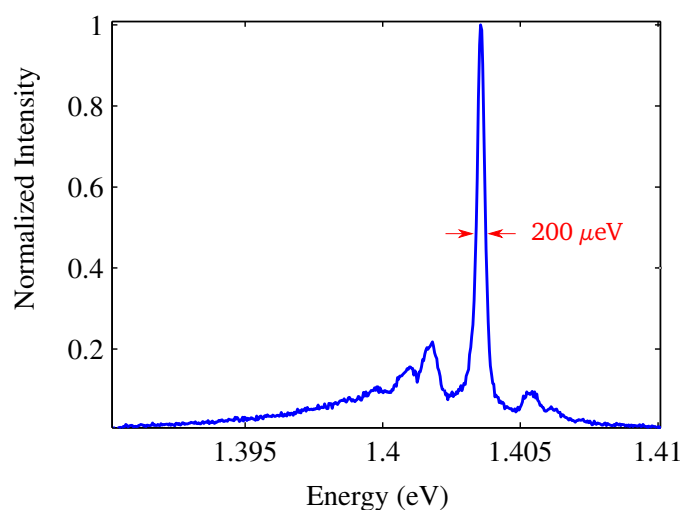


Figure 4.10 – Photoluminescence spectrum of a single carbon nanotube taken at 10 K. One can see a central line with a width of $200 \mu\text{eV}$ and two “wings” on either side, the high energy (or blue) wing being of lesser intensity than the lower energy (or red) wing. Details : (6, 4) nanotube. Excitation : 760 nm, linear polarization (along CNT axis), the excitation power is below the saturation limit, $P = 0.7 \cdot P_{sat}$.

coherence time of the exciton, including pure dephasing. As this line requires no absorption or emission of phonons, it is called the Zero Phonon Line (ZPL), as shown on figure 4.11a.

The red-side part of the spectrum corresponds to the emission of a photon of lower energy assisted by the emission of a phonon, as depicted on figure 4.11b. The phonon emission can occur for an arbitrary low temperature, and in particular, it can occur at the cryogenic temperature used in this experiment. The blue-side part of the spectrum corresponds to the emission of a photon of higher energy assisted by the absorption of a phonon (figure 4.11c). This phenomenon requires the existence of a phonon bath and is thus less likely at cryogenic temperature than at room temperature. Consequently, the asymmetry of the two wings of the spectrum is a direct insight in the local temperature at the location of the nanotube.

Spatial localization

The carbon nanotubes in this study have a diameter below 1 nm and a typical length of 500 nm. This means that with a confocal setup, limited by the Rayleigh criterion, the CNT photoluminescence must appear as a point-source.

In order to assess this characteristic, the integrated intensity of the PL was measured at different positions separated by a 100 nm. As expected for a point-like emitter, figure 4.12 shows that the emission map is diffraction limited. This phenomenon can be investigated further by means of super-localization : in that case, the intensity of the emission is fitted with a Gaussian in order to find its center.

4.2. LOW TEMPERATURE SINGLE NANOTUBE PHOTOLUMINESCENCE

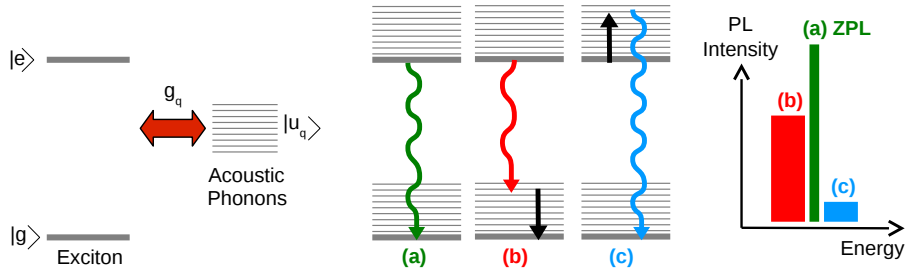


Figure 4.11 – Sketch of the coupling between the excitonic system ($|g\rangle, |e\rangle$) and the acoustic phonons ($|u_q\rangle$). The main line, or ZPL, (a) implies no interactions with the phonons. The red-wing of the spectrum (b) is due the emission of a phonon while the blue wing (c) is due the absorption of a phonon. At cryogenic temperature, the later mechanism is less likely than the former. Adapted from [92, p.61], with author’s permission.

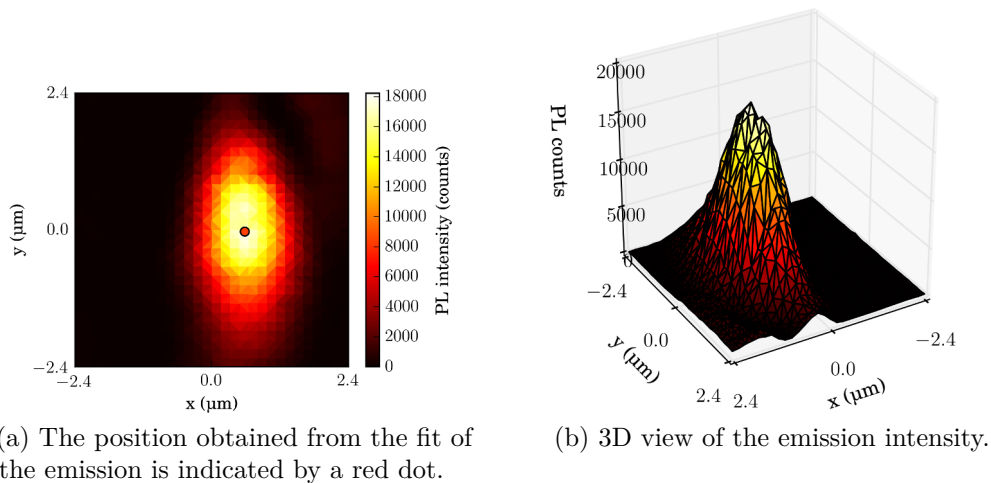


Figure 4.12 – Map of the emission intensity (at the energy of the nanotube) as a function of the excitation beam position. Experiment done with Théo Claude. Details : (8, 3) nanotube. Excitation : 760 nm, linear polarization (along CNT axis), below the saturation level. Figure layout by T. Claude.

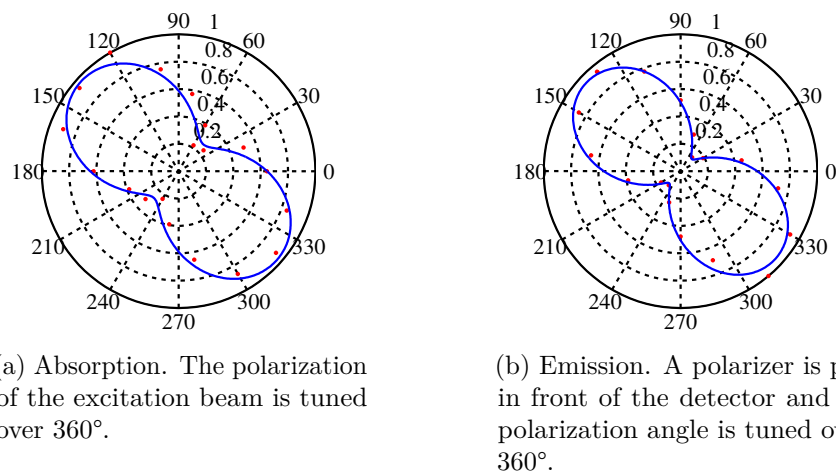


Figure 4.13 – Intensity of the Photoluminescence emission as a function of the polarization of (a) the excitation beam and (b) the detection setup. The experimental data are fit to obtain the extinction ratio. Details : (6,4) nanotube. Excitation 760 nm, $P = 0.7 \cdot P_{sat}$.

Such measurements are currently being performed by a fellow PhD candidate, Théo Claude, and give an accuracy of 20 nm. The result of such a localization process is indicated by a red dot in the map. With this method, in nanotubes having a length around 2 μm , several excitons are observed along the tube, separated by about 300 nm.

Polarization and anisotropy

As already stated in paragraph 2.2.1, carbon nanotubes have a very high aspect ratio, and thus undergo a strong depolarizing effect. This implies a strong anisotropy of both absorption and emission [104]. The figure 4.13a shows the intensity of the photoluminescence as a function of the excitation polarization while figure 4.13b shows the intensity of the PL as a function of the polarization of the detection.

The PL intensity I is fitted with the expression :

$$I(\theta) = A \cos^2(\theta - \theta_0) + B \sin^2(\theta - \theta_0) \quad (4.1)$$

where θ is the polarization angle of the excitation (or detection) and θ_0 is the preferential direction of the nanotube. The angles found for the excitation and the detection are the same within experimental accuracy. The *extinction ratio* (which means the PL intensity at its highest over the PL intensity at its lowest) is of the order of 5 to 10 in absorption and of the order of 10 to 20 in emission.

Indeed the nanotubes deposited are rarely straight. As the absorption occurs over the full nanotube length it has an effective aspect ratio different than its intrinsic

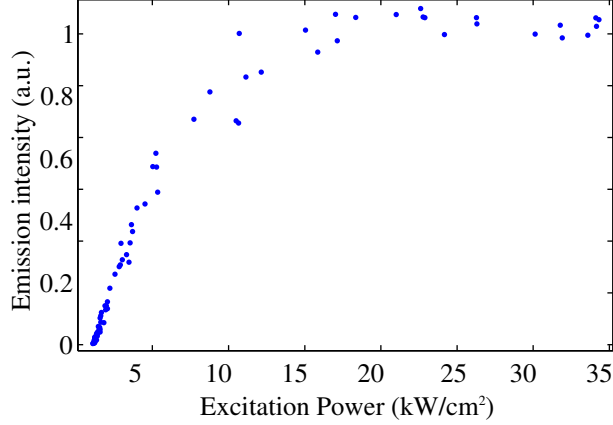


Figure 4.14 – Photoluminescence emission intensity as a function of the excitation power. Above a certain threshold (about a few kW cm^{-2} in continuous wave excitation), the emission intensity reaches its saturation level. Details : (6, 4) nanotube. Excitation : 760 nm, linear polarization (along CNT axis).

one. But the emission occurs over a length which is too low to be affected by such twists (a few nanometers, as stated in the previous paragraph). As a consequence, the emission has the intrinsic anisotropy of the emitter while the absorption has a reduced anisotropy. This explains why the extinction ratio is higher in emission than in absorption.

Saturation of the emission

The intensity of the integrated photoluminescence of a CNT, under pulsed excitation, as a function of the excitation power is presented in figure 4.14. One can clearly see a linear increase at low power followed by a saturation of the emission at higher power $P > P_{sat}$. This feature can be explained by considering the trapped exciton as a 2-level system [163], as discussed in section 4.2.1.

In the studies carried out here, the linear regime is overcome for an intensity of about a few kW cm^{-2} under continuous excitation, in excellent agreement with previous studies [26, 163, 164]. However, even for an emission intensity three times lower than the saturation limit, the signal-to-noise ratio remains good enough for the measurements performed throughout this work. Consequently, all the experiments reported here are done with an excitation power low enough to remain in the linear regime (between a third and a two thirds of the saturation level).

Exciton trapping

In the previous paragraphs, it was shown that the emission of a carbon nanotube arises from a section smaller than 20 nm, and that it saturates when the pump power

is increased. More over, Högele et al. [21] demonstrated in 2008 that nanotubes behave as single-photon emitters, which is confirmed in section 5.3.3. This means that the emission in the nanotube cannot arise from several sites at a time. In this paragraph, the origins of this phenomenon are discussed.

Excitons have a Bohr radius lower than 2 nm [117] (mean distance between the electron and the hole) and a lifetime around 100 ps. During this lifetime, the excitons can diffuse along the nanotube axis, over a typical distance $L_D = 100$ nm at room temperature [165, 166]. If two excitons are created in the nanotube at a distance smaller than L_D , it is very likely that they interact through an Auger process, also called Exciton-Exciton-Annihilation (EEA). In this process, one exciton recombines non-radiatively and its energy is transferred by Coulombic interaction to the other exciton. This process was evidenced experimentally [22, 23, 24]. It is extremely efficient due to the one-dimensional geometry and happens at rate a hundred times higher than the radiative decay¹⁴.

However, the nanotubes investigated in this work have a length around $L_D = 500$ nm, several times higher than the exciton diffusion length. Consequently, EEA cannot directly explain why only one exciton would survive over such a length. It is likely that emission in such a short nanotube arises from a single site with a size lower than L_D . The trapping of the exciton is fast, and around the trapping site, the Auger processes are possibly even faster than if the excitons are free to diffuse along the full axis [168].

The localization of excitons in carbon nanotubes was investigated by different works. In particular, reference [26] lists all the evidences of exciton localization in suspended carbon nanotubes. More over, Tip-Enhanced Near Field Optical Microscopy (TENOM) measurements at room temperature showed the presence of localization sites with a resolution of about 15 nm [25]. A slight decrease of the energy of the photoluminescence around these sites implies that the trapping is due to localized electrostatic potential wells of a few tenth of meV. These wells could be due to charges around the nanotubes, which may be brought by the surfactants used, or the polymer matrix in which they are embedded.

Recently, Hofmann et al. [169] investigated the trapping of excitons in carbon nanotubes by photoluminescence experiments both at room and cryogenic temperature. They conclude that trapping potentials ranging from a few meV to a few tens of meV arise from environmental disorder (adsorbate on the nanotube surface) as well as crystalline defects in the nanotube. As a matter of fact, the control of defects in carbon nanotubes is now a research field of its own, and led to increased efficiency and anti-bunching up to room temperature in doped nanotubes [27].

At cryogenic temperature, the diffusion length of excitons is unknown : it depends on the mobility, which itself depends on the surroundings of the nanotube. In our sample, the mean carbon nanotube length is 500 nm, though the exact distribution is unknown. Most of the observed nanotubes (at least 90%) displayed a single emission

¹⁴In fact, this rate strongly depends on the density of excitons, as discussed in [167, chap. 3].

line, and all the tubes investigated with a HBT setup displayed anti-bunching, including when the pumping rate was close to the saturation limit (which suggests the creation of several excitons). Even if the exact processes remain unclear, we can conclude that our nanotubes are sufficiently short, that the exciton diffusion length is sufficiently long, and that the excitons annihilation processes are sufficiently strong to obtain a single exciton much faster than the spontaneous emission lifetime.

4.2.2 Coupling to acoustic phonons

The PL spectra of carbon nanotubes, as introduced in the previous section, consist in three main features. The exciton is considered as a pseudo 2-level system. The relaxation from its excited state to the ground state (annihilation of the exciton) gives rise to a strong Lorentzian line, called the Zero Phonon Line (ZPL).

The two other features on both sides can be accounted for by phonon assisted processes : on the low energy side, the emission of a phonon and on the high energy side, the absorption of a phonon. In order to go beyond this qualitative approach, a Hamiltonian is introduced to model electron-phonon interactions.

Hamiltonian of the system

A model giving analytically the coupling between an electron and a phonon was introduced by Hung et al. [170] and improved by Duke et al. [171] in the case of colored centers. Krummeheur et al. [172] applied such a model in the case of localized excitons in semi-conducting quantum dots coupled to the phonons of the surrounding 3D matrix. More recently, Galand et al. [161] took into account the unidimensional character in order to apply it to CNTs. This study was completed by Vialla et al. [20] in our group, prior to this work.

The Hamiltonian of the system can be written as :

$$H = H_0 + H_{ep} \quad (4.2)$$

$$H_0 = E_g |g\rangle\langle g| + E_e |e\rangle\langle e| + \sum_{\vec{k}} \hbar\omega_k b_{\vec{k}}^\dagger b_{\vec{k}} \quad (4.3)$$

$$H_{ep} = |g\rangle\langle g| \exp\left(\sum_{\vec{k}} \lambda_{gg,k} (b_{\vec{k}}^\dagger + b_{\vec{k}})\right) + |e\rangle\langle e| \exp\left(\sum_{\vec{k}} \lambda_{ee,k} (b_{\vec{k}}^\dagger + b_{\vec{k}})\right) \quad (4.4)$$

The Hamiltonian can be divided in two parts. H_0 is the Hamiltonian without exciton-phonon interactions : the first two terms describe the energies of the ground state $|g\rangle$ and the excited state $|e\rangle$ of the exciton. The third term describes the phonon bath and involves a sum over all the wavevectors \vec{k} , with an energy $\hbar\omega_k$. $b_{\vec{k}}^\dagger$ and $b_{\vec{k}}$ are the creation and annihilation operators for phonons. Finally, H_{ep} describes the electron-phonon interactions, driven by the matrix element $\lambda_{gg,k}$ and $\lambda_{ee,k}$. In the following, $\lambda_{gg,k}$ is taken as zero and $\lambda_{ee,k}$ is noted λ_k .

The speed of sound in a CNT (about 2×10^4 m/s) is an order of magnitude higher than in the surrounding polymer matrix. As a consequence, the propagation of

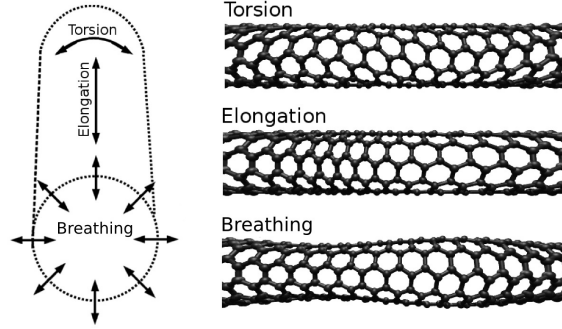


Figure 4.15 – Schema of the different acoustic phonon modes (radial breathing, elongation and torsion) in carbon nanotubes. Adapted from [92, p.63], with author's permission.

phonons from the nanotube to the matrix, or conversely, is suppressed. Thus, only the one dimensional phonons propagating in the nanotube itself are considered. Moreover, given the spectral width of the nanotube, the study is restricted to the phonons of low energy, introducing a broadening lower than 10 meV. As a consequence, the optical phonons, having an energy of about 200 meV are not taken into account.

Amongst the acoustic phonons, three types of deformations can occur : radial breathing, torsion and elongation, as depicted in figure 4.15. The radial breathing mode has an energy of about 35 meV to 45 meV for a zero wave-vector, with an almost flat dispersion. As it is too high to correspond to the broadening observed, it won't be taken into account in this work. The two other modes can be merged in one for the purpose of this study [173, 174]. This combined mode has a linear energy dispersion in the range of study, so the dispersion relation is $\omega_k = v|k|$ with $v = 2 \times 10^4$ m/s for all chiral species.

The propagation of an acoustic phonon along a CNT introduces a deformation of the atomic structure and thus of the potential felt by the charge carrier. This modification can be taken into account with a deformation potential D [173, 175]. The coupling potential U between the exciton and an acoustic phonon is related to the displacement of the atoms with respect to their equilibrium position \vec{u} by :

$$U = D \vec{\nabla} \cdot \vec{u} \quad (4.5)$$

The displacement itself can be written :

$$\vec{u} = \sum_{\vec{k}} \sqrt{\frac{\hbar \omega_k}{2\rho L v^2}} (b_{\vec{k}}^\dagger + b_{\vec{k}}) \vec{u}_{\vec{k}} \quad (4.6)$$

where $\rho = 1.7 \times 10^{-15}$ kg/m is the lineic mass of the nanotube, considered constant for the nanotubes investigated in this work. The $\vec{u}_{\vec{k}}$ are an orthonormal basis for the acoustic modes of wave-vector \vec{k} .

From the relation 4.5, one can rewrite the interaction Hamiltonian H_{ep} :

$$\sum_{\vec{k}} \lambda_k (b_k^\dagger + b_{\vec{k}}) = \langle \Psi | D \vec{\nabla} \cdot \vec{u} | \Psi \rangle \quad (4.7)$$

where Ψ is the wave-function of the exciton (normalization $\int dz |\Psi(z)|^2 = 1$, where z is the coordinate along the tube axis). The matrix elements λ_k can thus be written :

$$\lambda_q = \sqrt{\frac{\hbar \omega_k}{2\rho L v^2}} F(\omega_k) \quad (4.8)$$

where L is the length of the nanotube and F is a form factor defined by the relation :

$$F(\omega_k) = D \frac{v}{\omega_k} \sqrt{L} \int dz |\Psi(z)|^2 \frac{du_k(z)}{dz} \quad (4.9)$$

One can obtain the linear response function $\chi(t)$ after a Dirac excitation pulse [161, 172] :

$$\chi(t \geq 0) \propto i e^{-i\bar{\Omega}t} e^{-t/T_2} \exp \left[\sum_{\vec{k}} |\lambda_k / \hbar \omega_k|^2 (e^{-i\omega_k} - n_k(T) |e^{-i\omega_k t} - 1|^2 - 1) \right] \quad (4.10)$$

where $\bar{\Omega} = \Omega - \sum_k |\lambda_k|^2 / \hbar^2 \omega_k$ is the transition frequency. This frequency is shifted by the so-called polaron shift frequency compared to the bare system. The coherence time T_2 introduced takes into account the dephasing due to all the processes apart from the phonons. The term $n_k(T)$ is the occupation number (Bose-Einstein distribution).

By using this procedure, one can recover the PL spectrum of the nanotube. Indeed, the absorption spectrum can be obtained from eq. (4.10) by taking the imaginary part of the linear susceptibility (which is the Fourier transform of the response function). And the photoluminescence emission spectrum is the image mirror of the absorption spectrum with respect to the ZPL [172].

Confinement of the acoustic phonons

In the previous paragraph, a Hamiltonian describing the coupling between a nanotube exciton and its acoustic phonons was given. It was shown that the photoluminescence spectrum can be derived from a form factor defined in equation 4.9. If one considers that the phonons propagate as planar waves : $u_k(z) = e^{ikz} / \sqrt{L}$, the form factor rewrites :

$$F(\omega_k) = D \int dz |\Psi(z)|^2 e^{ikz} \quad (4.11)$$

Now let's consider that the exciton is localized on length σ . Its wave-function writes : $\Psi(z) = \pi^{-1/4} \sigma^{-1/2} \exp(-z^2/2\sigma^2)$. In that case the form factor F_0 reads :

$$F_0(\omega_k) = D \exp \left[-(\omega_k \sigma / 2v)^2 \right] \quad (4.12)$$

Here the form factor introduces a cutoff frequency : all the phonons with an energy above $2\hbar v/\sigma$ won't be able to couple due to the conservation of momentum. If the exciton is completely delocalized, $\sigma \rightarrow \infty$, then no acoustic phonons are able to couple to the exciton. Consequently, our model requires the exciton to be localized in carbon nanotubes, as already discussed in section 4.2.1.

To go further, one can consider the ratio α describing the probability of an emission in the ZPL over the total probability of emission (including the ZPL and the phonon wings). One can show that the ratio for CNT scales as [92, p. 66] :

$$\alpha \propto \omega_k^{Dim-2} \quad (4.13)$$

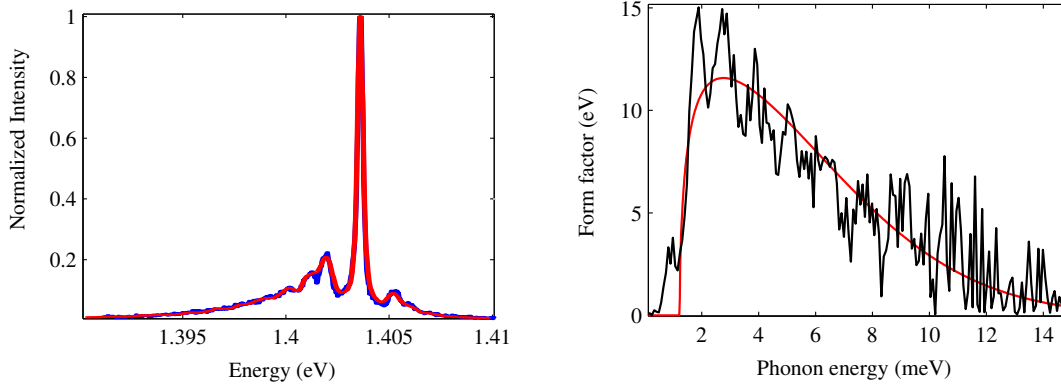
Where *Dim* is the dimension in the phonon bath. It is clear that for three-dimensional phonons, as in quantum dots for example [176, 177], the ones of lower energy are not coupled, and the shape of the ZPL is preserved. On the contrary, for a carbon nanotube, $\alpha \propto \omega_q^{-1}$. This means that the lower the energy of the phonon, the better it is coupled to the exciton. For phonons of very low energy, the ratio α diverges, which means that the ZPL merges into the phonon wings, giving rise to a large and asymmetrical profile. Even though this kind of profile is observed in some carbon nanotubes, it does not fit the spectrum displayed in figure 4.10, where the phonon wings are separated from the ZPL by a gap of a few meV.

In order to solve this issue, it is assumed that an acoustic barrier prevents the propagation of phonons below a certain energy along the nanotube axis. Physically this acoustic barrier could be due to mechanical interactions between the CNT and the surrounding matrix, residual amorphous carbon, or a mediation by the polymer wrapping of the nanotubes [178]. One can model the nanotube as a one-dimensional chain of masses and springs. An acoustic barrier of height $\hbar\omega_b(z)$ is introduced along the nanotube axis (z coordinate). The deformation modes u_q are given by :

$$-\omega_q^2 u_q(z) = v^2 \frac{d^2 u_q(z)}{dz^2} - \omega_b^2(z) u_q(z) \quad (4.14)$$

If the acoustic barrier is zero, one finds plane waves. However, if this acoustic barrier is finite, it can create a gap, blocking the propagation of the low energy waves. For the nanotubes, this translates into a gap for acoustic phonons. Typically a contact stiffness of 1 N/m would lead to a gap of 1 meV, which is typical for Van der Waals liaisons [179].

An other explanation for the acoustic barrier could come from self-trapping mechanisms [180] : in that case, due to a strong electron-phonon coupling, the charge carriers would deform the crystal lattice and lead to the creation of a potential well trapping the charge carriers themselves. This would explain the localization of the exciton and lead to a modification of the phonon density of states on an energy scale of about 1 meV.



(a) Photoluminescence spectrum of a single carbon nanotube taken at 10K, in blue as already shown in figure 4.10 and fit in red. (b) In black, the experimental form factor, numerically extracted from the photoluminescence spectrum, see eq. (4.10). In red, the form factor used for the fit.

Figure 4.16 – Photoluminescence of a carbon nanotube reproduced by the model developed in the text (fits in red). The deformation potential is $D = 18$ eV, the exciton localization length $\sigma = 3.3$ nm, the acoustic barrier $\hbar\omega_c = 1.2$ meV and the effective temperature 20 K. Same nanotube and conditions as in figure 4.10.

Whatever its physical origin, if an acoustic barrier of height $\hbar\omega_c$ is introduced over the full length L of the nanotube, the form factor rewrites :

$$F(\omega_q) = F_0(\tilde{\omega}_q) \frac{\text{Re}(\tilde{\omega}_q)}{\omega_q} \quad (4.15)$$

where $\tilde{\omega}_q = \sqrt{\omega_q^2 - \omega_c^2}$. This form factor is strictly zero for $\omega_q < \omega_c$: all the phonon modes of low energy are suppressed. This means that the ZPL is separated from the phonon wings by an energy corresponding to the phonon gap. Figure 4.16a shows the same nanotube than figure 4.10 with the fit corresponding to the model developed in this section. The parameters used for this fit are : deformation potential $D = 18$ eV, exciton localization length $\sigma = 3$ nm, acoustic barrier $\hbar\omega_c = 1.2$ meV and effective temperature 20 K. The corresponding form factor is displayed in figure 4.16b.

The model described in this section has a range of application larger than what was introduced : in particular it can reproduce the shape of all the photoluminescence spectra observed for suspended nanotubes as well as for micelle encapsulated nanotubes, as explained in [92, 20]. Moreover the temperature dependence of a photoluminescence spectrum is also well explained by the model : as expected, when the temperature increases, the emission broadens and the absorption of phonons becomes more likely, which means that the spectrum becomes more symmetrical. The temperature evolution of the PL spectrum of a nanotube is shown in figure 4.17 together with the corresponding fits.

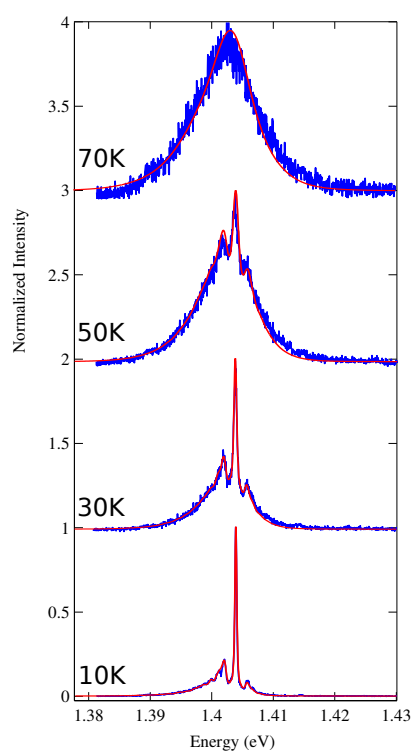


Figure 4.17 – The experimental PL intensity of a nanotube is given in blue for different temperatures. The fits done with the model given in the text are displayed in red. Same nanotube and conditions as in figure 4.10.

4.3 Spectral diffusion in Carbon Nanotubes

The photoluminescence signal by carbon nanotubes is never completely constant over time. Three types of phenomenon occur :

- *Bleaching* corresponds to a significant and irreversible decrease - or vanishing - of the emission intensity. Usually the signal decreases and disappears altogether after a few seconds or a few minutes. It is probably due to the presence of oxygen in the vicinity of the nanotube's wall [181]. Burying nanotubes in polystyrene (section (2.3.3)) prevented this phenomenon from happening in this study.
- *Blinking* corresponds to intermittent intensity variations - or vanishing - of the photoluminescence. The phenomenon is common to most single emitters and happens at time scales ranging from nanoseconds [182] to minutes [183]. It is most likely due to interactions between the exciton and the local environment of the nanotube and is strongly limited by polymer capping [164].
- *Spectral diffusion* also referred to as *spectral wandering* corresponds to a shift in the emission energy of the photoluminescence. It is also limited by polymer capping [164] but not completely suppressed. This section aims to give more details about this phenomenon.

4.3.1 Spectral diffusion of the ZPL

Spectral diffusion is not specific to carbon nanotubes. As it distorts the emission signal, its understanding and its suppression have been the focus of researchers for a long time. A model explaining this behavior is the quantum-confined Stark effect (QCSE) : the presence of an electric field around the emitter implies a shift of the electronic and hole states energies towards opposite directions, causing a change of the emission energy. This external field can also modify the separation between positive and negative charge carriers, leading to a change in the overlap of their wave-function and thus to a change of their recombination efficiency. However, the electron-hole interaction remains strong due to the confinement [184]. The link between an external field and a shift of the emission was experimentally demonstrated for quantum dots [185]. Furthermore, evidences were given for the induction of PL shift by the presence of an electrical charge at the surface of a nanorod [186].

The photoluminescence of nanotubes was first observed when they were isolated in micelles. The photoluminescence intermittency observed at the time, at room temperature, was ascribed to the presence of charges trapped near the exciton [187]. However, at room temperature, the spectral diffusion phenomenon is harder to observe as the spectral width of the emission typically overcomes the spectral jumps of the emission [188]. At cryogenic temperature, spectral diffusion was observed for the first time in 2004, happening over tens of meV at the second time scale [189]. The

origin of this spectral diffusion in carbon nanotubes is likely to come from interactions with the environment and more precisely the surfactant. Indeed, it was shown that CVD grown, surfactant free, nanotubes were displaying a stable emission [190].

More recently, Ai et al. [164] showed that burying carbon nanotubes in a polymer, namely poly(methyl methacrylate) (PMMA), implied a strong suppression of both the blinking and the spectral diffusion. The authors explain that heating the PMMA capped nanotubes enables to remove surface-bound waters molecules and prevents the apparition of spectral diffusion. However, they observe that after two weeks of exposure at ambient air, the sample degrades. An additional heat treatment eliminates again spectral diffusion. In this work, the polymer used is polystyrene because it is easily diluted in toluene (in which the PFO-wrapped nanotubes are diluted) and that the blinking and spectral diffusion was efficiently suppressed. An aging of the sample was observed : the spectral diffusion was almost inexistent with a fresh sample, but was strong after several months. Heating helped to decrease it but did not give as good results as with pristine samples.

Finally, it should be noted that the spectral diffusion of carbon nanotubes embedded in polystyrene was observed by Walden-Newman et al. [191]. Though the spectral diffusion was suppressed at the second time-scale, they showed that it remained strong at the nano-second time-scale, and consequently caused a broadening of the intrinsic linewidth of the emitter. In other words, when the ZPL FWHM of a nanotube is found to be 500 μeV on a spectrum acquired in one second, it is likely that the intrinsic FWHM is lower and that the observed FWHM is a convolution between the intrinsic one and the fast fluctuations of its emission energy.

4.3.2 Spectral diffusion of the Phonon Wings

Though the spectral diffusion of the main photoluminescence line of carbon nanotube is extensively discussed in the literature, its implications for the emission wings is rarely investigated.

Some researchers offer an explanation for the shape of the emission spectrum of carbon nanotubes based on spectral diffusion [26]. They assume that there are no interaction with phonons and that the spectrum simply consists in a Lorentzian line. This Lorentzian line undergoes spectral diffusion at a fast pace. The probability distribution of the line's energy is responsible for the shape of the spectrum observed at the second time scale.

The phonon coupling model is well evidenced by the investigations of Fabien Violla [92, 20], in particular by its ability to reproduce the temperature evolution of the spectrum (the blue/red wing ratio corresponds to a Boltzmann factor arising from the interactions with the phonon bath). This work offers to investigate the validity of this model in the context of spectral diffusion. If the overall shape of the nanotube spectrum is due to fast spectral diffusion, a spectral jump of the main line should not display any particular correlation with the spectral jumps undergone by the wings.

On the contrary, for all the nanotubes investigated in this work, the spectral diffusion consists in a shift of the whole spectrum (i.e. : the complete spectrum, including the ZPL and the wings is simply shifted, without distortion). Experimentally, the spectrum of a single carbon nanotube is acquired repeatedly during tens to hundreds of seconds with an exposure time of 1 s.

A first way to assess that the spectrum shifts without distortion is to plot the position of the ZPL and of the maxima of the two phonon wings. For each spectrum, these features can be fitted with a Lorentzian curve. As one can see in figure 4.18, the positions of the three peaks follow the same time variations. The correlation coefficient between two of them is above 98%.

However, this method gives information only on the maxima of the ZPL and the wings. It does not describe the full spectrum and is not well suited if the wing maxima are less pronounced. An other way to confirm that the spectrum is simply shifted is to use the two-sample Kolmogorov-Smirnov (KS) test [192]. This test gives the probability for two sets of data x_1 and x_2 to arise from the same distribution. It computes :

$$KS = \max_x (|F_1(x) - F_2(x)|) \quad (4.16)$$

where $F_i(x)$ is the proportion of x_i values less than or equal to x . Practically, this test returns zero if the two sets of data come from the same distribution and one if they are completely uncorrelated. To evaluate the accuracy of this test, let's see its output for shot noise : a random noise of amplitude \sqrt{I} (where I is the intensity of emission) is added to the spectrum of figure 4.18b . The process is repeated a hundred times, as shown in figure 4.19a, it yields a value of $KS = 0.033 \pm 0.004$. Thus, one can consider that two sets of data having $KS < 0.04$ are identical.

The KS test was applied to compare each spectra of figure 4.18a to the first spectrum. The result is shown if figure 4.19b. It yields a value of $KS = 0.03 \pm 0.01$. It can thus be concluded that all the spectra arise from the same distribution, with an accuracy close to the shot noise.

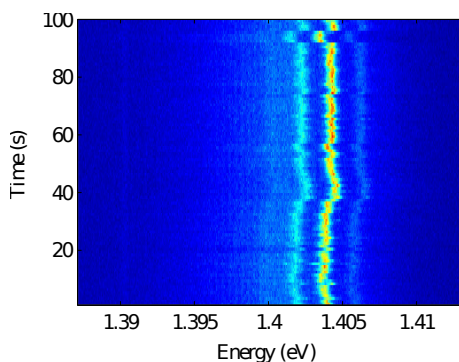
An other way to confirm that the shift is the same for the whole spectrum is to look at its derivative. As a matter of fact, the absence of distortion of the spectrum over time implies that the spectrum at $t + \delta t$: $S(E, t + \delta t)$ is simply the spectrum at t , $S(E, t)$, shifted by an energy δE :

$$S(E, t + dt) = S(E + \delta E, t) \quad (4.17)$$

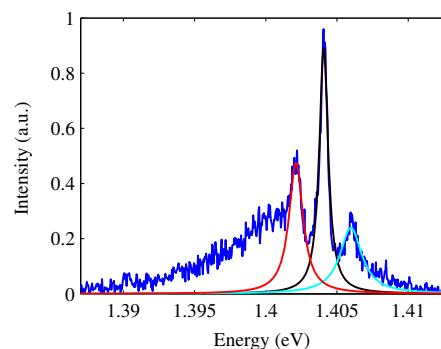
As a consequence :

$$S(E, t + dt) = S(E) + \frac{\partial S}{\partial E} \delta E \quad (4.18)$$

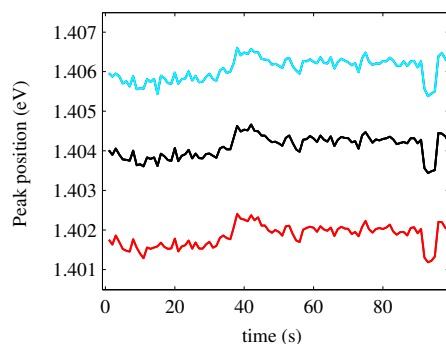
An the difference between the two spectra is proportional to the derivative of the spectrum :



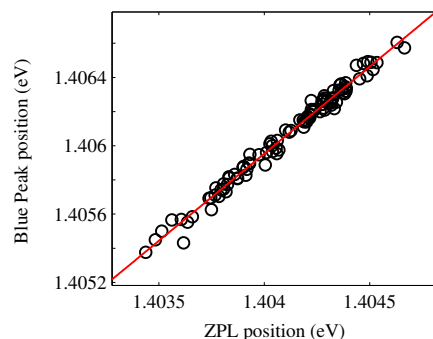
(a) Map displaying the intensity of the emission as a function of its energy and the time. Spectral diffusion of the ZPL is clearly visible.



(b) In blue, a spectrum acquired in 1 s (corresponding to one line in (a)). The position of the ZPL (resp. red wing, resp. blue wing) is located with a Lorentzian fit displayed in black (resp. red, resp. blue).

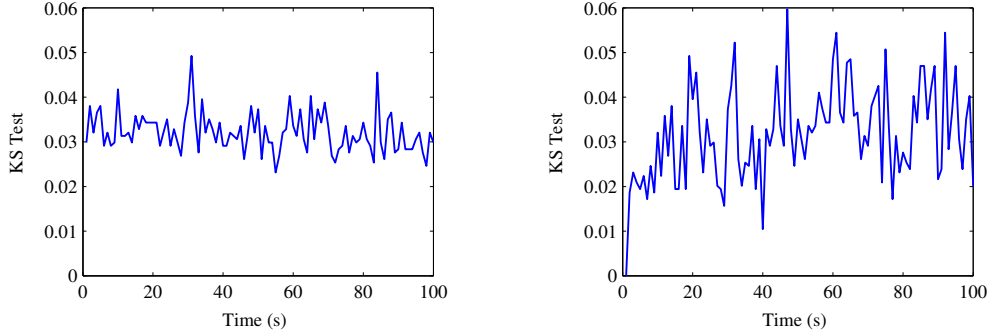


(c) The position of the three maxima indicated in (b) is displayed along time with the same color code.



(d) The black dots show the position of the blue wing maximum of intensity as a function of the position of the ZPL position. The red line is a linear fit.

Figure 4.18 – The photoluminescence spectrum of a (6, 4) nanotube is measured a hundred times consecutively with an exposure of 1 s. Details : cryogenic temperature 15 K, continuous-wave excitation at 760 nm, below the saturation level. Spectrometer grating : 1200 lines/cm



(a) For the spectrum of figure 4.18b plus the addition of a shot noise.

(b) For each line of figure 4.18a compared to the first line.

Figure 4.19 – Kolmogorov-Smirnov (KS) test.

$$S(E, t + dt) - S(E) = \frac{\partial S}{\partial E} \delta E \quad (4.19)$$

If the quantity is averaged over time, one gets :

$$\Delta S = \langle |S(E, t + dt) - S(E)| \rangle \propto \langle \left| \frac{\partial S}{\partial E} \right| \rangle \quad (4.20)$$

Finding a proportionality between ΔS and the average of the derivative $\langle \left| \frac{\partial S}{\partial E} \right| \rangle$ is a direct proof that eq. (4.17) is true. In figure 4.20, the average of the difference between consecutive spectra and the derivative of the mean spectrum¹⁵ are displayed. One can see that the experiment agrees well with the expected proportionality of these two quantities.

To conclude, all the measurements performed during this work tend to demonstrate that spectral diffusion at the second time scale shifts the photoluminescence spectrum of carbon nanotubes as a whole. It is a strong evidence in favor of the phonon model developed in section 4.2.2.

Conclusion

In this chapter, the home-built confocal setup used throughout this work was described in details. Given the excellent signal-to-noise ratio obtained, photoluminescence measurements of single carbon nanotubes were carried out, showing usual features : spatial localization, polarization anisotropy and saturation of the emission.

It was explained that the emission of carbon nanotubes most likely arises from

¹⁵In order to obtain the mean spectrum, all the lines in figure 4.20a are shifted to align the ZPL. The average is then done over the columns.

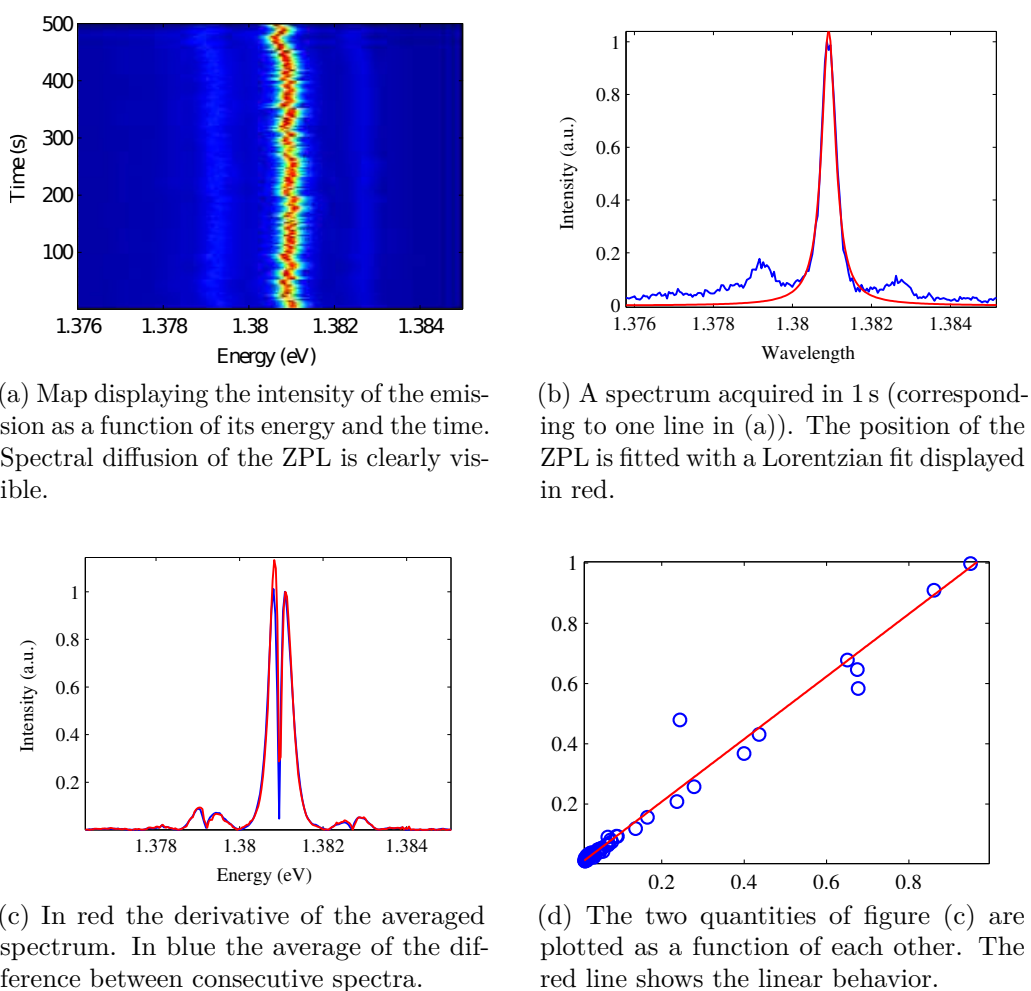


Figure 4.20 – The photoluminescence spectrum of a (9,1) nanotube is measured a hundred times consecutively with an exposure of 1 s. Details : cryogenic temperature 15 K, continuous-wave excitation at 760 nm, $P = 0.7 \cdot P_{sat}$. Spectrometer grating : 1200 lines/cm.

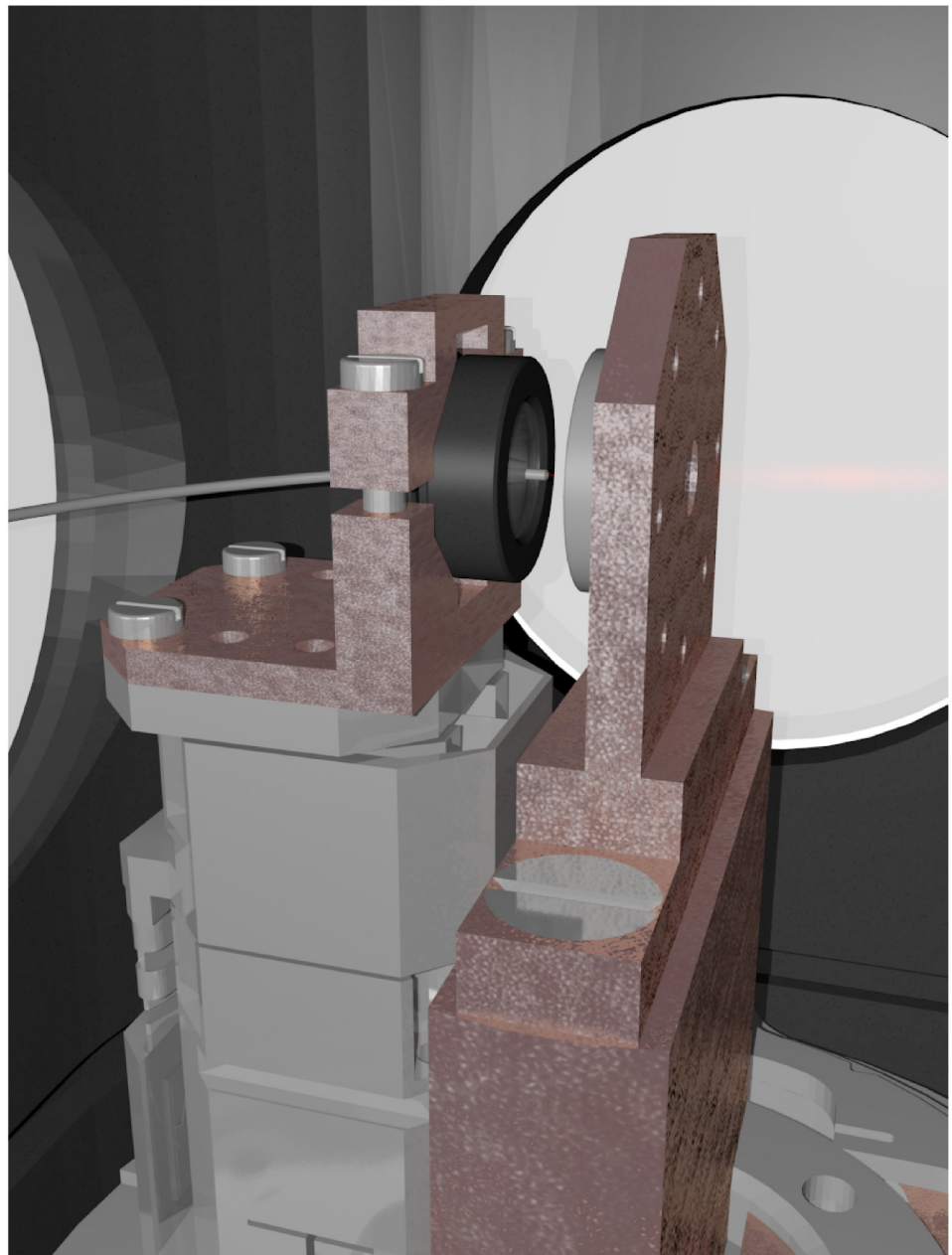
localized sites due to the environment or to crystalline defects in the nanotubes. Around these sites, excitons annihilate at a fast rate through Auger processes, which explains how nanotubes can emit anti-bunched light.

A model was given to account for the non-Lorentzian shape of the nanotubes photoluminescence : it consist in a main line called the ZPL and two wings coming from phonon assisted transitions. The asymmetry between the two wings is a direct measurement of the local temperature of the nanotube. Finally, the spectral diffusion phenomenon was explored in details and gave evidences for the phonon coupling model.

In chapter 5, the setup is described more completely to explain how the cavity is coupled to the confocal microscopy. And the Purcell enhancement obtained by the cavity coupling is investigated.

5

A PURCELL ENHANCED SINGLE-PHOTON SOURCE



Contents

5.1	Coupling a tunable cavity to the confocal microscope	132
5.1.1	Cavity Setup	132
	Cryostat organization	132
	Free-space to cavity switching	135
5.1.2	Lens-Fiber mounting principle	138
	Lens drilling principle	138
	Collection efficiency	138
	Fiber sticking and angle control	140
5.2	Measuring the Purcell Factor	141
5.2.1	Photon counts method	141
	Emission diagram	142
	Collection efficiency	144
	Results and discussion	146
5.2.2	Time domain method	149
	Principle	150
	Lifetime measurements	151
	Instrumental response	152
	Effect of the optical path	152
5.2.3	Experimental Results	154
	Radiative yield measurement	154
	Transient measurements	156
	Results and discussion	159
5.3	Single-photon source	162
5.3.1	Statistics of a light source	166
	Poissonian source	166
	Super-Poissonian source	167
	Sub-Poissonian source	168
5.3.2	Second order correlation function	168
	Classical definition	168
	Quantum definition	169
	Single-photon source criterion	171
5.3.3	Hanbury-Brown and Twiss setup	172
	Principle	172

HBT under continuous excitation	173
HBT under pulsed excitation	175
APD after-pulse cross-talk	177
Results and discussion	177

In 2008, Högele et al. [21] demonstrated for the first time that a carbon nanotube can behave as a single-photon source. In their experiment, a carbon nanotube in sodium dodecylbenzenesulfonate, deposited on a solid immersion lens, was observed individually at cryogenic temperature. The second-order correlation function measured at zero delay was as low as $g^{(2)}(0) = 0.03$, which is well below the single-photon emission criterion $g^{(2)}(0) < 0.5$ (see section 5.3.2). Since then, this result has been confirmed by Walden-Newman et al. [191] for carbon nanotubes embedded in polystyrene, with a value of $g^{(2)}(0) = 0.15$. More recently, Endo et al. [28] showed that the anti-bunching property of CNT can be conserved at room temperature, with $g^{(2)}(0) = 0.6$. And Ma et al. [27] showed that solitary oxygen dopants in nanotubes can yield single-photon emission at room temperature at the telecoms wavelengths ($g^{(2)}(0) = 0.32$).

The opening towards single-photon emission at room temperature in the telecoms bands makes nanotubes good candidates as single-photon sources. But several drawbacks must be overcome: their emission has a low quantum efficiency, is non-directional, and the coherence time is limited. Therefore, coupling a nanotube to a resonator is highly sought to improve their efficiency [88, 80, 85, 77], to obtain an emission directed into the cavity mode and to increase the spectral purity of the source. Unfortunately, due to the lack of control of the growth or deposition processes, current attempts rely on random spectral and spatial matching between a resonator (microdisks [87] or photonic crystals [32]) and randomly deposited nanotubes, putting strong limitations on the investigations of this technology.

In this work, the flexible setup introduced in section 1.3.3 is built, allowing to tune both spatially and spectrally a cavity to match any emitter. In chapter 3, the properties of the cavities formed by a laser-machined mirror at the apex of an optical fiber and a planar mirror were described. In particular, it was noted that if the fiber is movable, a change in the distance separating the mirrors corresponds to a spectral tuning of the cavity. Moreover, as the cavity is laterally defined by the fibered mirror, a transversal shift of the fiber brings the spatial tunability.

Given their easy tunability, fiber Fabry-Perot cavities are now more and more used in condensed matter [193, 138]. In particular, David Hunger who was one of the pioneers of this technology created a team dedicated to these devices. They used such fibered cavities for ultra-sensitive imaging of gold nanoparticles [194], for NV-center Purcell enhancement [195] as well as for Purcell-enhanced Raman spectroscopy of carbon nanotubes [89]. All these experiments were carried out at room temperature, which is best for applications, but blurs the intrinsic optical properties of nanotubes, in particular concerning exciton-phonon interactions (as explained in section 4.2). In our partner group, Benjamin Besga [196] had built a setup using a fiber Fabry-Perot

cavity in a helium bath to study quantum well polaritons. The same kind of setup was used by Miguel-Sanchez [197] with quantum dots. Nevertheless, in both cases the technique consists in moving the fiber blindly along the lateral axis. For CNT, the low PL emission signal and the high variability from one emitter to the other makes this method irrelevant. This is why a novel setup coupling a confocal microscope and a fiber Fabry-Perot cavity was built.

This chapter starts by describing the setup. After that two methods are discussed to show that the cavity induces a strong brightening of the nanotube and an acceleration of its spontaneous emission. Finally, it is shown that the cavity embedded nanotubes behave as single-photon sources, and more over that the emission energy is tunable.

5.1 Coupling a tunable cavity to the confocal microscope

In chapter 4, the confocal microscope setup built to characterize the nano-emitters in free-space was described. It is now time to explain how these emitters can be embedded in the fibered cavities. In fact, two main issues arise for such a coupling : spectral and spatial matching.

The spectral tunability issue was fully addressed in section 3.1 : the optical cavity is formed between the planar mirror on which the nanotubes are deposited and a mirror located at the apex of an optical fiber. Tuning the distance between the two of them makes it possible to bring the cavity in resonance with the emitter. Spatial tunability requires to be able to move laterally the fiber. In order to get this feature, as well as for the simplicity of the switching between free-space and cavity configurations, the fiber was integrated in the center of the confocal lens.

5.1.1 Cavity Setup

The free-space configuration and the confocal setup were described in chapter 4, however a full account of the whole setup is needed before explaining how the switch from free-space to cavity is performed.

Cryostat organization

Let's first give an overview of the setup : the confocal setup is the one described in section 4.1, with the possibility of exciting the nanotube either through the confocal lens or through the sample mirror. The only change concerning confocal microscopy is that the confocal lens is drilled and a fiber is inserted in its center, as depicted in fig. 5.1 and the schema of fig. 5.2. The effect of the hole on confocal microscopy is addressed in section 5.1.2. From now on, the confocal lens with the inserted fiber is referred to as the *objective* to simplify the notations.

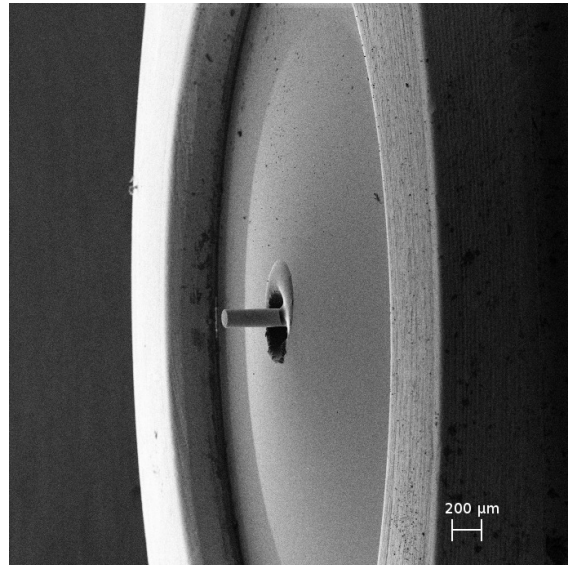


Figure 5.1 – Optical fiber stuck into an aspherical lens. Image taken with a scanning electron microscope.

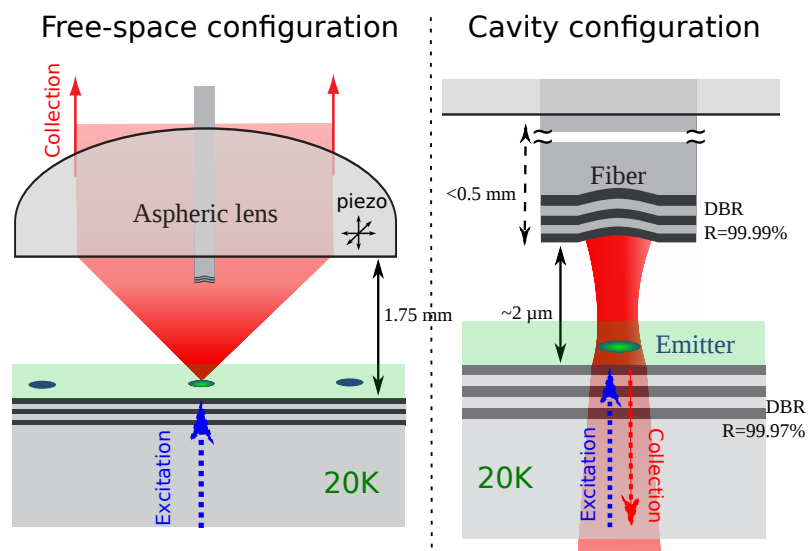


Figure 5.2 – Schema of the confocal and cavity setups. On the left, the emitter is observed in free-space, while on the right it is embedded in the microcavity. The excitation remains the same.

5.1. COUPLING A TUNABLE CAVITY TO THE CONFOCAL MICROSCOPE

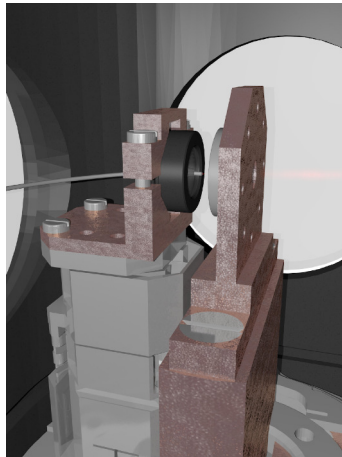


Figure 5.3 – (A larger version of this figure is on the front page of the chapter) Sketch of the setup inside the cryostat : on the left, the *objective* sits on three piezoelectrics. The fiber is inserted and stuck at its center. On the center, the sample is hold on a copper piece directly in contact with the cold finger of the cryostat. The emitted light is collected by a second lens located in the right part of the cryostat (not visible here).

It must be noted that for cooling, a closed-cycle cryostat¹, is used. It has the advantage of maintaining a chamber of 10 cm³ at a stable temperature between 4 K and 350 K during several weeks without any handling. The counterpart are the vibrations (about 5 nm) induced by the cryostat's compression and decompression cycles.

Three major elements are inside the cryostat : the first is obviously the sample. The second is the *objective* : as the fiber is sticked in it and has to come almost in contact with the sample, it cannot remain at ambient temperature nor be separated from the sample by a glass window. These two elements are depicted in fig. 5.3. The third element is an additional lens. It is used to focus the backside excitation and to collimate the output of the cavity.

The *objective* and the fiber are located on top of a stack of three piezoelectric devices², allowing to tune its position in the three orthogonal directions of space. At cryogenic temperatures, these piezoelectrics can move over 4 mm with a slip-stick process. Alternatively, they can move in a reproducible way over about 1 μ m. The coarse motion is used to switch from confocal to cavity configuration as well as for the spatial alignment of the cavity. The spectral coupling is managed with the reproducible motion.

The *objective* and the fiber are cooled, but as the piezoelectrics do not conduct heat as well as a metal, their temperature is most likely above the one of the sample. No particular investigation was made on this as there were no stringent conditions

¹Cryostation by Montana Instruments

²Attocubes ANC 350

on their temperature in the experiment. On the contrary, the greatest care was paid to the cooling of the sample which is exclusively hold by copper pieces, themselves directly in contact with the cold finger of the cryostat. The temperature sensor is directly positioned on the backside of the sample.

Free-space to cavity switching

Before giving more details about the additional parts of the setup, outside the cryostat, it is necessary to describe step by step how the switch from free-space to cavity configuration is done :

- First, a raster scan of the sample is done, and a carbon nanotube is selected (the criterion being its intensity of emission, its spectrum, etc...).
- The steering mirror is set to its medium position and the lens is moved so that the emitter is at its focal point.
- The excitation is switched to the backside. This step enables to keep the very same excitation in free-space and cavity. It ensures that the nanotube excited remains the same and that the effects observed, such as increased emission rate are due to the presence of the cavity and not to a change in the excitation. See section 5.2.1 for further details.
- The location of the nanotube is recorded by a camera which images the plane of the sample, as shown in figure 5.4.
- The fiber-lens ensemble is brought towards the sample. Light is injected in the fiber, so that the location of its tip can be monitored on the above mentioned camera. With this monitoring the position of the fiber can be corrected compared to the location of the nanotube even if the fiber travel path deviates from the lens optical axis.
- The collection path is switched to the cavity configuration. A telescope can be added and adjusted to ensure an optimal collection (it compensates for any misalignment of the lens in the cryostat which cannot be moved once the cryostat is closed).
- Finally, the cavity length is adjusted to fit the emission wavelength of the nanotube, as shown in figure 5.5.

This process is non-destructive so it is possible to switch back and forth from free-space to cavity configuration as many times as needed.

5.1. COUPLING A TUNABLE CAVITY TO THE CONFOCAL MICROSCOPE

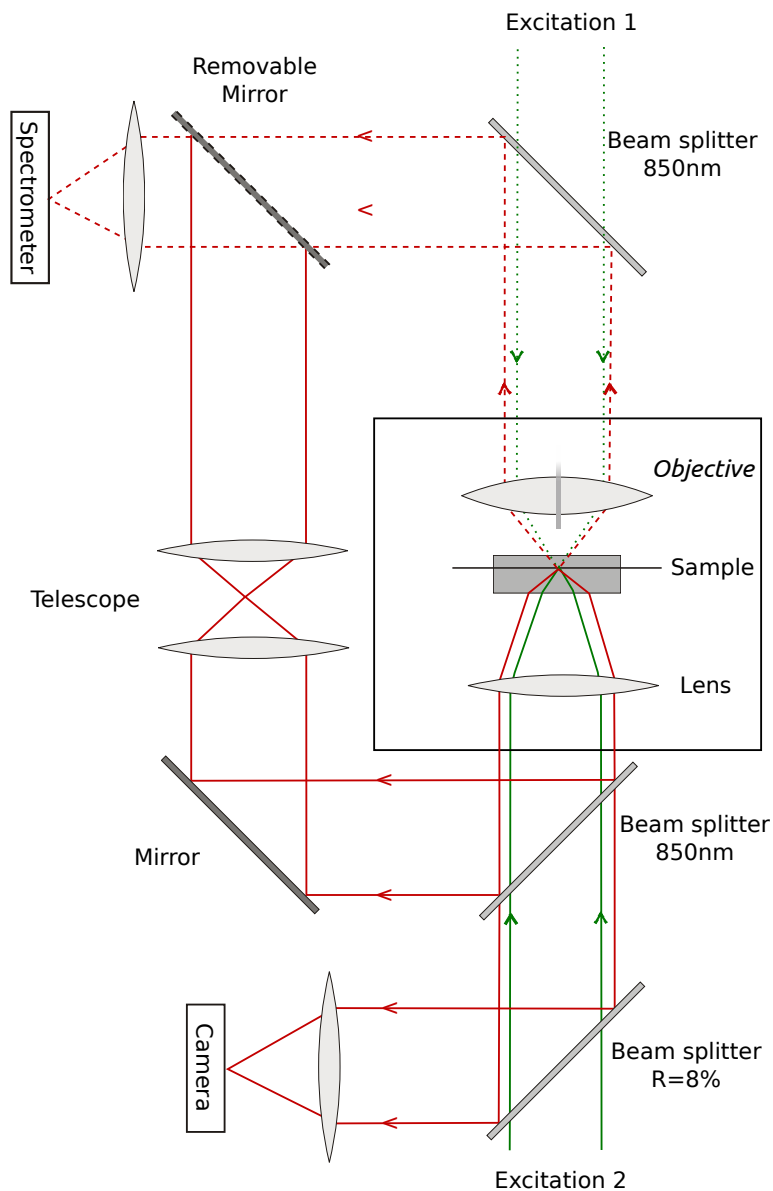


Figure 5.4 – Schema of the complete setup (the steering mirror and the confocal pinhole were not drawn for the sake of simplicity). The excitations paths are depicted in green, the dashed lines corresponds to a usual confocal microscope setup, the solid lines correspond to an excitation through the sample mirror. The collection paths are shown in red lines. The dashed ones corresponds to confocal microscopy while the solid lines correspond to cavity experiments. The switching is done with a removable mirror.

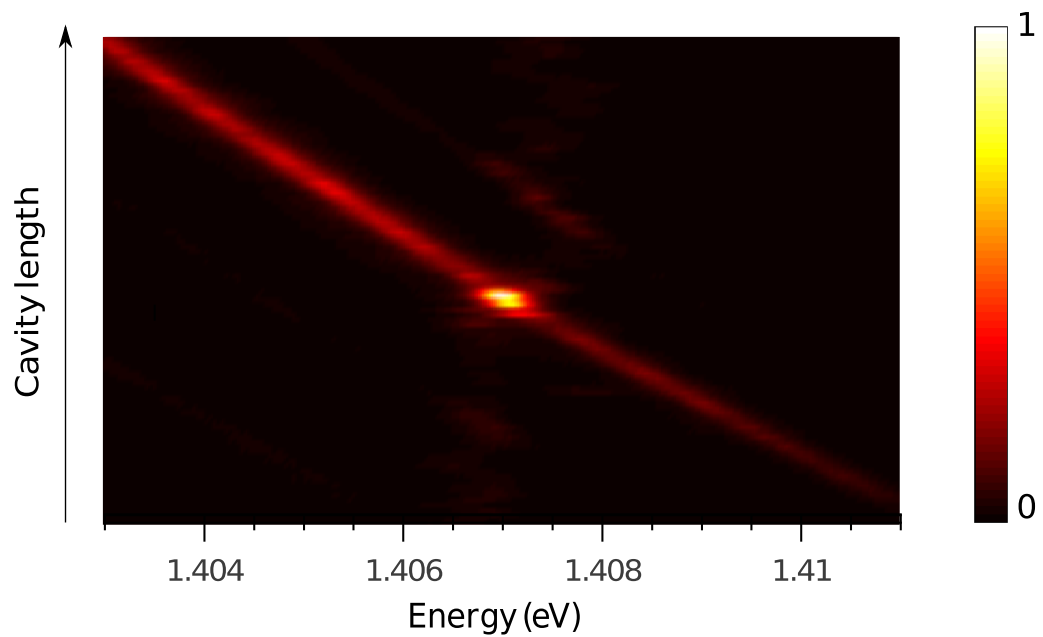


Figure 5.5 – Intensity of the photoluminescence (in colors) of a carbon nanotube embedded in cavity as a function of the emission energy and the cavity length. As the cavity length increases, the cavity modes shift towards low energies. Here the cavity mode is resonant with the CNT around 1.407 eV. Details : (6, 4) nanotube. Excitation : 760 nm, linear polarization (along CNT axis), $P = 0.7 \cdot P_{sat}$. This nanotube is referred to as *Aleph* in further figures.

5.1.2 Lens-Fiber mounting principle

One of the goals of the setup described here was the ability to switch from free-space experiments to cavity experiments, reproducibly, with as few re-alignment as possible. One possibility to couple the *objective* and the fiber was to stick the later on the side of the former. A disadvantage of this method comes from the fact that the lens width (including the mount) is about 6 mm. Then, the lateral shift to switch from cavity to free-space would have been 3 mm, a large distance which would have implied inconvenient drifts.

Thus, a second method was implemented : it consists in drilling the lens in its center to stick the fiber inside, as shown in figure 5.1. This way, a switch from free-space to cavity requires only a longitudinal move and very small lateral corrections. In the following, the drilling process is described and its consequences for confocal microscopy are investigated.

Lens drilling principle

The free-space experiments, as introduced in section 4.1, rely on a lens of numerical aperture 0.68, focal length 3.1 mm, and working distance 1.76 mm which collects the emission of the nano-object.

The hole diameter is about 400 μm , sufficiently large to let the fiber and its coating (diameter 250 μm) pass easily and sufficiently small to be able to stick the fiber once aligned. The first generation of lenses was processed in the mechanical workshop of the department by Nabil Garroum. For that, he used a drill of radius 0.2 mm to remove material by concentric circles. In order to avoid any crack in the lens, or any scratch at its surface, a layer of polymer (PMMA) was deposited before the drilling and removed afterwards. Currently, the drilling is performed by a company³, by means of pressurized air.

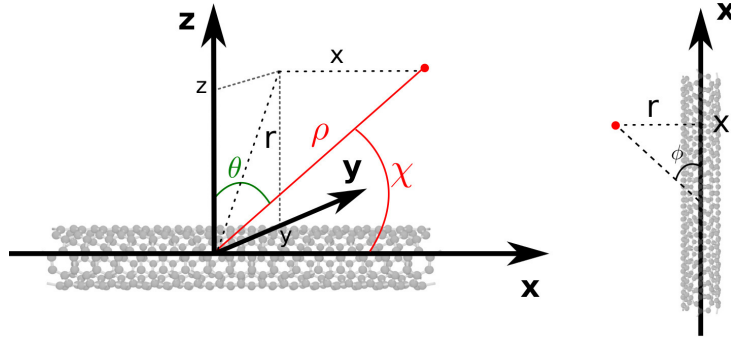
Collection efficiency

The greatest care was taken to measure how the drilling of the *objective* changed its properties for confocal microscopy. In appendix B, the ability of the objective to focus is experimentally assessed. The focalized spot waist is increased by less than 10%, and the resolving power change is estimated to be negligible. This is important important to keep the zone observed in confocal microscopy as low as possible. However, the most important characteristic for the confocal measurement is the collection efficiency, as it directly affects the estimation of the quantum efficiency of the emitter.

Let's consider that the emission of a nanotube is dipolar, so that the intensity I in a direction with angle χ with respect to the nanotube axis writes :

$$I \propto \sin^2(\chi) \tag{5.1}$$

³Precinet


 Figure 5.6 – Sketch of the nanotube emission intensity $I \propto \sin^2(\chi)$.

In Cartesian coordinates (with the nanotube axis along \vec{x} , see figure 5.6), it rewrites :

$$\begin{aligned} I &\propto 1 - \cos^2(\chi) \\ &\propto 1 - \frac{x^2}{r^2 + x^2} \\ &\propto 1 - \frac{x^2}{y^2 + z^2 + x^2} \end{aligned}$$

The spherical coordinates (ρ, θ, ϕ) are given by :

$$\begin{cases} x = \rho \cos(\phi) \sin(\theta) \\ \rho^2 = x^2 + y^2 + z^2 \end{cases} \quad (5.2)$$

One can rewrite the intensity :

$$I(\theta, \phi) \propto 1 - \cos^2(\phi) \sin^2(\theta) \quad (5.3)$$

This leads to the following expression for the intensity integrated over a cone of angle θ_{max} :

$$I_{integrated} \propto \int_0^{2\pi} \int_0^{\theta_{max}} I(\theta, \phi) \sin \theta d\theta d\phi \quad (5.4)$$

Here θ_{max} corresponds to the numerical aperture of the lens : $\theta_{max} = \text{asin}(NA)$. One can take into account the drilling by defining a minimum angle θ_{min} (for a hole radius of 200 μm and a focal length of 3 mm, $\theta_{min} = 4^\circ$) and perform the integration between θ_{min} and θ_{max} . The loss expected for the typical lenses used in this work, compared to the case without drilling, is expected to be below 2% (in good agreement with the experimental data of appendix B). The impact of the lens drilling on confocal

5.1. COUPLING A TUNABLE CAVITY TO THE CONFOCAL MICROSCOPE

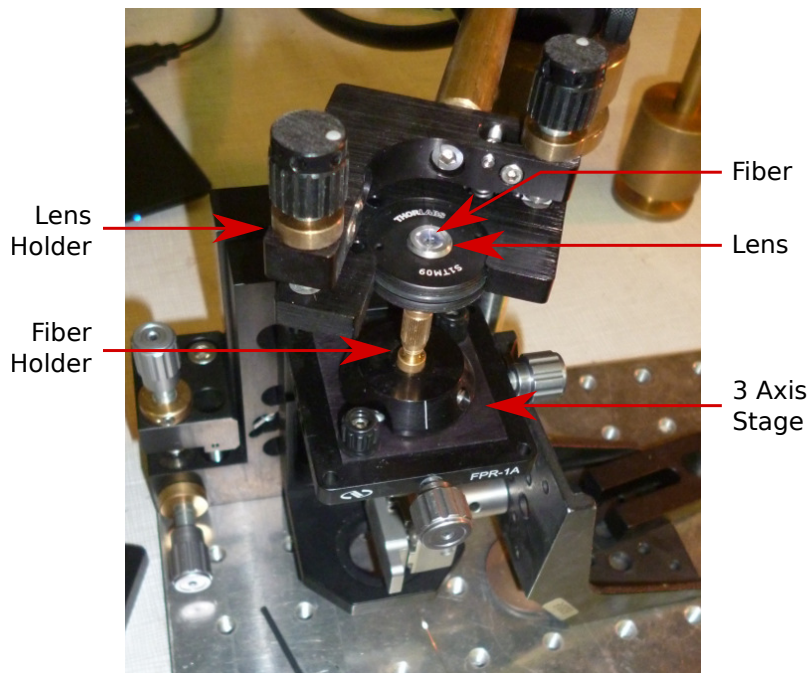


Figure 5.7 – Fiber sticking post.

microscopy is thus considered to be negligible.

Fiber sticking and angle control

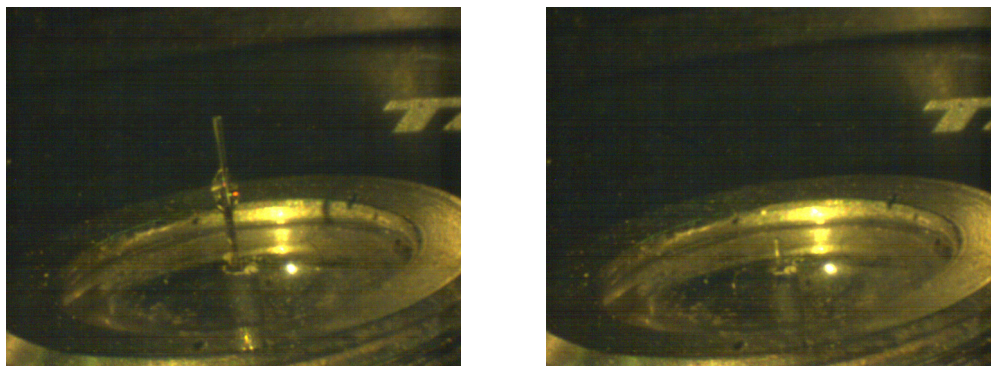
The final goal of the fiber sticking is to enable the creation of a high finesse microcavity with a low volume. The challenges are twofold : first one wants to center the fiber on the optical axis of the lens, so that a simple translation of the ensemble is sufficient to switch between cavity and free-space configuration. Second, the angle made by the fiber with the optical axis of the lens has to be small so that the cavity axis is parallel to it.

After the fiber is shot and a mirror is deposited at its apex, the unprocessed end of the fiber is inserted into the lens. The fiber is then pulled until less than a centimeter protrudes. The fiber is held (by the part below the lens) by a holder mounted on a three axis micrometer stage. It enables to center the fiber precisely and to tune finely how much it protrudes from the lens. See the picture in figure 5.7.

The lens itself is held by a mirror mount which enables to control precisely its orientation, and thereby the angle between the optical axis and the fiber axis.

In order to control the centering and the angle, the position of the fiber is monitored with a long working distance objective either from the top or horizontally in two perpendicular directions. When the fiber position is considered correct, a drop of UV glue⁴ is deposited on the fiber just above the lens, as shown in figure 5.8. Then

⁴OP-4-20641



(a) A drop of glue deposited on the fiber.

(b) Fiber at its final position

Figure 5.8 – Fiber sticking process imaged with a long working distance objective.

by lowering and raising repeatedly the fiber, the glue flows down into the drilled hole. The process is repeated three times to ensure that a sufficient amount of glue is present.

Finally, the fiber is lowered until half a millimeter sticks out, and the lens is exposed to UV during 60 s. The free end of the fiber is spliced to a common acrylate fiber equipped with a connector to facilitate further operations.

5.2 Measuring the Purcell Factor

In chapter 1 the Purcell factor was introduced for an atom as well as the generalized Purcell factor which applies for a broad emitter. This factor accounts for the increase in the spontaneous emission rate of the emitter when it is coupled to a cavity. As a carbon nanotube has a low quantum yield (see section 5.2.3), an increase in the radiative rate directly translates into an equivalent increase of the brightness, even for an excitation intensity below the saturation limit.

In an experimentalist point of view, an obvious measurement of this factor consists in comparing the photon counts with and without the cavity. This method is discussed as well as its drawback. Then, an other way to measure the Purcell factor, relying on a direct measurement of the lifetime, is given.

5.2.1 Photon counts method

In order to characterize the increase in the emission rate due to the Purcell effect, one can count the number of photons per second emitted in free-space, and compare it to the number of photons emitted per second by the same nanotube once embedded in the cavity. Nevertheless, one has to take into account the fact that part of the increase is due to the better directionality of the emission in the cavity mode. For this reason, the emission diagrams were investigated both in free-space and in cavity.

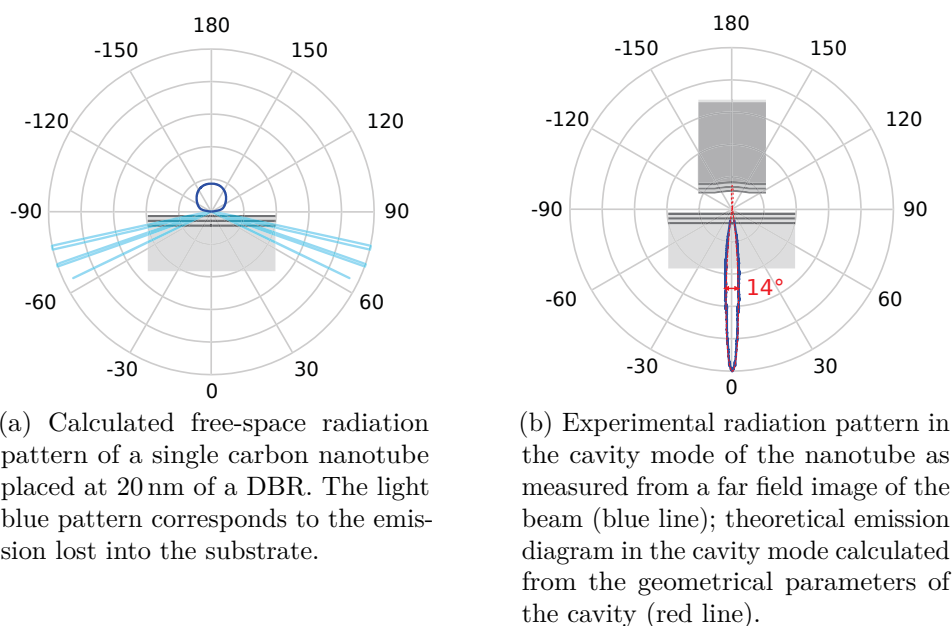


Figure 5.9 – Emission diagrams of a nanotube (a) in free-space and (b) in the cavity mode. The diagrams are normalized to the integrated emission.

All the results presented in this section were taken with fiber A, as defined in section 3.2.2.

Emission diagram

In the setup used in this study, the carbon nanotube is embedded in a polymer matrix with a typical thickness of 120 nm and deposited at the surface of a Distributed Bragg Reflector (DBR), as described in section 2.3.3. The emission diagram is thus affected by the mirror. As the structure of the DBR is known (see section 3.2.2), the emission of a dipole antenna located 20 nm above its surface can be computed [198]. The result is shown in figure 5.9a.

One can note that a part (about 60%) of the emission is directed in the half-space above the mirror (dark blue line) but an other part (about 40%) leaks into the substrate and is lost (light blue). Concerning the emission into the upper half-space, the collection is limited by the numerical aperture of the collection lens. The one used for confocal microscopy has a numerical aperture $NA = 0.68$ (details in section 4.1). From the computed emission diagram, it is estimated that around 21% of the nanotube emission in free-space is collected. This value, and its uncertainty, are discussed with more details in the next section.

Let's examine the emission diagram of a nanotube in cavity. It is useful here to recall that asymmetrical mirrors are used so that the output is mostly directed through the planar mirror (section 3.3.2). Theoretically, the output of the cavity

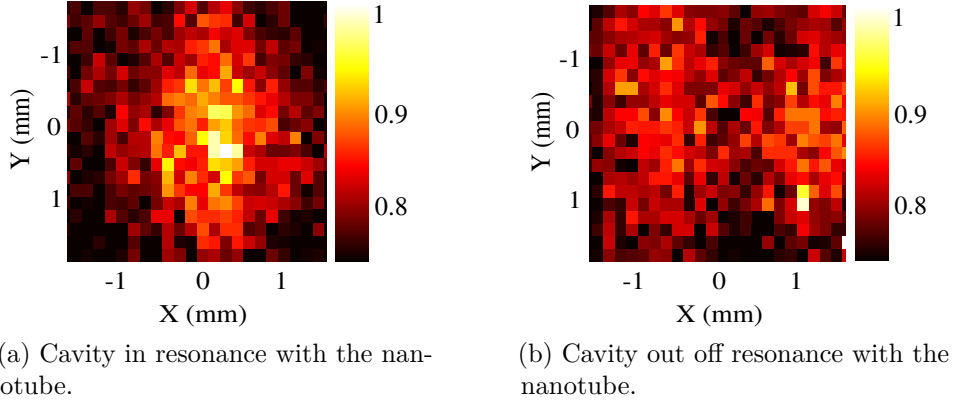


Figure 5.10 – A transverse section of the optical beam coming from the planar output of the cavity. Details : (9, 1) nanotube. Excitation : cw, 760 nm, linear polarization (along CNT axis), $P = 0.7 \cdot P_{sat}$. Collection with a multimode optical fiber and a 10 nm bandpass filter centered on nanotube emission wavelength (902 nm).

can be approximated by a cone of half-angle θ_{out} , given by :

$$\theta_{out} = \frac{\lambda}{\pi w_0} \quad (5.5)$$

where λ is the wavelength of the emission and w_0 is the waist of the mode, defined by the geometrical parameters of the cavity (eq. (3.11)). Typically for the cavities used in this work, the waist spans between 1 μm and 2.5 μm , which means that the output angle is in the range $7^\circ < \theta_{out} < 16^\circ$.

The emission in the cavity configuration is collected with an aspherical lens of numerical aperture $NA = 0.5$ located 12.5 mm behind the emitter. In order to check that the cavity behaves as expected, a far field image of its output beam was recorded. For that, a multimode fiber with a core of 105 μm , was used to record the intensity profile of the output beam. This fiber was located on two micro-controlled translation stages that were used to raster-scan the transverse section of the beam. At each point, the intensity collected by the fiber was measured with an avalanche photodiode⁵.

Even with the cavity enhancement of the emission, such a measure is a challenge regarding the signal-to-noise ratio. In order to make sure that the signal collected actually arose from a carbon nanotube and not from the scattering of the excitation laser, the measurement was systematically repeated with the cavity tuned out of resonance of a few nm. The corresponding maps are shown in figure 5.10.

The same measurement was repeated in two planes along the beam axis, separated by 1 m, to estimate the beam divergence. The waist of the beam was found to be $w_0 = 1.5 \pm 2 \text{ mm}$ at both positions (collimated beam). For a point-source like

⁵IDQ100

emitter located at the focal point of a lens of focal $f = 12.5$ mm, this corresponds to a half-angle $\theta = \text{atan}(w_0/f) = 7^\circ$. This fitted well with the theoretical prediction for the cavity in use (radius of curvature $\mathcal{R} = 50$ μm and cavity length of 3.5 μm). The calculated cavity mode waist was 2.3 μm leading to a theoretical divergence half-angle $\theta_{out} = 7.1^\circ$.

Collection efficiency

The collection efficiencies of the setup both in free-space and cavity are given below. For each optical element, the transmission was measured carefully and regularly throughout the duration of this work.

These measurements were done with a power-meter, measuring at 900 nm (the mean wavelength of the nanotubes under study). It consisted in measuring the intensity of the light shone on the optical elements and the intensity transmitted (or reflected in the case of dichroic mirrors)⁶. The numbers given in table 5.1 are averages, and the error bars correspond to the standard deviation over all measurements. Let's recall that the full sketch of the experiment is given in figure 5.4.

Free-space In free-space, it was established in section 5.2.1 that the collection of the objective is 0.21 of the light emitted by a carbon nanotube. In fact, a strong source of uncertainty in the detection efficiency comes from the distance between the nanotube and the surface of the DBR, which is not controlled in the deposition process : the nanotubes are randomly dispersed⁷ between the surface of the mirror and the thickness of the polystyrene layer. In order to evaluate the uncertainty, the collection efficiency is computed as a function of the distance between the DBR surface and the nanotube. As one can see in figure 5.11, the efficiency increases almost linearly with the distance between a vanishing distance (0.1) and 120 nm (the thickness of this layer, 0.31).

In the experiments carried out during this work, the brightest nanotubes were always selected. This means that the nanotubes studied were most likely in the positions where the collection efficiency is above 0.21 (average position). The real collection efficiency is thus 0.25 ± 0.06 . However, we chose to retain the minimum value, 0.21, as the collection efficiency in order to give the most conservative estimations of the Purcell factor (the collection efficiency is underestimated, which leads to an over estimate of the free-space photon emission and thus to an underestimation of the Purcell factor).

Once the emission of the carbon nanotube is collected by the lens, it passes through the window of the cryostat with a transmission of 0.95 ± 0.02 . Then the light

⁶As often as possible, the transmission of several elements together was measured in order to decrease the relative uncertainty. However, for practical reasons it remains more convenient to separate the setup into the few sub-parts outlined in table 5.1 than to measure the transmission of the full setup at a time.

⁷A way to improve it would be the use of a second polymer not solvable in toluene as a spacer, and then the addition of a very thin layer of nanotubes in polystyrene at the desired height.

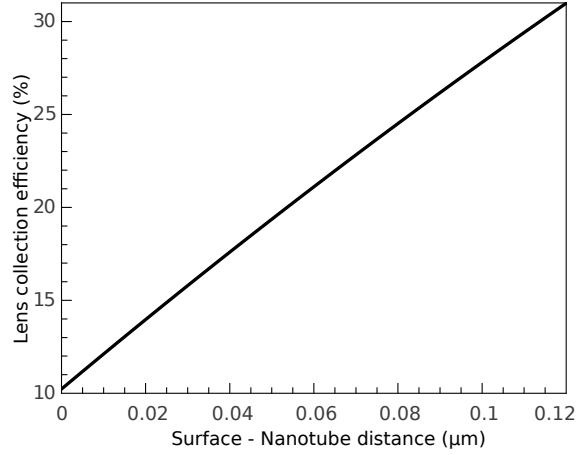


Figure 5.11 – Calculation of the collection efficiency of the aspherical lens used in the confocal microscope setup as a function of the distance between the nanotube and the top of the DBR.

Transmission / yield	Free-space configuration	Cavity configuration
Extraction $\beta_e = F_p/(1 + F_p)$		0.83 – 0.99
Cavity asymmetry		0.88 ± 0.02
Collection lens	0.21 ± 0.06	0.97 ± 0.01
Cryostat window	0.95 ± 0.02	0.95 ± 0.02
Telecentric lens system	0.70 ± 0.08	
Dichroic mirror	0.97 ± 0.01	0.97 ± 0.01
Other optical parts (total)	0.55 ± 0.05	0.55 ± 0.05
Spectrometer efficiency	0.50 ± 0.05	0.50 ± 0.05
Total efficiency ($\beta_e = 1$)	0.037 ± 0.015	0.21 ± 0.03

Table 5.1 – Transmission or yield of all optical parts in the setup. The first lines are derived from the parameters of the experiment. All the following ones come from repeated measurements and the uncertainty given comes from the standard deviation of these measurements. As explained in the text, many optics are similar or shared between cavity and free-space configurations.

passes by the telecentric lens system designed for the steering mirror (section 4.1.1) with a transmission of 0.70 ± 0.08 . The dichroic mirror which separates the emission from the excitation reflects 0.97 ± 0.01 of the light at 900 nm. The set of mirrors that precedes the spectrometer transmits 0.55 ± 0.05 of the light.

In order to evaluate the efficiency of the spectrometer, a light beam at 900 nm was shone on its entrance slit. An intensity of 4.5 ± 5 nW was measured with a power-meter. After the addition of an optical density of 4.5 ± 0.2 , the number of counts recorded by the spectrometer was 33000 ± 200 . By repeating this measurement several times, the efficiency of the spectrometer was evaluated to 0.50 ± 0.05 .

Cavity The mirrors of the cavity have asymmetric reflectivities, so that 0.88 ± 0.02 of the signal goes out through the planar mirror. The output mode of the cavity has an angular aperture sufficiently low to be entirely collected by the lens inside the cryostat. The transmission of that lens is estimated to 0.97 ± 0.01 . The cryostat window and the dichroic mirror used are similar to ones used for the free-space path. The optics between the dichroic mirror and the spectrometer, as well as the spectrometer itself are the same as in free-space.

Finally, one obtains a total efficiency of $\epsilon_{FS} = 0.037 \pm 0.015$ in free-space configuration against $\epsilon_{cav} = 0.21 \pm 0.03$ in cavity configuration. This difference arises mostly from the difference in the emission diagrams and the better ability to collect the very directional light coming out of the cavity. In the same way, the relative uncertainty in free-space (50%) is much higher than in cavity (15%) because of the uncertainty on the free-space emission collection by the confocal lens.

Results and discussion

In the previous paragraphs, it was concluded that the collection efficiency of the setup is about six times better for an emission in cavity than in free-space. Consequently, a natural way to evaluate the Purcell factor consists in comparing the intensity collected in the cavity mode with respect to the intensity collected in free-space, after correction for the collection efficiencies.

Nevertheless, the emission intensities in both configurations do not compare readily : in the free-space case, the emission spans over a bandwidth of several meV (ZPL and phonon wings). Whereas in the cavity mode, the emission is spectrally narrow, as defined by the cavity's spectral width (about 33 μ eV or 8 GHz). In fact, the cavity vibrates at high frequency (in the kilohertz range, which means faster than the typical exposure time of the measurements carried out), as stated in section 3.4.2. Thus, the emission in the cavity mode on a time scale over 100 ms rather spans over a 330 ± 20 μ eV or 80 ± 5 GHz spectral range.

The question which arises for an emitter larger than the cavity is the following : is there a Purcell effect (meaning that the spontaneous emission rate of the CNT is enhanced) or is there only a spectral filtering by the cavity ? In order to answer this question, comparing the integrated intensities does not yield a straightforward

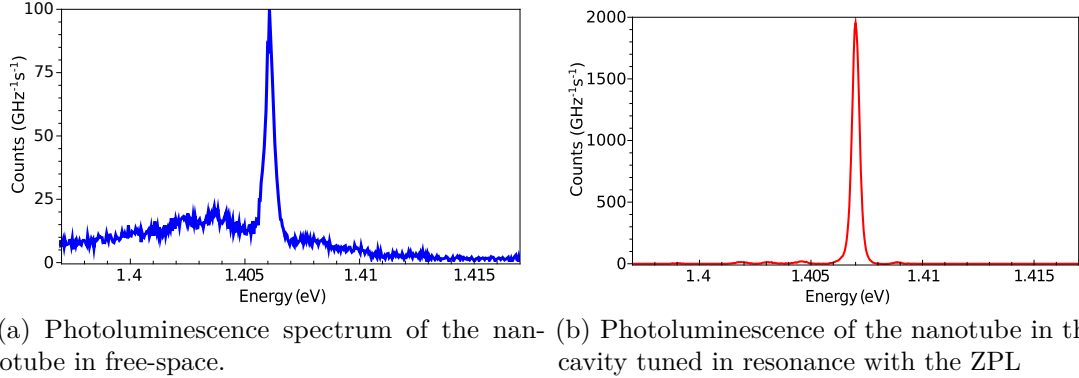


Figure 5.12 – Photoluminescence of the same single CNT given in photons \cdot GHz $^{-1}$ s $^{-1}$. Nanotube *Aleph*, see details in fig. 5.5.

answer if the Purcell factor is not significantly higher than one. The proper way to address this question is to compare photon spectral densities [138].

In figure 5.12, the photoluminescence spectrum of a single carbon nanotube is expressed in photons \cdot GHz $^{-1}$ s $^{-1}$ for the free-space and the cavity mode. One can clearly see that the photon density at the maximum is enhanced by a factor of 20^8 . Once the six-fold better collection in cavity is taken into account, it yields a photon density enhancement of 3 ± 2 . It can be concluded from this measurements that the Purcell factor for this nanotube in this cavity is 3 ± 2 . The vibrations of the cavity may lead to an underestimate of the Purcell factor, as discussed in appendix C.

In order to ensure that this increase is not due to an experimental artifact, we checked a specific signature of the Purcell effect : its volume dependence. Every increase of the cavity length by a $\lambda/2$ step implies a significant change in the cavity volume and consequently in the Purcell factor (eq. (1.62) shows that $F_p^* \propto 1/V$).

For this measurement, the excitation density must be controlled with the utmost care. Indeed, the data of figure 5.12 are taken with the continuous-wave excitation source described in section 4.1.2 (used non-resonantly). At the excitation wavelength $\lambda_{ex} = 760$ nm, the mirrors of the cavity have a low reflectivity. Nevertheless, even a cavity formed by mirrors with a low reflectivity, can create a significant change in the local intensity (typically a contrast of 2 between maximum and minimum local intensities for a symmetrical reflectivity as low as 4%). As emission and excitation are not at the same wavelength, a step of $\lambda/2$ for the emission does not correspond to step of $\lambda_{ex}/2$ for the excitation. Thus, with every change in the cavity length, there is a change in the excitation intensity. And, as the excitation is done below the saturation limit, a change in the excitation intensity linearly impacts the number of

⁸The two signals can be fitted to Lorentzian of spectral width 300 ± 5 μ eV in free-space and 330 ± 5 μ eV for this particular cavity spectrum. For Lorentzian distributions, the ratio of the integrated value to the peak value is proportional to the FWHM. As a consequence, the enhancement factor defined by the integrated value is 10% higher than the one defined on the maximum value in this case.

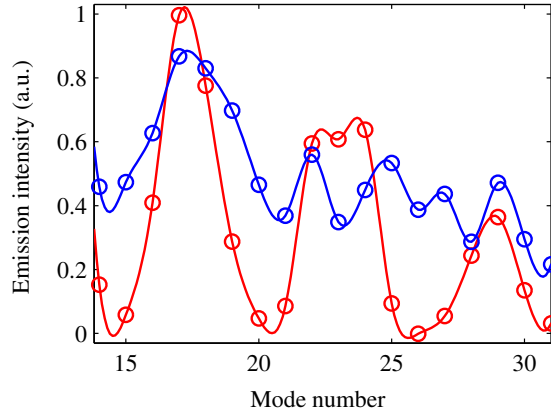


Figure 5.13 – Emission intensity of a (9, 1) nanotube as a function of the cavity’s mode number for an excitation centered at 760 nm, linearly polarized along the nanotube axis, $P = 0.7 \cdot P_{sat}$. In red the excitation spectral width is 50 kHz, while in blue it amounts to 10 nm (4 THz). The dots correspond to experimental data while the lines are a guide to the eye.

photons emitted and thus the estimation of the Purcell factor.

In figure 5.13, the red curve shows the nanotube’s emission intensity as a function of the cavity’s mode number under continuous wave excitation (spectral width of 50 kHz). One can clearly see oscillations coming from the change in the excitation intensity. Furthermore, the envelope decreases slowly, in a pattern which fits well with the expected $1/V$ dependence.

In order to address this artifact, it was decided to use a broad excitation to blur the interferences. The source used was a supercontinuum⁹ with a repetition rate of 40 MHz and an emission spanning from the UV to the infrared. A set of filters enabled to choose the excitation spectral width, while keeping its mean around 760 nm. The blue curve in figure 5.13 shows the emission intensity of the same nanotube, under supercontinuum excitation with a width of 10 nm (4 THz). A diminution of the oscillations compared to the red case is visible.

Increasing further the spectral width of the excitation yielded a complete suppression of the oscillations. Figure 5.14 presents the emission intensity of a single carbon nanotube as a function of the volume of the cavity for such an excitation. The cavity is swept back and forth twice in order to make sure that the effect is not due to a drift over time. The oscillations are almost invisible, and the dependence in $1/V$ is clearly visible.

One may ascribe this feature to a misalignment artifact. Indeed, if the fiber axis and the *objective* optical axis are misaligned, it implies that a change in the cavity length also changes the lateral position of the cavity. However, a length change of $10\lambda/2 = 4.5 \mu\text{m}$, for an angle of 5° , would lead to a shift of $0.4 \mu\text{m}$, only 20% of the

⁹Fianium WL-SC-400-4

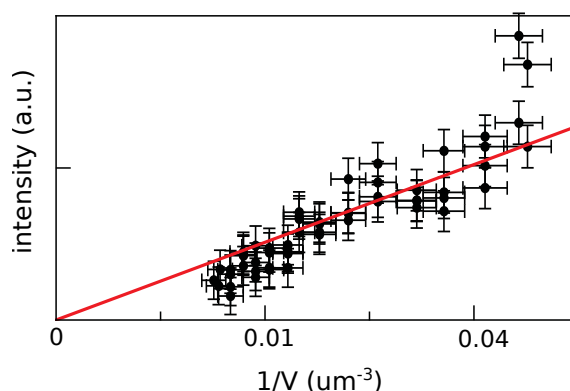


Figure 5.14 – Photoluminescence of a single (9, 1) CNT in the cavity as a function of the mode volume when the cavity length is increased by steps of $\lambda/2$. The cavity is swept back and forth twice to eliminate any artifact. The excitation is done with a supercontinuum and a spectral width of 30 nm centered on 760 nm, linearly polarized along the nanotube axis and below the $P = 0.7 \cdot P_{sat}$.

mode waist. Due to this shift the position of the emitter with respect to the cavity mode maximum of intensity would change, leading to a Gaussian decrease in the intensity. The linear behavior shown in fig. 5.14 shows that this misalignment effect is negligible compared to the change of volume.

Let's note a posteriori that the excitation density effect had been taken into account for measurements such as the one of figure 5.13. In this particular case, the cavity length was such that the intensity for a 760 nm continuous wave excitation was 1.05 ± 0.1 higher than in free-space.

The linear dependence in $1/V$ strongly supports the description of the nanotube-cavity coupling in terms of Purcell effect. From the evaluation of the collection intensities, one can estimate that the Purcell factor is about 3. Nevertheless, this result suffers from a large uncertainty coming mostly from two points : the calibration of the interference effects of the cavity on the excitation and the estimated emission diagram in free-space. Even if the first source of error was perfectly taken care of, the error would still amount to 30%. In order to get a better accuracy for the quantitative value of the Purcell factor, it was decided to obtain a direct insight into the Purcell effect by investigating in the time domain.

5.2.2 Time domain method

The method presented here consists in measuring directly the radiative rate of the emitter via time-resolved photoluminescence [36]. It presents several assets : first the measurements are weakly sensitive to the excitation density and thus do not suffer from the distortion of the excitation by the cavity. Second, the collection efficiency becomes a simple proportionality factor and can be let aside if the effect is expressed in term of the coupling g .

Principle

Let's recall that a single carbon nanotube, at least in free-space, has a quantum yield well below 10%. In other words, if an excitation is absorbed, there is a high probability that it decays non-radiatively, with a decay rate γ_{NR} . And there is a much smaller probability for it to decay radiatively, with a rate γ_R . The total decay rate of the emitter in the free-space γ_{FS} reads :

$$\gamma_{FS} = \gamma_R + \gamma_{NR} \quad (5.6)$$

The quantum yield of the emitter η is the ratio of the radiative rate to the total decay rate :

$$\eta = \frac{\gamma_R}{\gamma_R + \gamma_{NR}} \quad (5.7)$$

Now, one can consider what happens if the emitter is placed into a cavity. In the case of plasmonics, a metallic antenna is placed in the vicinity of the emitter and the non-radiative rate increases when the distance reduces, leading eventually to a drop in the quantum efficiency [67]. On the contrary here, the non-radiative rate of the emitter remains unchanged by the cavity¹⁰ and every increase in the radiative rate directly increases the quantum yield.

Experimentally, the coupling of an emitter to a cavity can induce a suppression of the spontaneous emission [199]. On the contrary here, the probability to emit into the leaky modes (ie : those not confined by the cavity) γ_R is nearly equal to its value in free-space. As a matter of fact, the solid angle encompassed by the cavity is small [46]). For a cavity of length $5 \mu\text{m}$ and a waist $2 \mu\text{m}$ (fiber A), one can consider that a cone of half angle 22° is obstructed by the cavity, which means about 8% of the half-space. For a cavity of length $2.5 \mu\text{m}$ and waist $1 \mu\text{m}$ (fiber C), the result is the same. The probability to emit inside the cavity mode is given by the (generalized) Purcell factor F_p^* multiplied by the radiative rate (by definition). Consequently, everything happens as if the radiative rate was multiplied by $1 + F_p^*$:

$$\text{FS} \longrightarrow \text{Cavity} \quad (5.8)$$

$$\gamma_R \longrightarrow \gamma_R \cdot (1 + F_p^*) \quad (5.9)$$

Finally, the decay rate of the emitter in the cavity γ_{cav} is given by :

$$\gamma_{cav} = \gamma_R(1 + F_p^*) + \gamma_{NR} \quad (5.10)$$

From this equation, one can already infer an important piece of information : the Purcell effect only modifies the radiative rate of the emitter. Since $\gamma_R \ll \gamma_{NR}$, the change in the decay rates introduced by the cavity is expected to be small.

¹⁰The distance between the emitter and the top mirror remains much larger than in plasmonic resonators and dielectric materials do not have Joule losses.

Let's introduce the lifetimes of the emitter in the free-space τ_{FS} and in the cavity τ_{cav} :

$$\tau_{FS} = \frac{1}{\gamma_{FS}} \quad (5.11)$$

$$\tau_{cav} = \frac{1}{\gamma_{cav}} \quad (5.12)$$

The Purcell factor can be expressed as [200] :

$$F_p^* = \frac{\gamma_{cav} - \gamma_{FS}}{\gamma_R} \quad (5.13)$$

$$= \frac{1}{\eta} \left(\frac{\gamma_{cav}}{\gamma_{FS}} - 1 \right) \quad (5.14)$$

$$= \frac{1}{\eta} \left(\frac{\tau_{FS}}{\tau_{cav}} - 1 \right) \quad (5.15)$$

Where η is the free-space quantum yield defined in eq. (5.7). One must note that the generalized Purcell factor, in equation 1.62, was derived for a broad emitter which remains Lorentzian. It applies only to the ZPL of the spectrum. Consequently, the efficiency η is restricted to the ZPL¹¹. The ratio of intensities between the ZPL and the full spectrum is called Branching Ratio BR (section 4.2.1) and typically ranges between 0.3 and 0.9. Consequently, the link between the efficiency η and the total efficiency η_{tot} including the phonon wings is given by (all the quantities being defined in free-space) :

$$\eta = BR \cdot \eta_{tot} \quad (5.16)$$

In order to measure the Purcell factor, one needs only three quantities : the lifetimes (or radiative rates) of the emitter in free-space and in cavity as well as the quantum yield of the emitter.

Lifetime measurements

In order to measure the lifetime, a pulsed source is used to excite the nano-object and the delay between the excitation and the subsequent spontaneous emission event is recorded. The sequence is repeated and a histogram of the delays is built.

In order to perform this experiment a start-stop counter¹², with a resolution of 4ps, is used. The start channel monitors a TTL signal coming from the laser and indicating the repetition rate. The stop channel is linked to an APD which counts the arrival of the photons emitted by the carbon nanotube, as depicted in figure 5.15.

¹¹In other words, the emission in the wings is regarded as leaks for the equivalent two-level system describing the ZPL [200]

¹²Picoharp 300

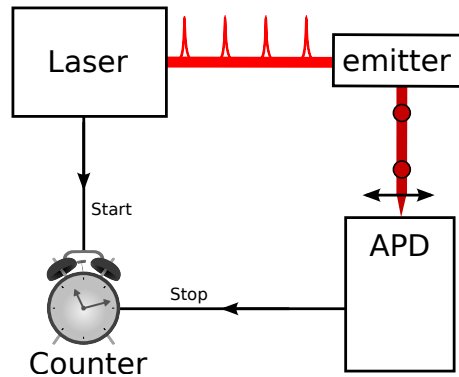


Figure 5.15 – Schema of the lifetime measurement setup.

Obviously, the excitation impulsion which triggers the “start” of the counter is not the same as the one leading to the emission of the photon detected on the stop channel. But, as the excitation is periodic, the delay between the excitation and the detection can be mapped onto a fraction of the period between two excitations (here $\tau_R = 12.5$ ns).

Instrumental response

The histogram gives the probability distribution of the decay from the excited state. In the simplest case, this decay is a mono-exponential which characteristic time is the lifetime τ_1 of the emitter.

The measurement works out easily if the lifetime τ_1 is much higher than the typical response time of detection system. In our case, the counter has an accuracy of 4 ps, which is negligible compared to the typical lifetime of the nanotubes. But the APD used in this experiment¹³ has typical response time $\tau_D \sim 40$ ps which limits the global resolution of the system.

In order to measure the so called instrumental response function (IRF) of the system, attenuated laser pulses are sent directly on the detector and the corresponding histogram is built¹⁴. One can clearly see in figure 5.16 that the instrumental response is far from a Dirac delta. The characteristic decrease time found by a mono-exponential fit is 40 ± 5 ps.

The histograms measured with such a setup display a convolution of the IRF with the intrinsic decay. A deconvolution process is thus necessary to obtain an estimate of the intrinsic decay time, as explained in detail in section 5.2.3.

Effect of the optical path

In the experiments conducted during this work, the lifetime of a carbon nanotube in free-space is compared to its lifetime in cavity. In order to ensure that the

¹³IDQ100

¹⁴It is noteworthy that the jitter of the laser is taken into account in this IRF measurement.

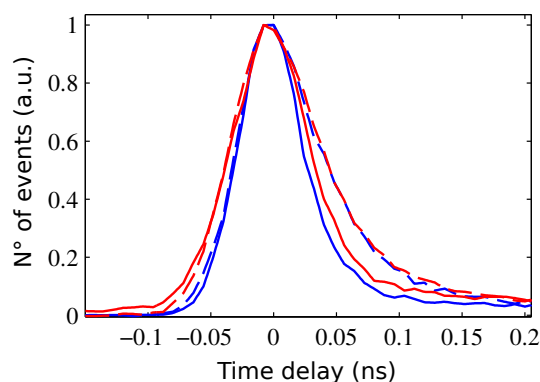


Figure 5.16 – Instrumental response. In blue at 800 nm, in red at 860 nm. The solid line corresponds to a coupling through a single mode fiber while the dashed line corresponds to a coupling through a multimode one.

measurement reflects the intrinsic difference between these two quantities one must control that no elements in the setup can warp the excitation pulse or induce a delay in the photon detection.

The excitation is done with a pulsed Ti:Sa and remains identical for time-domain studies in free-space and in cavity, as explained in 4.1.2. The effect of the cavity itself is called photon storage. It is systematically measured and the details are given in paragraph 5.2.3.

Finally the detection path is almost identical, as described in 5.1.1. One must note, that contrarily to the schema on figure 5.4, for time domain experiments, the output of the cavity is not injected into a spectrometer but into a fiber, which is directly connected to the APD.

A photon passing through a fiber undergoes a delay which depends on its reflexion angle inside the fiber (in ray optics description). This means that a random delay is added to the photons passing through. In the case of single-mode fibers, this delay depends directly on the fiber's core size. In terms of guided modes, this corresponds to the modal group velocity dispersion and is of course much lower for a single-mode fiber. However, as one can see in figure 5.16, the effect of multi-mode fibers on the IRF amounts to only 10 ps and flattens the variations with the input wavelength. This led us to give priority to the ease of coupling and to use multimode fibers¹⁵ (with a core of 50 μm). For all the lifetime measurements performed during this work, the same counter, the same APD, and the same fiber were used to ensure that no distortion could come from these elements. The effect of all these elements, included the group velocity dispersion of the fiber, are taken into account in the measured IRF.

¹⁵Thorlabs M43L05

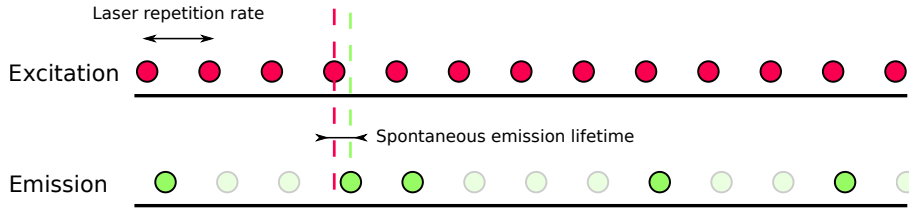


Figure 5.17 – Schematic view of the nanotube’s efficiency (when excited at its saturation level). In red, the pumping pulses (promoting the NT in its excited state), separated by the repetition rate of the laser ($\tau_R = 12.5 \text{ ns}$). In green, the nanotube relaxes after a time given by its spontaneous emission lifetime ($\tau_{FS} \ll \tau_R$). This relaxation can be either radiative (plain green) or most likely non-radiative (faint green)

5.2.3 Experimental Results

In this section, the emitter’s quantum efficiency is investigated and the experimental results for the time-domain measurement of the Purcell factor are given.

Radiative yield measurement

In section 4.2.1, it was explained that the emission in CNTs probably arises from a single localized exciton. In order to measure the radiative yield of this effective two-level system, the PL intensity is measured as a function of the excitation power under pulsed excitation.

Due to Auger processes, each excitation pulse leads to the existence of either zero or one exciton in the system. When the excitation intensity is increased up to the saturation level, one (and only one) excitation is in the system. The corresponding energy can either relax radiatively or non-radiatively, as depicted in figure 5.17. Consequently, the quantum yield at saturation is given by the number of photons N_{em} emitted divided by the repetition frequency f_{rep} of the excitation laser :

$$\eta = \frac{N_{em}}{f_{rep}} \quad (5.17)$$

As the collection efficiency ϵ_{FS} was calibrated in paragraph 5.2.1, the quantum yield can be retrieved from the count rate at saturation¹⁶ :

$$\eta = \frac{\text{count rate}}{f_{rep}} \cdot \frac{1}{\epsilon_{FS}} \quad (5.18)$$

The saturation measurement of the nanotube *Aleph* already investigated in figure 5.12 is given in figure 5.18. One can clearly see an increase in the count rate when the excitation intensity is increased, until it reaches the saturation plateau.

¹⁶Let’s recall that the count rate is taken as the integral of the ZPL, as stated in equation (5.16).

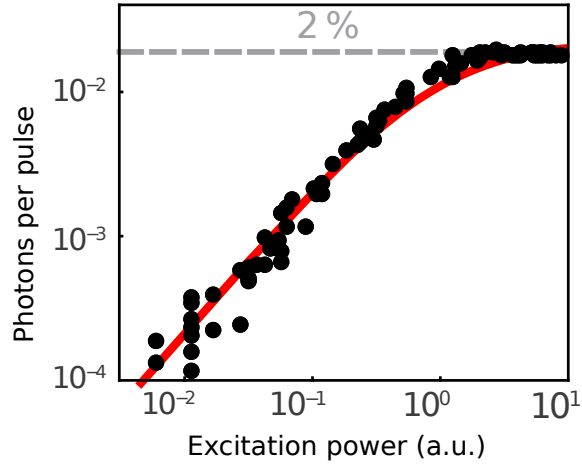


Figure 5.18 – Saturation measurement of a single CNT. The number of photons per pulse takes into account the collection efficiency (photons per pulse = count rate $\cdot \frac{1}{\epsilon_{FS}}$). The black dots correspond to experimental points while the solid red curve corresponds to the saturation model for a two-level emitter as described in the text. The saturation plateau is depicted by a dashed gray line and the saturation value, 2% is indicated. Nanotube *Aleph*, see details in fig. 5.5.

The intensity I as a function of the excitation power P is fitted to the following function :

$$I = I_0 \frac{P/P_{sat}}{1 + P/P_{sat}} \quad (5.19)$$

This function is typical of the saturation of a two-level system¹⁷. The parameter I_0 introduced here gives the count rate saturation level. The quantum yield η is obtained by dividing this count rate by the collection efficiency ϵ_{FS} . Here the excitation laser used is the one described in section 4.1.2, with a repetition rate of 80 MHz. The radiative yield for this particular nanotube is estimated to $2 \pm 0.5\%$, where the uncertainty arises from the evaluation of the collection efficiency.

During this work, the radiative yields of tens of single CNTs were measured. We found values comprised between 1% and 5%, with an average of 2.5%. These values are consistent with previous estimations [41].

¹⁷For some nanotubes the saturation does not follow this law : either the plateau is much sharper, or sometimes one can observe a slight decrease in the count rate above a certain threshold. But in every case, a maximum plateau is easily defined and is taken as the saturation limit to estimate η .

Transient measurements

In order to retrieve the Purcell factor, one needs to measure the lifetime both in free-space and in cavity. The lifetimes can be obtained by time-resolved photoluminescence with the setup described in section 5.2.2 : a single CNT is excited with a pulsed source and a histogram of the delay between the excitation and the collection of a photon is built.

In free-space, once an excitation is created, there is a probability η to emit a photon with a characteristic time τ_{FS} . This photon is detected through a collection path containing in particular a multimode fiber and an Avalanche Photodiode (APD). Consequently, the transient of the nanotube in the free-space $S_{NT,FS}$ is a convolution of its intrinsic response $R_{NT,FS}(t)$ and the instrumental response $R_{inst}(t)$ (already introduced in section 5.2.2) :

$$S_{NT,FS}(t) = (R_{NT,FS} * R_{inst})(t) \quad (5.20)$$

It must be emphasized that the typical lifetime of the CNTs used in this work is 100 ps while the instrumental response characteristic time is around 40 ps. The later is thus non-negligible and a careful deconvolution is necessary to retrieve τ_{FS} .

In the cavity, the transient signal $S_{NT,cav}(t)$ is slightly more complex because the photon emitted by the nanotube is stored into the cavity during a typical time τ_{stor} , as explained in section 3.4.2. The transient of an empty cavity $S_{cav}(t)$ is a convolution between the response of the cavity $R_{cav}(t)$ (driven by τ_{stor}) and the instrumental response :

$$S_{cav}(t) = (R_{cav} * R_{inst})(t) \quad (5.21)$$

And the transient of a carbon nanotube in the cavity is a convolution of the transient of the empty cavity with the response of the nanotube itself $R_{NT,cav}(t)$ (driven by τ_{cav}) :

$$S_{NT,cav}(t) = (R_{NT,cav} * S_{cav})(t) \quad (5.22)$$

$$= (R_{NT,cav} * R_{cav} * R_{inst})(t) \quad (5.23)$$

In order to get the lifetimes, four measurements are performed at the CNT emission wavelength, using the same pulsed laser for the excitation (section 4.1.2) :

1. The instrumental response $R_{inst}(t)$, measured by shining directly the attenuated excitation laser on the detection system.
2. The CNT free-space transient $S_{NT,FS}(t)$.
3. The CNT cavity transient $S_{NT,cav}(t)$.
4. And the empty cavity transient $S_{cav}(t)$.

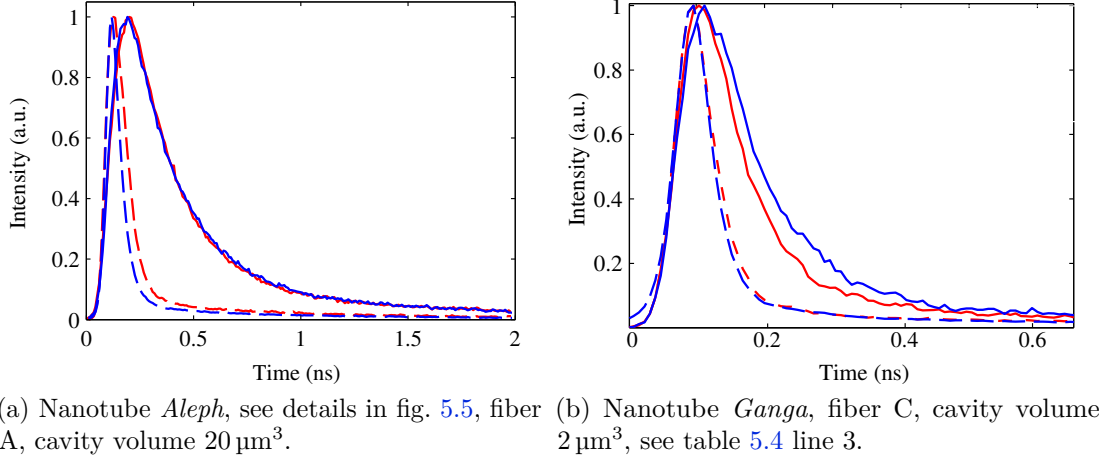


Figure 5.19 – Transient measurements for two nanotubes. Dashed blue line : instrumental response $R_{inst}(t)$; solid blue line : CNT free-space transient $S_{NT,FS}(t)$; solid red line CNT cavity transient $S_{NT,cav}(t)$; and red dashed line : empty cavity transient $S_{cav}(t)$.

They are displayed in figure 5.19 for the nanotube *Aleph*.

A change in the intrinsic response of the nanotube cannot be directly extracted from the measurements of the transients in free-space and in cavity because of the cavity storage time. But a simple cross-convolution can overcome this issue. Let's consider the following purely experimental quantities¹⁸ :

$$S^{FS} = (S_{NT,FS} * S_{cav})(t) = (M * R_{NT,FS})(t) \quad (5.24)$$

$$S^{cav} = (S_{NT,cav} * R_{inst})(t) = (M * R_{NT,cav})(t) \quad (5.25)$$

$$\text{With } M = (R_{inst} * R_{inst} * R_{cav})(t) \quad (5.26)$$

As can readily be seen from their expressions, these quantities combine the measured instrumental responses with the experimental signals in a way such that they only differ by the intrinsic response of the emitter in free-space or in cavity. Therefore, any change of the apparent dynamics of these signals can directly be ascribed to a change in the intrinsic response. Although this approach is not usable for a quantitative analysis, it allows for a direct visual comparison of the decays. In figures 5.20 and 5.21, one can clearly see that the cavity decay is faster than the free-space decay. Let's emphasize that this method gives a direct proof of a cavity induced reduction of the lifetime, and thus of a Purcell effect, without any assumption on the shape of the decays, nor any assumption on the quantum yield of the emitter.

¹⁸Let's recall the the convolution products commute.

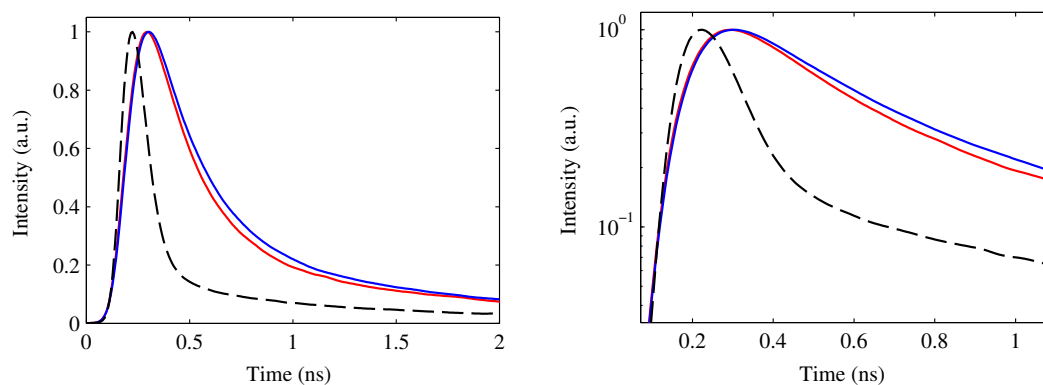


Figure 5.20 – Cross convoluted transient of the nanotube. The solid red line corresponds to S^{cav} , the solid blue line to S^{FS} and the dashed black one is the reference M . It is clearly visible both in linear scale (left) and log scale (right) that the cavity decay is faster than the free-space decay. Nanotube *Aleph*, see details in fig. 5.5.

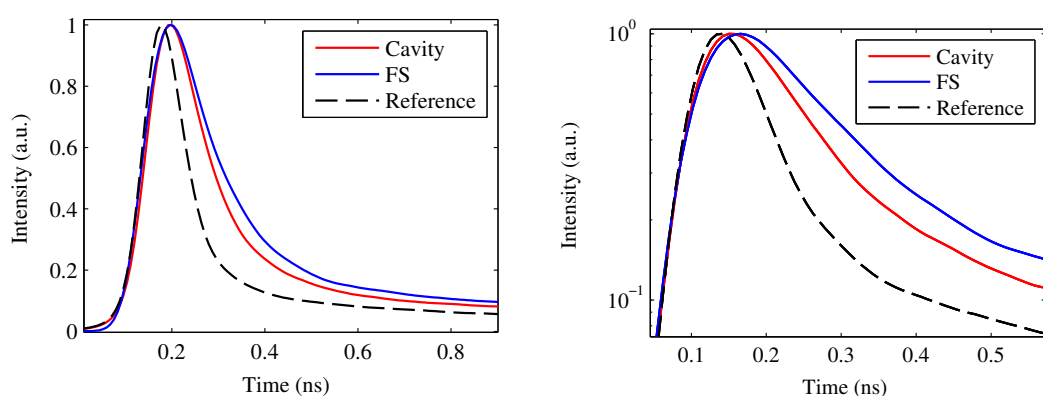


Figure 5.21 – Cross convoluted transient of the nanotube. Same as figure 5.20 but on the nanotube *Ganga* (see table 5.4 line 3). The cavity mode volume is smaller, thus the spontaneous emission rate acceleration is more visible.

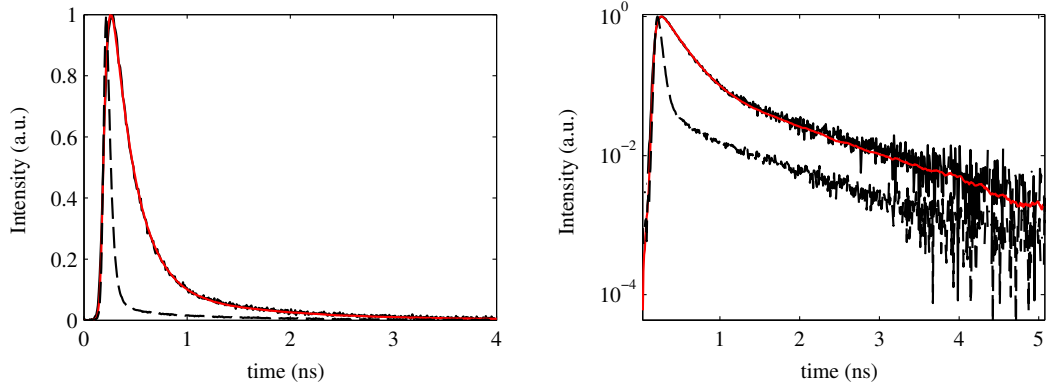


Figure 5.22 – The solid black line corresponds to the free-space transient $S_{NT,FS}(t)$ while the dashed black one corresponds to the instrumental response $R_{inst}(t)$. The convolution of the latest by a mono-exponential decay of characteristic time $\tau_{FS} = 183$ ps corresponds to the solid red line (the long times tail originates from the IRF). On the left, linear scales ; on the right semi-log scale. Nanotube *Aleph*, see details in fig. 5.5.

Results and discussion

As could already be expected since paragraph 5.2.2, the change introduced by the cavity is quite small because the Purcell effect only affects the radiative rate, which amounts only to 2% of the total. But even such little variations are significant [201]. In order to go beyond the qualitative approach of figure 5.20 and give a quantitative value for the Purcell factor, the lifetimes must be extracted from the transients. For that, it is assumed that the nanotube responses in free-space $R_{NT,FS}$ and in cavity $R_{NT,cav}$ are mono-exponential decays $e^{-t/\tau} \cdot \Theta(t)$, with characteristic times given by the lifetimes τ_{FS} and τ_{cav} . Here $\Theta(t)$ is the Heaviside function, ensuring that the nanotube response is zero before the excitation.

The free-space lifetime could thus be extracted by a deconvolution of the free-space transient $S_{NT,FS}(t)$ with the instrumental response $R_{inst}(t)$. In fact, a numerical deconvolution often yields disappointing results, which is why the results were obtained the other way around : the instrumental response $R_{inst}(t)$ is convolved with a mono-exponential decay of characteristic time τ until it fits the free-space transient $S_{NT,FS}(t)$. Figure 5.22 shows that this procedure fits very well the free-space transient, justifying a posteriori the use of a mono-exponential decay. The result for the nanotube *Aleph* is $\tau_{FS} = 183 \pm 4$ ps.

The cavity lifetime can be evaluated following the same procedure : the empty cavity transient $S_{cav}(t)$ is convolved with a mono-exponential decay in order to fit the nanotube's cavity transient $S_{NT,cav}(t)$ ¹⁹. Figure 5.23 shows the result for the nanotube *Aleph*. Once again the fit is very well suited to the experimental data, and

¹⁹Note that as $\gamma^* \gg \kappa$, the storage time is almost unchanged, as discussed in section (1.2.1).

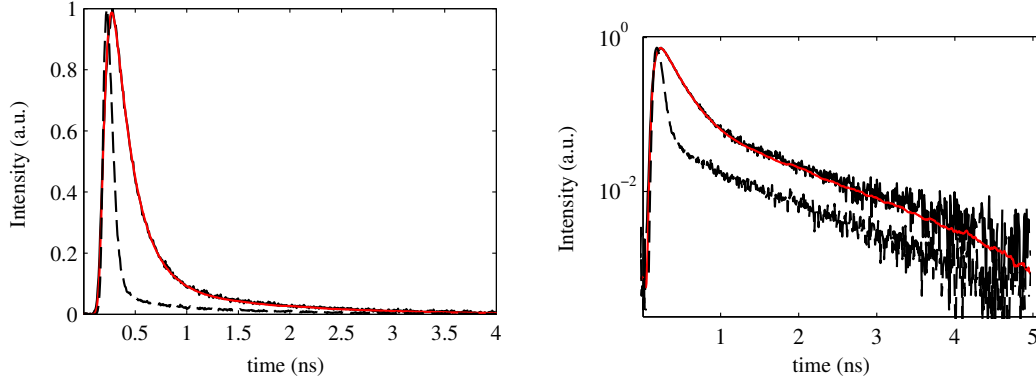


Figure 5.23 – The solid black line corresponds to the cavity transient $S_{NT,cav}(t)$ while the dashed black line corresponds to the empty cavity transient $S_{cav}(t)$. The convolution of the latest by a mono-exponential decay of characteristic time $\tau_{cav} = 203$ ps corresponds to the solid red line. On the left, linear scales ; on the right semi-log scale. Nanotube *Aleph*, see details in fig. 5.5.

the value extracted is $\tau_{cav} = 203 \pm 4$ ps.

Actually, for a single CNT, each transient is always acquired several times to ensure that the lifetime difference is not due to a fluctuation. An example is given for nanotube *Aleph* in fig. 5.24. By repeating the measurement several times and taking the standard deviation, the typical uncertainty is estimated to ± 4 ps. Even though the lifetime decrease due to the cavity was limited for the cavity formed with fiber A, averaging several measurement yielded a clear difference between the cavity and the free-space behaviors.

The lifetimes were also measured by going back and forth between cavity and free-space configuration for several nanotubes. As the lifetimes remained within the error bars, it is clear that the difference does not come from burning, partial bleaching, or aging of the CNT. Finally, the lifetime of a single CNT in cavity was measured as function of the excitation intensity. As one can see in figure 5.25, no significant change was observed over a decade. This ensures that even if the excitation power is modified by interferences in the cavity (as discussed in paragraph 5.2.1), it does not distort significantly the evaluation of the Purcell factor.

Finally, the relative change in the lifetime for the nanotube *Aleph* is estimated to 0.10 ± 0.03 , while the quantum yield is estimated to 0.02 ± 0.005 . The Purcell factor for this nanotube is thus $F_p^* = 5 \pm 2$. In other words, the radiative yield of the CNT nanotube is enhanced by a factor of 6. The percentage of light emitted into the cavity mode, also called extraction, is given by [36] :

$$\beta_e = \frac{F_p^*}{1 + F_p^*} \quad (5.27)$$

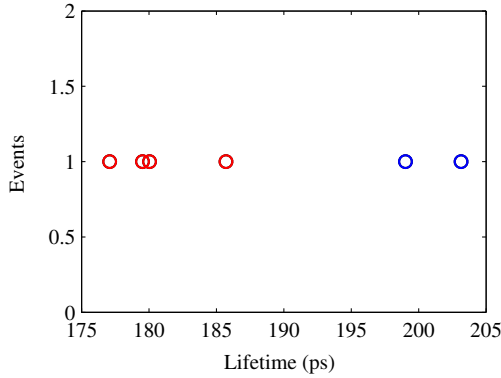


Figure 5.24 – Lifetime extracted from transient measurements for nanotube *Aleph*, see details in fig. 5.5. In blue, free-space measurements, in red cavity measurements.

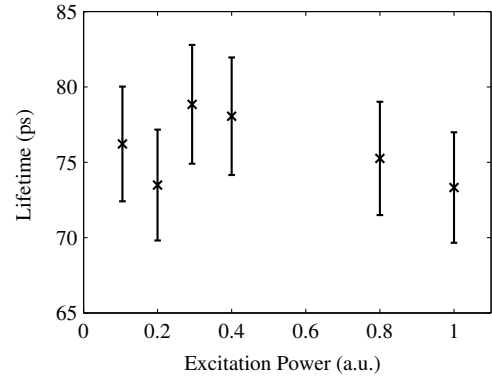


Figure 5.25 – Cavity lifetime of a single (9, 1) carbon nanotube (extracted by the method explained in the text) as a function of the excitation power (cw, 760 nm, linear polarization along the nanotube axis). No significant change is observed over a decade. The error bars show the typical uncertainty ± 4 ps.

It amounts to 0.83 ± 0.05 . The effective efficiency β of the single-photon source in cavity, i.e. the number of photons emitted into the cavity mode per excitation pulse, is defined in eq. (1.63). Here $R = \gamma_R F_p^* = \eta \gamma_{FS} F_p^*$, which leads to the formula :

$$\beta = \frac{\eta F_p^*}{1 + \eta F_p^* \left(1 + \frac{\gamma_{FS}}{\kappa}\right)} \quad (5.28)$$

For this nanotube, it amounts to 0.10 ± 0.03 (five times better than in free-space).

Now, let's compare this experimental value to the theoretical value predicted by formula (1.62). For this nanotube, fiber A is used, so the volume of the cavity is $20 \pm 2 \lambda^3$ (section 3.2). The quality factor is limited by the emitter's one, which can be extracted from the PL spectrum displayed in figure 5.12²⁰ : $Q_{em} \simeq 4700 \pm 100$. Finally, the optical index in the surroundings of the nanotube is the one of polystyrene : $n = 1.6$. From this value, one obtains $F_p^* = 5 \pm 1$, in excellent agreement with the experimental value.

Nevertheless, as the reader may have noticed, the error on the experimental result is just as large as the error made with the photon counts method. One source of uncertainty is the evaluation of the relative lifetime change. However, this uncertainty can be decreased by having emitters with larger lifetimes or by enhancing the Purcell effect. Furthermore, it can be reduced by increasing the statistics (ie averaging repeated measurements). Unfortunately, the estimation of the Purcell effect also

²⁰The quality factor is simply the ZPL energy over its spectral width, about 300 μ eV

relies on the estimation of η which relies itself on the collection efficiency in the free-space ϵ_{FS} . Any error on ϵ_{FS} creates systematical bias in the evaluation of the Purcell factor.

A way to bypass the collection efficiency is to focus on the coupling factor g between the nanotube and the cavity. We recall that eq. (1.57) gives a direct link between the Purcell factor F_p and the coupling factor. In the case of a broad emitter ($\gamma^* \gg \gamma + \kappa$) one obtains the simplified expression :

$$F_p^* = \frac{4g^2}{\gamma_R \gamma^*} \quad (5.29)$$

where γ_R is the radiative lifetime and γ^* the pure dephasing. The latter is retrieved from the FWHM of the free-space spectrum :

$$\hbar(\gamma + \gamma^*) \simeq \hbar\gamma^* = FWHM \quad (5.30)$$

With the help of eq. (5.15), one gets an expression of g as a function of the lifetimes :

$$g = \frac{1}{2} \sqrt{\gamma^* \left(\frac{1}{\tau_{cav}} - \frac{1}{\tau_{FS}} \right)} \quad (5.31)$$

This quantity does not depend on the calibration of the setup. For the nanotube *Aleph* investigated here, the corresponding energy is $\hbar g \sim 5 \pm 2 \mu\text{eV}$.

Along this work, tens of nanotubes were investigated with time-resolved photoluminescence. Obviously, CNTs showed strong variations of their properties from one specimen to another. This comes from several reasons, ranging from possible intrinsic crystalline defects to variable local environment effects. This induces a large distribution of emission wavelengths, linewidths or quantum yields. However, despite this variability, the effect of the cavity was consistently observed as an acceleration of the recombination. A relative reduction of lifetime of the order of 5 to 30% was observed, while the free-space radiative yield spanned the 1 – 5% range, leading to Purcell factors between 3 and 120. Similarly, the coupling g measured ranged from 5 μeV to 70 μeV . All these values are displayed in tables 5.2, 5.3 and 5.4. As expected, the Purcell factor and coupling values found with fiber B and C were significantly higher than with fiber A, which had a larger volume.

5.3 Single-photon source

Using two different methods, one consisting in counting the photons emitted and one in the time-domain, it has clearly been shown that the single carbon nanotubes under study undergo a Purcell effect once coupled to a cavity. Now, it is necessary to check that this cavity embedding does not affect the anti-bunching observed in the PL emission by other teams [21, 191].

The subject is introduced by giving a few details about the statistics of a light

Parameter	ZPL Position	FWHM	Q	BR	η_{tot}	τ_{FS}	τ_{cav}	τ_{stor}	F_p^*	hg	β_e	β
Unit	eV	μeV	ZPL/total	%	ps	ps	ps	ps		μeV	%	%
25/03	1.382	740	1900	0.82	3.7	80	50	50	20	30	95	30
13/04	1.384	760	1800	0.33	2.1	73	63	36	23	16	96	13
18/04	1.376	550	2500	0.43	2.4	53	43	39	18	20	98	16
21/04	1.383	850	1600	0.3	3.2	75	60	29	22	22	96	19
05/05	1.381	580	2400	0.3	3.7	116	107	28	6.5	8	88	7
11/05	1.416	300	4700	0.65	3.5	203	183	35	5	5	83	10
12/05	1.388	620	2200	0.7	7	121	104	50	3.5	12	78	14
13/05	1.385	440	3100	0.85	2.3	90	80	83	6	10	86	10
Mean	1.386	600	2500	0.55	3.3	100	85	45	17	15	90	15
STD	0.01	180	1000	0.25	1.7	45	45	18	15	8	7	7
Uncertainty	0.1%	1.5%	1.5%	3%	20%	4%	4%	10%	40%	20%	5%	30%

Table 5.2 – Table summing up the relevant parameters for Purcell factor evaluation for the nanotubes investigated in 2015 with fiber A (as defined in table 3.1). Cavity volume $V \simeq 20\lambda^3$. The mean value is an average over the columns, while the last line gives the typical relative uncertainty (coming from repeated measurements or uncertainty propagation). Nanotube *Aleph* is indicated in bold letters.

Parameter	ZPL Position	FWHM	Q	BR	η_{tot}	τ_{FS}	τ_{cav}	τ_{stor}	F_p^*	$\hbar g$	β_e	β
Unit	eV	μeV		ZPL/total	%	ps	ps	ps		μeV	%	%
19/02	1.400	2050	700	0.53	4.3	120	45	50	73	68	99	50
23/02	1.348	825	1600	0.64	1.3	316	256	58	29	10	97	18
24/02	1.357	880	1500	0.70	2	135	114	23	13	14	93	15
30/03	1.391	970	1400	0.7	2*	47	36	31	22	32	96	20
04/04	1.348	1900	700	0.50	2*	48	35	34	37	49	97	23
19/04	1.385	570	2400	0.60	2*	76	69	31	8.5	11	90	9
06/05	1.396	720	1900	0.84	2*	68	47	66	26	28	96	24
12/05	1.393	590	2300	0.37	4.6	56	37	26	24	28	96	25
Mean	1.377	1000	1600	0.61	2.5	108	80	40	30	30	95	23
STD	0.02	600	700	0.15	1.2	90	75	15	20	20	3	12

Table 5.3 – Table summing up the relevant parameters to evaluate the Purcell factor for the nanotubes investigated in 2016 with fiber B (3.1). Cavity volume $V \simeq 5\lambda^3$. *During the months of March and April 2016, due to an experimental artifact, the quantum efficiency was not measured. The value retained for the corresponding tube is 2% (our average). This may lead to an error in the estimated Purcell factor, but does not affect the coupling factor g . The uncertainties are similar to the ones of table 5.2.

Parameter	ZPL Position	FWHM	Q	BR	η_{tot}	τ_{FS}	τ_{cav}	τ_{stor}	F_p^*	$\hbar g$	β_e	β
Unit	eV	μeV		ZPL/total	%	ps	ps	ps		μeV	%	%
16/08	1.377	500	2700	0.45	1.2	61	37	13	120	30	99	36
23/08	1.366	675	2000	0.40	3	227	146	15	46	16	98	35
24/08	1.403	410	3500	0.40	2	71	45	15	72	23	99	34
30/08	1.320	420	3100	0.40	1.6	189	108	18	117	16	99	41
31/08	1.398	720	2000	0.41	3	54	22	20	123	57	99	49
Mean	1.373	590	2600	0.42	2.1	120	72	16	98	30	99	39
STD	0.03	120	300	0.02	0.8	80	50	3	33	17	0.5	6

Table 5.4 – Table summing up the relevant parameters to evaluate the Purcell factor for the nanotubes investigated in 2016 with fiber C (3.1). Cavity volume $V \simeq 2\lambda^3$. Nanotube *Ganga* is indicated in bold letters. The uncertainties are similar to the ones of table 5.2.

source and then the second order correlation function is defined in order to characterize a single-photon source. Afterwards, the experimental details of the Hanbury-Brown and Twiss setup are given and finally the results are shown and analyzed.

5.3.1 Statistics of a light source

It is now of common knowledge for non-physicists that light can behave both as a wave and as a stream of particles called photons. This section focuses on the statistical properties arising from the later description. In particular, three different statistics (Poissonian, super-Poissonian and sub-Poissonian) are introduced. It is shown that the latest can be understood only in the photonic point of view.

For now, one can recall that in the case of a light beam observed with a photon counter (such as an avalanche photodiode), the photon flux Φ is defined as the average number of photons passing through a cross-section of the beam per unit of time :

$$\Phi = \frac{P}{\hbar\omega} \quad (5.32)$$

where P is the power in the cross-section, ω the frequency of light and $\hbar\omega$ the energy of a single-photon. The count rate of the detector Φ_D is the average number of counts recorded by the detector per unit of time :

$$\Phi_D = \eta_D \Phi = \eta_D \frac{P}{\hbar\omega} \quad (5.33)$$

where η_D is the detector quantum efficiency, defined as the number of counts per incident photon.

Both quantities introduced here are time averages. Observing a stable beam at long time scales with a photon detector yields a stable value for the count rate and consequently for the photon flux. But at very short time scales, the number of photons counted by unit of time shows fluctuations due to the discrete nature of photons.

Poissonian source

The light coming from an ideal single mode laser is a coherent planar wave of frequency ω , phase ϕ , wavevector $k = \omega/c$ and constant electric field amplitude \mathcal{E}_0 propagating along x axis :

$$\mathcal{E}(x, t) = \mathcal{E}_0 \sin(kx - \omega t + \phi) \quad (5.34)$$

The intensity of this beam - defined as the the mean of the Poynting vector - is constant (as \mathcal{E}_0 and ϕ are constant). Consequently, the average flux of photon Φ is constant.

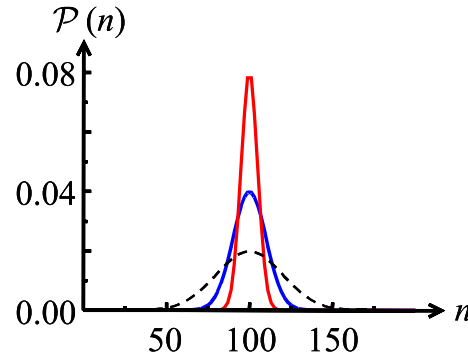


Figure 5.26 – Photon statistics for a Poissonian light (in blue), a super-Poissonian light (in dashed black) and a sub-Poissonian light (in red). The distributions are computed with the same mean number $\bar{n} = 100$. Adapted from [42, (ch. 5)].

At first, it would be natural to think that the beam is composed of a stream of photons regularly spaced in time. But it is not the case : there are some fluctuations on short time scales. Let's consider a beam of constant power P , containing an average number of photons \bar{n} per segment of length L :

$$\bar{n} = \Phi \frac{L}{c} \quad (5.35)$$

The probability $\mathcal{P}(n)$ to find exactly n photons in a segment of length L is given by [42, (ch. 5)] :

$$\mathcal{P}(n) = \frac{\bar{n}^n}{n!} e^{-\bar{n}} \quad n \in \mathbb{N} \quad (5.36)$$

This equation corresponds to a Poissonian distribution (see figure 5.26 for a sketch). The fluctuations of such a source around its mean value, called the variance, is equal to the square of the standard deviation Δn . One can show that for a Poissonian source [42, (ch. 5)] :

$$\Delta n = \sqrt{\bar{n}} \quad (5.37)$$

In other words, even if such a source has an average of 1 photon per unit of time τ , it has a variance of 1. In a given amount of time τ , the number of photons emitted is typically between 0 and 2, with a non-zero probability of being over 2. Such a random source can obviously never be a single-photon source (i.e. : a source yielding one and only one photon per given unit of time).

Super-Poissonian source

A super-Poissonian source is a source for which the standard deviation exceeds the square root of its mean value :

$$\Delta n > \sqrt{\bar{n}} \quad (5.38)$$

Any classical incoherent source behaves as a super-Poissonian source. It is in particular the case of thermal sources for example. Such a source is depicted in figure 5.26.

Sub-Poissonian source

A sub-Poissonian source is a less noisy source than a Poissonian one : it has a narrower photon distribution defined by :

$$\Delta n < \sqrt{\bar{n}} \quad (5.39)$$

As already stated, a Poissonian source is the less noisy one in classical physics. It means that a sub-Poissonian source is characteristic of the quantum nature of light. Let's imagine a source emitting photons one by one, with a interval of time τ constant between two photons. Then the number of photons emitted during a time T is the floor value of the ratio T/τ . This number is perfectly constant and the standard deviation is zero²¹.

It is also possible to imagine sub-Poissonian photon sources with a non-zero variance, as shown in figure 5.26. The amount of time between two photons is not constant, but more regular than in the case of a Poissonian source.

5.3.2 Second order correlation function

In the previous section, a classification of light was introduced, as a function of its photon statistics. Now another way to quantify light fluctuations, according to the second order correlation function $g^{(2)}(\tau)$, is introduced. The experimental setup used for the measurement of the second-order correlation function is described in section 5.3.3.

Classical definition

One can consider two intensity measurements separated by a time delay τ . The mean of the product of intensities is the correlation function of the intensity. The second order correlation function is this function normalized by the mean intensities :

$$g^{(2)}(\tau) = \frac{\langle I(t)I(t+\tau) \rangle}{\langle I(t) \rangle \langle I(t+\tau) \rangle} = \frac{\langle \mathcal{E}^*(t)\mathcal{E}^*(t+\tau)\mathcal{E}(t+\tau)\mathcal{E}(t) \rangle}{\langle \mathcal{E}^*(t)\mathcal{E}(t) \rangle \langle \mathcal{E}^*(t+\tau)\mathcal{E}(t+\tau) \rangle} \quad (5.40)$$

where \mathcal{E} is the electric field, I the intensity, and $\langle \dots \rangle$ denotes a time average over a long period.

²¹However, unlike the coherent light emitted by lasers, single-photons phase is random.

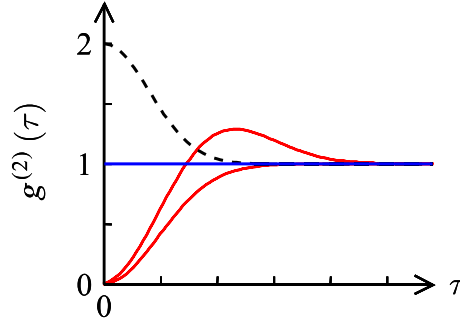


Figure 5.27 – Correlation function for a Poissonian source (in blue), a super-Poissonian source (in dashed black) and two different sub-Poissonian sources (in red). adapted from [42, (ch. 6)].

This autocorrelation function is even and the Cauchy’s inequality gives the following boundaries for its values :

$$\begin{aligned} g^{(2)}(\tau) &\geq 0 \text{ if } \tau \neq 0 \\ g^{(2)}(0) &\geq 1 \end{aligned} \quad (5.41)$$

In the case of a Poissonian (coherent) source, one simply gets $g^{(2)}(\tau) = 1$ for all times, as shown in figure 5.27. This just shows that the average time between two photons is completely random, as depicted in figure 5.28. For a super-Poissonian source, the second-order correlation function increases above 1, which means that the photons tend to stick together. They are referred to as “bunched”. Nevertheless, a description of a sub-Poissonian source cannot be given within this frame. It is necessary to introduce a quantum definition of $g^{(2)}(\tau)$.

Quantum definition

The definition we gave for the second order correlation function can be extended to a quantum approach :

$$g^{(2)}(\mathbf{r}_1 t_1, \mathbf{r}_2 t_2; \mathbf{r}_2 t_2, \mathbf{r}_1 t_1) = \frac{\langle \hat{E}^-(\mathbf{r}_1 t_1) \hat{E}^-(\mathbf{r}_2 t_2) \hat{E}^+(\mathbf{r}_2 t_2) \hat{E}^+(\mathbf{r}_1 t_1) \rangle}{\langle \hat{E}^-(\mathbf{r}_1 t_1) \hat{E}^+(\mathbf{r}_1 t_1) \rangle \langle \hat{E}^-(\mathbf{r}_2 t_2) \hat{E}^+(\mathbf{r}_2 t_2) \rangle} = \frac{\langle \hat{a}^\dagger \hat{a}^\dagger \hat{a} \hat{a} \rangle}{\langle \hat{a}^\dagger \hat{a} \rangle^2} \quad (5.42)$$

where the operator electric field is defined by :

$$\hat{\mathbf{E}}(\mathbf{r}, t) = \hat{\mathbf{E}}^+(\mathbf{r}, t) + \hat{\mathbf{E}}^-(\mathbf{r}, t) \quad (5.43)$$

$$\hat{\mathbf{E}}^+(\mathbf{r}, t) = i \sum_{\mathbf{k}} (\hbar\omega/2\epsilon_0 V)^{1/2} \boldsymbol{\epsilon}_{\mathbf{k}} \hat{a}_{\mathbf{k}} \exp(-i\omega_{\mathbf{k}}t + i\mathbf{k} \cdot \mathbf{r}) \quad (5.44)$$

$$\hat{\mathbf{E}}^-(\mathbf{r}, t) = (\hat{\mathbf{E}}^+(\mathbf{r}, t))^\dagger \quad (5.45)$$

In this case, the averages $\langle \dots \rangle$ are done with the density operator. Where \hat{a}^\dagger and \hat{a} are creation and annihilation operators respectively.

If one takes a perfectly coherent state, defined by the relation $\hat{a}|\alpha\rangle = \alpha|\alpha\rangle$, one recovers the fact that $g^{(2)}(\tau) = 1$ for a Poissonian source.

Let's now consider the Hanbury-Brown and Twiss (HBT) experiment. In this experiment, a light source is shone on a 50% beam splitter and the two outputs of the beam splitter are monitored with photon counters. In order to understand better what happens in the sub-Poissonian case, $g^{(2)}(\tau)$ can be written as a function of the number of photons counted by the two detectors [42, (ch. 6)] :

$$g^{(2)}(\tau) = \frac{\langle n_1(t)n_2(t+\tau) \rangle}{\langle n_1(t) \rangle \langle n_2(t+\tau) \rangle} \quad (5.46)$$

where $n_1(t)$ and $n_2(t+\tau)$ are the number of photons counted by the detectors at time t and $t+\tau$. From this formula it is clear that $g^{(2)}(\tau)$ depends on the joint probability to detect a photon at time t on the first detector and a photon at time $t+\tau$ on the second detector. In particular, $g^{(2)}(0)$ corresponds to the probability for two photons to arrive at the same time on the two detectors, and thus to be emitted simultaneously.

Let's consider the different kinds of sources : in any case, at long delays, the probabilities of detection become uncorrelated and $g^{(2)}(\tau \rightarrow \infty) = 1$. For a coherent source, the probability to detect a photon on detector 2 after having detected one on detector 1 is the same for any delay as the photons are emitted randomly. It confirms that for such an emitter, $g^{(2)}(\tau) = 1$. For a bunched emitter, the photons tend to be emitted together, and thus to arrive on the beam splitter together. Consequently, if a photon is detected on the first detector, there is a comparatively higher probability to detect a photon on the other detector at the same time. One recovers the fact that for such an emitter $g^{(2)}(0) > 1$.

Now let's consider a sub-Poissonian source, for which the photons are anti-bunched. If a photon is detected on detector 1, there is a comparatively lower probability to find a photon on the second detector, and one gets $g^{(2)}(0) < 1$. In particular, if an emitter is perfectly anti-bunched, two photons are never emitted together, and one gets $g^{(2)}(0) = 0$. Two examples of correlation functions for anti-bunched emitters are displayed in figure 5.27. The first shows anti-bunching while the second displays anti-bunching followed by bunching. This means that two photons are never emitted together but tend to be emitted with a given delay.

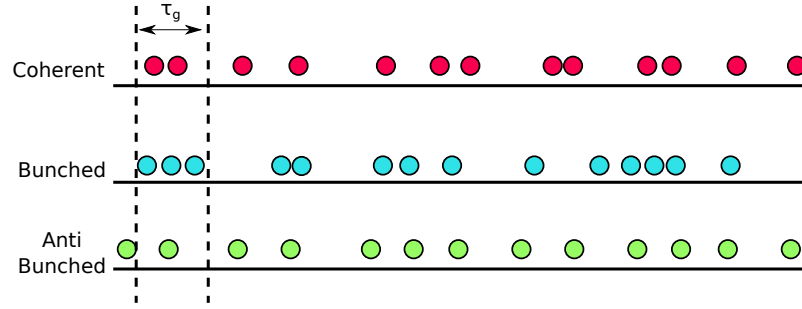


Figure 5.28 – Stream of photons for the three different kinds of source : coherent, bunched and anti-bunched. In the case of coherent light, the time space between photons is random. In the case of bunched light, they tend to stick together. On the contrary, in the case of anti-bunched light, photons are regularly spaced. Typically in a period of time τ_g as defined in the text, one finds one and only one photon emitted.

Single-photon source criterion

In the quantum picture of the second order correlation function, it is possible to have values ranging between 0 and 1 at zero delay : $1 \geq g^{(2)}(0) \geq 0$. In this case, the light source is referred to as anti-bunched.

In fact, it is possible to show that two uncorrelated single-photon sources emitting together lead to $g^{(2)}(0) \geq 0.5$ (for a complete discussion of the emission of uncorrelated single-photon sources, refer to [83]). Consequently, it is commonly considered that the criterion for a “single-photon source” is to have $g^{(2)}(0) < 0.5$.

Until now we used many common-sens expressions such as “at the same time”, “one by one” or “well separated from each other”. As physicists, such vague qualifications are obviously unsatisfying. Let’s now try to define what is a “simultaneous” emission.

For that, let’s take a simple two level system with a lifetime τ_{FS} pumped incoherently with a pumping rate r . The evolution of such a system is given by :

$$\begin{cases} \frac{d\rho_e}{dt} = -\frac{\rho_e}{\tau_{FS}} + r\rho_g \\ \rho_g = 1 - \rho_e \end{cases} \quad (5.47)$$

where ρ_g and ρ_e are the populations of the ground and excited states. If at $t = 0$, a photon is emitted, one has $\rho_e(t = 0) = 0$. The solution of the system is thus given by :

$$\rho_e(t) = \frac{r\tau_{FS}}{1 + r\tau_{FS}} \left(1 - e^{-(r + \frac{1}{\tau_{FS}})t} \right) \quad (5.48)$$

For a two-level system, the probability of emission of a photon at a time τ is proportional to the population of the excited state. And the detection of a photon at $t = 0$ projects the system in its fundamental state. Thus one obtains :

$$g^{(2)}(\tau) = \frac{\rho_e(|\tau|)}{\rho_e(\infty)} \Big|_{\rho_g(0)=1} \quad (5.49)$$

$$= 1 - e^{-\tau/\tau_g} \quad (5.50)$$

where $\tau_g = (r + \frac{1}{\tau_{FS}})^{-1}$. Consequently, the second order correlation function displays a dip around zero delay. It is equal to zero at $\tau = 0$ and increases towards 1 on a time scale given by τ_g . If the two-level system is pumped at a rate much faster than its own decay rate, the typical time delay between two photons is given by the repetition rate of the excitation r^{-1} . On the contrary, if the two-level system is pumped at a lower rate, the typical time interval between the emission of two photons is its lifetime τ_{FS} .

To conclude, we call “single-photon source” a source with a second-order correlation function dropping below 0.5 at zero delay. The photons emitted by such a source are typically separated in time by the lifetime of the source. The situation is depicted in figure 5.28.

5.3.3 Hanbury-Brown and Twiss setup

In order to measure the second-order correlation function, a single detector is needed. However, every detector has a dead-time, i.e. a time during which it can't detect a second photon after the detection of a first. As this dead-time is much higher than the typical rate of emission, it prevents from measuring a clear anti-bunching. As a consequence, a two detectors configuration is commonly used. The Hanbury-Brown and Twiss interferometer was designed by the two eponymous physicists, in order to record intensity correlations in stellar physics. Even though it was not its primary goal, this setup is now widely used to assess if a light emitter behaves as a single-photon source.

Principle

The setup, as introduced in paragraph 5.3.2, is made of a 50% cube splitter and two avalanche photodiodes (APD) used to detect the arrival of a photon, as depicted in figure 5.29. The two detectors and the correlation device give the joint probability for two photons to arrive on the two detectors with a delay τ .

The two APD detectors²², emit a TTL impulsion when they detect a photon (with an efficiency of 40% at 900 nm).

The correlation device has two channels : a START channel, which starts a counter when a photon is detected, and a STOP channel which stops the counter when a photon is detected (see fig. 5.30a). The time elapsed between the START

²²Perkin Helmer SPCM-AQRH-16

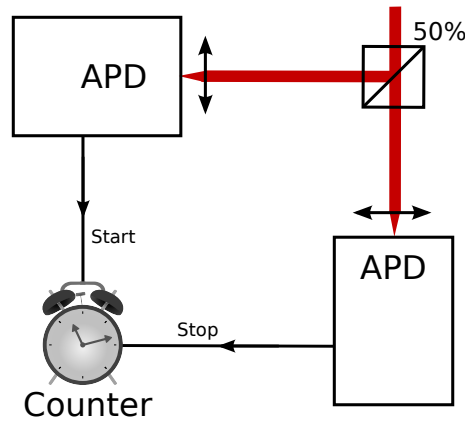


Figure 5.29 – Schema of a Hanbury-Brown and Twiss interferometer.

and the STOP is then recorded : it is the delay τ . The experiment is run during a time sufficiently long to build a histogram of the delays.

A negative delay has no physical sense as the counter must be started before it is stopped. However, a usual experimental trick consists in connecting the APDs to the correlation counter with BNC cables of unbalanced length. This enables to arbitrarily shift the position of the zero delay (in our case, the zero delay between the arrival of two photons on the beam splitter corresponds to a delay of 300 ns on the counter). The histogram obtained has negative delays with respect to the shifted origin of the delays axis.

Finally, after an appropriate integration time, one gets a correlation histogram, as shown in figure 5.30b. The measurement must be normalized with respect to long delays²³. Indeed, for a long delay $\tau \rightarrow \infty$, the probabilities n_1 and n_2 are no longer correlated and one gets $g^{(2)}(\tau \rightarrow \infty) = 1$ ²⁴. Once normalized, the histogram corresponds to the autocorrelation of the source [42, chap. 6]. If a dip is present at zero delay, it means that the photons are anti-bunched.

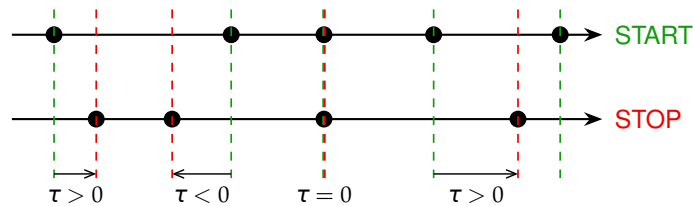
HBT under continuous excitation

Nevertheless, the visibility of this dip at zero delay depends strongly on the times scales of different processes.

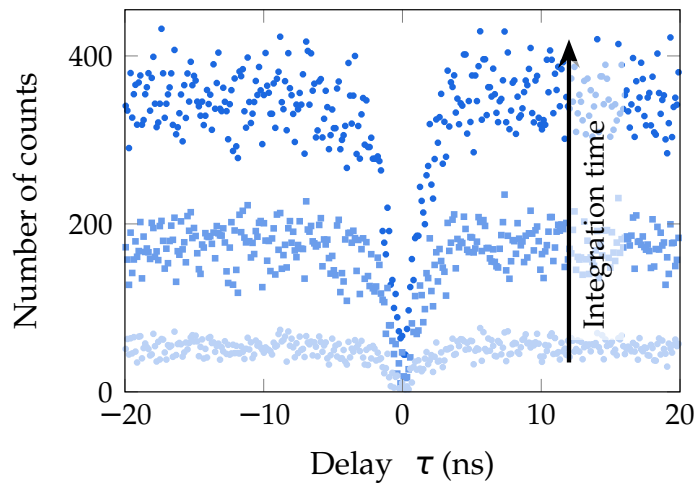
Indeed, the correlation counter has an accuracy of a few picoseconds, but the APD used here have a resolution of 400 ps, a few times the typical lifetime of a carbon

²³An other way to normalize the histogram is to perform the same measurement, during the same time, in the same conditions with a coherent source having the same average intensity than the source investigated.

²⁴Technically, the normalization is done for times much greater than the lifetime of the emitter. However, at longer time scales, the start-stop method no longer delivers the second order correlation function. Indeed, if the time delay is too high, the counter will have had a high probability of being stopped before this delay is reached. This artifact's consequence is that the values obtained for such long times drop below 1.



(a) The Hanbury-Brown and Twiss setup enables to measure the delay between each pair of photons



(b) A histogram of these delays is built. The graph here shows the evolution of this histogram when the integration time is increased. The data are taken from [202] (experiment on quantum dots).

Figure 5.30 – Principle of a photon correlation measurement.

nanotube. The global resolution of the system is thus limited by the instrumental response function (IRF) of the detectors - about 400 ps.

Now, let's consider the simple model introduced in section 5.3.2. The anti-bunching dip has a characteristic time $\tau_g = 100$ ps :

$$g_s^{(2)}(\tau) = 1 - e^{-\tau/\tau_g} \quad (5.51)$$

For the sake of simplicity, the effect of the IRF is modeled as a convolution with a gaussian of lifetime $\tau_R = 2\sqrt{2\ln(2)}b = 400$ ps.

$$R(t) = e^{-\frac{t^2}{2b^2}} \quad (5.52)$$

The autocorrelation function $g_m^{(2)}(\tau)$ obtained from the normalized HBT histogram corresponds to the convolution of $g_s^{(2)}(\tau)$ with $R(t)$. At zero delay, the numerical result is :

$$g_m^{(2)}(0) = 0.62 \quad (5.53)$$

In other words, due to the IRF, even a perfectly anti-bunched CNT, observed without any background or noise would lead only to a drop of 40% at zero delay in the autocorrelation function, which is above the single-photon criterion.

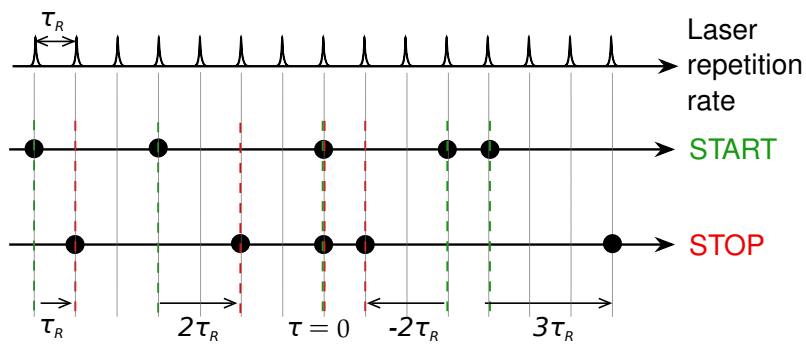
HBT under pulsed excitation

This can be overcome with pulsed excitation. Indeed, if the CNT is excited by brief pulses (about 100 fs) separated by intervals much longer than its own lifetime ($\tau_R = 12.5$ ns here, for a lifetime of 100 ps), it behaves as a pulsed emitter.

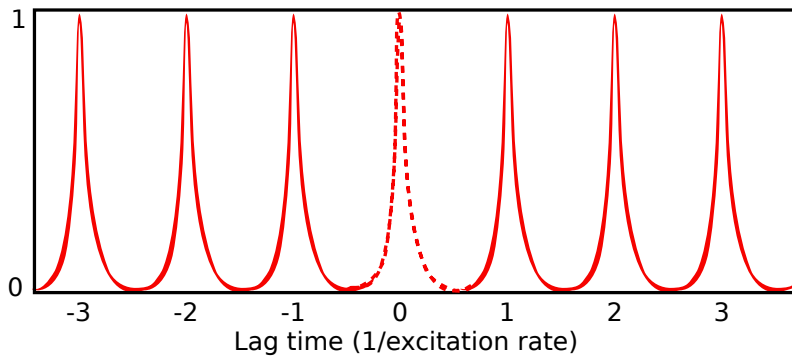
When the carbon nanotube is shone with a sufficiently intense excitation, at least one photon is absorbed. It leads to the emission of either zero photon (non radiative decay), one photon (anti-bunching) or several photons (no anti-bunching).

Taking the point of view of the detectors, if a photon arrives on the start detector, either a photon arrives on the stop detector from the same excitation pulse (the two photons are separated by a time lesser than the resolution of the detectors) or the photon arrives with a later excitation pulse (the two photons are separated by n times the repetition rate of the laser, n being an integer).

This means that the autocorrelation signal under pulsed excitation is composed of a series of peaks, having a time width of the order of the resolution of the detectors and separated by the repetition rate of the laser, as shown in figure 5.31. Anti-bunching is marked by the vanishing of the peak at zero delay (it never happens than the same pulse of excitation leads to the emission of more than one photon). It does not depend on the resolution of the detectors and can drop down to zero for a perfect single-photon emitter.



(a) A photon can be emitted only when the emitter is reached by an excitation pulse. The delay between START and STOP is thus a multiple of the laser repetition rate.



(b) Correlation measurement under pulsed excitation. The central peak (dashed line) disappears for a single-photon source.

Figure 5.31 – HBT under pulsed excitation

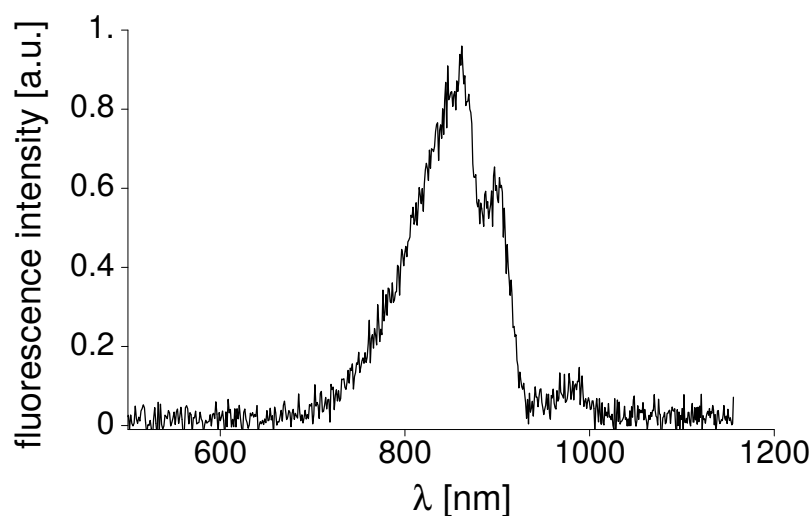


Figure 5.32 – After-pulse emission spectrum of a typical Avalanche Photodiode, from [203].

APD after-pulse cross-talk

Even though the APD resolution issue was bypassed by using pulsed excitation, another issue called “Cross talk” remains.

Indeed, silicon Avalanche Photodiodes are used because of their low dark count rate and high quantum efficiency. In order to detect efficiently single-photons, the diode is reversely biased above breakdown voltage. When a photon arrives, it triggers a discharge and a current... but also a luminescence signal called after-pulse.

Even though this emission is quite weak, it leads to the detection of the breakdown flash by the other APD. This means that the histogram contains a number of photo-events which are not linked to the carbon nanotube emission.

As shown in figure 5.32, from ref. [203] the emission of the APD ranges from 700 nm to 1000 nm, which falls clearly in the range of this study (850 nm to 950 nm). In order to minimize the cross talk effect we slightly tilted the optical paths leading from the beam-splitter to the APDs in order to limit the probability for a photon to travel directly from one to another. Furthermore, we systematically placed a 10 nm bandpass filter, centered on the CNT wavelength, in front of each detector. By means of this spectral filtering, the cross-talk features remain visible in the histogram, but do not affect the measurement.

Results and discussion

Experimentally, we carried out pulsed HBT measurements on several CNT both in free-space and in cavity. In every case, the second order correlation function at zero delay was found to be much lower than 0.5, which is the criterion we retained for a single-photon source.

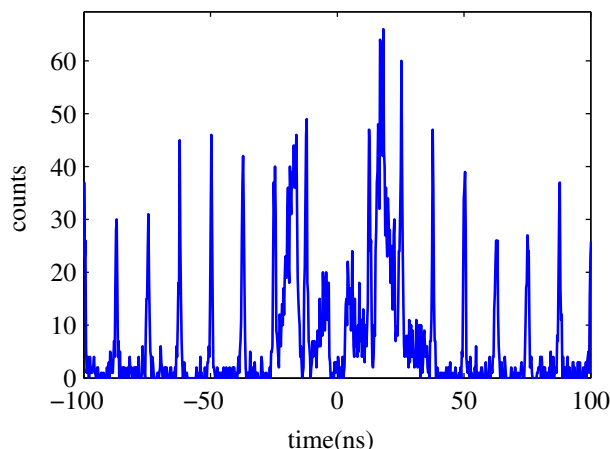


Figure 5.33 – Intensity correlation measurements of a nanotube in free-space obtained in a Hanbury-Brown and Twiss setup under pulsed excitation. The missing peak at zero delay $g^{(2)}(0) = 0.05 \pm 0.03$ shows that the nanotube behaves as a single-photon source. The signal between the first and second peaks corresponds to APD cross-talk.

In figure 5.33 we give the histogram coming from the HBT measurement of a single nanotube in free-space. One can see a series of peaks spaced by a time $\tau_R = 12.5$ ns corresponding to the repetition rate of the laser. The peak at zero-delay is largely suppressed, and the estimated value is $g^{(2)}(0) = 0.05 \pm 0.03$ ²⁵. Between the suppressed peak and the two peaks at $\pm\tau_R$, as well as between these peaks and the ones at $\pm 2\tau_R$, one can see the signature of the APD cross-talks described in section 5.3.3.

The same measurement was carried out on the same carbon nanotube once coupled to our micro-cavity, tuned in resonance with the ZPL. As one can see in figure 5.34a, the cavity and the Purcell enhancement do not change the single-photon emitter behavior of the cavity. For this particular nanotube, the value found is $g^{(2)}(0) = 0.03 \pm 0.02$. If the value is slightly smaller than in free-space, it is most likely not related to a change in the source but to the fact that we collect a much greater number of photons in cavity mode. As the HBT signal depends quadratically on the input intensity, the signal-to-noise ratio is lower in free-space.

For the free-space experiment and even more clearly for the cavity experiment, one can see that the peaks siding the suppressed one have a comparatively higher intensity than the following ones. An extended view of $g^{(2)}(\tau)$ in cavity is given in figure 5.34b for this purpose²⁶.

Such bunching features were observed by Walden-Newman et al. [191]. More precisely, they observed bunching when a part of the spectrum was selected with a 10 nm bandpass filter. However, if they filtered the emission by a 40 nm bandpass

²⁵The uncertainty arises from the shot noise.

²⁶Let's note that the values of $g^{(2)}(0)$ indicated here were taken by removing the almost negligible background and by normalizing with the value of $g^{(2)}(\tau)$ far away from these bunching features.

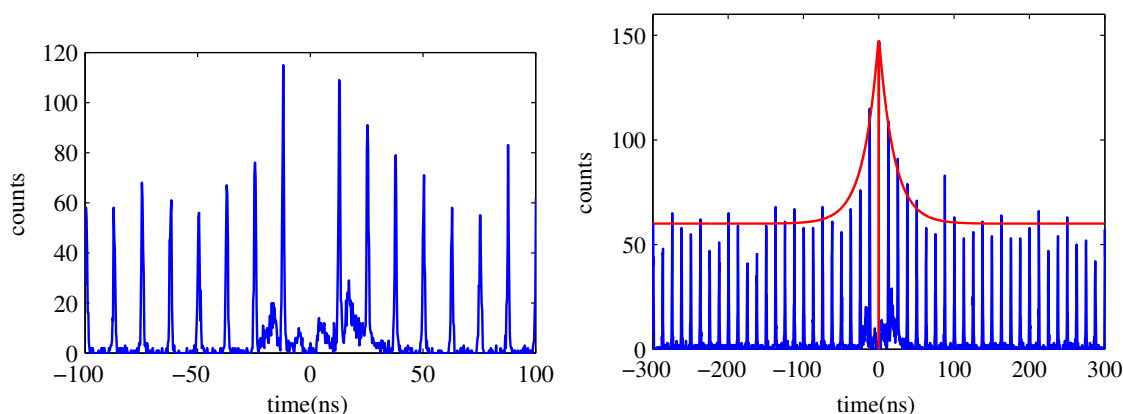


Figure 5.34 – Intensity correlation measurements of a nanotube in cavity obtained in a HBT setup under pulsed excitation. The missing peak at time $g^{(2)}(0) = 0.03$ shows that the nanotube still behaves as a single-photon source. A zoom is given to show the bunching feature at short time scale and the normalization at long time scale. The solid red line corresponds to the model of eq. 5.54.

filter, covering the full CNT spectrum, no bunching was visible. Consequently, they ruled out the coherent or thermal properties of the emitter that would lead to bunching features.

The authors offered an explanation to this bunching : spectral diffusion. Let's consider a filter selecting the right part of the spectrum, noted R. Then a conditional probability is created for the coincidence measurement : if a photon from R starts the HBT counter, then there is a high probability that a photon from R stops it. This probability decreases with time as the emitter may have jumped out of the spectral window. The time delay between two events is the a measure of the time spent by the emitter in region R.

The resulting correlation function writes :

$$g^2(\tau, R) = \left(1 + \left(\frac{\gamma_{SD}}{\gamma_H} - 1 \right) e^{-\gamma_{SD}\tau} \right) (1 - e^{-\gamma_{FS}\tau}) \quad (5.54)$$

where γ_H is the rate for hopping in and out of the filter spectral range, γ_{FS} is the spontaneous emission rate and γ_{SD} is the spectral diffusion rate. In fig. 5.34b, this model was plotted for $\gamma_{SD} = 0.05 \text{ ns}^{-1}$, $1/\gamma_{FS} = 100 \text{ ps}$ and $\gamma_H = 0.4\gamma_{SD}$ ²⁷. The good agreement between the model and the experimental data supports the theory of a bunching induced by spectral diffusion.

²⁷In [191], γ_{SD} is comprised between 0.05 ns^{-1} and 1 ns^{-1} , $1/\gamma_{FS}$ between “less than 400 ps” and 2 ns, while $1/3\gamma_{SD} < \gamma_H < 2/3\gamma_{SD}$.

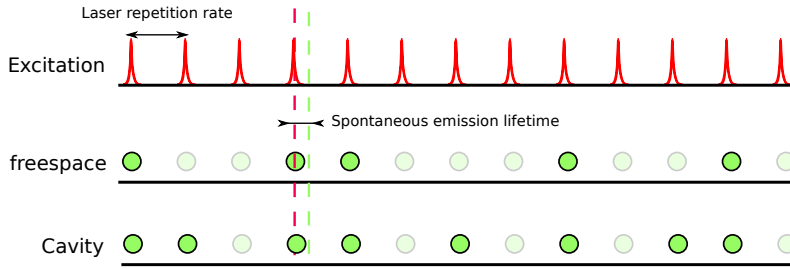


Figure 5.35 – In red, the excitation pulses of the laser, separated by the repetition rate of the laser ($\tau_R = 12.5$ ns). In green, the nanotube relaxes after a time given by its spontaneous emission lifetime ($\tau_{FS} \ll \tau_R$).

Conclusion

Figure 5.35 sums up schematically the results of this chapter : the nanotubes are excited by a non-resonant pulsed laser. In free-space, the probability for them to relax radiatively is very low, while in cavity it increases strongly while retaining a pronounced anti-bunching character. The coupling factor g is estimated to range from $5 \mu\text{eV}$ to $70 \mu\text{eV}$, which means an order of magnitude below the intrinsic linewidth of the nanotubes $\hbar\gamma^* \sim 500 \mu\text{eV}$.

Let's compare the CNT-based single-photon source obtained with the state-of-the-art for quantum dots. In 2016, Somaschi et al. [11] coupled a quantum dot to a micro-pillar cavity of quality factor 12000 and obtained a Purcell factor of 7.6. With an effective quality factor limited by the emitter's spectral width to a few thousands and an effective mode volume as low as $2\lambda^3$, we obtain Purcell factors F_p^* between 5 and 120.

In the work of Somaschi et al., the quantum efficiency of the emitter was near unity, however the brightness was limited to 65% - which is already a very high value for quantum dots - due to the limited extraction value. In our case, the intrinsic efficiency η of the carbon nanotubes is around 2%, but the Purcell effect directly increases it, and the extractions β_e obtained are above 98% for the lowest mode volume cavities. Consequently, the effective efficiency (single-photon generation efficiency into the cavity mode) β is commonly above 30% and reaches up to 50%. It is worth noting that this value is higher than the efficiency obtained by chemical brightening (18% in [204]). Given the asymmetry of the cavity, the brightness of our device can reach up to 40%.

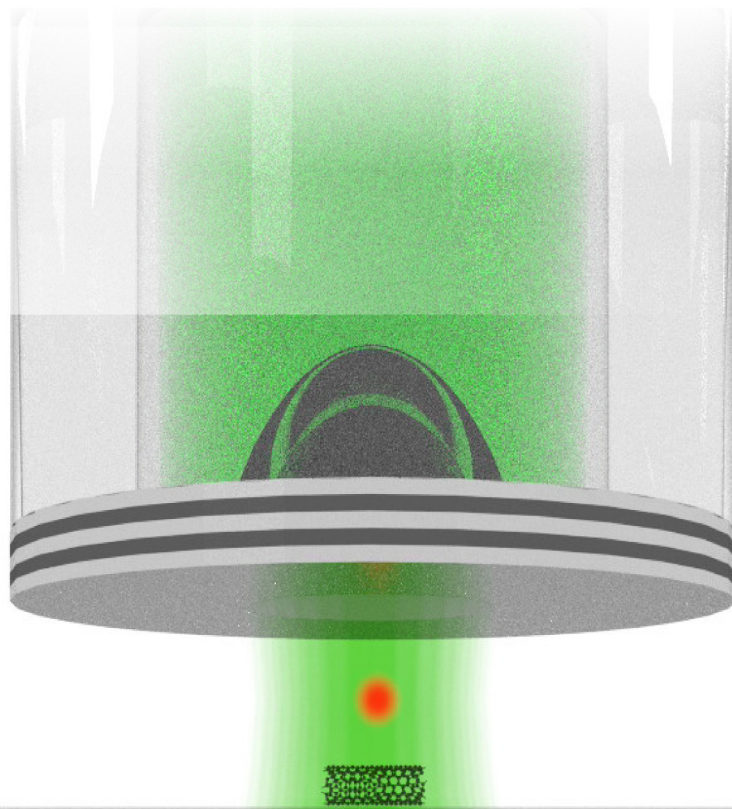
Somaschi et al. show a strong anti-bunching, with $g_2(0) = 0.0028 \pm 0.0012$ and an indistinguishability of 0.9956 ± 0.0045 (for a brightness of 15%). In our case, $g_2(0) = 0.03 \pm 0.02$. However, this estimation is not limited by the intrinsic behavior of the nanotubes but by the limitations of our measurement (shot noise, residual effect of the APDs cross-talk). The indistinguishability of the cavity-coupled CNT remains to be experimentally measured, but should be quite low, around 0.25 [205].

To conclude, the source obtained by coupling a single carbon nanotube to a

fiber Fabry-Perot micro-cavity displays a strong anti-bunching and its brightness is catching up with the state-of-the-art for other emitters. For applications, the main challenges faced are the switch from visible range to telecoms bands, the indistinguishability and the possibility to work at room temperature.

6

EFFICIENCY OF A CAVITY COUPLED NANOTUBE



Contents

6.1	Cavity efficiency including the phonon wings : theoretical approach	185
6.1.1	Evolution of the populations	185
	Absorption and emission	186
	Hamiltonian	187
	Master equation	187
6.1.2	Cavity efficiency	188
	Expression of the cavity efficiency	188
	Phenomenological interpretation	189
	Efficiency of the ZPL emission	190
6.2	Experimental derivation of the cavity efficiency	191
6.2.1	Experimental “reconstructed” spectra	192
	Step-by step method	192
	Fast-scan method	194
6.2.2	Fit of the experimental data	197
	Absorption spectrum	197
	Fit quality	197
6.2.3	Evolution with cavity volume	198
	Aspect of the spectra	198
	Comparison with other methods	199
	Asymptotic behavior	202

Introduction

In chapter 4, we showed that a single carbon nanotube coupled to a cavity in resonance with its Zero Phonon Line is a single-photon source with a Purcell enhanced efficiency. However, these characteristics are not restricted to the coupling with the ZPL. It turns out that the spontaneous emission is equally enhanced if the cavity is tuned in resonance with one of the phonon wings of the nanotube. We measured the auto-correlation function of the source obtained for a detuning of up to 5 meV. With $g^{(2)}(\tau) = 0.02 \pm 0.02$, figure 6.1 clearly demonstrates a strong anti-bunching. In opposition to atomic like emitters, such as quantum dots, the nanotubes have a large spectrum, ranging over about 15 meV (4 THz). Whenever the cavity is in resonance with a part of the spectrum, it acts as the effective emitter, with a spectral width of 8 GHz (or 80 GHz including the vibrations), incoherently pumped by the carbon

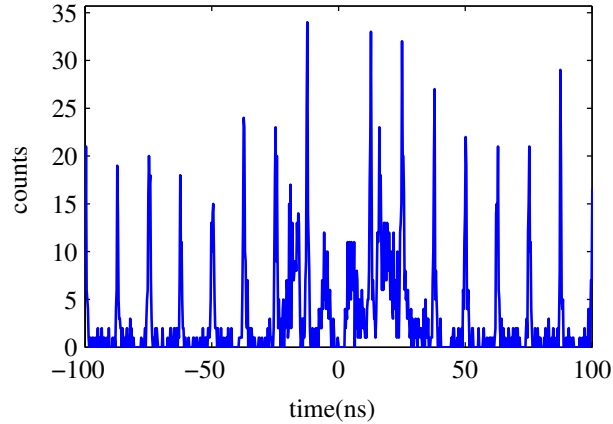


Figure 6.1 – Intensity correlation measurements of a nanotube in a cavity tuned in resonance with one of its phonon wings. With $g^{(2)}(\tau) = 0.02 \pm 0.02$, the anti-bunching is as strong as when it is tuned in resonance with the ZPL.

nanotube. This cavity feeding effect brings a widely tunable single-photon source, opening the way to multiplexing (i.e. combining signals with different wavelengths).

As explained in chapter 3, the phonon wings are a series of replica of the exciton purely electronic transition line, shifted by the phonon energy. Such an unconventional spectrum is typical of CNTs. Understanding its consequences in terms of Purcell effect is of paramount importance as it is responsible for the spectral tunability of the single-photon source. The micro-cavity described in chapter 3 is used to handle the exciton-phonon coupling.

The coupling of a non-Lorentzian spectrum with a cavity is beyond the generalized Purcell model derived in chapter 1. We propose a new model in this chapter to account for this effect. Then, the experimental measurements of the single-photon source efficiency in cavity, over the full nanotube spectrum, is explored thoroughly.

6.1 Cavity efficiency including the phonon wings : theoretical approach

In this section, the model of the Purcell factor described in section 1.3.1 is upgraded in order to understand the role of the exciton-phonon coupling in the presence of a cavity.

6.1.1 Evolution of the populations

In the first part of this section, the Hamiltonian of the system is introduced and the populations evolution are obtained from the master equation.

The derivations may seem cumbersome to the reader. As a consequence, only the main steps are presented and the details are left to appendix D.

Absorption and emission

In chapter 4, an Hamiltonian was introduced to account for the exciton-phonon coupling in free-space. It reads :

$$H_{e-p} = \hbar\omega_X\sigma^+\sigma^- + \hbar\sum_{\vec{k}}\omega_k b_{\vec{k}}^\dagger b_{\vec{k}} + \hbar\sigma^+\sigma^-\sum_{\vec{k}}(g_k b_{\vec{k}} + g_k^* b_{\vec{k}}^\dagger) \quad (6.1)$$

Where the first term is the energy of the exciton, the second describes the effective acoustic phonon bath, with a sum over wavevector \vec{k} and the last corresponds to the coupling g_k for each phonon mode k with the exciton (section (4.2.2)). Krummheuer et al. showed that the absorption spectrum of a carbon nanotube in free-space $S_{fs}^{abs}(\omega)$ can be expressed as a function of its emission frequency ω_X , its decay rate γ , the pure dephasing it undergoes γ^* and a function $K(t)$ taking into account the interactions with the phonon bath [172, 206, chap. 4.3.4] :

$$S_{fs}^{abs}(\omega) = 2Re\left[\int_0^\infty dt e^{i(\omega-\omega_X)t} e^{-\frac{\gamma+\gamma^*}{2}t} K(t)\right] \quad (6.2)$$

with $\int_{-\infty}^\infty S^{abs}(\omega)d\omega = 2\pi$ and :

$$K(t) = \prod_k \exp\left(\frac{|g_k|^2}{\omega_k^2} \left(e^{-i\omega_k t} - n(k)|e^{-i\omega_k t} - 1|^2 - 1\right)\right) \quad (6.3)$$

$$n(k) = \frac{1}{e^{-\hbar\omega_k/k_b t} - 1} \quad (6.4)$$

Furthermore, the emission spectrum $S_{fs}^{emi}(\omega)$ is the mirror of the absorption spectrum with respect to the ZPL (as a single electronic transition, assisted by phonons absorption or emission, is considered here) [172], thus :

$$S_{fs}^{emi}(\omega) = 2Re\left[\int_0^\infty dt e^{i(\omega-\omega_X)t} e^{-\frac{\gamma+\gamma^*}{2}t} K^*(t)\right] \quad (6.5)$$

The effect of the cavity, acting as a simple spectral filter (no dipole-cavity coupling), is modeled by a convolution with a Lorentzian spectrum centered in zero with a width κ :

$$\mathcal{L}_{cav}(\omega) = \frac{1}{1 + \left(\frac{2\omega}{\kappa}\right)^2} \quad (6.6)$$

The cavity modified absorption and emission spectra are defined by :

$$\tilde{S}^{abs}(\omega) = \frac{(S_{fs}^{abs} * \mathcal{L}_{cav})(\omega)}{\int \mathcal{L}_{cav}(\omega)d\omega} \quad (6.7)$$

$$\tilde{S}^{emi}(\omega) = \frac{(S_{fs}^{emi} * \mathcal{L}_{cav})(\omega)}{\int \mathcal{L}_{cav}(\omega)d\omega} \quad (6.8)$$

Hamiltonian

In the presence of the cavity, the Hamiltonian of equation (6.1) is modified and reads [206] :

$$H = H_{e-p} + \hbar\omega_c a^\dagger a + i\hbar g(a^\dagger \sigma^- - a\sigma^+) \quad (6.9)$$

The second term describes the energy the cavity mode (at the cavity resonant frequency ω_c) while the last, already introduced in chapter 1, gives the coupling g between the exciton and the cavity. In analogy with section 1.3.1, the damping and dephasing term are introduced as Lindblad operators in the master equation :

$$L[C]\rho \equiv C\rho C^\dagger - \frac{1}{2}(C^\dagger C\rho + \rho C^\dagger C) \quad (6.10)$$

And the three operators taking into account respectively the cavity leaking rate κ , the spontaneous emission rate γ , and the pure dephasing γ^* are $C_1 \equiv \sqrt{\kappa}a$, $C_2 \equiv \sqrt{\gamma}\sigma^-$ and $C_3 \equiv \sqrt{\gamma^*}\sigma^+\sigma^-$.

In order to simplify the expression of the Hamiltonian, the polaron shift is introduced : the unitary transformation U is given by $U \equiv \sigma^+\sigma^- \otimes D + \sigma^-\sigma^+ \otimes \mathbb{1}$, with $D = e^{-\Omega}$ and $\Omega \equiv \sum_{\vec{k}} \left(\frac{g_{\vec{k}}^*}{\omega_k} b_{\vec{k}}^\dagger - \frac{g_{\vec{k}}}{\omega_k} b_{\vec{k}} \right)$. The Hamiltonian in the polaron frame reads :

$$\tilde{H} \equiv U^\dagger H U = \hbar\tilde{\omega}_X \sigma^+ \sigma^- + \hbar \sum_{\vec{k}} \omega_k b_{\vec{k}}^\dagger b_{\vec{k}} + \hbar\omega_{\text{cav}} a^\dagger a + i\hbar g(a^\dagger \sigma^- e^{-\Omega} - a\sigma^+ e^{\Omega}) \quad (6.11)$$

Where the polaron shift energy is absorbed in the definition of the exciton energy :

$$\tilde{\omega}_X = \omega_X - \sum_{\vec{k}} \left(\frac{g_{\vec{k}}^2}{\omega_k} \right) \quad (6.12)$$

For the ease of reading, the notation ω_X remains in use in further equations. We also note that in the polaron transformation picture, C operators become $\tilde{C} \equiv U^\dagger C U$, namely $\tilde{C}_1 = \sqrt{\kappa}a$, $\tilde{C}_2 = \sqrt{\gamma}\sigma^- e^{-\Omega}$ and $\tilde{C}_3 = \sqrt{\gamma^*}\sigma^+\sigma^-$.

Master equation

In the interaction picture, the master equation is given by :

$$\frac{d}{dt}\rho_I(t) = \frac{1}{i\hbar}[V_I(t), \rho_I(t)] + \sum_{j=1}^3 L[C_j] \rho_I \quad (6.13)$$

$$V_I = i\hbar g \left(e^{-i\delta t} e^{-\Omega_I(t)} a^\dagger \sigma^- - e^{i\delta t} e^{\Omega_I(t)} a \sigma^+ \right) \quad (6.14)$$

where $\delta = \omega_X - \omega_c$, $\Omega_I(t) = e^{it} \sum_{\vec{k}} \omega_k b_{\vec{k}}^\dagger b_{\vec{k}} \Omega e^{-it} \sum_{\vec{k}} \omega_k b_{\vec{k}}^\dagger b_{\vec{k}}$ and the sum corresponds

6.1. CAVITY EFFICIENCY INCLUDING THE PHONON WINGS : THEORETICAL APPROACH

to the three Lindblad operators C in the interaction picture. The populations evolution are given by :

$$\frac{d\langle a^\dagger a \rangle}{dt} = g e^{i\delta t} \langle e^{\Omega_I(t)} a \sigma^+ \rangle + g e^{-i\delta t} \langle e^{-\Omega_I(t)} a^\dagger \sigma^- \rangle - \kappa \langle a^\dagger a \rangle \quad (6.15)$$

$$\frac{d\langle \sigma^+ \sigma^- \rangle}{dt} = -g e^{i\delta t} \langle e^{\Omega_I(t)} a \sigma^+ \rangle - g e^{-i\delta t} \langle e^{-\Omega_I(t)} a^\dagger \sigma^- \rangle - \gamma \langle \sigma^+ \sigma^- \rangle \quad (6.16)$$

6.1.2 Cavity efficiency

In this section, we investigate a particular phenomenon : an excitation in the matter $t = 0$ which decays in the cavity mode and subsequently leaks out via the losses κ . This process can be straightforward or can include several back and forth between the cavity and the matter. The efficiency of this process, i.e. the efficiency of our single photon source, is thus given by the integrated probability of decay from the cavity towards the environment, $\beta = \kappa \int_0^\infty dt \langle a^\dagger a \rangle$ [207].

Expression of the cavity efficiency

As shown in appendix D, the terms in the population evolutions read :

$$e^{i\delta t} \langle e^{\Omega_I(t)} a \sigma^+ \rangle = g \int_0^t ds e^{(i\delta - \gamma_{all})(t-s)} \left(\langle \sigma^+ \sigma^- (s) e^{\Omega_I(t)} e^{-\Omega_I(s)} \rangle - \langle a^\dagger a (s) e^{-\Omega_I(s)} e^{\Omega_I(t)} \rangle \right) \quad (6.17)$$

Where the notation $\langle \sigma^+ \sigma^- (s) e^{\Omega_I(t)} e^{-\Omega_I(s)} \rangle$ stands for $Tr(\rho_I(s) \sigma^+ \sigma^- e^{\Omega_I(t)} e^{-\Omega_I(s)})$. In order to go further, one can use the Non-Interaction Blip Approximation introduced by Leggett et al. [208]. Here it means that the phonon bath is weakly modified by the exciton-photon evolution. Dekker [209, 210] and Orth et al. [211] showed that it is equivalent to :

$$\langle \sigma^+ \sigma^- (s) e^{\Omega_I(t)} e^{-\Omega_I(s)} \rangle \stackrel{\text{NIBA}}{\approx} \langle \sigma^+ \sigma^- (s) \rangle Tr(\rho_{th} e^{\Omega_I(t)} e^{-\Omega_I(s)}) \quad (6.18)$$

Where ρ_{th} is the density matrix at thermal equilibrium. The second part of the right hand side of this equation depends only on the time difference $t - s$. As shown in [206], this trace can be expressed as a function of $K(t)$:

$$Tr(\rho_{th} e^{-\Omega_I(s)} e^{\Omega_I(t)}) = K^*(t-s) \quad (6.19)$$

As a consequence, the population evolutions can be expressed in terms of the same $K(t)$ function :

$$e^{i\delta t} \langle e^{\Omega_I(t)} a \sigma^+ \rangle \simeq g \int_0^t ds e^{(i\delta - \gamma_{all})(t-s)} \left(\langle \sigma^+ \sigma^- (s) \rangle K(t-s) - \langle a^\dagger a (s) \rangle K^*(t-s) \right) \quad (6.20)$$

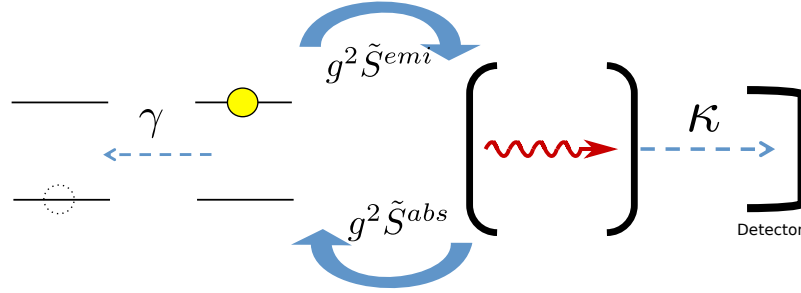


Figure 6.2 – The system is composed of a pseudo-two level system which decays with a rate γ and has an absorption/emission spectrum $\tilde{S}^{abs}/\tilde{S}^{emi}$. The decay can happen either as a loss or towards the cavity mode. When a photon is in the cavity mode, it can be either reabsorbed or extracted towards a detector. This simple sketch enables to understand how to compute the efficiency of the emitter in the cavity (namely the probability for it to decay by emitting a photon which is subsequently extracted).

where $\gamma_{all} = \gamma + \gamma^* + \kappa$.

With the help of equations (6.2) and (6.5), the efficiency of the cavity-coupled nanotube, at the cavity energy $\hbar\omega_c$, can be written as a function of the emission and absorption spectra :

$$\beta(\omega_c) = \frac{\kappa \tilde{S}^{emi}(\omega_c)}{\kappa \tilde{S}^{emi}(\omega_c) + \gamma \tilde{S}^{abs}(\omega_c) + \frac{\kappa \gamma}{g^2}} \quad (6.21)$$

Phenomenological interpretation

This formula can be understood in a simple way. As depicted in figure 6.2, the system is composed of :

- A two-level system (plus interactions with phonons) which decays from its excited state to its ground state at a rate γ
- A cavity which can switch from the excited state (a photon in the cavity) to its ground state (no photon in the cavity) at a rate κ .
- The excited two-level system can decay by emitting a photon in the cavity. At a given energy $\hbar\omega$, the probability for this decay is proportional to the Purcell factor, thus to the coupling g^2 , and the relative intensity of the emission at this energy $\tilde{S}^{emi}(\omega)$.
- Conversely, the excited cavity can decay when the photon is absorbed by the two level system with a rate proportional to $\tilde{S}^{abs}(\omega)$ and the coupling g^2 .

The probability of decay for the cavity coupled two-level system is given by $\gamma_{cav}(\omega) = \gamma + g^2 \tilde{S}^{emi}(\omega)$, the second term describing the acceleration due to the Purcell effect. The total decay probability for the cavity, which is the inverse of the

6.1. CAVITY EFFICIENCY INCLUDING THE PHONON WINGS : THEORETICAL APPROACH

storage time, is given by $\gamma_{storage}(\omega) = \kappa + g^2 \tilde{S}^{abs}(\omega)$. The second term corresponds to a decrease in the storage time, due to the probability for a photon to be absorbed by the nanotube. The four events described above can be written in terms of probabilities :

$$p_{NT \rightarrow Cav}(\omega) = \frac{g^2 \tilde{S}^{emi}(\omega)}{\gamma + g^2 \tilde{S}^{emi}(\omega)} \quad (6.22)$$

$$p_{NT \rightarrow Loss}(\omega) = \frac{\gamma}{\gamma + g^2 \tilde{S}^{emi}(\omega)} \quad (6.23)$$

$$p_{Cav \rightarrow Det}(\omega) = \frac{\kappa}{\kappa + g^2 \tilde{S}^{abs}(\omega)} \quad (6.24)$$

$$p_{Cav \rightarrow NT}(\omega) = \frac{g^2 \tilde{S}^{abs}}{\kappa + g^2 \tilde{S}^{abs}(\omega)} \quad (6.25)$$

Where NT denotes the nanotubes, Cav the cavity, $Loss$ pure losses (a photon emitted out of the cavity mode or a non-radiative decay), Det a photon extracted from the cavity and detected (useful loss). The efficiency corresponds to the probability for an excitation in the matter to decay into the cavity and to decay from the cavity towards a detector. Taking into account the possibility of re-absorption, the efficiency is given by :

$$\beta = p_{NT \rightarrow Cav} (1 + p_{Cav \rightarrow NT} p_{NT \rightarrow Cav} + \dots + (p_{Cav \rightarrow NT} p_{NT \rightarrow Cav})^n + \dots) p_{Cav \rightarrow Det} \quad (6.26)$$

And one recovers the equation 6.21.

Efficiency of the ZPL emission

In the previous chapters, only the coupling between a Lorentzian emitter and a cavity mode was considered. In such a case, let's compare the efficiency formula (6.21) with the results of chapter 1. The ZPL of a nanotube can be modeled by Lorentzian of width $\gamma + \gamma^*$. For the emission and the absorption spectra, one has :

$$S^{ZPL}(\omega) = \frac{4\pi}{\gamma + \gamma^*} \frac{1}{1 + \left(\frac{2(\omega - \omega_X)}{\gamma + \gamma^*}\right)^2}$$

Where $\hbar\omega_X$ is the exciton energy. Its convolution with $\mathcal{L}_{cav}(\omega)$ leads to a spectrum in cavity given by :

$$\tilde{S}^{ZPL}(\omega) = \frac{4\pi}{\gamma_{all}} \frac{1}{1 + \left(\frac{2(\omega - \omega_c)}{\gamma_{all}}\right)^2}$$

As a consequence, at the the cavity resonance frequency $\tilde{S}^{emi}(\omega_c) = \tilde{S}^{abs}(\omega_c) = \frac{4\pi}{\gamma_{all}}$. And the efficiency reads :

$$\beta_{Lorentzian} = \frac{\kappa}{\kappa + \gamma + \frac{\kappa\gamma\gamma_{all}}{4g^2}}$$

This result is exactly the one of eq. (1.63).

Now, the full nanotube spectrum $S^{emi}(\omega)$ is composed of the Lorentzian $S^{ZPL}(\omega)$ and the phonon wings $S^{PW}(\omega)$. Let's write it as a function of the branching ratio BR :

$$S^{emi}(\omega) = BR \cdot S^{ZPL}(\omega) + (1 - BR) \cdot S^{PW}(\omega) \quad (6.27)$$

The $K(t)$ function can also be written in two parts

$$K(t) = K^{ZPL}(t) + K^{PW}(t) \quad (6.28)$$

With $K^{ZPL}(t) \equiv BR$. By definition, the phonon wings do not contribute to the main line : $\left[\int_0^\infty e^{i\delta t} K^{PW}(t) dt \right]_{\delta=0} = 0$. As a consequence, one can approximate $K(t) \simeq K^{ZPL}(t)$ in the population evolutions of eq. (6.16), leading to :

$$\frac{d\langle a^\dagger a \rangle}{dt} \approx 2g^2 BR \cdot Re \left[\int_0^t ds e^{-\gamma_{all}(t-s)} \left(\langle \sigma^+ \sigma^- \rangle - \langle a^\dagger a \rangle \right) \right] - \kappa \langle a^\dagger a \rangle \quad (6.29)$$

$$\frac{d\langle \sigma^+ \sigma^- \rangle}{dt} \approx -2g^2 BR \cdot Re \left[\int_0^t ds e^{-\gamma_{all}(t-s)} \left(\langle \sigma^+ \sigma^- \rangle - \langle a^\dagger a \rangle \right) \right] - \gamma \langle \sigma^+ \sigma^- \rangle \quad (6.30)$$

For a pure dephasing γ^* much larger than the other losses, it leads to :

$$\frac{d\langle a^\dagger a \rangle}{dt} \approx 2g^2 BR \cdot \left(\langle \sigma^+ \sigma^- \rangle - \langle a^\dagger a \rangle \right) - \kappa \langle a^\dagger a \rangle \quad (6.31)$$

$$\frac{d\langle \sigma^+ \sigma^- \rangle}{dt} \approx -2g^2 BR \cdot \left(\langle \sigma^+ \sigma^- \rangle - \langle a^\dagger a \rangle \right) - \gamma \langle \sigma^+ \sigma^- \rangle \quad (6.32)$$

These expressions are the same than the ones of eq. (1.52) provided that the coupling is replaced by $g\sqrt{BR}$. To conclude, the coupling g^{tot} of the whole dipole (including the ZPL and the phonon wings) with the cavity is related to the ZPL coupling g^{ZPL} by :

$$g^{ZPL} = g^{tot} \sqrt{BR} \quad (6.33)$$

6.2 Experimental derivation of the cavity efficiency

In the previous section, the efficiency of an emitter (such as a carbon nanotube) in a cavity was derived in a very general way. It depends on five quantities : first the leaking rate of the cavity κ , second the decay rate of the emitter in the absence of

the cavity γ , third the coupling between the emitter and the cavity, and finally the absorption and emission spectra of the emitter.

In the following, the methods to measure the efficiency spectra are explained and the results of the fit to the theoretical model are given. The cavity length is varied to explore the dependence of the effect on the mode volume, and the asymptotic limits of the efficiency are given.

6.2.1 Experimental “reconstructed” spectra

For a given cavity length, the output spectrum can not be directly compared to the free-space spectrum as it covers only a small spectral portion of it. Nevertheless, if one sweeps the cavity energy, one obtains a “reconstructed spectrum” that maps out the efficiency of the CNT-cavity coupling as a function of the detuning. Even though this process is technically very simple, many biases can arise : first, if the nanotube undergoes spectral diffusion during the sweep, the reconstructed spectrum is distorted. Second, one must take care of cavity’s higher order modes contribution. One may also expect a distortion arising from the relative position of the nanotube to the field intensity maximum as a function of the energy of the cavity. However, the spectrum of a nanotube is only 10 nm broad (including the phonon wings) while $\lambda/2 \approx 450$ nm, and the intensity variation is slow close to a field maximum. As a consequence this effect is completely negligible.

Two different techniques are described below to reconstruct the cavity efficiency spectrum : one consists in sweeping the cavity length step by step at a slow pace. The second consists in scanning the cavity length at a fast pace in order to obtain an overall integration time as short as the free-space one.

Step-by step method

As the cavity linewidth (80 GHz to 500 GHz or 300 μ eV to 2 meV, depending on the vibrations) remains below the full nanotube spectrum width (at least 5 meV), a way to reconstruct the efficiency of the NT-cavity coupling consists in changing the cavity length step by step. Each step must be small enough so that there is an overlap in the range of wavelengths covered by the cavity for two consecutive positions. A spectrum is acquired at each step. Such a measurement is given in figure 6.3a : the map shows the intensity of the output of the cavity as a function of the emission energy (abscissa) and cavity length (ordinate).

In order to obtain the efficiency spectrum of the cavity coupled emitter from the map of figure 6.3a, two options are available : one consists in simply summing the map along its columns. If the dwell time of the cavity is identical for all wavelengths, the reconstructed spectrum fairly maps out the coupling efficiency. However, when the cavity TEM_{00} mode is tuned out of resonance with the ZPL towards the low energy, the cavity’s TEM_{01} mode can be in resonance with the blue side of the NT spectrum (this depends on the spacing between the transverse mode, which

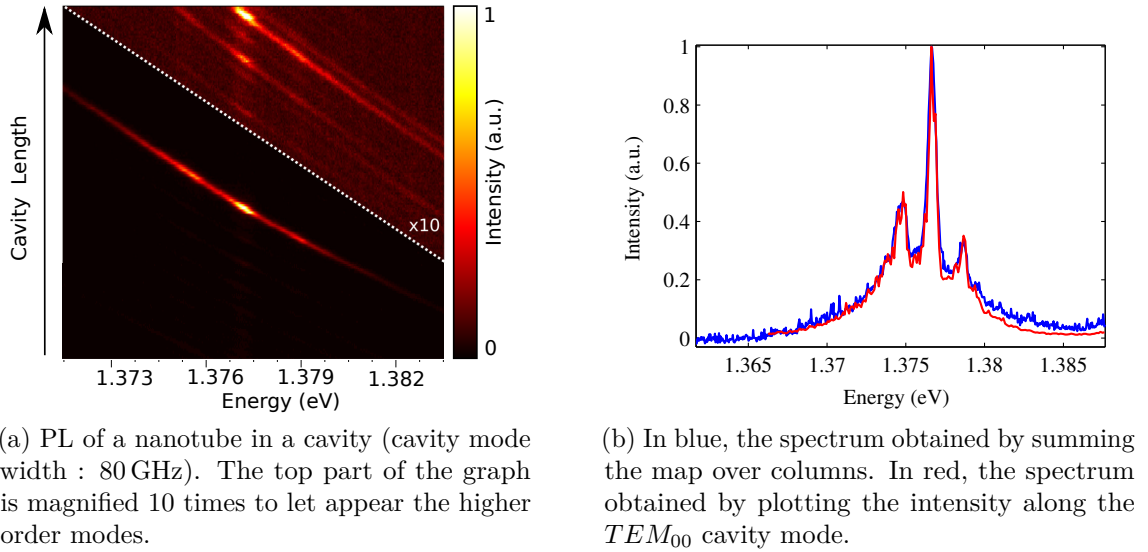


Figure 6.3 – Contribution of the high order mode for a cavity with low vibrations.

ultimately depends on the radius of curvature and length of the cavity, as shown in eq. (3.15)). More over, for a given cavity mode n , a small contribution of the high order mode of the $n - 1$ series can appear. As one can see in figure 6.3b, the contribution of the high order modes is usually much lower, if not negligible, than the one of the TEM_{00} .

Typically, each line in fig. 6.3a corresponds to an acquisition of 1 s, and it takes tens to hundreds of seconds to complete the full spectrum. As the acquisition time in free-space is typically of 1 s, a direct comparison is complicated due to residual spectral diffusion at time-scales longer than 1 s, which can disrupt the measurement. Indeed, when a measurement is repeated over and over on a same nanotube it yields some variability. These variations are neither seen with all the nanotubes nor all the time with a given nanotube. One explanation for these variations could be that during the runs, the cavity shifts sideways and thus decreases the coupling with the nanotube. An other explanation could be the intrinsic variability of the nanotube's emission spectrum. Indeed, for some nanotubes, spectral diffusion does not restrict to a mere spectral shift, but some changes in the spectral shape can occur during a short time every now and then. As the cavity acquisitions are long, such changes could occur during the acquisition, leading to a distortion of the spectrum.

This step by step method was used at the beginning of the study, with very stable nanotubes, studied with fiber A. In particular, the spectra shown in chapter 5 and the data published in [212] are done this way. Nevertheless, due to the lack of reproducibility with fibers B and C (small radius of curvature), this method was discarded for the study presented in this chapter.

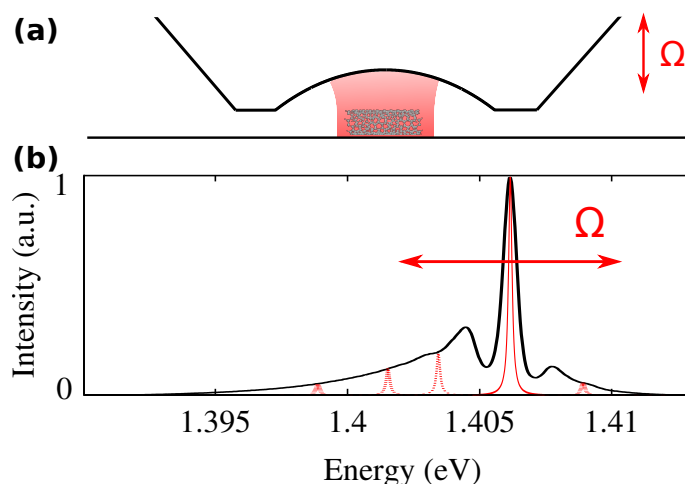


Figure 6.4 – a) A nanotube is in the cavity formed by a plane mirror and a concave one at the tip of an optical fiber. The cavity length oscillates at frequency Ω to cover the full nanotube spectrum. b) A single nanotube PL spectrum in solid black. The spectrum of the cavity, when in resonance with the ZPL, is depicted in solid red. As the cavity length oscillates, the cavity spectrum is shifted to the dashed red positions.

Fast-scan method

The TEM_{00} mode of the cavity is positioned at an energy just below the red-wing of the nanotube's spectrum. By means of a fast longitudinal translation with the piezo stage, its position is then tuned up to an energy just above the blue-wing of the nanotube's spectrum. The process is repeated back and forth about 25 times in 1 s. This process is depicted in fig. 6.4. Assuming that, in average, the cavity spends an equal amount of time at each position¹, the output obtained is directly proportional to the CNT-cavity coupling efficiency. With this fast scan method, the total acquisition time is the same than the acquisition time in free-space ; and the possible effects of residual spectral diffusion are the same. The price to pay for this shorter acquisition time is obviously a decrease in the signal intensity compared to the step by step method.

In order to evaluate the reproducibility of the measurements, a method consists in acquiring a given number of spectra, with the fast-scan method, and to evaluate how different they are from each other. Actually, most of the spectra are similar, but a few of them differ strongly : they typically display a lower maximum intensity and

¹It is not trivial that that the driven motion of the cavity and its additional natural vibration end up with a equal amount of time spent at each position. Let's first note that the spectral range of the tuning is chosen so that the start or stop position are out of resonance, so that an excess of time spent in these positions does not affect the measurement. Furthermore, this fast-scan was tried while sending a white light in an empty cavity. The output intensity was constant as a function of the wavelength, showing the absence of measurable distortions.

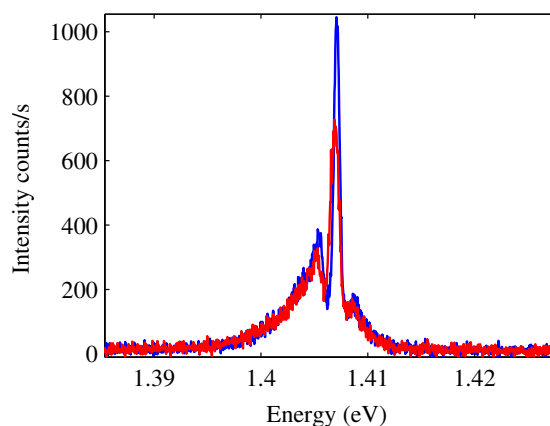


Figure 6.5 – In blue the cavity coupled nanotube’s spectrum, obtained by the fast scanning method. In red, the same measure taken a few seconds later : significant differences in the ZPL and wing intensities are observable. Experimental details : pulse wave excitation at 800 nm at $0.7 \cdot P_{sat}$. Temperature 15 K. The nanotube under study has already been introduced as *Ganga*, refer to table 5.4. Unless otherwise mentioned, all the following figures are obtained under the same experimental condition with the same nanotube.

a broader spectral width, as shown in figure 6.5. This effect may be due spectral diffusion or blinking, as discussed in section 6.2.1.

Analyzing all the spectra individually is not necessary and may be particularly unsuited if the emission intensity, and thus the signal-to-noise ratio, is low. Consequently, it is interesting to work with averaged spectra. Let’s take fig. 6.6 as an example : it shows two maps with fifty acquisitions for a single nanotube. On the left, are the raw data, and on the right the processed data. The residual spectral diffusion is taken care of by shifting the spectra with respect to the ZPL before summing. In order to eliminate the distorted spectra, the ZPL is fitted to a Lorentzian for each spectrum. Here, the 36 spectra kept have a mean of $410 \pm 30 \mu\text{eV}$ while 14 spectra discarded have a mean width larger than $600 \mu\text{eV}$.

The result of the average with and without the distorted spectra is given in figure 6.7. The difference is moderate, but the presence of these distorted spectra can lead to an over estimate of the intensity emitted in the wings compared to the intensity emitted in the ZPL. As this would lead to an overestimate of the coupling efficiency, the distorted spectra are systematically removed from our measurements.

Finally, several bunches of fifty measurements are performed. Each bunch is averaged as described. In figure 6.8, one can see that this method is very reproducible. This is why it was chosen to carry out all the following measurement that way.

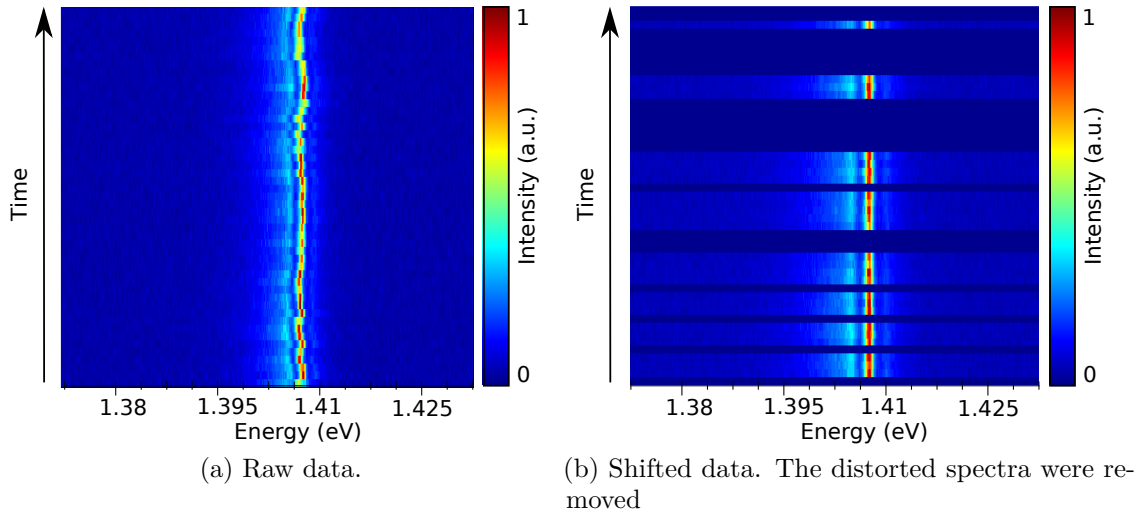


Figure 6.6 – Repeated PL spectrum measurements for a carbon nanotube in cavity. Each horizontal line corresponds to a different run. Nanotube *Ganga*, refer to fig. 6.5 and table 5.4.

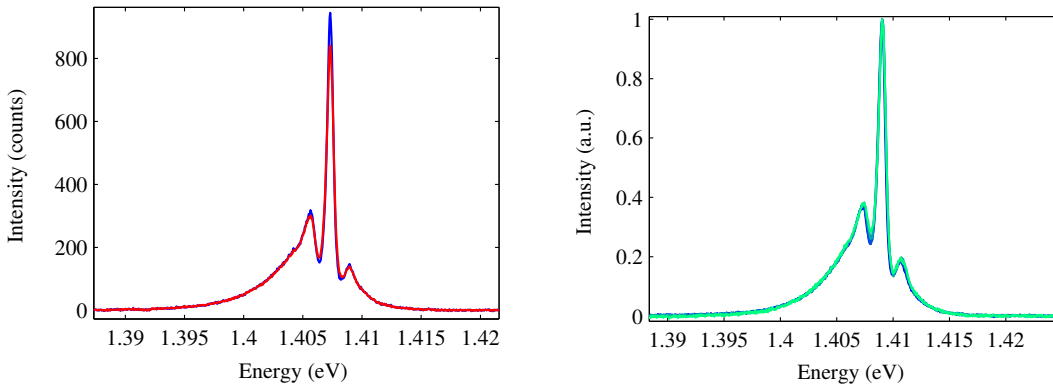


Figure 6.7 – In blue the cavity coupled nanotube’s spectrum, obtained by shifting the scans and removing the distorted ones and averaging all the remaining ones. In red, the average without removing the distorted spectra . Nanotube *Ganga*, refer to fig. 6.5 and table 5.4.

Figure 6.8 – Repeated PL spectrum measurements for a carbon nanotube in cavity. Each color corresponds to an average of fifty runs. Nanotube *Ganga*, refer to fig. 6.5 and table 5.4.

6.2.2 Fit of the experimental data

In the formula giving the efficiency in cavity, some parameters can be evaluated independently. The cavity leaking rate κ for example can be estimated either from the parameters of the mirrors (transmission and losses) or from an empty cavity ring-down spectroscopy, as described in section 3.4.2. The decay rate of the emitter in the absence of the cavity, noted γ is the same as the decay rate measured in free-space γ_{fs} in section 5.2.3. It can thus be obtained from transient measurements in free-space.

In order to fit the experimental cavity efficiency to the model of eq. (6.21), γ and κ were systematically obtained by these independent methods. This way, the only free parameter of the fit was g , which is the key parameter of the effect investigated.

Absorption spectrum

The expression of the cavity efficiency in equation (6.21) includes the absorption spectrum of the emitter. Unfortunately, the absorption spectrum of a single nanotube is difficult to access experimentally because of its low absorption cross-section [213]. This means that the absorption is below the signal-to-noise ratio of a typical absorption experiment. In order to overcome this issue, Liu et al. [214] used crossed-polarization techniques to record the absorption of an individual nanotube on S_{22} . However, the absorption on S_{11} (ie : corresponding to the observed emission energy) remains out of reach at the present time.

In chapter 3, the typical photoluminescence spectrum of a nanotube was described and its main features were explained. It consists in a main Lorentzian line called the ZPL and phonon-wings. For a Lorentzian line at energy ω_X , the corresponding absorption is a Lorentzian line at the same energy ω_X [172].

In the case of a photon emission at $\omega_X - \delta\omega$ assisted by the emission of a phonon with energy $\delta\omega$, the corresponding absorption happens when a photon at energy $\omega_X + \delta\omega$ is absorbed and a phonon with energy $\delta\omega$ is emitted. In other words, the absorption spectrum is the mirror image of the emission spectrum with respect to ω_X . One can consider that a localized exciton coupled to phonons in a nanotube is similar to the case of a molecule containing a two-level system coupled to the vibrational modes of the molecule. It is thus no surprise that the phenomenology is similar to the Franck-Condon effect. Practically, the emission spectrum of each nanotube investigated is recorded and the corresponding absorption is numerically obtained, as shown in fig. 6.9.

Fit quality

In fig. 6.10, the blue dots show the efficiency of a nanotube in cavity², measured as described in section 6.2.1. The black dashed line is the normalized free-space

²The experiment is done under pulsed excitation, so as to compare directly with the transient measurement experiments discussed in chapter 5.

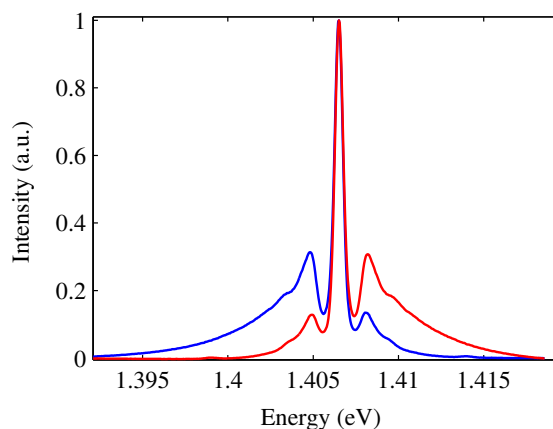


Figure 6.9 – In blue the emission spectrum of a single carbon nanotube in free-space. In red, the absorption spectrum is numerically obtained by taking the mirror image with respect to the ZPL (an approximation valid in the case of a single electronic transition coupled to a phonon bath). Average over a hundred spectra acquired in 1 s. Nanotube *Ganga*, refer to fig. 6.5 and table 5.4

photoluminescence spectrum. The difference between the two is clearly visible : in the cavity, the phonon wings are enhanced compared to the main line.

The absorption spectrum is obtained as described above. The cavity leaking rate is $1/\kappa = 15$ ps and the emission rate in free-space is $1/\gamma_{FS} = \tau_{FS} = 71$ ps. The experimental efficiency is fitted to eq. (6.21), as depicted with a red line in the figure. The value obtained for the coupling is $\hbar g^{tot} = 36$ μ eV. It corresponds to an efficiency of $\beta = 30\%$ at the peak of the spectrum, as reported on the right axis of the figure.

As one can see, the fit captures very well the change of relative intensity in the different parts of the spectrum. In order to estimate the uncertainty on the measured value of g^{tot} , the experiment is repeated ten times and each set of data is fitted. The typical standard deviation is 10% of the mean value.

6.2.3 Evolution with cavity volume

In this section, the cavity length is tuned to investigate how the exciton-phonon-cavity coupling evolves as a function of the cavity mode volume.

Aspect of the spectra

As already introduced in section 5.2.1, the tunability of the fibered micro-cavity can be used to measure the effect of the coupling for several orders of the Fabry-Perot and thus different mode volumes. In the case of the cavity used in the following experiments, formed with fiber C, the minimum length obtained corresponds to $6\frac{\lambda}{2}$ (mainly due to the concave depression depth and the field penetration in the mirrors). Though this length is the one for which the highest Purcell factor is obtained, it

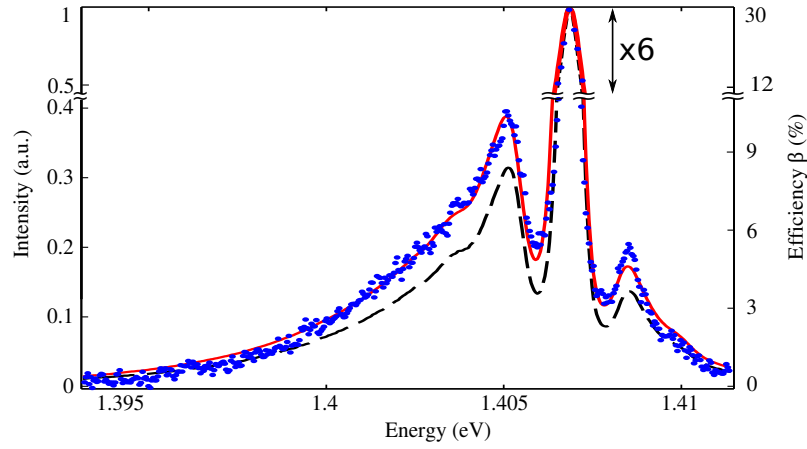


Figure 6.10 – In dashed black, the experimental emission spectrum in free-space. The blue dots give the measured efficiency in cavity (left scale). The red line is a fit obtained from eq. (6.21). The resulting efficiency is given by the right scale. Average over a hundred spectra acquired in 1 s (total). Nanotube *Ganga*, refer to fig. 6.5 and table 5.4.

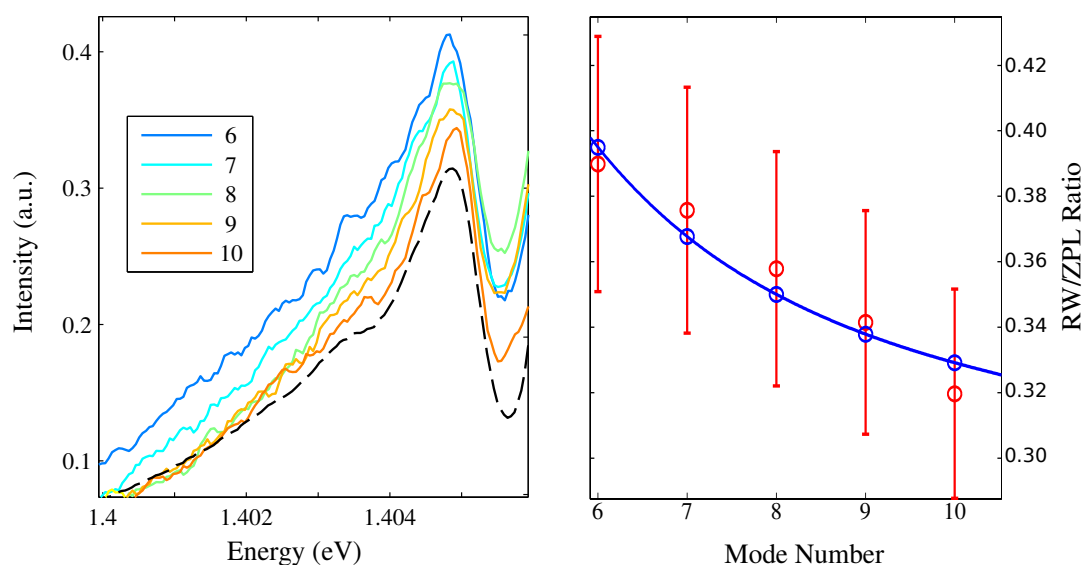
is possible to explore the coupling for different cavity lengths (and thus different mode volumes), provided that the cavity remains stable. Here, the cavity radius of curvature is $10\ \mu\text{m}$, so the stability limit is about $20\frac{\lambda}{2}$.

However, the measurements carried out are restricted to a narrower range for two reasons. First a constraint of time : acquiring enough spectra to obtain uncertainty estimation is a long process. Even though the nanotubes used in this study are buried in polystyrene, they still display variations over time and it is consequently better to minimize the amount of time between measurements that are compared. The second reason is that the Purcell effect decreases with the volume. This means that the longer the cavity length, the longer the acquisition time for a given signal-to-noise ratio. In the different sets of experiments carried out, cavity lengths up to $12\frac{\lambda}{2}$ were explored. Here we present a more restricted study, but with better accuracy, and for which all the data were acquired within 24h.

In figure 6.11a, a zoom is made on the red phonon wing of the carbon nanotube and the evolution as a function of the cavity mode number is visible in color plots. As the reader can see, when the cavity volume decreases, the phonon wing increases at a faster pace than the ZPL. In order to exemplify this phenomenon, the ratio of maximum intensity between the red wing and the ZPL is plot in fig. 6.11b. A theoretical estimation, arising from eq. (6.21) is given in blue.

Comparison with other methods

Each efficiency spectrum displayed in figure 6.11 can be fitted to the model given in eq. (6.21), and a coupling factor g^{tot} can be extracted. In figure 6.12a, one can see that this coupling factor evolution is consistent with the square root of the volume, as



(a) Evolution of the intensity of the same nanotube coupled for selected mode volumes, labeled by mode number. The dashed line is the free-space spectrum. The x axis gives the energy of the cavity mode. The spectra are normalized at the ZPL (maximum equal to 1).

(b) Red dots : Ratio of intensity between the maximum of the red wing and the maximum of the ZPL as a function of the mode number. The errorbars come from repeated measurements. The solid blue line gives a theoretical estimation, coming from eq. (6.21). The blue dots underline the value obtained for a given mode number.

Figure 6.11 – Efficiency spectra for a cavity coupled CNT as a function of the mode number (from $6\frac{\lambda}{2}$ to $10\frac{\lambda}{2}$). Each curve corresponds to an average over fifty spectra acquired in 1 s (total). Nanotube *Ganga*, refer to fig. 6.5 and table 5.4

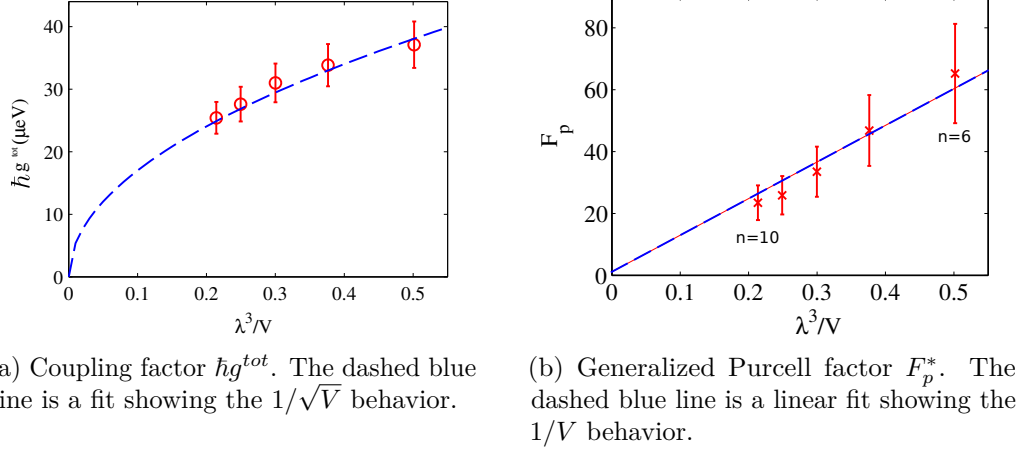


Figure 6.12 – Coupling factors and Purcell factors for different mode volumes extracted from eq. (6.21) in red. The mode volume is deduced from the cavity free spectral range (FSR). Each point is obtained from an average over fifty spectra acquired in 1 s (total). The measurement is repeated 10 times to obtain error bars. Nanotube *Ganga*, refer to fig. 6.5 and table 5.4

expected from eq. (5.31). In fig. 6.12b, the Purcell factor is obtained from eq. (5.29), with a quantum yield $\eta_{tot} = 2 \pm 1\%^3$. The slope of $F_p^* = f(\lambda^3/V)$ gives an estimated quality factor of 6500 ± 3500 , while the measured one is 3500 ± 100 . We ascribe this discrepancy to an underestimation of the free-space quantum yield of this nanotube.

The value of g^{tot} obtained from the above mentioned fits can be compared to the value of g^{ZPL} obtained from the transient method by means of eq. (6.33). For the nanotube *Ganga*, the branching ratio is $BR = 0.40$. The transient measurement method was presented in section 5.2.3 : the free-space and cavity transient of the same nanotube are measured and the corresponding coupling factor g^{ZPL} is obtained from eq. (5.31).

The result of the transient measurement is compared to the value obtained from the model in figure 6.13 : the black crosses give the value of g^{ZPL} extracted from transient measurements (the corresponding error bars come from the uncertainty in the extraction of the lifetimes). One can see that the two different estimations (cavity efficiency fit in red, transient measurement in black) are in good agreement with each other. The slightly lower values obtained from the transient method could be explained by the vibrations of the cavity, as discussed in appendix C.

³The uncertainty on the efficiency is higher than the one announced in section 5.2.1, due to a change of lens/fiber as well as an aging of the sample, potentially modifying the effective collection efficiency of our setup.

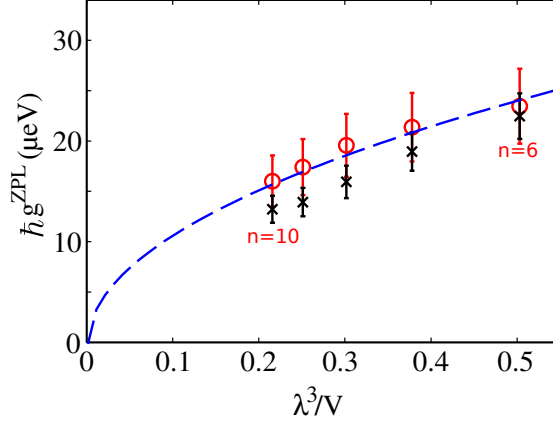


Figure 6.13 – Coupling factors g^{ZPL} for different mode volumes, from lifetime measurements (black crosses), and spectrum distortion as given by eq. (6.21) (red dots). The dashed blue line shows the $1/\sqrt{V}$ behavior. The mode volume is deduced from the cavity free spectral range (FSR). Each point is obtained from an average over fifty spectra acquired in 1 s. The measure is repeated 10 times to obtain error bars. Nanotube *Ganga*, refer to fig. 6.5 and table 5.4

Asymptotic behavior

In the measurements, the coupling between a single carbon nanotube and the cavity remains below 50 μeV , which is roughly an order of magnitude lower than the spectral width of the ZPL. For such coupling values, it was shown in figures 6.10 and 6.11 that the single-photon source efficiency increases faster when the cavity is tuned in resonance with the phonon wings than with the ZPL.

In order to understand better this effect, it is worth exploring the asymptotic behavior of eq. (6.21). Let's explore the case in which the cavity is in resonance with the ZPL, at a frequency ω_{ZPL} and the coupling overcomes the loss rates ($g \gg \kappa, \gamma$)⁴. Since, at the ZPL frequency, the normalized absorption and emission intensity are equal, the efficiency is simply the photonic losses over the total losses :

$$\beta_{g \rightarrow \infty}(\omega_{ZPL}) = \frac{\kappa}{\kappa + \gamma} \quad (6.34)$$

When the cavity is in resonance with a phonon wing at $\omega_{ZPL} + \delta\omega$, the absorption and emission spectra are related to each other through a Boltzmann distribution :

$$\frac{\tilde{S}^{emi}(\omega_{ZPL} + \delta\omega)}{\tilde{S}^{abs}(\omega_{ZPL} + \delta\omega)} \approx \exp\left(-\frac{\hbar\delta\omega}{k_b T}\right) \quad (6.35)$$

where T is the temperature, and k_b the Boltzmann constant. The asymptotic behavior is given by :

⁴In such a case, one switches to the strong coupling regime, and a Rabi splitting becomes visible. However the formula for the integrated efficiency β should still hold.

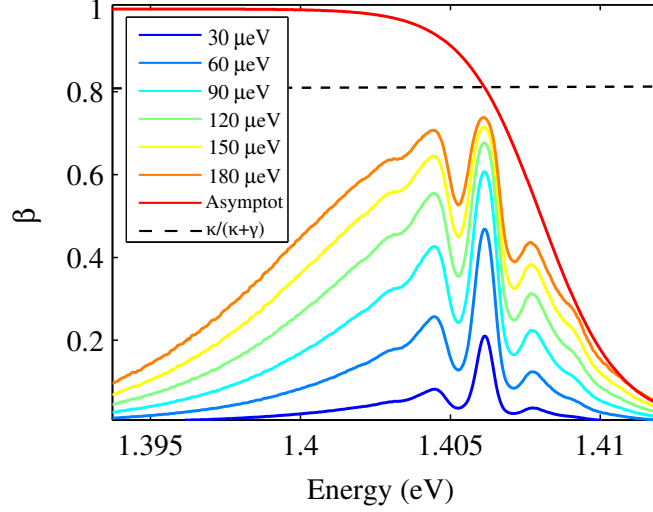


Figure 6.14 – Theoretical evolution of the efficiency spectrum for different couplings $\hbar g^{tot}$ (still low enough to remain in the weak coupling regime). The red line corresponds to the asymptotic efficiency $\beta_{g \rightarrow \infty}(\omega_{ZPL} + \delta\omega)$ while the dashed black one corresponds to the ZPL limit $\frac{\kappa}{\kappa + \gamma}$. Here $T = 15$ K. Nanotube *Ganga*, refer to table 5.4.

$$\beta_{g \rightarrow \infty}(\omega_{ZPL} + \delta\omega) = \frac{\kappa}{\kappa + \gamma \exp(-\frac{\hbar\delta\omega}{k_b T})} \quad (6.36)$$

In figure 6.14, the cavity efficiency is simulated for different couplings $\hbar g^{tot}$ for the nanotube investigated in section 6.2.3. The asymptotic limit for the ZPL is drawn in dashed black and the asymptotic behavior of the spectrum is depicted by a solid red line. At the limit the efficiency is almost constant on the red side, but remains lower on the blue side because at low temperature the absorption of phonons is suppressed.

In other words, this phenomenon can be viewed as a non-coherent exchange of energy : on the blue side, a photon emitted in the cavity mode has a high chance of being reabsorbed (emission of a phonon) before it leaks out. On the contrary, on the red side, if a photon is emitted in the cavity mode, it has very low chances of being reabsorbed because it would need the absorption of a phonon. Interestingly, for high coupling values, this process enables to overcome the usual limit of eq. (6.34) and to reach a near unity efficiency.

Conclusion

In chapter 5, we had shown that cavity embedded carbon nanotube displayed a strong anti-bunching when the cavity mode was resonant with their zero phonon line. In this chapter, we have demonstrated that it was the case even when the cavity

was tuned in resonance with one of the two wings of the spectrum, and we have measured the effective single-photon source efficiency of the source as a function of the cavity energy.

In order to account for the Purcell enhancement of the wings, we developed a theoretical model, extending the results described in chapter 1 to a non-Lorentzian emitter. In this model, the system is composed of an emitter box which can decay towards the environment (pure loss) at a rate γ and towards the cavity box at a rate proportional to the coupling g^2 and the emission spectrum of the nanotube \tilde{S}^{emi} . An excitation in this second box can leak out of the cavity (useful losses) at a rate κ or be reabsorbed with a rate proportional to the coupling g^2 and the absorption spectrum of the nanotube \tilde{S}^{abs} .

The experimental measurement were fitted to the efficiency predicted with this model, and the evolution of the efficiency was observed as a function of the cavity volume. Decreasing the cavity volume, or more generally increasing the coupling g , yields a faster increase of the phonon wings than of the ZPL. At the asymptotic limit, the efficiency of red side of spectrum should approach unity (while the blue side efficiency would remain limited at cryogenic temperature). The range of tunability obtained, spanning over several meV), could be a milestone towards multiplexing with single-photon sources.

Conclusion

Individual single-wall carbon nanotubes are impressive for their mechanical and electronic properties [14, 15]. Their optical study has also yielded appealing results, such as the tunability of the emission energy with the diameter, the electrical excitation [82] and the ability to behave as a single-photon source [21]. However, their emission origins remain unclear, its efficiency is low and the unusual spectral shape of the photoluminescence results from peculiar electron-phonon coupling.

In such quasi one-dimensional nanostructures, the exciton binding as well as the dynamical carrier interactions (Auger effects) are particularly strong. Consequently, these original emitters may bring up new features in the cavity quantum electrodynamics regime, when few - an ultimately one - excitations are tightly coupled to a very limited number of emission modes.

In order to dig into these phenomena, our approach was to study the very same single emitter in free-space and in the CQED regime by means of an adjustable cavity. For that, we built a spectrally and spatially tunable Fabry-Perot cavity. The nanotubes were deposited on a planar mirror, and a second mirror was manufactured at the apex of an optical fiber. This configuration enabled a reproducible and reversible free-space to cavity switch by bringing the fiber at the location of the emitter and by adjusting the distance between the two mirrors to tune the frequency of the cavity. This cavity device has numerous assets : mode volumes as low as $2\ \mu\text{m}^3$, quality factors up to 10^5 , adaptability to any kind of emitter within its reflection stop-bands, possibility to compare the behavior of the very same emitter with and without the cavity, ability to change the mode volume (adjusting the length by steps of $\lambda/2$), and ability to couple the emission to a fiber, which is convenient for applications.

With this setup we observed the rise of cavity quantum electrodynamics effects with carbon nanotubes by analyzing the evolution of the dipole-cavity coupling as a function of the cavity volume. For the lowest volumes, we obtained a strong acceleration of the spontaneous emission rate, due to Purcell factors above 100. In such cases, 99% of the light was emitted into the cavity mode, and the effective efficiency of the source reached up to 50%, leading to a brightness of up to 10%. The anti-bunching of photons was demonstrated both in free-space and in cavity, with a typical value of the second-order correlation function at zero delay of 0.03 ± 0.02 .

It turned out that the Purcell enhancement, as well as the anti-bunched emission, were strong not only at the ZPL frequency but also when the cavity was in resonance with any part of the phonon broaden nanotube spectrum. In order to account for this effect, we extended the generalized Purcell model [35] to emitters undergoing exciton-phonon coupling. We showed that the emission in the wings was enhanced more strongly than on the main line, and that eventually, if the coupling increased, the efficiency should remain low on the blue side but should tend toward unity on the red side. This would lead to an almost constant efficiency over a spectral range more than a hundred times higher than the cavity spectral width, opening the way

to extensive multiplexing.

This experiment has a number of perspectives. In terms of applications, the efficiency could be increased by reducing the volume of the cavity (by reducing the concave mirror depression depth, for example) and by obtaining carbon nanotubes with lower spectral widths. Indeed, CNTs have all their atoms at their surface, and thus controlling the surroundings or wrapping them into chemical molecules is a mean of tuning their optical properties [215]. Electrical excitation is already well studied [29] and could be implemented with this setup for a stamped or suspended nanotube. Interestingly, as quantum transport in nanotubes is well investigated, Coulomb blockade [216] could be used to control the injection of charge carriers, and thus master a single-photon source at the single excitation level. In the telecoms bands, single-photon emission was demonstrated [27, 28]. Switching to such wavelengths would only require to change the diameter of the nanotubes. Going to room temperature may require more efforts. Though it doesn't prevent anti-bunching [27], it is accompanied by a broadening of the emission, and a consequent collapse of the Purcell factor. In the dielectric cavity approach, an alternative path using plasmonic resonators is considered.

For quantum cryptography, a figure of merit yet to be demonstrated is indistinguishability. In free-space, the indistinguishability, given by the ratio between the spontaneous emission rate to the total dephasing, is below 2%. However, when a nanotube is coupled to a cavity, the cavity acts as the effective emitter, incoherently pumped by the nanotube. With our parameters, the theoretical indistinguishability, obtained from the work of Grange et al. [205], would be 25%. Counter intuitively, this value could increase if the ratios κ/γ and g/γ decreased. For example, going to room temperature, and thus broadening the spectrum, may significantly improve the indistinguishability (at the expense of the brightness).

Beyond the weak coupling regime, two other pathways would be interesting. The first would be a single-nanotube based laser. In that case, the cavity finesse must be increased in order to let the storage time overcome the spontaneous emission lifetime. Several photons would then co-exist in the cavity mode, while the nanotube would be repopulated by the pump, leading to stimulated emission.

Nevertheless, the most interesting prospect relies in the strong coupling regime. Currently, the ratio between the coupling and the losses $g/(\gamma + \gamma^*) \sim 0.1$ falls an order of magnitude too low. However, in the last months, several groups have demonstrated photoluminescence signals with a spectral width $\hbar(\gamma + \gamma^*) < 50 \mu\text{eV}$, roughly an order of magnitude lower than our current values. With such emitters, the strong coupling seems reachable, provided that the cavity linewidth remains below this value, and measurable if no artifacts (such as vibrations) broaden the cavity width. In this regime, the exchange of energy between the cavity and the nanotube becomes coherent, leading to mixed light-matter quasi-particles called cavity polaritons.

The physics of cavity polaritons strongly depends on the dimensionality of their matter part. The two-dimensional cavity polaritons have yielded Bose-Einstein

CONCLUSION

condensation [217], as well as the generation of twin photons [218], while their zero-dimensional counterparts are investigated for optical single-photon switches [219]. Due to their narrow diameter (below 1 nm), the high interaction between charge carriers and the associated strength in the exciton binding, carbon nanotubes are expected to give rise to strong non-linear polaritonic effects. In particular, the Rabi splitting is proportional to the square root of the number of photons in the cavity. If a photon is resonantly absorbed, then a second absorption is blocked because the corresponding transition is no longer resonant. This photon blockade effect is a path to all optical information processing.

To conclude, this work showed that carbon nanotubes are excellent candidates for an on-demand efficient single-photon source at room temperature in the telecoms wavelengths. Further strengthening of the coupling may open the way to the very rich physics of one-dimensional cavity polaritons. And conversely, cavity polaritons could be a tool to understand better the diffusion, and localization properties of excitons in carbon nanotubes. Finally, the original setup built here is extremely versatile and could be used to couple to other types of emitters, such as nano-diamonds or molecules.

REFERENCES

Writing a thesis is a long, and sometimes complicated, task. Especially when it comes to introduction chapters : one must explain in its own way some theories and concepts that have already been very well written in other works. It is no secret that such chapters are often very alike each other from one thesis to the next. Before giving all the references, I would like to list a few thesis I closely followed while writing the introductory part of this work :

- In the first chapter, the Jaynes-Cummings Hamiltonian discussion was inspired from the thesis of Valerian Giesz [45].
- In the same chapter, the discussion of the different kinds of solid-state emitters was inspired by the work of Mathieu Munsch [55].
- The chapter introducing the basic concepts concerning carbon nanotube follows a long series of works from the group, namely the thesis of Sebastien Berger [41], Fabien Vialla [92] and Benjamin Langlois [93].
- The chapter concerning the properties of fibered Fabry-Perot cavities is closely inspired by the works of our collaborators in LKB, in particular the theses of Benjamin Besga [137] and Sebastien Garcia [149].
- In chapter 4, the paragraph concerning exciton trapping and Auger benefited from the work of Christophe Galland [168].
- Finally, the discussion about phonon wings is a summary of the extensive work published by Fabien Vialla [92].

The full list of references is given below :

- [1] Albert Einstein. The photoelectric effect. *Ann. Phys*, 17(132):4, 1905. 1, 259
- [2] G. N. Lewis. "i therefore take the liberty of proposing for this hypothetical new atom, which is not light but plays an essential part in every process of radiation, the name photon.". *Nature*, 118(18):874–875, Dec. 1926. 1, 259
- [3] H. J. Kimble, M. Dagenais, and L. Mandel. Photon antibunching in resonance fluorescence. *Phys. Rev. Lett.*, 39:691–695, Sep 1977. 1, 259
- [4] Philippe Grangier, Gerard Roger, and Alain Aspect. Experimental evidence for a photon anticorrelation effect on a beam splitter: a new light on single-photon interferences. *EPL (Europhysics Letters)*, 1(4):173, 1986. 1, 259

-
- [5] C. K. Hong and L. Mandel. Experimental realization of a localized one-photon state. *Phys. Rev. Lett.*, 56:58–60, Jan 1986. [1](#), [259](#)
- [6] Artur K Ekert. Quantum cryptography based on bell’s theorem. *Physical review letters*, 67(6):661, 1991. [1](#), [259](#)
- [7] Alexios Beveratos, Rosa Brouri, Thierry Gacoin, André Villing, Jean-Philippe Poizat, and Philippe Grangier. Single photon quantum cryptography. *Physical Review Letters*, 89(18):187901, 2002. [1](#), [259](#)
- [8] Gilles Brassard, Norbert Lütkenhaus, Tal Mor, and Barry C. Sanders. Limitations on practical quantum cryptography. *Phys. Rev. Lett.*, 85:1330–1333, August 2000. [1](#)
- [9] Emanuel Knill, Raymond Laflamme, and Gerald J Milburn. A scheme for efficient quantum computation with linear optics. *nature*, 409(6816):46–52, 2001. [1](#), [259](#)
- [10] Jeremy L O’Brien, Akira Furusawa, and Jelena Vučković. Photonic quantum technologies. *Nature Photonics*, 3(12):687–695, 2009. [1](#), [259](#)
- [11] N Somaschi, V Giesz, L De Santis, JC Loredano, MP Almeida, G Hornecker, SL Portalupi, T Grange, C Anton, J Demory, et al. Near-optimal single-photon sources in the solid state. *Nature Photonics*, 2016. [1](#), [180](#), [259](#)
- [12] Kristiaan De Greve, Leo Yu, Peter L McMahon, Jason S Pelc, Chandra M Natarajan, Na Young Kim, Eisuke Abe, Sebastian Maier, Christian Schneider, Martin Kamp, et al. Quantum-dot spin-photon entanglement via frequency downconversion to telecom wavelength. *Nature*, 491(7424):421–425, 2012. [1](#), [260](#)
- [13] Sumio Iijima et al. Helical microtubules of graphitic carbon. *nature*, 354(6348):56–58, 1991. [1](#), [62](#), [260](#)
- [14] J.-P. Salvetat, J.-M. Bonard, N.H. Thomson, A.J. Kulik, L. Forró, W. Benoit, and L. Zuppiroli. Mechanical properties of carbon nanotubes. *Applied Physics A*, 69(3):255–260, 1999. [2](#), [205](#), [260](#)
- [15] Erik T Thostenson, Zhifeng Ren, and Tsu-Wei Chou. Advances in the science and technology of carbon nanotubes and their composites: a review. *Composites science and technology*, 61(13):1899–1912, 2001. [2](#), [205](#), [260](#)
- [16] Michael J O’connell, Sergei M Bachilo, Chad B Huffman, Valerie C Moore, Michael S Strano, Erik H Haroz, Kristy L Rialon, Peter J Boul, William H Noon, Carter Kittrell, et al. Band gap fluorescence from individual single-walled carbon nanotubes. *Science*, 297(5581):593–596, 2002. [2](#), [64](#), [65](#), [102](#), [260](#)

REFERENCES

- [17] Frank Henrich, Wenshan Li, Regina Fischer, Sergei Lebedkin, Ralph Krupke, and Manfred M Kappes. Length-sorted, large-diameter, polyfluorene-wrapped semiconducting single-walled carbon nanotubes for high-density, short-channel transistors. *ACS nano*, 10(2):1888–1895, 2016. [2](#), [63](#), [260](#)
- [18] Feng Wang, Gordana Dukovic, Louis E Brus, and Tony F Heinz. The optical resonances in carbon nanotubes arise from excitons. *Science*, 308(5723):838–841, 2005. [2](#), [59](#), [260](#)
- [19] Yuhei Miyauchi, Riichiro Saito, Kentaro Sato, Yutaka Ohno, Shinya Iwasaki, Takashi Mizutani, Jie Jiang, and Shigeo Maruyama. Dependence of exciton transition energy of single-walled carbon nanotubes on surrounding dielectric materials. *Chemical physics letters*, 442(4):394–399, 2007. [2](#), [60](#), [260](#)
- [20] F. Vialla, Y. Chassagneux, R. Ferreira, C. Roquelet, C. Diederichs, G. Cassabois, Ph. Roussignol, J. S. Lauret, and C. Voisin. Unifying the low-temperature photoluminescence spectra of carbon nanotubes: The role of acoustic phonon confinement. *Phys. Rev. Lett.*, 113:057402, July 2014. [2](#), [4](#), [20](#), [103](#), [110](#), [116](#), [120](#), [123](#), [260](#)
- [21] Alexander Hoge, Christophe Galland, Martin Winger, and Atac Imamoglu. Photon antibunching in the photoluminescence spectra of a single carbon nanotube. *Physical Review Letters*, 100(21):217401, 2008. [2](#), [7](#), [115](#), [131](#), [162](#), [205](#), [260](#)
- [22] Ying-Zhong Ma, Leonas Valkunas, Susan L. Dexheimer, Sergei M. Bachilo, and Graham R. Fleming. Femtosecond spectroscopy of optical excitations in single-walled carbon nanotubes: Evidence for exciton-exciton annihilation. *Phys. Rev. Lett.*, 94:157402, April 2005. [2](#), [115](#), [260](#)
- [23] Silvia M. Santos, Bertrand Yuma, Stéphane Berciaud, Jonah Shaver, Mathieu Gallart, Pierre Gilliot, Laurent Cognet, and Brahim Lounis. All-optical trion generation in single-walled carbon nanotubes. *Phys. Rev. Lett.*, 107:187401, October 2011. [2](#), [115](#), [260](#)
- [24] Yoichi Murakami and Junichiro Kono. Existence of an upper limit on the density of excitons in carbon nanotubes by diffusion-limited exciton-exciton annihilation: Experiment and theory. *Physical Review B*, 80(3):035432, 2009. [2](#), [115](#), [260](#)
- [25] Carsten Georgi, Alexander A. Green, Mark C. Hersam, and Achim Hartschuh. Probing exciton localization in single-walled carbon nanotubes using high-resolution near-field microscopy. *ACS Nano*, 4(10):5914–5920, 2010. PMID: 20857945. [2](#), [115](#), [260](#)

-
- [26] Matthias S Hofmann, Jan T Glückert, Jonathan Noé, Christian Bourjau, Raphael Dehmel, and Alexander Högele. Bright, long-lived and coherent excitons in carbon nanotube quantum dots. *Nature nanotechnology*, 8(7):502–505, 2013. [2](#), [66](#), [114](#), [115](#), [123](#), [260](#)
- [27] Xuedan Ma, Nicolai F Hartmann, Jon KS Baldwin, Stephen K Doorn, and Han Htoon. Room-temperature single-photon generation from solitary dopants of carbon nanotubes. *Nature nanotechnology*, 10(8):671–675, 2015. [2](#), [7](#), [115](#), [131](#), [206](#), [260](#), [263](#)
- [28] Takumi Endo, Junko Ishi-Hayase, and Hideyuki Maki. Photon antibunching in single-walled carbon nanotubes at telecommunication wavelengths and room temperature. *Applied Physics Letters*, 106(11):–, 2015. [2](#), [7](#), [131](#), [206](#), [260](#), [263](#)
- [29] Felix Pyatkov, Valentin Futterling, Svetlana Khasminskaya, Benjamin S. Flavel, Frank Hennrich, Manfred M. Kappes, Ralph Krupke, and Wolfram H. P. Pernice. Cavity-enhanced light emission from electrically driven carbon nanotubes. *Nature Photon*, 10(6):420–427, April 2016. [2](#), [7](#), [33](#), [34](#), [206](#), [260](#), [263](#)
- [30] Svetlana Khasminskaya, Felix Pyatkov, Karolina Słowik, Simone Ferrari, Oliver Kahl, Vadim Kovalyuk, Patrik Rath, Andreas Vetter, Frank Hennrich, Manfred M Kappes, et al. Fully integrated quantum photonic circuit with an electrically driven light source. *Nature Photonics*, 10(11):727–732, 2016. [2](#), [7](#), [33](#), [260](#)
- [31] Edward Mills Purcell. Spontaneous emission probabilities at radio frequencies. *Physical Review*, 69:681, 1946. [2](#), [7](#), [12](#), [261](#)
- [32] R Miura, S Imamura, R Ohta, A Ishii, X Liu, T Shimada, S Iwamoto, Y Arakawa, and YK Kato. Ultralow mode-volume photonic crystal nanobeam cavities for high-efficiency coupling to individual carbon nanotube emitters. *Nature communications*, 5, 2014. [3](#), [38](#), [39](#), [131](#), [261](#), [263](#)
- [33] David Hunger, Tilo Steinmetz, Yves Colombe, Christian Deutsch, Theodor W Hänsch, and Jakob Reichel. A fiber fabry-perot cavity with high finesse. *New Journal of Physics*, 12(6):065038, 2010. [3](#), [69](#), [76](#), [78](#), [88](#), [93](#), [261](#)
- [34] Alexia Auffeves, Jean-Michel Gérard, and Jean-Philippe Poizat. Pure emitter dephasing: A resource for advanced solid-state single-photon sources. *Phys. Rev. A*, 79:053838, May 2009. [3](#), [20](#), [261](#)
- [35] A. Auffeves, D. Gerace, J.-M. Gérard, M. França Santos, L. C. Andreani, and J.-P. Poizat. Controlling the dynamics of a coupled atom-cavity system by pure dephasing. *Phys. Rev. B*, 81(24):245419, June 2010. [3](#), [20](#), [22](#), [205](#), [261](#)

REFERENCES

- [36] JM Gérard, B Sermage, B Gayral, B Legrand, E Costard, and V Thierry-Mieg. Enhanced spontaneous emission by quantum boxes in a monolithic optical microcavity. *Physical review letters*, 81(5):1110, 1998. [7](#), [25](#), [149](#), [160](#)
- [37] AV Akimov, A Mukherjee, CL Yu, DE Chang, AS Zibrov, PR Hemmer, H Park, and MD Lukin. Generation of single optical plasmons in metallic nanowires coupled to quantum dots. *Nature*, 450(7168):402–406, 2007. [7](#), [27](#)
- [38] J. P. Reithmaier, G. Sek, A. Löffler, C. Hofmann, S. Kuhn, S. Reitzenstein, L. V. Keldysh, V. D. Kulakovskii, T. L. Reinecke, and A. Forchel. Strong coupling in a single quantum dot-semiconductor microcavity system. *Nature*, 432(7014):197–200, November 2004. [7](#), [25](#)
- [39] N Le Thomas, U Woggon, O Schöps, MV Artemyev, M Kazes, and U Banin. Cavity qed with semiconductor nanocrystals. *Nano letters*, 6(3):557–561, 2006. [7](#)
- [40] Young-Shin Park, Andrew K Cook, and Hailin Wang. Cavity qed with diamond nanocrystals and silica microspheres. *Nano letters*, 6(9):2075–2079, 2006. [7](#)
- [41] S Berger, C Voisin, G Cassabois, C Delalande, Philippe Roussignol, and X Marie. Temperature dependence of exciton recombination in semiconducting single-wall carbon nanotubes. *Nano letters*, 7(2):398–402, 2007. [7](#), [155](#), [209](#)
- [42] Mark Fox. *Quantum Optics: An Introduction: An Introduction*. OUP Oxford, 2006. [9](#), [16](#), [167](#), [169](#), [170](#), [173](#)
- [43] Serge Haroche and Jean-Michel Raimond. *Exploring the quantum: atoms, cavities, and photons*. Oxford university press, 2006. [13](#)
- [44] Lucio Claudio Andreani, Giovanna Panzarini, and Jean-Michel Gérard. Strong-coupling regime for quantum boxes in pillar microcavities: Theory. *Physical Review B*, 60(19):13276, November 1999. [13](#), [14](#), [80](#)
- [45] Valérien Giesz. *Cavity-enhanced Photon-Photon Interactions With Bright Quantum Dot Sources*. PhD thesis, Université Paris-Saclay, 2015. [15](#), [209](#)
- [46] D. J. Heinzen, J. J. Childs, J. E. Thomas, and M. S. Feld. Enhanced and inhibited visible spontaneous emission by atoms in a confocal resonator. *Phys. Rev. Lett.*, 58:1320–1323, March 1987. [17](#), [150](#)
- [47] Ph Goy, JM Raimond, M Gross, and S Haroche. Observation of cavity-enhanced single-atom spontaneous emission. *Physical review letters*, 50(24):1903, 1983. [17](#), [18](#)
- [48] Jochen Dreyer. *Atomes de Rydberg et cavités : observation de la décohérence dans une mesure quantique*. Theses, Université Pierre et Marie Curie - Paris VI, January 1997. [18](#)

-
- [49] Wolf von Klitzing, Romain Long, Vladimir S Ilchenko, Jean Hare, et al. Tunable whispering gallery modes for spectroscopy and cqed experiments. *New journal of physics*, 3(1):14, 2001. [19](#)
- [50] Lefevreseguin Collot, V Lefevre-Seguin, M Brune, JM Raimond, and S Haroche. Very high-q whispering-gallery mode resonances observed on fused silica microspheres. *EPL (Europhysics Letters)*, 23(5):327, 1993. [19](#)
- [51] P. Borri, W. Langbein, S. Schneider, U. Woggon, R. L. Sellin, D. Ouyang, and D. Bimberg. Ultralong dephasing time in InGaAs quantum dots. *Phys. Rev. Lett.*, 87:157401, September 2001. [20](#)
- [52] A. Berthelot, I. Favero, G. Cassabois, C. Voisin, C. Delalande, Ph. Roussignol, R. Ferreira, and J. M. Gerard. Unconventional motional narrowing in the optical spectrum of a semiconductor quantum dot. *Nat Phys*, 2(11):759–764, November 2006. [20](#)
- [53] Xuedan Ma, Oleksiy Roslyak, Feng Wang, Juan G. Duque, Andrei Piryatinski, Stephen K. Doorn, and Han Htoon. Influence of exciton dimensionality on spectral diffusion of single-walled carbon nanotubes. *ACS Nano*, 8(10):10613–10620, 2014. PMID: 25251324. [20](#), [66](#)
- [54] Matthew W. Graham, Ying-Zhong Ma, Alexander A. Green, Mark C. Hersam, and Graham R. Fleming. Pure optical dephasing dynamics in semiconducting single-walled carbon nanotubes. *The Journal of Chemical Physics*, 134(3):034504, 2011. [20](#)
- [55] Mathieu Munsch. *Étude du régime de Purcell pour une boîte quantique unique dans une microcavité semiconductrice. Vers une non-linéarité optique géante*. PhD thesis, Université Joseph-Fourier-Grenoble I, 2009. [25](#), [209](#)
- [56] Adrien Dousse, Jan Suffczyński, Alexios Beveratos, Olivier Krebs, Aristide Lemaître, Isabelle Sagnes, Jacqueline Bloch, Paul Voisin, and Pascale Senellart. Ultrabright source of entangled photon pairs. *Nature*, 466(7303):217–220, 2010. [25](#)
- [57] O Gazzano, S Michaelis de Vasconcellos, C Arnold, A Nowak, E Galopin, I Sagnes, L Lanco, A Lemaître, and P Senellart. Bright solid-state sources of indistinguishable single photons. *Nature communications*, 4:1425, 2013. [25](#)
- [58] Emmanuelle Peter, Pascale Senellart, David Martrou, Aristide Lemaître, J Hours, JM Gérard, and Jacqueline Bloch. Exciton-photon strong-coupling regime for a single quantum dot embedded in a microcavity. *Physical review letters*, 95(6):067401, 2005. [26](#)

REFERENCES

- [59] B Gayral, J-M Gérard, B Sermage, A Lemaitre, and C Dupuis. Time-resolved probing of the purcell effect for InAs quantum boxes in GaAs microdisks. *Applied Physics Letters*, 78(19):2828–2830, 2001. [26](#)
- [60] Se-Heon Kim, Sun-Kyung Kim, and Yong-Hee Lee. Vertical beaming of wavelength-scale photonic crystal resonators. *Physical Review B*, 73(23):235117, 2006. [27](#)
- [61] Yoshihiro Akahane, Takashi Asano, Bong-Shik Song, and Susumu Noda. High-Q photonic nanocavity in a two-dimensional photonic crystal. *Nature*, 425(6961):944–947, 2003. [26](#)
- [62] Dirk Englund, David Fattal, Edo Waks, Glenn Solomon, Bingyang Zhang, Toshihiro Nakaoka, Yasuhiko Arakawa, Yoshihisa Yamamoto, and Jelena Vučković. Controlling the spontaneous emission rate of single quantum dots in a two-dimensional photonic crystal. *Physical review letters*, 95(1):013904, 2005. [27](#)
- [63] S Laurent, S Varoutsis, L Le Gratiet, A Lemaître, I Sagnes, F Raineri, A Levenson, I Robert-Philip, and I Abram. Indistinguishable single photons from a single-quantum dot in a two-dimensional photonic crystal cavity. *Applied Physics Letters*, 87(16):163107, 2005. [27](#)
- [64] Tomoyuki Yoshie, Axel Scherer, J Hendrickson, G Khitrova, HM Gibbs, G Rupper, C Ell, OB Shchekin, and DG Deppe. Vacuum rabi splitting with a single quantum dot in a photonic crystal nanocavity. *Nature*, 432(7014):200–203, 2004. [27](#)
- [65] Mark S Tame, KR McEney, ŞK Özdemir, J Lee, SA Maier, and MS Kim. Quantum plasmonics. *Nature Physics*, 9(6):329–340, 2013. [27](#)
- [66] Giuliana Di Martino, Yannick Sonnefraud, Stéphane Kéna-Cohen, Mark Tame, Sahin K. Ozdemir, M. S. Kim, and Stefan A. Maier. Quantum statistics of surface plasmon polaritons in metallic stripe waveguides. *Nano Letters*, 12(5):2504–2508, 2012. PMID: 22452310. [28](#)
- [67] Rémi Carminati, J-J Greffet, C Henkel, and JM Vigoureux. Radiative and non-radiative decay of a single molecule close to a metallic nanoparticle. *Optics Communications*, 261(2):368–375, 2006. [27](#), [150](#)
- [68] Alberto G Curto, Giorgio Volpe, Tim H Taminiau, Mark P Kreuzer, Romain Quidant, and Niek F van Hulst. Unidirectional emission of a quantum dot coupled to a nanoantenna. *Science*, 329(5994):930–933, 2010. [27](#)
- [69] Martin Kuttge, F. Javier García de Abajo, and Albert Polman. Ultrasmall mode volume plasmonic nanodisk resonators. *Nano Letters*, 10(5):1537–1541, 2010. [27](#)

-
- [70] Yiyang Gong and Jelena Vučković. Design of plasmon cavities for solid-state cavity quantum electrodynamics applications. *Applied physics letters*, 90(3):033113, 2007. [27](#)
- [71] Nina Mauser, Nicolai Hartmann, Matthias S Hofmann, Julia Janik, Alexander Hogele, and Achim Hartschuh. Antenna-enhanced optoelectronic probing of carbon nanotubes. *Nano letters*, 14(7):3773–3778, 2014. [27](#)
- [72] Nathalie P. de Leon, Brendan J. Shields, Chun L. Yu, Dirk E. Englund, Alexey V. Akimov, Mikhail D. Lukin, and Hongkun Park. Tailoring light-matter interaction with a nanoscale plasmon resonator. *Phys. Rev. Lett.*, 108:226803, May 2012. [28](#)
- [73] Antonio Badolato, Kevin Hennessy, Mete Atatüre, Jan Dreiser, Evelyn Hu, Pierre M Petroff, and Atac Imamoglu. Deterministic coupling of single quantum dots to single nanocavity modes. *Science*, 308(5725):1158–1161, 2005. [28](#)
- [74] A. Dousse, L. Lanco, J. Suffczyński, E. Semenova, A. Miard, A. Lemaître, I. Sagnes, C. Roblin, J. Bloch, and P. Senellart. Controlled light-matter coupling for a single quantum dot embedded in a pillar microcavity using far-field optical lithography. *Phys. Rev. Lett.*, 101:267404, December 2008. [28](#)
- [75] Valerie C Moore, Michael S Strano, Erik H Haroz, Robert H Hauge, Richard E Smalley, Judith Schmidt, and Yeshayahu Talmon. Individually suspended single-walled carbon nanotubes in various surfactants. *Nano letters*, 3(10):1379–1382, 2003. [29](#)
- [76] Etienne Gauffrès, Nicolas Izard, Xavier Le Roux, Saïd Kazaoui, Delphine Marris-Morini, Eric Cassan, and Laurent Vivien. Optical microcavity with semiconducting single-wall carbon nanotubes. *Optics express*, 18(6):5740–5745, 2010. [29](#), [30](#)
- [77] D. Legrand, C. Roquelet, G. Lanty, Ph. Roussignol, X. Lafosse, S. Bouchoule, E. Deleporte, C. Voisin, and J. S. Lauret. Monolithic microcavity with carbon nanotubes as active material. *Applied Physics Letters*, 102(15), 2013. [30](#), [31](#), [131](#)
- [78] M. Fujiwara, D. Tsuya, and H. Maki. Electrically driven, narrow-linewidth blackbody emission from carbon nanotube microcavity devices. *Applied Physics Letters*, 103(14):–, 2013. [30](#)
- [79] Etienne Gauffrès, Nicolas Izard, Adrien Noury, Xavier Le Roux, Gilles Rasigade, Alexandre Beck, and Laurent Vivien. Light emission in silicon from carbon nanotubes. *ACS Nano*, 6(5):3813–3819, May 2012. [30](#), [31](#)

REFERENCES

- [80] Adrien Noury, Xavier Le Roux, Laurent Vivien, and Nicolas Izard. Controlling carbon nanotube photoluminescence using silicon microring resonators. *Nanotechnology*, 25(21):215201, 2014. [30](#), [32](#), [131](#)
- [81] Yuriy Zakharko, Arko Graf, Stefan P. Schießl, Bernd Hähnlein, Jörg Pezoldt, Malte C. Gather, and Jana Zaumseil. Broadband tunable, polarization-selective and directional emission of (6,5) carbon nanotubes coupled to plasmonic crystals. *Nano Lett.*, 16(5):3278–3284, May 2016. [32](#), [33](#)
- [82] Svetlana Khasminskaya, Feliks Pyatkov, Benjamin S. Flavel, Wolfram H. Pernice, and Ralph Krupke. Waveguide-integrated light-emitting carbon nanotubes. *Advanced Materials*, 26(21):3465–3472, Mar 2014. [33](#), [205](#)
- [83] Thierry Bastin, C Thiel, E Solano, J von Zanthier, and GS Agarwal. Quantum imaging with uncorrelated single photon sources. In *Optical Engineering+ Applications*, pages 70920C–70920C. International Society for Optics and Photonics, 2008. [35](#), [171](#)
- [84] Thomas Mueller, Megumi Kinoshita, Mathias Steiner, Vasili Perebeinos, Ageeth A Bol, Damon B Farmer, and Phaedon Avouris. Efficient narrow-band light emission from a single carbon nanotube p–n diode. *nature nanotechnology*, 5(1):27–31, 2010. [35](#)
- [85] Fengnian Xia, Mathias Steiner, Yu-ming Lin, and Phaedon Avouris. A microcavity-controlled, current-driven, on-chip nanotube emitter at infrared wavelengths. *Nature nanotechnology*, 3(10):609–613, 2008. [35](#), [131](#)
- [86] Shuang Liang, Ze Ma, Gongtao Wu, Nan Wei, Le Huang, Huixin Huang, Huaping Liu, Sheng Wang, and Lian Mao Peng. Microcavity-integrated carbon nanotube photodetectors. *ACS Nano*, 10(7):6963–6971, July 2016. [36](#)
- [87] S. Imamura, R. Watahiki, R. Miura, T. Shimada, and Y. K. Kato. Optical control of individual carbon nanotube light emitters by spectral double resonance in silicon microdisk resonators. *Applied Physics Letters*, 102(16), 2013. [36](#), [37](#), [131](#)
- [88] R. Watahiki, T. Shimada, P. Zhao, S. Chiashi, S. Iwamoto, Y. Arakawa, S. Maruyama, and Y. K. Kato. Enhancement of carbon nanotube photoluminescence by photonic crystal nanocavities. *Applied Physics Letters*, 101(14):–, 2012. [37](#), [131](#)
- [89] Thomas Hümmer, Jonathan Noe, Matthias S Hofmann, Theodor W Hänsch, Alexander Högele, and David Hunger. Cavity-enhanced raman microscopy of individual carbon nanotubes. *Nat Comms*, 7, July 2016. [39](#), [40](#), [131](#)

-
- [90] Sebastian Stapfner, Lukas Ost, David Hunger, Jakob Reichel, Ivan Favero, and Eva Maria Weig. Cavity-enhanced optical detection of carbon nanotube brownian motion. *Applied Physics Letters*, 102(15):151910, 2013. [39](#)
- [91] Sébastien Berger. *Etude optique de la dynamique des interactions électroniques dans des nanotubes de carbone*. PhD thesis, Université Pierre et Marie Curie-Paris VI, 2007. [46](#), [56](#)
- [92] Fabien Violla. *Interaction between carbon nanotubes and their physico-chemical environment : towards the control of the optical properties*. Theses, Université Pierre et Marie Curie - Paris VI, March 2014. [46](#), [60](#), [110](#), [112](#), [117](#), [119](#), [120](#), [123](#), [209](#)
- [93] Benjamin Langlois. *Propriétés optiques hors-équilibre des nanotubes de carbone nus ou fonctionnalisés*. PhD thesis, 2014. Thèse de doctorat dirigée par Voisin, Christophe Physique Paris, Ecole normale supérieure 2014. [46](#), [60](#), [209](#)
- [94] Gordana Dukovic, Milan Balaz, Peter Doak, Nina D Berova, Ming Zheng, Robert S Mclean, and Louis E Brus. Racemic single-walled carbon nanotubes exhibit circular dichroism when wrapped with DNA. *Journal of the American Chemical Society*, 128(28):9004–9005, 2006. [47](#)
- [95] A. H. Castro Neto, F. Guinea, N. M. R. Peres, K. S. Novoselov, and A. K. Geim. The electronic properties of graphene. *Rev. Mod. Phys.*, 81:109–162, January 2009. [49](#)
- [96] JW Mintmire and CT White. Universal density of states for carbon nanotubes. *Physical Review Letters*, 81(12):2506, 1998. [50](#), [52](#)
- [97] S. Reich, C. Thomsen, and J. Maultzsch. *Carbon Nanotubes*. Wiley, 2008. [51](#), [52](#)
- [98] P.Y Yu and M. Cardona. *Fundamentals of semiconductors : Physics and Materials Properties*. Springer Berlin Heidelberg, 2010. [52](#), [57](#)
- [99] Ermin Malic, Matthias Hirtschulz, Frank Milde, Andreas Knorr, and Stephanie Reich. Analytical approach to optical absorption in carbon nanotubes. *Phys. Rev. B*, 74:195431, November 2006. [53](#)
- [100] A. Grüneis, R. Saito, Ge. G. Samsonidze, T. Kimura, M. A. Pimenta, A. Jorio, A. G. Souza Filho, G. Dresselhaus, and M. S. Dresselhaus. Inhomogeneous optical absorption around the K point in graphite and carbon nanotubes. *Phys. Rev. B*, 67:165402, April 2003. [53](#)
- [101] Seiji Uryu and Tsuneya Ando. Exciton absorption of perpendicularly polarized light in carbon nanotubes. *Physical Review B*, 74(15):155411, 2006. [53](#)

REFERENCES

- [102] J Jiang, R Saito, A Grüneis, G Dresselhaus, and MS Dresselhaus. Optical absorption matrix elements in single-wall carbon nanotubes. *Carbon*, 42(15):3169–3176, 2004. [54](#)
- [103] Lucio Claudio Andreani. Optical transitions, excitons, and polaritons in bulk and low-dimensional semiconductor structures. In *Confined electrons and photons*, pages 57–112. Springer, 1995. [54](#)
- [104] J. Lefebvre, J. M. Fraser, P. Finnie, and Y. Homma. Photoluminescence from an individual single-walled carbon nanotube. *Phys. Rev. B*, 69:075403, February 2004. [54](#), [113](#)
- [105] M. F. Islam, D. E. Milkie, C. L. Kane, A. G. Yodh, and J. M. Kikkawa. Direct measurement of the polarized optical absorption cross section of single-wall carbon nanotubes. *Phys. Rev. Lett.*, 93:037404, July 2004. [54](#)
- [106] Matthew Y Sfeir, Tobias Beetz, Feng Wang, Limin Huang, XM Henry Huang, Mingyuan Huang, J Hone, Stephen O’Brien, JA Misewich, Tony F Heinz, et al. Optical spectroscopy of individual single-walled carbon nanotubes of defined chiral structure. *Science*, 312(5773):554–556, 2006. [56](#)
- [107] David E Aspnes and AA Studna. Dielectric functions and optical parameters of si, ge, gap, gaas, gasb, inp, inas, and insb from 1.5 to 6.0 ev. *Physical Review B*, 27(2):985, 1983. [59](#)
- [108] Claus F Klingshirn. *Semiconductor optics*. Springer Science & Business Media, 2012. [59](#)
- [109] Rodney Loudon. One-dimensional hydrogen atom. *American Journal of Physics*, 27(9):649–655, 1959. [59](#)
- [110] Fausto Rossi and Elisa Molinari. Coulomb-induced suppression of band-edge singularities in the optical spectra of realistic quantum-wire structures. *Physical review letters*, 76(19):3642, 1996. [59](#)
- [111] Vasili Perebeinos, J. Tersoff, and Phaedon Avouris. Scaling of excitons in carbon nanotubes. *Phys. Rev. Lett.*, 92:257402, June 2004. [59](#)
- [112] Feng Wang, Yang Wu, Mark S. Hybertsen, and Tony F. Heinz. Auger recombination of excitons in one-dimensional systems. *Phys. Rev. B*, 73:245424, June 2006. [59](#)
- [113] T Someya, H Akiyama, and H Sakaki. Enhanced binding energy of one-dimensional excitons in quantum wires. *Physical review letters*, 76(16):2965, 1996. [59](#)

-
- [114] J. Maultzsch, R. Pomraenke, S. Reich, E. Chang, D. Prezzi, A. Ruini, E. Molinari, M. S. Strano, C. Thomsen, and C. Lienau. Exciton binding energies in carbon nanotubes from two-photon photoluminescence. *Phys. Rev. B*, 72:241402, December 2005. [59](#)
- [115] Jacques Lefebvre and Paul Finnie. Excited excitonic states in single-walled carbon nanotubes. *Nano letters*, 8(7):1890–1895, 2008. [59](#)
- [116] D. T. Nguyen, C. Voisin, Ph. Roussignol, C. Roquelet, J. S. Lauret, and G. Cassabois. Elastic exciton-exciton scattering in photoexcited carbon nanotubes. *Phys. Rev. Lett.*, 107:127401, September 2011. [59](#)
- [117] Larry Lüer, Sajjad Hoseinkhani, Dario Polli, Jared Crochet, Tobias Hertel, and Guglielmo Lanzani. Size and mobility of excitons in (6, 5) carbon nanotubes. *Nature physics*, 5(1):54–58, 2009. [59](#), [115](#)
- [118] Rodrigo B. Capaz, Catalin D. Spataru, Sohrab Ismail-Beigi, and Steven G. Louie. Diameter and chirality dependence of exciton properties in carbon nanotubes. *Phys. Rev. B*, 74:121401, September 2006. [59](#)
- [119] Ermin Malic and Andreas Knorr. *Graphene and Carbon Nanotubes: Ultrafast Optics and Relaxation Dynamics*. John Wiley & Sons, 2013. [60](#)
- [120] Flávio Plentz, Henrique B. Ribeiro, Ado Jorio, Michael S. Strano, and Marcos A. Pimenta. Direct experimental evidence of exciton-phonon bound states in carbon nanotubes. *Phys. Rev. Lett.*, 95:247401, December 2005. [61](#), [62](#)
- [121] O. N. Torrens, M. Zheng, and J. M. Kikkawa. Energy of k -momentum dark excitons in carbon nanotubes by optical spectroscopy. *Phys. Rev. Lett.*, 101:157401, October 2008. [61](#), [62](#)
- [122] Ryusuke Matsunaga, Kazunari Matsuda, and Yoshihiko Kanemitsu. Origin of low-energy photoluminescence peaks in single carbon nanotubes: k -momentum dark excitons and triplet dark excitons. *Phys. Rev. B*, 81:033401, January 2010. [61](#), [62](#)
- [123] Eduardo B. Barros, Rodrigo B. Capaz, Ado Jorio, Georgii G. Samsonidze, Antonio G. Souza Filho, Sohrab Ismail-Beigi, Catalin D. Spataru, Steven G. Louie, Gene Dresselhaus, and Mildred S. Dresselhaus. Selection rules for one- and two-photon absorption by excitons in carbon nanotubes. *Phys. Rev. B*, 73:241406, June 2006. [61](#)
- [124] I. B. Mortimer and R. J. Nicholas. Role of bright and dark excitons in the temperature-dependent photoluminescence of carbon nanotubes. *Phys. Rev. Lett.*, 98:027404, January 2007. [61](#)

REFERENCES

- [125] Morgane Gandil, Kazunari Matsuda, Philippe Tamarat, and Brahim Lounis. Magneto-photoluminescence spectroscopy of bright and dark excitons in isolated semiconducting single-walled carbon nanotubes. In *Trends in Nanotechnology International Conference*, 2015. 61
- [126] Joseph M Singer and Joseph Grumer. Carbon formation in very rich hydrocarbon-air flames i. studies of chemical content, temperature, ionization and particulate matter. In *Symposium (International) on Combustion*, volume 7, pages 559–569. Elsevier, 1958. 62
- [127] Mukul Kumar and Yoshinori Ando. Chemical vapor deposition of carbon nanotubes: a review on growth mechanism and mass production. *Journal of nanoscience and nanotechnology*, 10(6):3739–3758, 2010. 63
- [128] Pavel Nikolaev, Michael J Bronikowski, R Kelley Bradley, Frank Rohmund, Daniel T Colbert, KA Smith, and Richard E Smalley. Gas-phase catalytic growth of single-walled carbon nanotubes from carbon monoxide. *Chemical physics letters*, 313(1):91–97, 1999. 63
- [129] Giulio Lolli, Liang Zhang, Leandro Balzano, Nataphan Sakulchaicharoen, Yongqiang Tan, and Daniel E Resasco. Tailoring (n, m) structure of single-walled carbon nanotubes by modifying reaction conditions and the nature of the support of como catalysts. *The Journal of Physical Chemistry B*, 110(5):2108–2115, 2006. 63
- [130] Jean-Sébastien Lauret, Christophe Voisin, Guillaume Cassabois, Claude Delalande, Ph Roussignol, Oliver Jost, and L Capes. Ultrafast carrier dynamics in single-wall carbon nanotubes. *Physical review letters*, 90(5):057404, 2003. 64
- [131] Andreas Thess, Roland Lee, Pavel Nikolaev, and Hongjie Dai. Crystalline ropes of metallic carbon nanotubes. *Science*, 273(5274):483, 1996. 64
- [132] Adrian Nish, Jeong-Yuan Hwang, James Doig, and Robin J Nicholas. Highly selective dispersion of single-walled carbon nanotubes using aromatic polymers. *Nature nanotechnology*, 2(10):640–646, 2007. 65
- [133] Nicolas Izard, Said Kazaoui, Kenji Hata, Toshiya Okazaki, Takeshi Saito, Sumio Iijima, and Nobutsugu Minami. Semiconductor-enriched single wall carbon nanotube networks applied to field effect transistors. *Applied Physics Letters*, 92(24):243112, 2008. 65
- [134] Stéphane Berciaud, Laurent Cognet, Philippe Poulin, R Bruce Weisman, and Brahim Lounis. Absorption spectroscopy of individual single-walled carbon nanotubes. *Nano letters*, 7(5):1203–1207, 2007. 66

-
- [135] Ibrahim Sarpkaya, Zhengyi Zhang, William Walden-Newman, Xuesi Wang, James Hone, Chee W Wong, and Stefan Strauf. Prolonged spontaneous emission and dephasing of localized excitons in air-bridged carbon nanotubes. *Nature communications*, 4, 2013. [66](#)
- [136] Yves Colombe, Tilo Steinmetz, Guilhem Dubois, Felix Linke, David Hunger, and Jakob Reichel. Strong atom–field coupling for Bose–Einstein condensates in an optical cavity on a chip. *Nature*, 450(7167):272–276, 2007. [69](#)
- [137] Benjamin Besga. *Micro-cavité Fabry Perot fibrée: une nouvelle approche pour l'étude des polaritons dans des hétérostructures semi-conductrices*. PhD thesis, Université Pierre et Marie Curie-Paris VI, 2013. [69](#), [82](#), [209](#)
- [138] Roland Albrecht, Alexander Bommer, Christian Deutsch, Jakob Reichel, and Christoph Becher. Coupling of a single nitrogen-vacancy center in diamond to a fiber-based microcavity. *Phys. Rev. Lett.*, 110:243602, June 2013. [69](#), [131](#), [147](#)
- [139] Roland Albrecht, Alexander Bommer, Christoph Pauly, Frank Mücklich, Andreas W. Schell, Philip Engel, Tim Schröder, Oliver Benson, Jakob Reichel, and Christoph Becher. Narrow-band single photon emission at room temperature based on a single nitrogen-vacancy center coupled to an all-fiber-cavity. *Applied Physics Letters*, 105(7):–, 2014. [69](#)
- [140] Julia Benedikter, Hanno Kaupp, Thomas Hümmer, Yuejiang Liang, Alexander Bommer, Christoph Becher, Anke Krueger, Jason M Smith, Theodor W Hänsch, and David Hunger. A cavity-enhanced single photon source based on the silicon vacancy center in diamond. *arXiv preprint arXiv:1612.05509*, 2016. [69](#)
- [141] A. E. Siegman. *Lasers*. University Science Books, new edition, May 1986. [70](#), [71](#)
- [142] G Rempe, R Lalezari, RJ Thompson, and HJ Kimble. Measurement of ultralow losses in an optical interferometer. *Optics Letters*, 17(5):363–365, 1992. [76](#)
- [143] Raoul Stöckle, Christian Fokas, Volker Deckert, Renato Zenobi, Beate Sick, Bert Hecht, and Urs P Wild. High-quality near-field optical probes by tube etching. *Applied Physics Letters*, 75(2):160–162, 1999. [76](#)
- [144] Jining Sun, J Li, RRJ Maier, Duncan Paul Hand, William Neil MacPherson, MK Miller, James Millar Ritchie, and X Luo. Fabrication of a side aligned optical fibre interferometer by focused ion beam machining. *Journal of Micromechanics and Microengineering*, 23(10):105005, 2013. [76](#)
- [145] K Watanabe, Jonathan Schrauwen, Arne Leinse, DV Thourhout, Rene Heideman, and Roel Baets. Total reflection mirrors fabricated on silica waveguides with focused ion beam. *Electronics letters*, 45(17):883–884, 2009. [76](#)

REFERENCES

- [146] ME Shaheen, JE Gagnon, and BJ Fryer. Femtosecond laser ablation behavior of gold, crystalline silicon, and fused silica: a comparative study. *Laser Physics*, 24(10):106102, 2014. [76](#)
- [147] Rei Kitamura, Laurent Pilon, and Mirosław Jonasz. Optical constants of silica glass from extreme ultraviolet to far infrared at near room temperature. *Applied optics*, 46(33):8118–8133, 2007. [76](#)
- [148] Konstantin Ott, Sébastien Garcia, Ralf Kohlhaas, Peter Rosenbusch, and Jakob Reichel. Long high finesse fiber fabry-perot resonators, 2015. [77](#)
- [149] Sébastien Garcia. *Fiber interfaces between single atoms and single photons*. Theses, Ecole normale supérieure, September 2015. [77](#), [78](#), [79](#), [99](#), [209](#)
- [150] David Hunger, Christian Deutsch, Russell J Barbour, Richard J Warburton, and Jakob Reichel. Laser micro-fabrication of concave, low-roughness features in silica. *AIP Advances*, 2(1):012119, 2012. [78](#)
- [151] Julia Benedikter, Thomas Hümmer, Matthias Mader, Benedikt Schlederer, Jakob Reichel, Theodor W Hänsch, and David Hunger. Transverse-mode coupling and diffraction loss in tunable fabry-pérot microcavities. *arXiv preprint arXiv:1502.01532*, 2015. [79](#), [85](#), [93](#)
- [152] LR Brovelli and U Keller. Simple analytical expressions for the reflectivity and the penetration depth of a Bragg mirror between arbitrary media. *Optics communications*, 116(4):343–350, 1995. [81](#)
- [153] Aurélien A. P. Trichet, Philip R. Dolan, David M. Coles, Gareth M. Hughes, and Jason M. Smith. Topographic control of open-access microcavities at the nanometer scale. *Opt. Express*, 23(13):17205–17216, June 2015. [85](#)
- [154] RE Wagner and WJ Tomlinson. Coupling efficiency of optics in single-mode fiber components. *Applied optics*, 21(15):2671–2688, 1982. [88](#)
- [155] W. B. Joyce and B. C. DeLoach. alignment of Gaussian beams. *Appl. Opt.*, 23(23):4187–4196, December 1984. [88](#)
- [156] A Asadpour and H Golnabi. Fiber output beam shape study using imaging technique. *Applied Sci*, 10:312–318, 2010. [90](#)
- [157] HEJ Bennett and JO Porteus. Relation between surface roughness and specular reflectance at normal incidence. *JOSA*, 51(2):123–129, 1961. [92](#)
- [158] Jean M Bennett. Recent developments in surface roughness characterization. *Measurement Science and Technology*, 3(12):1119, 1992. [92](#)

-
- [159] Giel Berden, Rudy Peeters, and Gerard Meijer. Cavity ring-down spectroscopy: Experimental schemes and applications. *International Reviews in Physical Chemistry*, 19(4):565–607, 2000. [95](#)
- [160] WE Moerner and David P Fromm. Methods of single-molecule fluorescence spectroscopy and microscopy. *Review of Scientific Instruments*, 74(8):3597–3619, 2003. [104](#)
- [161] Christophe Galland, Alexander Högele, Hakan E. Türeci, and Ata ç Imamoğlu. Non-Markovian decoherence of localized nanotube excitons by acoustic phonons. *Phys. Rev. Lett.*, 101(6):067402, August 2008. [110](#), [116](#), [118](#)
- [162] H. Htoon, M. J. O’Connell, S. K. Doorn, and V. I. Klimov. Single carbon nanotubes probed by photoluminescence excitation spectroscopy: The role of phonon-assisted transitions. *Phys. Rev. Lett.*, 94(12):127403, April 2005. [110](#)
- [163] Stéphane Berciaud, Laurent Cognet, and Brahim Lounis. Luminescence decay and the absorption cross section of individual single-walled carbon nanotubes. *Phys. Rev. Lett.*, 101:077402, August 2008. [114](#)
- [164] Nan Ai, William Walden-Newman, Qiang Song, Sokratis Kalliakos, and Stefan Strauf. Suppression of blinking and enhanced exciton emission from individual carbon nanotubes. *ACS Nano*, 5(4):2664–2670, 2011. PMID: 21375256. [114](#), [122](#), [123](#)
- [165] C-X Sheng, Zeev Valentine Vardeny, AB Dalton, and RH Baughman. Exciton dynamics in single-walled nanotubes: Transient photoinduced dichroism and polarized emission. *Physical Review B*, 71(12):125427, 2005. [115](#)
- [166] Laurent Cognet, Dmitri A Tsyboulski, John-David R Rocha, Condell D Doyle, James M Tour, and R Bruce Weisman. Stepwise quenching of exciton fluorescence in carbon nanotubes by single-molecule reactions. *Science*, 316(5830):1465–1468, 2007. [115](#)
- [167] Bertrand kei Yuma et al. *Etude de la dynamique des états excités des nanotubes du carbone mono-paroi*. PhD thesis, Strasbourg, 2013. [115](#)
- [168] Christophe Galland. *Quantum optics with single-wall carbon nanotubes*. Theses, Eidgenössische Technische Hochschule Zürich (ETHZ), April 2010. [115](#), [209](#)
- [169] Matthias S. Hofmann, Jonathan Noé, Alexander Kneer, Jared J. Crochet, and Alexander Högele. Ubiquity of exciton localization in cryogenic carbon nanotubes. *Nano Lett.*, April 2016. [115](#)
- [170] Kun Huang and Avril Rhys. Theory of light absorption and non-radiative transitions in f-centres. In *Proceedings of the Royal Society of London A*:

REFERENCES

- Mathematical, Physical and Engineering Sciences*, volume 204, pages 406–423. The Royal Society, 1950. [116](#)
- [171] C. B. Duke and G. D. Mahan. Phonon-broadened impurity spectra. i. density of states. *Phys. Rev.*, 139:A1965–A1982, September 1965. [116](#)
- [172] B. Krummheuer, V. M. Axt, and T. Kuhn. Theory of pure dephasing and the resulting absorption line shape in semiconductor quantum dots. *Phys. Rev. B*, 65:195313, May 2002. [116](#), [118](#), [186](#), [197](#), [256](#)
- [173] G. Pennington and N. Goldsman. Low-field semiclassical carrier transport in semiconducting carbon nanotubes. *Phys. Rev. B*, 71:205318, May 2005. [117](#)
- [174] D. T. Nguyen, C. Voisin, Ph. Roussignol, C. Roquelet, J. S. Lauret, and G. Cassabois. Phonon-induced dephasing in single-wall carbon nanotubes. *Phys. Rev. B*, 84:115463, September 2011. [117](#)
- [175] Hidekatsu Suzuura and Tsuneya Ando. Phonons and electron-phonon scattering in carbon nanotubes. *Phys. Rev. B*, 65:235412, May 2002. [117](#)
- [176] L Besombes, K Kheng, L Marsal, and H Mariette. Acoustic phonon broadening mechanism in single quantum dot emission. *Physical Review B*, 63(15):155307, 2001. [119](#)
- [177] I Favero, Guillaume Cassabois, R Ferreira, D Darson, C Voisin, J Tignon, C Delalande, G Bastard, Ph Roussignol, and JM Gérard. Acoustic phonon sidebands in the emission line of single inas/gaas quantum dots. *Physical Review B*, 68(23):233301, 2003. [119](#)
- [178] Ibrahim Sarpkaya, Ehsaneh D Ahmadi, Gabriella D Shepard, Kevin S Mistry, Jeffrey L Blackburn, and Stefan Strauf. Strong acoustic phonon localization in copolymer wrapped carbon nanotubes. *ACS nano*, 2015. [119](#)
- [179] Alexander V Savin, Bambi Hu, and Yuri S Kivshar. Thermal conductivity of single-walled carbon nanotubes. *Physical Review B*, 80(19):195423, 2009. [119](#)
- [180] Mijin Kim, Lyudmyla Adamska, Nicolai F Hartmann, Hyejin Kwon, Jin Liu, Kirill A Velizhanin, Yanmei Piao, Lyndsey Rae Powell, Brendan Meany, Stephen K Doorn, et al. Fluorescent carbon nanotube defects manifest substantial vibrational reorganization. *The Journal of Physical Chemistry C*, 2016. [119](#)
- [181] Carsten Georgi, Nicolai Hartmann, Tobias Gokus, Alexander A Green, Mark C Hersam, and Achim Hartschuh. Photoinduced luminescence blinking and bleaching in individual single-walled carbon nanotubes. *ChemPhysChem*, 9(10):1460–1464, 2008. [122](#)

-
- [182] PH Sher, JM Smith, PA Dalgarno, RJ Warburton, X Chen, PJ Dobson, SM Daniels, NL Pickett, and P O'Brien. Power law carrier dynamics in semiconductor nanocrystals at nanosecond timescales. *Applied Physics Letters*, 92(10):101111, 2008. [122](#)
- [183] Pavel Frantsuzov, Masaru Kuno, Boldizsar Janko, and Rudolph A Marcus. Universal emission intermittency in quantum dots, nanorods and nanowires. *Nature Physics*, 4(7):519–522, 2008. [122](#)
- [184] D. A. B. Miller, D. S. Chemla, T. C. Damen, A. C. Gossard, W. Wiegmann, T. H. Wood, and C. A. Burrus. Band-edge electroabsorption in quantum well structures: The quantum-confined stark effect. *Phys. Rev. Lett.*, 53:2173–2176, November 1984. [122](#)
- [185] S. A. Empedocles and M. G. Bawendi. Quantum-confined stark effect in single CdSe nanocrystallite quantum dots. *Science*, 278(5346):2114–2117, 1997. [122](#)
- [186] J. Müller, J. M. Lupton, A. L. Rogach, J. Feldmann, D. V. Talapin, and H. Weller. Monitoring surface charge movement in single elongated semiconductor nanocrystals. *Phys. Rev. Lett.*, 93:167402, October 2004. [122](#)
- [187] K Matsuda, Yoshihiko Kanemitsu, K Irie, Toshiharu Saiki, T Someya, S Miyauchi, and S Maruyama. Photoluminescence intermittency in an individual single-walled carbon nanotube at room temperature. *Applied Physics Letters*, 86(12):123116, 2005. [122](#)
- [188] Achim Hartschuh, Hermenegildo N Pedrosa, Jeffrey Peterson, Libai Huang, Pascal Anger, Huihong Qian, Alfred J Meixner, Mathias Steiner, Lukas Novotny, and Todd D Krauss. Single carbon nanotube optical spectroscopy. *ChemPhysChem*, 6(4):577–582, 2005. [122](#)
- [189] Han Htoon, MJ O'Connell, PJ Cox, SK Doorn, and Victor I Klimov. Low temperature emission spectra of individual single-walled carbon nanotubes: Multiplicity of subspecies within single-species nanotube ensembles. *Physical review letters*, 93(2):027401, 2004. [122](#)
- [190] Oliver Kiowski, Sergei Lebedkin, Frank Hennrich, and Manfred M. Kappes. Single-walled carbon nanotubes show stable emission and simple photoluminescence spectra with weak excitation sidebands at cryogenic temperatures. *Phys. Rev. B*, 76:075422, August 2007. [123](#)
- [191] William Walden-Newman, Ibrahim Sarpkaya, and Stefan Strauf. Quantum light signatures and nanosecond spectral diffusion from cavity-embedded carbon nanotubes. *Nano Letters*, 12(4):1934–1941, 2012. [123](#), [131](#), [162](#), [178](#), [179](#)

REFERENCES

- [192] Hubert W Lilliefors. On the kolmogorov-smirnov test for normality with mean and variance unknown. *Journal of the American Statistical Association*, 62(318):399–402, 1967. [124](#)
- [193] Ziyun Di, Helene V Jones, Philip R Dolan, Simon M Fairclough, Matthew B Wincott, Johnny Fill, Gareth M Hughes, and Jason M Smith. Controlling the emission from semiconductor quantum dots using ultra-small tunable optical microcavities. *New Journal of Physics*, 14(10):103048, 2012. [131](#)
- [194] Matthias Mader, Jakob Reichel, Theodor W. Hansch, and David Hunger. A scanning cavity microscope. *Nat Commun*, 6, June 2015. [131](#)
- [195] Hanno Kaupp, Thomas Hümmer, Matthias Mader, Benedikt Schleder, Julia Benedikter, Philip Haeusser, Huan-Cheng Chang, Helmut Fedder, Theodor W Hänsch, and David Hunger. Purcell-enhanced single-photon emission from nitrogen-vacancy centers coupled to a tunable microcavity. *arXiv preprint arXiv:1606.00167*, 2016. [131](#)
- [196] Benjamin Besga, Cyril Vaneph, Jakob Reichel, Jérôme Estève, Andreas Reinhard, Javier Miguel-Sánchez, Ata ç Imamoglu, and Thomas Volz. Polariton boxes in a tunable fiber cavity. *Phys. Rev. Applied*, 3:014008, January 2015. [131](#)
- [197] Javier Miguel-Sánchez, Andreas Reinhard, Emre Togan, Thomas Volz, Atac Imamoglu, Benjamin Besga, Jakob Reichel, and Jérôme Estève. Cavity quantum electrodynamics with charge-controlled quantum dots coupled to a fiber fabry-perot cavity. *New Journal of Physics*, 15(4):045002, 2013. [132](#)
- [198] CE Reed, J Giergiel, JC Hemminger, and S Ushioda. Dipole radiation in a multilayer geometry. *Physical Review B*, 36(9):4990, 1987. [142](#)
- [199] W Jhe, A Anderson, EA Hinds, D Meschede, L Moi, and S Haroche. Suppression of spontaneous decay at optical frequencies: Test of vacuum-field anisotropy in confined space. *Physical review letters*, 58(7):666, 1987. [150](#)
- [200] Andrei Faraon, Paul E Barclay, Charles Santori, Kai-Mei C Fu, and Raymond G Beausoleil. Resonant enhancement of the zero-phonon emission from a colour centre in a diamond cavity. *Nature Photonics*, 5(5):301–305, 2011. [151](#)
- [201] R. G. DeVoe and R. G. Brewer. Observation of superradiant and subradiant spontaneous emission of two trapped ions. *Phys. Rev. Lett.*, 76:2049–2052, March 1996. [159](#)
- [202] Raphaël Proux. *Indistinguishability of the photons emitted by a semiconductor quantum dot under continuous-wave resonant excitation*. Theses, École Normale Supérieure (Paris), November 2015. [174](#)

-
- [203] Christian Kurtsiefer, Patrick Zarda, Sonja Mayer, and Harald Weinfurter. The breakdown flash of silicon avalanche photodiodes-back door for eavesdropper attacks? *Journal of Modern Optics*, 48(13):2039–2047, 2001. [177](#)
- [204] Yuhei Miyauchi, Munechiyo Iwamura, Shinichiro Mouri, Tadashi Kawazoe, Motoichi Ohtsu, and Kazunari Matsuda. Brightening of excitons in carbon nanotubes on dimensionality modification. *Nature Photonics*, 7(9):715–719, 2013. [180](#)
- [205] Thomas Grange, Gaston Hornecker, David Hunger, Jean-Philippe Poizat, Jean-Michel Gérard, Pascale Senellart, and Alexia Auffèves. Cavity-funneled generation of indistinguishable single photons from strongly dissipative quantum emitters. *Phys. Rev. Lett.*, 114:193601, May 2015. [180](#), [206](#), [264](#)
- [206] Gerald D Mahan. *Many-particle physics*. Springer Science & Business Media, 2013. [186](#), [187](#), [188](#), [256](#)
- [207] Gaston Hornecker, Alexia Auffèves, and Thomas Grange. Influence of phonons on solid-state cavity-qed investigated using nonequilibrium green’s functions. *arXiv preprint arXiv:1609.09754*, 2016. [188](#)
- [208] A. J. Leggett, S. Chakravarty, A. T. Dorsey, Matthew P. A. Fisher, Anupam Garg, and W. Zwerger. Dynamics of the dissipative two-state system. *Rev. Mod. Phys.*, 59:1–85, January 1987. [188](#), [252](#)
- [209] H. Dekker. Noninteracting-blip approximation for a two-level system coupled to a heat bath. *Phys. Rev. A*, 35:1436–1437, February 1987. [188](#), [252](#)
- [210] H Dekker. Dynamics of the dissipative two-state system: The noninteracting-blip approximation. *Physica A: Statistical Mechanics and its Applications*, 141(2-3):570–574, 1987. [188](#), [252](#)
- [211] Peter P. Orth, Adilet Imambekov, and Karyn Le Hur. Nonperturbative stochastic method for driven spin-boson model. *Phys. Rev. B*, 87:014305, Jan 2013. [188](#), [252](#)
- [212] A. Jeantet, Y. Chassagneux, C. Raynaud, Ph. Roussignol, J. S. Lauret, B. Besga, J. Estève, J. Reichel, and C. Voisin. Widely tunable single-photon source from a carbon nanotube in the purcell regime. *Phys. Rev. Lett.*, 116:247402, June 2016. [193](#)
- [213] Fabien Violla, Cyrielle Roquelet, Benjamin Langlois, Géraud Delport, Silvia Morim Santos, Emmanuelle Deleporte, Philippe Roussignol, Claude Delalande, Christophe Voisin, and Jean-Sébastien Lauret. Chirality dependence of the absorption cross section of carbon nanotubes. *Phys. Rev. Lett.*, 111:137402, September 2013. [197](#)

REFERENCES

- [214] Kaihui Liu, Xiaoping Hong, Qin Zhou, Chenhao Jin, Jinghua Li, Weiwei Zhou, Jie Liu, Enge Wang, Alex Zettl, and Feng Wang. High-throughput optical imaging and spectroscopy of individual carbon nanotubes in devices. *Nature nanotechnology*, 8(12):917–922, 2013. [197](#)
- [215] Cyrielle Roquelet, Benjamin Langlois, Fabien Vialla, Damien Garrot, Jean-Sébastien Lauret, and Christophe Voisin. Light harvesting with non covalent carbon nanotube/porphyrin compounds. *Chemical Physics*, 413:45–54, 2013. [206](#)
- [216] MR Delbecq, Vivien Schmitt, FD Parmentier, Nicolas Roch, JJ Viennot, Gwendal Fève, Benjamin Huard, Christophe Mora, Audrey Cottet, and Takis Kontos. Coupling a quantum dot, fermionic leads, and a microwave cavity on a chip. *Physical Review Letters*, 107(25):256804, 2011. [206](#)
- [217] Jacek Kasprzak, M Richard, S Kundermann, A Baas, P Jeambrun, JMJ Keeling, FM Marchetti, MH Szymańska, R Andre, JL Staehli, et al. Bose–einstein condensation of exciton polaritons. *Nature*, 443(7110):409–414, 2006. [207](#), [261](#)
- [218] Carole Diederichs, Jérôme Tignon, Gregor Dasbach, Cristiano Ciuti, Aristide Lemaître, Jacqueline Bloch, Ph Roussignol, and Claude Delalande. Parametric oscillation in vertical triple microcavities. *Nature*, 440(7086):904–907, 2006. [207](#), [261](#)
- [219] Thomas Volz, Andreas Reinhard, Martin Winger, Antonio Badolato, Kevin J Hennessy, Evelyn L Hu, and Ataç Imamoğlu. Ultrafast all-optical switching by single photons. *Nature Photonics*, 6(9):605–609, 2012. [207](#), [261](#)
- [220] B Richards and E Wolf. Electromagnetic diffraction in optical systems. ii. structure of the image field in an aplanatic system. In *Proceedings of the Royal Society of London A: Mathematical, Physical and Engineering Sciences*, volume 253, pages 358–379. The Royal Society, 1959. [237](#), [238](#)
- [221] Gert Zumofen, Nassiredin M Mojarad, and Mario Agio. Light scattering by an oscillating dipole in a focused beam. *arXiv preprint arXiv:0901.4807*, 2009. [237](#)
- [222] EH Linfoot and E Wolf. Diffraction images in systems with an annular aperture. *Proceedings of the Physical Society. Section B*, 66(2):145, 1953. [240](#)
- [223] P Mukherjee and LN Hazra. Two point resolution of annular apertures. [240](#)

GLOSSARY

- (n, m) Chiral indices of a nanotube
- β Efficiency, defined as the number of photons emitted into the cavity mode per excitation pulse
- $\beta_e = \frac{F_p^*}{1 + F_p^*}$ Extraction, i.e. percentage of photons emitted into the cavity mode.
- $\delta = \omega_c - \omega_{em}$ Frequency detuning between the cavity mode and the emitter
- ϵ_{cav} Cavity collection efficiency
- ϵ_{FS} Free-space collection efficiency
- $\eta = \frac{\gamma_R}{\gamma_R + \gamma_{NR}}$ Free-space quantum efficiency of the ZPL, i.e. number of photons emitted in the ZPL per excitation pulse
- $\eta_{tot} = \eta/BR$ Free-space quantum efficiency of the nanotube, i.e. number of photons emitted in the full spectrum per excitation pulse
- γ Spontaneous emission rate in free-space
- γ^* Pure dephasing
- $\gamma_{all} = \kappa + \gamma + \gamma^*$
- $\gamma_{cav} = 1/\tau_{cav}$ Spontaneous emission rate in cavity
- $\gamma_{FS} = \gamma = 1/\tau_{FS}$ Spontaneous emission rate in free-space
- γ_{NR} Non Radiative rate of a CNT (including the emission in the phonon wings)
- γ_R ZPL Radiative rate of a CNT, i.e. number of photons emitted in the ZPL per second
- $\kappa = 1/\tau_{stor}$ Cavity decay rate
- \mathcal{F} Finesse of the cavity
- \mathcal{L} Losses in a dielectric mirror
- \mathcal{R} Radius of curvature
- \mathcal{T} Transmission of a dielectric mirror

ω_c Cavity mode resonant frequency

\vec{C}_h Nanotube chiral vector

\vec{T} Nanotube translation vector

$\tau_R = 1/f_{rep}$ Repetition rate of the excitation laser

θ Nanotube chiral angle

$\theta_{out} = \frac{\lambda}{\pi w_0}$ Cavity output half-angle

BR Branching Ratio, i.e. intensity emitted in the ZPL over intensity emitted in the full spectrum (ZPL + wings)

c Speed of light

d_t Nanotube diameter

DoS Density of states

f' Focal length of a lens

$F_p = \frac{3Q(\lambda/n)^3}{4\pi^2V}$ Purcell factor

$F_p^* = \frac{3Q_{eff}(\lambda/n)^3}{4\pi^2V}$ Generalized Purcell factor

g Coupling factor (between a dipole and a cavity mode)

$g^{(2)}(\tau)$ Second order auto-correlation function

g^{ZPL} Coupling factor explicitly restricted to the coupling between the ZPL and the cavity mode

I Intensity

k_b Boltzman constant

L Cavity length

n Optical index

NA Numerical Aperture

P Excitation power

P_{sat} Excitation power at which the saturation is reached

GLOSSARY

$Q = \frac{\omega_c}{\kappa}$ Quality factor of the cavity mode

$Q_{eff} = (\frac{1}{Q} + \frac{1}{Q_{em}})^{-1}$ Effective quality factor (emitter + cavity)

T Temperature (in Kelvins)

V Geometrical volume of a cavity

V_{eff} Effective mode volume of a cavity

w_0 Waist of a cavity mode

APD Avalanche Photodiode

SWNT Single Wall Carbon Nanotubes

BRF Birefringent Filter

CCD Charged Coupled Device

DBR Distributed Bragg Reflector

FSR Free Spectral Range

BR Branching Ratio

FWHM Full Width at Half Maximum

ZPL Zero Phonon Line

APPENDIX A : DERIVATIONS

A.1 A tunable fiber Fabry-Perot microcavity

A.1.1 Beam waist

The waist is on the planar mirror, so $z_0 = 0$. On the concave mirror, the curvature is $R_n(L) = \mathcal{R}$. From 3.8, one gets :

$$\begin{cases} R_n(L) = L \left(1 + \left(\frac{z_R^n}{L} \right)^2 \right) & = \mathcal{R} \\ (z_R^n)^2 = L^2 \left(\frac{\mathcal{R}}{L} - 1 \right) & = \left(\frac{\pi w_0^2}{\lambda_n} \right)^2 \\ w_{0,n}^2 = \frac{L \lambda_n}{\pi} \sqrt{\frac{\mathcal{R}}{L} - 1} \end{cases}$$

A.1.2 Fiber mode

The radius of curvature immediately after the crossing of the concave mirror is given by $R_f = \frac{\mathcal{R}}{n_f - 1}$. Let's assume that the waist is still w_f , the waist at the output of the fiber. From equations 3.7 and 3.8, and taking the concave mirror as the origin, one has :

$$\begin{cases} w_f(0) = w_{0,f} \sqrt{1 + \left(\frac{z_0}{z_{R,f}} \right)^2} & = w_f \\ z_0^2 = z_{R,f}^2 \left(\left(\frac{w_f}{w_{0,f}} \right)^2 - 1 \right) \\ R_f(0) = (-z_{0,f}) \left(1 + \left(\frac{z_{R,f}}{z_{0,f}} \right)^2 \right) & = R_f \\ R_f(0) = -z_{R,f} \sqrt{\left(\frac{w_f}{w_{0,f}} \right)^2 - 1} \left(1 + \frac{1}{\left(\frac{w_f}{w_{0,f}} \right)^2 - 1} \right) \end{cases}$$

Using the definition of $z_{R,f}$, given in eq. 3.10, one gets the waist of the fiber mode :

$$\begin{cases} R_f & = \frac{\pi}{\lambda} \left(\frac{w_f^2}{\sqrt{\left(\frac{w_f}{w_{0,f}} \right)^2 - 1}} \right) \\ w_{0,f} & = \frac{w_f}{\sqrt{\frac{1}{R_f^2} \left(\frac{\pi w_f^2}{\lambda} \right)^2 + 1}} \end{cases}$$

The waist position is the given by :

$$\begin{cases} z_{0,f}^2 &= z_{R,f}^2 \left(\frac{1}{R_f^2} \left(\frac{\pi w_f^2}{\lambda} \right)^2 \right) \\ z_{0,f} &= \frac{\left(\frac{\pi w_f^2}{\lambda} \right)^2}{R_f \left(\frac{1}{R_f^2} \left(\frac{\pi w_f^2}{\lambda} \right)^2 + 1 \right)} \end{cases}$$

Finally, let's define $Z_f = \frac{\pi w_f^2}{\lambda}$ and come back to an origin on the planar mirror :

$$\begin{cases} w_{0,f} &= \frac{w_f}{\sqrt{1 + \left(\frac{Z_f}{R_f} \right)^2}} \\ z_{0,f} &= L + \frac{Z_f^2}{R_f \left(1 + \left(\frac{Z_f}{R_f} \right)^2 \right)} \end{cases}$$

APPENDIX B : DRILLED OBJECTIVE

This appendix reviews the properties of the drilled objective used for confocal-cavity experiments.

B.1 Numerical Aperture

In order to test the effect of the drilling on the lens focusing abilities, the setup depicted in figure B.1 is mounted. A collimated laser beam (HeNe, 635 nm) is sent on the *objective*. Then a high numerical aperture objective (NA=0.7) is used to observe the image focal point of the *objective*. The plan is imaged with a magnification of 75 on a camera, with pixels of $5 \mu\text{m}^1$. An example is given on figure B.2.

With the help of this setup, the intensity in the focal plane is measured. The cylindrical symmetry of the problem was taken into account by averaging the intensity measured on concentric circles, taking the maximum of the intensity as the center. On figure B.3a the intensity as a function of the distance to this point is plotted for the same lens before and after the drilling.

In order to model what happens, one can consider that the incoming beam is a linearly polarized planar wave, homogeneous over the full lens clear aperture. The focalization is computed following the work of Richards and Wolf on aplanetic systems [220] : any ray converging towards the focal point (fig B.4) of the lens crosses the gaussian reference sphere \mathcal{F} at the height at which the corresponding incident ray entered the system in the objective space. This sphere has a radius f (focal of the lens) and is centered on the image focal point of the lens.

The height h of the incident ray is thus given by $h = f \sin(\theta)$, where θ is the divergence angle of the converging ray. As the energy is conserved, the incoming beam (plane wave) carries as much energy as the output beam (spherical wave). In polar coordinates (θ, ϕ) :

$$|E_2| = |E_1| \cdot \cos^{1/2}\theta \quad (\text{B.1})$$

A thorough computation gives the field at the focal point F' [221] :

$$\mathbf{E}_f(\rho, \phi, z) = -A_0 [i(\mathcal{I}_0 + \mathcal{I}_2 \cos 2\phi)\hat{\mathbf{e}}_x + \mathcal{I}_2 \cos 2\phi \hat{\mathbf{e}}_y + 2\mathcal{I}_1 \cos \phi \hat{\mathbf{e}}_z] \quad (\text{B.2})$$

with A_0 the amplitude, k the wavevector and :

¹Thorlabs DCC1545C

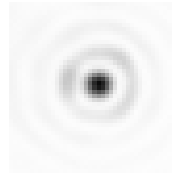
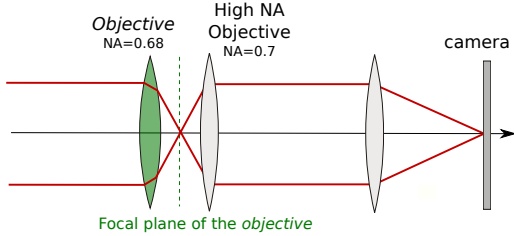
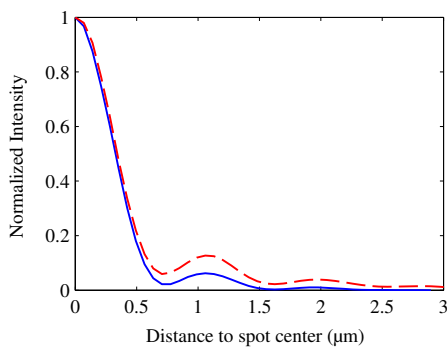
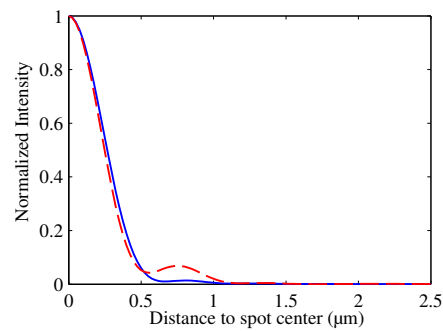


Figure B.1 – Schema of the setup with which the *objective* properties are evaluated : a plane wave is focused with the *objective* and the image plan is observed with a high numerical aperture objective.

Figure B.2 – Image of the image focal plane of the drilled *objective*. The colors are inverted.



(a) Experimental



(b) Theoretical

Figure B.3 – Intensity of the beam as a function of the distance to the spot center. In blue, the lens before drilling, in red after drilling.

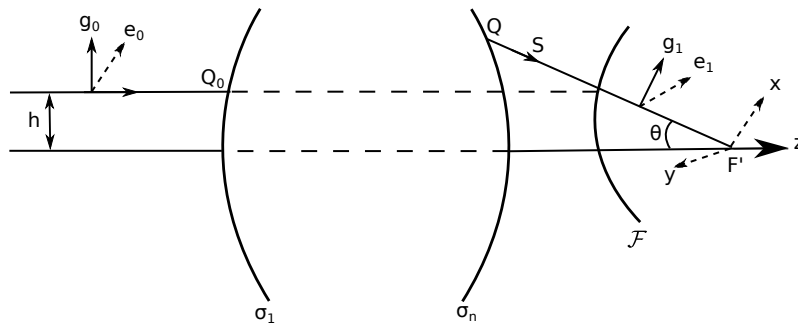


Figure B.4 – The focal sphere is noted \mathcal{F} . A ray emerging from the optical system meets this focal sphere at the same height h at which the corresponding ray entered the system in object space. Adapted from [220].

$$\begin{cases} \mathcal{I}_0(\rho, z, \alpha) = \int_0^{NA} \sqrt{\cos\theta} \sin\theta \cdot (1 + \cos\theta) J_0(k\rho\sin\theta) e^{ikz\cos\theta} d\theta \\ \mathcal{I}_1(\rho, z, \alpha) = \int_0^{NA} \sqrt{\cos\theta} \sin^2\theta \cdot J_1(k\rho\sin\theta) e^{ikz\cos\theta} d\theta \\ \mathcal{I}_2(\rho, z, \alpha) = \int_0^{NA} \sqrt{\cos\theta} \sin\theta \cdot (1 - \cos\theta) J_2(k\rho\sin\theta) e^{ikz\cos\theta} d\theta \end{cases} \quad (\text{B.3})$$

where NA is the numerical aperture of the lens and J_n are the Bessel functions.

In order to model the complete imaging setup, the same computation must be done again to simulate the high numerical aperture objective and the lens which focuses on the camera. The effect is to spread the image. It can be taken into account with a Bessel function :

$$\mathbf{E}_{image}(\rho_i, \phi_i, z = 0) = \int_0^{\theta_{max}} \int_0^{2\pi} E_{focal}(\rho, \phi, 0) \frac{J_1(k\epsilon\alpha)}{k\epsilon\alpha} \rho d\rho d\phi \quad (\text{B.4})$$

Where ϵ is the distance between the position of the object point (ρ, ϕ) and the position image point (ρ_i, ϕ_i) considered. The simulations for a drilled and a not-drilled lens are plotted in figure B.3b. One can see that the agreement with the experimental data is good for the first lobe but much less for the next ones. This limitation may come from the fact that a plane wave was considered in input, while experimentally a gaussian beam was sent on the lens.

The waist of the focused beam is defined as :

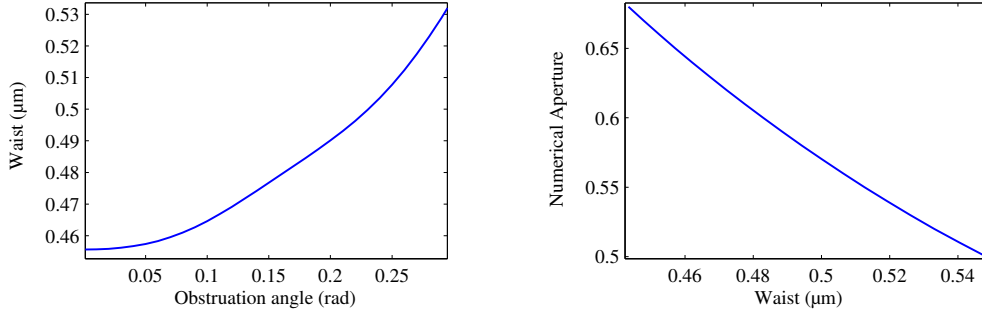
$$\omega = \sqrt{2\pi} \frac{\int_0^\infty E_f(r)^2 \cdot r dr}{\int_0^\infty E_f(r)^2 dr} \quad (\text{B.5})$$

From the simulation one can derive this waist as a function of the obstructed angle θ_{min} at the center of the lens² (integration between $\text{asin}(\theta_{min})$ and NA), as shown in figure B.5a. An effective numerical aperture can be defined as the numerical aperture giving the same waist for a non-drilled lens (integration between 0 and $NA_{effective}$), as shown in figure B.5b. Thereby, one can estimate that the effective focal spot waist is increased by less than 10% - in good agreement with experimental data - and that the effective numerical aperture of the drilled lens is 0.62 instead of 0.68 for the original lens.

B.2 Resolving power

An other figure of merit of a lens is its angular resolution, or resolving power, which means its ability to separate point-like emitters located at a small angular distance from each other. Rayleigh stated that two point sources are separated when the principal diffraction maximum of one image coincides with the first minimum of the other. Considering a circular lens, the Rayleigh criterion is given by

²This angle is simply the hole radius divided by the focal of the lens.



(a) Waist as a function of the obstructed angle at the center.

(b) Effective Numerical Aperture as a function of the waist.

Figure B.5 – From the simulations described in the text, one can get the effective numerical aperture of the lens, which drops from 0.68 to 0.62 after drilling.

$$\theta = 1.22 \frac{\lambda}{D} \quad (\text{B.6})$$

where λ is the wavelength and D is the clear aperture (diameter) of the lens. For a drilled lens, it can be considered that the aperture is a ring, with a ratio ϵ between the clear aperture diameter and the obstructed diameter. The intensity after such an aperture is [222, 223] :

$$I(\theta) = \frac{I_0}{(1 - \epsilon^2)^2} \left(\frac{2J_1(x)}{x} - \frac{2\epsilon J_1(\epsilon x)}{x} \right)^2 \quad (\text{B.7})$$

With $x = \frac{\pi}{\lambda} D \sin \theta$. Resolving $\frac{2J_1(x)}{x} - \frac{2\epsilon J_1(\epsilon x)}{x} = 0$, gives the first zero of the intensity. A numerical computation gives the new Rayleigh criterion, for $\epsilon = 0.1$:

$$\theta = 1.21 \frac{\lambda}{D} \quad (\text{B.8})$$

The resolving power of the drilled lens is almost unchanged compared to the pristine lens.

APPENDIX C : EFFECT OF THE VIBRATIONS

This appendix attempts to discuss the effect of the cavity vibrations, described in section 3.4.2, on the estimation of the Purcell factor made in chapter 5.

In order to understand this effect, it is important to sort the timescales. First, the spontaneous emission decay time is around 100 ps. Second, the vibrations (i.e. the random changes in the cavity mode's energy) happen on the millisecond range. Finally, the acquisitions take seconds to hours. Consequently, one can decouple the different phenomenons happening at different timescales. During a whole absorption and spontaneous emission event, the cavity has a given spectral position. As the acquisition happens on timescales much longer, it simply corresponds to an integral over the different detuning explored by the cavity.

For the sake of simplicity, only the ZPL of the nanotubes is considered here. Furthermore, the spectral diffusion (which would correspond to a random shift in the nanotube emission energy on nanosecond to minutes timescales) is not taken into account. Consequently, the spectrum of the emitter is approximated by a Lorentzian of width $\hbar(\gamma_{FS} + \gamma^*) = 300 \mu\text{eV}$ centered on a emission energy E , where $\hbar\gamma^*$ is the pure dephasing and $\hbar\gamma_{FS} = 6.6 \mu\text{eV}$ corresponds to a free-space lifetime $\tau_{FS} = 1/\gamma_{FS} = 100 \text{ ps}$.

The cavity mode is modeled by a Lorentzian line of spectral width $\hbar\kappa = 30 \mu\text{eV}$ at an energy detuned of $\hbar\delta$ compared to the emission energy of the CNT. The vibrations are modeled as a Gaussian probability distribution for the detuning δ :

$$P(\delta) = A e^{-(\hbar\delta)^2/2\alpha^2} \quad (\text{C.1})$$

Where the FWHM of the Gaussian is $2\sqrt{2\ln(2)}\alpha = 10\hbar\kappa$ (typical value measured for fiber A), and $A^{-1} = \int_{-\infty}^{\infty} e^{-(\hbar\delta)^2/2\alpha^2} d\delta$ is the normalization factor.

Photon count method Let's recall the expression of the radiative rate of the nanotube in cavity $R(\delta)$. From eq. (1.55) and (1.56), one gets :

$$R(\delta) = \frac{4g^2}{\gamma_{all} \left(1 + \left(\frac{2\delta}{\gamma_{all}} \right)^2 \right)} \quad (\text{C.2})$$

Where $\hbar g = 30 \mu\text{eV}$ is the coupling strength, and $\gamma_{all} = \kappa + \gamma_{FS} + \gamma^*$.

The effect of the vibrations on the photon counts can thus be encompassed in a factor V :

$$V = \left(\int_{-\infty}^{\infty} \frac{P(\delta)}{1 + \left(\frac{2\delta}{\gamma_{all}}\right)^2} d\delta \right)^{-1} \quad (\text{C.3})$$

$$F_p^* = V \cdot F_{measured}^*$$

For the parameters given above, $V = 1.35$. In other words, the generalized Purcell factor measured by the photon counts method, without taking into account the effect of the vibrations, is underestimated by 35%.

Transient measurement method However, in the case of the lifetime measurement, the effect of the vibrations is more subtle : when the cavity is detuned from the nanotube, the lifetime increases, but the flux of photon decreases. Consequently, the more the cavity is spectrally detuned, the less this position contributes to the measurement.

The intrinsic lifetime of the nanotube in cavity (at resonance, without vibrations) τ_{cav} can be obtained from eq. (5.31) :

$$\tau_{cav} = \left(\frac{1}{\tau_{FS}} + \frac{4g^2}{\gamma_{all}} \right)^{-1} \quad (\text{C.4})$$

With the parameters above, $\tau_{cav} = 62$ ps. Given eq. (1.55), the lifetime measured as a function of the detuning $\tau(\delta)$ can be expressed as :

$$\tau(\delta) = \left(\frac{1}{\tau_{FS}} + \frac{4g^2}{\gamma_{all} \left(1 + \left(\frac{2\delta}{\gamma_{all}}\right)^2\right)} \right)^{-1} \quad (\text{C.5})$$

The intensity emitted as a function of the time $I(t)$ is given by :

$$I(t) \propto \int_{-\infty}^{\infty} P(\delta) \cdot R(\delta) \cdot e^{-t/\tau(\delta)} d\delta \quad (\text{C.6})$$

This quantity is numerically computed for the parameters given above, as shown in fig. (C.1). The output is fitted to a mono-exponential decay, and the characteristic time τ_{cav}^* is extracted. The effect of the vibrations on the estimation of the Purcell factor are given by :

$$V_2 = \frac{\tau_{FS}/\tau_{cav} - 1}{\tau_{FS}/\tau_{cav}^* - 1}$$

$$F_p^* = V_2 \cdot F_{measured}^*$$

Here, one finds $V_2 = 1.27$, or an experimental underestimation of 27%, which is slightly more accurate than the value obtained for the photon counts method.

Appendix C. Effect of the vibrations

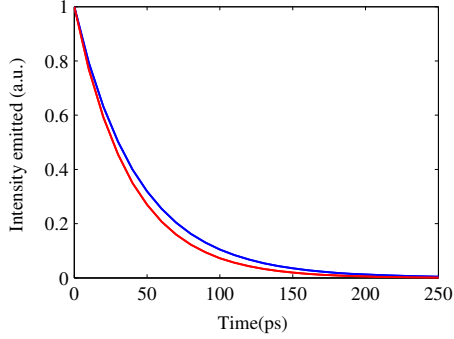


Figure C.1 – Simulation of the transient of a CNT in cavity with (blue) and without (red) vibrations.

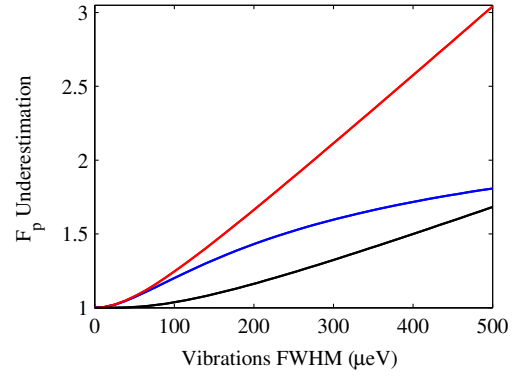


Figure C.2 – Underestimation of the Purcell factor as a function of the FWHM of the vibrations of the cavity. In red the photon count method factor V , in blue the transient method factor V_2 and in black the ratio V/V_2 .

However, one can see in fig. (C.2) that if the vibrations increase this discrepancy increases (almost linearly). Consequently, we conclude that the transient measurement method, though not immune the cavity vibrations, gives in general better estimations than the photon counts method.

APPENDIX D : CAVITY EFFICIENCY WITH PHONON COUPLING

The present appendix aims to give a detailed derivation of the model introduced in chapter 6. Let's recall that in all this model, we remain in the weak coupling regime. In order to ease the reading, the structure remains similar to the one of the corresponding chapter and the main formulas are redundant. In this way, the reader willing to read the full derivation doesn't need to go back and forth between the main chapter and the following work.

D.1 Populations evolution of the system

D.1.1 Hamiltonian of the system

Hamiltonian

The Hamiltonian of the system is given by:

$$H = \hbar\omega_X\sigma^+\sigma^- + \hbar\sum_{\vec{k}}\omega_k b_{\vec{k}}^\dagger b_{\vec{k}} + \hbar\omega_{\text{cav}}a^\dagger a + \hbar\sigma^+\sigma^-\sum(g_k b_{\vec{k}} + g_k^* b_{\vec{k}}^\dagger) + i\hbar g(a^\dagger\sigma^- - a\sigma^+) \quad (\text{D.1})$$

The damping and dephasing terms are described in the Lindblad form in the master equation, given by $L[C]\rho \equiv C\rho C^\dagger - \frac{1}{2}(C^\dagger C\rho + \rho C^\dagger C)$. Three terms are used for cavity losses $C_1 \equiv \sqrt{\kappa}a$, for exciton lifetime $C_2 \equiv \sqrt{\gamma}\sigma^-$ and for pure dephasing $C_3 \equiv \sqrt{\gamma^*}\sigma^+\sigma^-$. Details :

$$L[C_1]\rho \equiv \kappa a\rho a^\dagger - \frac{\kappa}{2}(a^\dagger a\rho + \rho a^\dagger a) \quad (\text{D.2})$$

$$L[C_2]\rho \equiv \gamma\sigma^-\rho\sigma^+ - \frac{\gamma}{2}(\sigma^+\sigma^-\rho + \rho\sigma^+\sigma^-) \quad (\text{D.3})$$

$$L[C_3]\rho \equiv \gamma^*\sigma^+\sigma^-\rho\sigma^+\sigma^- - \frac{\gamma^*}{2}(\sigma^+\sigma^-\sigma^+\sigma^-\rho + \rho\sigma^+\sigma^-\sigma^+\sigma^-) \quad (\text{D.4})$$

$$= \gamma^*\sigma^+\sigma^-\rho\sigma^-\sigma^+ - \frac{\gamma^*}{2}(\sigma^+\sigma^-\rho + \rho\sigma^+\sigma^-) \quad (\text{D.5})$$

Polaron transformation

Now, let's use the polaron transformation (which diagonalize the Hamiltonian in the absence of exciton-cavity coupling). The unitary transformation U is given by

D.1. POPULATIONS EVOLUTION OF THE SYSTEM

$U \equiv \sigma^+ \sigma^- \otimes D + \sigma^- \sigma^+ \otimes \mathbb{1}$, $D = e^{-\Omega}$ and $\Omega \equiv \sum_{\vec{k}} \left(\frac{g_{\vec{k}}^*}{\omega_k} b_{\vec{k}}^\dagger - \frac{g_{\vec{k}}}{\omega_k} b_{\vec{k}} \right)$.

Let's focus first on the effect of the displacement operator D over the phonon operators. We note $\xi_k = \frac{g_k}{\omega_k}$, in the following expressions :

$$D^\dagger b_{\vec{k}} D = b_{\vec{k}} - \xi_k^* \quad (\text{D.6})$$

$$D^\dagger b_{\vec{k}}^\dagger D = b_{\vec{k}}^\dagger - \xi_k \quad (\text{D.7})$$

$$D^\dagger D = 1 \quad (\text{D.8})$$

Thanks to these relations, we can rewrite :

$$\begin{cases} D^\dagger \omega_k b_{\vec{k}}^\dagger b_{\vec{k}} D &= \omega_k (b_{\vec{k}}^\dagger - \xi_k) (b_{\vec{k}} - \xi_k^*) \\ &= \omega_k b_{\vec{k}}^\dagger b_{\vec{k}} - (g_k b_{\vec{k}} + g_k^* b_{\vec{k}}^*) + \frac{g_k^2}{\omega_k} \end{cases} \quad (\text{D.9})$$

The $\frac{g_k^2}{\omega_k}$ term is the polaron shift. Let's renormalize the energies in order to remove it (in the following calculation, the tilde label is dropped) :

$$\tilde{\omega}_X = \omega_X - \sum_{\vec{k}} \left(\frac{g_{\vec{k}}^2}{\omega_k} \right) \quad (\text{D.10})$$

By applying the full operator U we get :

$$U^\dagger \omega_k b_{\vec{k}} b_{\vec{k}} U = \omega_k b_{\vec{k}} b_{\vec{k}} - \sigma^+ \sigma^- (g_k b_{\vec{k}} + g_k^* b_{\vec{k}}^*) \quad (\text{D.11})$$

And the other part of the Hamiltonian with phonons writes :

$$D^\dagger \sigma^+ \sigma^- \sum (g_k b_{\vec{k}} + g_k^* b_{\vec{k}}^*) D = \sigma^+ \sigma^- \left(g_k (b_{\vec{k}} - \xi_k) + g_k^* (b_{\vec{k}} - \xi_k^*) \right) \quad (\text{D.12})$$

$$= \sigma^+ \sigma^- \left(g_k b_{\vec{k}} + g_k^* b_{\vec{k}}^* - \frac{g_k^2}{\omega_k} \right) \quad (\text{D.13})$$

Finally, we get the following expression for the full Hamiltonian :

$$\tilde{H} \equiv U^\dagger H U = \hbar \omega_X \sigma^+ \sigma^- + \hbar \sum_{\vec{k}} \omega_k b_{\vec{k}} b_{\vec{k}} + \hbar \omega_{\text{cav}} a^\dagger a + i \hbar g (a^\dagger \sigma^- e^{-\Omega} - a \sigma^+ e^{\Omega}) \quad (\text{D.14})$$

In the polaron transformation picture, C operators became $\tilde{C} \equiv U^\dagger C U$, namely $\tilde{C}_1 = \sqrt{\kappa} a$, $\tilde{C}_2 = \sqrt{\gamma} \sigma^- e^{-\Omega}$ and $\tilde{C}_3 = \sqrt{\gamma^*} \sigma^+ e^{\Omega}$. Let's give an example of computation :

$$U^\dagger C_2 U = (\sigma^+ \sigma^- \otimes D^\dagger + \sigma^- \sigma^+ \otimes \mathbb{1}) \sqrt{\gamma} \sigma^- (\sigma^+ \sigma^- \otimes D + \sigma^- \sigma^+ \otimes \mathbb{1}) \quad (\text{D.15})$$

$$= \sigma^- \sigma^+ \sqrt{\gamma} \sigma^- \sigma^+ \sigma^- \otimes D \quad (\text{D.16})$$

$$= \sqrt{\gamma} \sigma^- e^{-\Omega} \quad (\text{D.17})$$

D.1.2 Master equation

Time evolution in the interaction Picture The next step is to study the time evolution in the interaction picture. The non-interacting Hamiltonian is given by :

$$H_0 = \hbar \omega_X \sigma^+ \sigma^- + \hbar \sum_{\vec{k}} \omega_k b_{\vec{k}} b_{\vec{k}} + \hbar \omega_{\text{cav}} a^\dagger a \quad (\text{D.18})$$

In the interaction picture representation, the time evolution of an operator X reads $X_I(t) = e^{iH_0 t/\hbar} X e^{-iH_0 t/\hbar}$. Here the interaction is given by :

$$V = i\hbar g (a^\dagger \sigma^- e^{-\Omega} - a \sigma^+ e^{\Omega}) \quad (\text{D.19})$$

Let's compute the different terms :

$$e^{iH_0 t/\hbar} a e^{-iH_0 t/\hbar} = e^{i\hbar \omega_{\text{cav}} t a^\dagger a} a e^{-i\hbar \omega_{\text{cav}} t a^\dagger a} \quad (\text{D.20})$$

Let's recall that for an operator X , we the Campbell-Hausdorff formula reads :

$$e^{i\hbar \omega_{\text{cav}} a^\dagger a} X e^{-i\hbar \omega_{\text{cav}} a^\dagger a} = X + \hbar \omega_{\text{cav}} [i t a^\dagger a, X] + \frac{(\hbar \omega_{\text{cav}})^2}{2} [i t a^\dagger a, [i t a^\dagger a, X]] + \dots \quad (\text{D.21})$$

Here we have $X = a$ and $[a^\dagger a, a] = -a$. Thus we obtain :

$$e^{iH_0 t/\hbar} a e^{-iH_0 t/\hbar} = e^{-i\hbar \omega_{\text{cav}} t} a \quad (\text{D.22})$$

$$e^{iH_0 t/\hbar} a^\dagger e^{-iH_0 t/\hbar} = e^{i\hbar \omega_{\text{cav}} t} a^\dagger \quad (\text{D.23})$$

Now let's focus on the σ^+ operator :

$$e^{iH_0t/\hbar}\sigma^+e^{-iH_0t/\hbar} = e^{i\hbar\omega_Xt}\sigma^+e^{-i\hbar\omega_Xt} \quad (D.24)$$

$$= \left(\sum_n \frac{(i\hbar\omega_Xt)^n}{n!} (\sigma^+\sigma^-)^n \right) \sigma^+ \left(\sum_n \frac{(-i\hbar\omega_Xt)^n}{n!} (\sigma^+\sigma^-)^n \right) \quad (D.25)$$

$$= \left(1 + \sum_{n>0} \frac{(i\hbar\omega_Xt)^n}{n!} (\sigma^+\sigma^-)^n \right) \sigma^+ \left(1 + \sum_{n>0} \frac{(-i\hbar\omega_Xt)^n}{n!} (\sigma^+\sigma^-)^n \right) \quad (D.26)$$

$$= \sigma^+ + \sum_{n>0} \frac{(i\hbar\omega_Xt)^n}{n!} \quad (D.27)$$

$$= e^{i\hbar\omega_Xt}\sigma^+ \quad (D.28)$$

$$e^{iH_0t/\hbar}\sigma^-e^{-iH_0t/\hbar} = e^{-i\hbar\omega_Xt}\sigma^- \quad (D.29)$$

Finally, the time evolution of the interaction Hamiltonian is given by :

$$V_I = i\hbar g \left(e^{-i\hbar\delta t} e^{-\Omega_I(t)} a^\dagger \sigma^- - e^{i\hbar\delta t} e^{\Omega_I(t)} a \sigma^+ \right) \quad (D.30)$$

Where $\delta = \omega_X - \omega_c$ and $\Omega_I(t) = e^{it \sum_{\vec{k}} \omega_k b_{\vec{k}}^\dagger b_{\vec{k}}} \Omega e^{-it \sum_{\vec{k}} \omega_k b_{\vec{k}}^\dagger b_{\vec{k}}}$

Master Equation The master equation is then given by:

$$\frac{d}{dt} \rho_I(t) = \frac{1}{i\hbar} [V_I(t), \rho_I(t)] + \sum_{j=1}^3 L[C_{jI}] \rho_I \quad (D.31)$$

where the sum corresponds to the three Lindblad operators \mathcal{C} in the interaction picture. The population of a given state A can be obtained from :

$$\frac{d \langle A \rangle}{dt} = \frac{d \text{Tr}(\rho A)}{dt} = \text{Tr}(\dot{\rho} A) \quad (D.32)$$

$$= \text{Tr} \left(\left(\frac{1}{i\hbar} [V_I(t), \rho] + L[C_{jI}] \rho \right) A \right) \quad (D.33)$$

$$= -\text{Tr} \left(\frac{1}{i\hbar} \rho [V_I(t), A] \right) + \text{Tr}(L[C_{jI}] A) \quad (D.34)$$

$$= -\frac{1}{i\hbar} \langle [V_I(t), A] \rangle + \text{Tr}(L[C_{jI}] A) \quad (D.35)$$

Moreover, we have :

$$Tr(L[C_j]A) = Tr(C_j \rho C_j^\dagger A - \frac{1}{2} C_j^\dagger C \rho A - \frac{1}{2} \rho C_j^\dagger C A) \quad (D.36)$$

$$= \langle C_j^\dagger A C \rangle - \frac{1}{2} \langle C_j^\dagger C A \rangle - \frac{1}{2} \langle A C_j^\dagger C \rangle \quad (D.37)$$

$$= -\frac{1}{2} \langle [A, C_j^\dagger] C \rangle - \frac{1}{2} \langle C^\dagger [C, A] \rangle \quad (D.38)$$

Let's compute the population evolution for $\langle a^\dagger a \rangle$:

$$\frac{d\langle a^\dagger a \rangle}{dt} = -\frac{1}{i\hbar} \langle [V_I(t), a^\dagger a] \rangle + Tr(L[C_{jI}]a^\dagger a) \quad (D.39)$$

$$= -g \langle e^{-i\hbar\delta t} e^{-\Omega_I(t)} [a^\dagger \sigma^-, a^\dagger a] - e^{i\hbar\delta t} e^{\Omega_I(t)} [a\sigma^+, a^\dagger a] \rangle \quad (D.40)$$

$$-\frac{1}{2} \langle [a^\dagger a, \sqrt{\kappa} a^\dagger] \sqrt{\kappa} a \rangle - \frac{1}{2} \langle \sqrt{\kappa} a^\dagger [\sqrt{\kappa} a, a^\dagger a] \rangle \quad (D.41)$$

$$= -g \langle e^{-i\hbar\delta t} e^{-\Omega_I(t)} a^\dagger [a^\dagger, a] \sigma^- - e^{i\hbar\delta t} e^{\Omega_I(t)} [a, a^\dagger] \sigma^+ \rangle \quad (D.42)$$

$$-\frac{\kappa}{2} \langle a^\dagger [a, a^\dagger] a \rangle - \frac{\kappa}{2} \langle a^\dagger [a, a^\dagger] a \rangle \quad (D.43)$$

$$= g e^{i\delta t} \langle e^{\Omega_I(t)} a \sigma^+ \rangle + g e^{-i\delta t} \langle e^{-\Omega_I(t)} a^\dagger \sigma^- \rangle - \kappa \langle a^\dagger a \rangle \quad (D.44)$$

The same procedure leads to the other population evolution :

$$\frac{d\langle \sigma^+ \sigma^- \rangle}{dt} = -\frac{1}{i\hbar} \langle [V_I(t), \sigma^+ \sigma^-] \rangle + Tr(L[C_{jI}]\sigma^+ \sigma^-) \quad (D.45)$$

$$= -g \langle e^{-i\hbar\delta t} e^{-\Omega_I(t)} [a^\dagger \sigma^-, \sigma^+ \sigma^-] - e^{i\hbar\delta t} e^{\Omega_I(t)} [a\sigma^+, \sigma^+ \sigma^-] \rangle \quad (D.46)$$

$$-\frac{1}{2} \langle [\sigma^+ \sigma^-, \sqrt{\gamma} \sigma^+ e^\Omega] \sqrt{\gamma} \sigma^- e^{-\Omega} \rangle - \frac{1}{2} \langle \sqrt{\gamma} e^{-\Omega} \sigma^+ [\sqrt{\gamma} \sigma^- e^\Omega, \sigma^+ \sigma^-] \rangle \quad (D.47)$$

$$= -g e^{i\delta t} \langle e^{\Omega_I(t)} a \sigma^+ \rangle - g e^{-i\delta t} \langle e^{-\Omega_I(t)} a^\dagger \sigma^- \rangle - \gamma \langle \sigma^+ \sigma^- \rangle \quad (D.48)$$

D.2 Derivation of the coherence term

D.2.1 Trace splitting

In the following, the term $\langle e^{\Omega_I(t)} a \sigma^+ \rangle$ is derived. The three other coherence terms can be derived in an analogous way, and the results are given as well.

First, the trace can be split in two parts, one over the system composed of the exciton and the cavity mode, labeled with the index S , and the other over the phonon bath, labeled with the index B . Since $e^{\Omega_I(t)}$ is acting on the phonons only, one obtains :

$$\langle e^{\Omega_I(t)} a \sigma^+ \rangle = Tr_B \left(Tr_S \left(\rho_I(t) a \sigma^+ \right) e^{\Omega_I(t)} \right) \quad (D.49)$$

D.2. DERIVATION OF THE COHERENCE TERM

The next step is to formally integrate the partial trace. We first note that, if we restrict the study to maximum one excitation in the light or in the matter, one gets :

$$Tr_S\left(\sum_{j=1}^3 L[\tilde{C}_1]\rho a\sigma^+\right) = Tr_S\left(\left(\kappa a\rho a^\dagger - \frac{\kappa}{2}(a^\dagger a\rho + \rho a^\dagger a)\right) a\sigma^+\right) \quad (D.50)$$

$$= Tr_S\left(\kappa\rho a^\dagger a a\sigma^+ - \frac{\kappa}{2}(\rho a a^\dagger a\sigma^+ + \rho a^\dagger a a\sigma^+)\right) \quad (D.51)$$

$$= Tr_S\left(-\frac{\kappa}{2}(\rho a\sigma^+)\right) \quad (D.52)$$

$$= -\frac{\kappa}{2}Tr_S(\rho_I(t)a\sigma^+) \quad (D.53)$$

$$Tr_S\left(\sum_{j=1}^3 L[\tilde{C}_2]\rho a\sigma^+\right) = Tr_S\left(\left(\gamma\sigma^-\rho\sigma^+ - \frac{\gamma}{2}(\sigma^+\sigma^-\rho + \rho\sigma^+\sigma^-)\right) a\sigma^+\right) \quad (D.54)$$

$$= Tr_S\left(\gamma\rho\sigma^+\sigma^+\sigma^- a - \frac{\gamma}{2}(\rho a\sigma^+\sigma^+\sigma^- + \rho a\sigma^+\sigma^-\sigma^+)\right) \quad (D.55)$$

$$= Tr_S\left(-\frac{\gamma}{2}(\rho a\sigma^+)\right) \quad (D.56)$$

$$= -\frac{\gamma}{2}Tr_S(\rho_I(t)a\sigma^+) \quad (D.57)$$

$$Tr_S\left(\sum_{j=1}^3 L[\tilde{C}_3]\rho a\sigma^+\right) = Tr_S\left(\left(\gamma^*\sigma^+\sigma^-\rho\sigma^-\sigma^+ - \frac{\gamma^*}{2}(\sigma^+\sigma^-\rho + \rho\sigma^+\sigma^-)\right) a\sigma^+\right) \quad (D.58)$$

$$= Tr_S\left(\gamma^*\rho\sigma^-\sigma^+ a\sigma^+\sigma^+\sigma^- - \frac{\gamma^*}{2}(\rho a\sigma^+\sigma^+\sigma^- + \rho a\sigma^+\sigma^-\sigma^+)\right) \quad (D.59)$$

$$= Tr_S\left(-\frac{\gamma^*}{2}(\rho a\sigma^+)\right) \quad (D.60)$$

$$= -\frac{\gamma^*}{2}Tr_S(\rho_I(t)a\sigma^+) \quad (D.61)$$

Finally :

$$Tr_S\left(\sum_{j=1}^3 L[\tilde{C}_j]\rho a\sigma^+\right) = -\frac{\gamma + \gamma^* + \kappa}{2}Tr_S(\rho_I(t)a\sigma^+) \quad (D.62)$$

This implies that :

$$\begin{aligned} \frac{d}{dt}Tr_S(\rho_I(t)a\sigma^+) &= \frac{1}{i\hbar} \langle [V_I(t), \rho_I(t)a\sigma^+] \rangle + \sum_{j=1}^3 L[C_{jI}]\rho_I(t)a\sigma^+ \quad (D.63) \\ &= \frac{1}{i\hbar}Tr_S([V_I(t), \rho_I(t)]a\sigma^+) - \frac{\gamma + \gamma^* + \kappa}{2}Tr_S(\rho_I(t)a\sigma^+) \end{aligned}$$

Here we have an equation of the form $\frac{dX}{dt} + \gamma_{all}X = \frac{1}{i\hbar}Y$, with $\gamma_{all} = \frac{\gamma + \gamma^* + \kappa}{2}$. Consequently, the previous equation can be formally integrated as (we suppose no coherence at the initial time $t = 0$) :

$$Tr_S(\rho_I(t)a\sigma^+) = \frac{1}{i\hbar} \int_0^t ds e^{-\frac{\gamma + \gamma^* + \kappa}{2}(t-s)} Tr_S([V_I(s), \rho_I(s)]a\sigma^+) \quad (D.64)$$

Applying the trace over the phonon bath part to the previous expression leads to:

$$e^{i\delta t} \langle e^{\Omega(t)} a\sigma^+ \rangle = e^{i\delta t} Tr_B \left(Tr_S(\rho_I(t)a\sigma^+) e^{\Omega_I(t)} \right) \quad (D.65)$$

$$= e^{i\delta t} Tr_B \left(\frac{1}{i\hbar} \int_0^t ds e^{-\gamma_{all}(t-s)} Tr_S([V_I(s), \rho_I(s)]a\sigma^+) e^{\Omega_I(t)} \right) \quad (D.66)$$

$$= \frac{1}{i\hbar} \int_0^t ds e^{i\delta t} e^{-\gamma_{all}(t-s)} Tr \left([V_I(s), \rho_I(s)]a\sigma^+ e^{\Omega_I(t)} \right) \quad (D.67)$$

Let's use the expression of V_I :

$$\begin{aligned} [V_I(s), \rho_I(s)]a\sigma^+ &= i\hbar g [e^{-i\hbar\delta s} e^{-\Omega_I(s)} a^\dagger \sigma^- - e^{i\hbar\delta s} e^{\Omega_I(s)} a\sigma^+, \rho_I(s)]a\sigma^+ \quad (D.68) \\ &= i\hbar g \left(e^{-i\hbar\delta s} e^{-\Omega_I(s)} [a^\dagger \sigma^-, \rho_I(s)]a\sigma^+ - e^{i\hbar\delta s} e^{\Omega_I(s)} [a\sigma^+, \rho_I(s)]a\sigma^+ \right) \quad (D.69) \end{aligned}$$

As we are tracing, we can use circular permutations :

$$Tr([a^\dagger \sigma^-, \rho_I(s)]a\sigma^+) = Tr(a^\dagger \sigma^- \rho_I(s)a\sigma^+ - \rho_I(s)a^\dagger \sigma^- a\sigma^+) \quad (D.70)$$

$$= Tr(\rho_I(s)aa^\dagger \sigma^+ \sigma^- - \rho_I(s)a^\dagger a\sigma^- \sigma^+) \quad (D.71)$$

$$= Tr(\rho_I(s)(1 + a^\dagger a)\sigma^+ \sigma^- - \rho_I(s)a^\dagger a(1 + \sigma^+ \sigma^-)) \quad (D.72)$$

$$= Tr(\rho_I(s)\sigma^+ \sigma^- - \rho_I(s)a^\dagger a) \quad (D.73)$$

$$Tr([a\sigma^+, \rho_I(s)]a\sigma^+) = Tr(a\sigma^+ \rho_I(s)a\sigma^+ - \rho_I(s)a\sigma^+ a\sigma^+) \quad (D.74)$$

$$= Tr(\rho_I(s)a\sigma^+ a\sigma^+ - \rho_I(s)a\sigma^+ a\sigma^+) \quad (D.75)$$

$$= 0 \quad (D.76)$$

The commutator rewrites :

$$[V_I(s), \rho_I(s)]a\sigma^+ = i\hbar g e^{-i\hbar\delta s} e^{-\Omega_I(s)} \text{Tr} \left(\rho_I(s) \sigma^+ \sigma^- - \rho_I(s) a^\dagger a \right) \quad (\text{D.77})$$

And finally the coherence term is given by :

$$e^{i\delta t} \langle e^{\Omega(t)} a \sigma^+ \rangle = g \int_0^t ds e^{(i\delta - \gamma_{all})(t-s)} \left(\langle \sigma^+ \sigma^-(s) e^{\Omega_I(t)} e^{-\Omega_I(s)} \rangle - \langle a^\dagger a(s) e^{-\Omega_I(s)} e^{\Omega_I(t)} \rangle \right) \quad (\text{D.78})$$

Where the notation $\langle \sigma^+ \sigma^-(s) e^{\Omega_I(t)} e^{-\Omega_I(s)} \rangle$ stands for $\text{Tr}(\rho_I(s) \sigma^+ \sigma^- e^{\Omega_I(t)} e^{-\Omega_I(s)})$.

D.2.2 Non-Interacting Blip Approximation

In 1987, Leggett et al. published a review about the dynamics of a dissipative two-level system [208]. In this review, several approximations that were already employed in the literature were formally combined into the so-called non-interacting blip approximation (NIBA). The NIBA can be applied to the exciton-phonon in cavity system. The approximations correspond first to the introduction of the free-bath dynamics and second to the fact that the bath reduced density matrix remains unperturbed by the exciton-phonon state. Though the NIBA was first introduced as path integrals, Dekker [209, 210] and Orth et al. [211] showed that it is equivalent to :

$$\langle \sigma^+ \sigma^-(s) e^{\Omega_I(t)} e^{-\Omega_I(s)} \rangle \stackrel{\text{NIBA}}{\approx} \langle \sigma^+ \sigma^-(s) \rangle \text{Tr}(\rho_{th} e^{\Omega_I(t)} e^{-\Omega_I(s)}) \quad (\text{D.79})$$

where ρ_{th} is the equilibrium thermal density matrix of the bath.

D.2.3 Trace over the phonon bath

Product of displacement operators

Let's recall that $\Omega_I(t) = e^{i\hbar \sum_{\vec{k}} \omega_k b_{\vec{k}}^\dagger b_{\vec{k}}} \Omega e^{-i\hbar \sum_{\vec{k}} \omega_k b_{\vec{k}}^\dagger b_{\vec{k}}}$, $\Omega = \sum_{\vec{k}} \left(\frac{g_{\vec{k}}^*}{\omega_k} b_{\vec{k}} - \frac{g_{\vec{k}}}{\omega_k} b_{\vec{k}}^\dagger \right)$ and the displacement operator is defined as : $D = e^{-\Omega}$. For a generic displacement operator $D_\alpha = e^{\alpha b^\dagger} - e^{\alpha^* b}$, we have :

$$D_\alpha D_\beta = D_{\alpha+\beta} e^{\frac{1}{2}(\alpha\beta^* - \alpha^*\beta)} \quad (\text{D.80})$$

$$e^{i\omega t b^\dagger} D_\alpha e^{-i\omega t b} = D_{\alpha e^{i\omega t}} \quad (\text{D.81})$$

Here we can write (for a single phonon mode) :

$$D = e^{-\Omega} = D_{-g_k^*/\omega_k} \quad (\text{D.82})$$

$$D^\dagger = e^{\Omega} = D_{g_k^*/\omega_k} \quad (\text{D.83})$$

Thus :

$$e^{\Omega_I(t)} = e^{i\hbar \sum_{\vec{k}} \omega_k b_{\vec{k}} b_{\vec{k}}^\dagger} D_{g_k^*/\omega_k} e^{-i\hbar \sum_{\vec{k}} \omega_k b_{\vec{k}}^\dagger b_{\vec{k}}} \quad (\text{D.84})$$

$$= D_{g_k^*/\omega_k} e^{i\omega_k t} \quad (\text{D.85})$$

$$e^{-\Omega_I(s)} = D_{-g_k^*/\omega_k} e^{i\omega_k s} \quad (\text{D.86})$$

$$e^{\Omega_I(t)} e^{-\Omega_I(s)} = D_{g_k^*/\omega_k} e^{i\omega_k t} D_{-g_k^*/\omega_k} e^{i\omega_k s} \quad (\text{D.87})$$

Let's note $\alpha = g_k^*/\omega_k e^{i\omega_k t}$ and $\beta = -g_k^*/\omega_k e^{i\omega_k s}$. Then :

$$\frac{1}{2}(\alpha\beta^* - \alpha^*\beta) = \frac{1}{2} \frac{|g_k|^2}{\omega_k^2} \left(-e^{i\omega_k(t-s)} + e^{-i\omega_k(t-s)} \right) \quad (\text{D.88})$$

$$= -i \frac{|g_k|^2}{\omega_k^2} \sin(\omega_k(t-s)) \quad (\text{D.89})$$

The product of displacement operators becomes :

$$e^{\Omega_I(t)} e^{-\Omega_I(s)} = e^{-i \frac{|g_k|^2}{\omega_k^2} \sin(\omega_k(t-s))} D_{g_k^*/\omega_k} (e^{i\omega_k t} - e^{i\omega_k s}) \quad (\text{D.90})$$

Tracing a displacement operator

At the thermal equilibrium ($\beta_{th} = 1/kT$), the density matrix is given by :

$$\rho_{th} = (1 - e^{-\hbar\omega\beta_{th}}) \sum_n e^{-\hbar\omega\beta_{th}n} |n\rangle\langle n| \quad (\text{D.91})$$

For a displacement operator, we have :

$$\text{Tr}(\rho_{th} D_\alpha) = \sum_m \langle m| (1 - e^{-\hbar\omega\beta_{th}}) \sum_n e^{-\hbar\omega\beta_{th}n} |n\rangle\langle n| D_\alpha |m\rangle \quad (\text{D.92})$$

$$= (1 - e^{-\hbar\omega\beta_{th}}) \sum_n e^{-\hbar\omega\beta_{th}n} \langle n| D_\alpha |n\rangle \quad (\text{D.93})$$

Let's show that :

$$\langle n| D_\alpha |n\rangle = e^{-|\alpha|^2/2} L_n(|\alpha|^2) \quad (\text{D.94})$$

where the Laguerre polynomials are given by :

D.2. DERIVATION OF THE COHERENCE TERM

$$L_n(x) = \frac{e^x}{n!} \frac{d^n}{dx^n} (e^{-x} x^n) \quad (\text{D.95})$$

We note x_{pq} :

$$x_{pq} = \langle p | e^{i\omega t a^\dagger a} D e^{-i\omega t a^\dagger a} | q \rangle \quad (\text{D.96})$$

$$D = e^{\alpha a^\dagger - \alpha^* a} = e^{-|\alpha|^2/2} e^{\alpha a^\dagger} e^{-\alpha^* a} \quad (\text{D.97})$$

Then its expression is given by :

$$x_{pq} = e^{i\omega t(p-q)} \langle p | D_\alpha | q \rangle \quad (\text{D.98})$$

$$= e^{-|\alpha|^2/2} e^{i\omega t(p-q)} \langle p | e^{\alpha a^\dagger} e^{-\alpha^* a} | q \rangle \quad (\text{D.99})$$

$$= e^{-|\alpha|^2/2} e^{i\omega t(p-q)} \sum_{l,m} \frac{1}{l!m!} (\alpha)^m (-\alpha^*)^l \langle p | (a^\dagger)^m a^l | q \rangle \quad (\text{D.100})$$

$$\Rightarrow \text{if } p - m \geq 0 \text{ then } p - m = q - l \Rightarrow p - q = m - l \quad (\text{D.101})$$

$$\Rightarrow \text{if } p - m < 0 \text{ then it's zero} \quad (\text{D.102})$$

$$= e^{-|\alpha|^2/2} \sum_{l,m} \frac{1}{l!m!} e^{i\omega t(m-l)} (\alpha)^m (-\alpha^*)^l \langle p | (a^\dagger)^m a^l | q \rangle \quad (\text{D.103})$$

$$= e^{-|\alpha|^2/2} \sum_{l,m} \frac{1}{l!m!} (\alpha e^{i\omega t})^m (-\alpha e^{i\omega t})^l \langle p | (a^\dagger)^m a^l | q \rangle \quad (\text{D.104})$$

$$= \langle p | D_{\alpha e^{i\omega t}} | q \rangle \quad (\text{D.105})$$

Thus :

$$\langle n | D_\alpha | n \rangle = e^{-|\alpha|^2/2} \sum_m \frac{1}{m!m!} (-|\alpha|^2)^m \langle n | (a^\dagger)^m a^m | n \rangle \quad (\text{D.106})$$

$$= e^{-|\alpha|^2/2} \sum_{m=0}^n \frac{1}{m!m!} (-|\alpha|^2)^m \sqrt{\frac{n!}{(n-m)!}} \sqrt{\frac{n!}{(n-m)!}} \quad (\text{D.107})$$

$$= e^{-|\alpha|^2/2} \sum_{m=0}^n \frac{(-1)^m}{m!} \binom{n}{m} (|\alpha|^2)^m \quad (\text{D.108})$$

$$= e^{-|\alpha|^2/2} L_n(|\alpha|^2) \quad (\text{D.109})$$

Consequently, we obtain :

$$Tr(\rho_{th}D_\alpha) = (1 - e^{-\omega\beta_{th}})e^{-|\alpha|^2/2} \sum_n (e^{-\omega\beta_{th}})^n L_n(|\alpha|^2) \quad (D.110)$$

$$= (1 - e^{-\omega\beta_{th}})e^{-|\alpha|^2/2} \frac{1}{1 - e^{-\omega\beta_{th}}} \exp\left(-\frac{|\alpha|^2 e^{-\omega\beta_{th}}}{1 - e^{-\omega\beta_{th}}}\right) \quad (D.111)$$

$$= \exp\left(-\frac{|\alpha|^2}{2} \left(1 + 2\frac{e^{-\omega\beta_{th}}}{1 - e^{-\omega\beta_{th}}}\right)\right) \quad (D.112)$$

And

$$\langle n \rangle = Tr(\rho_{th}\hat{n}) = \frac{e^{-\omega\beta_{th}}}{1 - e^{-\omega\beta_{th}}} \quad (D.113)$$

We finally get :

$$Tr(\rho_{th}D_\alpha) = \exp\left(-\frac{|\alpha|^2}{2}(1 + 2\langle n \rangle)\right) \quad (D.114)$$

Trace for the relevant displacement operator

Until now we have considered only one mode k . But, as all the modes commute with each other, the result for all the modes are simply the product of the results for each mode. In the exponential, this becomes a sum over the modes k .

$$Tr(\rho_{th}e^{\Omega_I(t)}e^{-\Omega_I(s)}) \quad (D.115)$$

$$= Tr\left(\rho_{th}e^{-i\frac{|g_k|^2}{\omega_k^2}\sin(\omega_k(t-s))} D_{g_k^*/\omega_k(e^{i\omega_k t} - e^{i\omega_k s})}\right) \quad (D.116)$$

$$= \prod_k e^{-i\frac{|g_k|^2}{\omega_k^2}\sin(\omega_k(t-s))} \exp\left(-\frac{|g_k^*/\omega_k(e^{i\omega_k t} - e^{i\omega_k s})|^2}{2}(1 + 2n(k))\right) \quad (D.117)$$

$$= \prod_k \exp\left(\frac{1}{2}\frac{|g_k|^2}{\omega_k^2}(-e^{i\omega_k(t-s)} + e^{-i\omega_k(t-s)}) - \frac{1}{2}\frac{|g_k|^2}{\omega_k^2}|(e^{i\omega_k t} - e^{i\omega_k s})|^2(1 + 2n(k))\right) \quad (D.118)$$

$$= \prod_k \exp\left(\frac{1}{2}\frac{|g_k|^2}{\omega_k^2}(-e^{i\omega_k(t-s)} + e^{-i\omega_k(t-s)} - (2 - e^{i\omega_k(t-s)} - e^{-i\omega_k(t-s)})(1 + 2n(k)))\right) \quad (D.119)$$

$$= \prod_k \exp\left(\frac{|g_k|^2}{\omega_k^2}(e^{-i\omega_k(t-s)} - 2n(k) - n(k)(e^{i\omega_k(t-s)} - e^{-i\omega_k(t-s)} - 1))\right) \quad (D.120)$$

$$= \prod_k \exp\left(\frac{|g_k|^2}{\omega_k^2}(e^{-i\omega_k(t-s)} - n(k)|e^{-i\omega_k(t-s)} - 1|^2 - 1)\right) \quad (D.121)$$

$$\equiv K(t-s) \quad (D.122)$$

By following the same procedure, we can get :

$$Tr(\rho_{th}e^{-\Omega_I(s)}e^{\Omega_I(t)}) = K^*(t-s) \quad (D.123)$$

And :

$$e^{i\delta t} \langle e^{\Omega(t)} a \sigma^+ \rangle = g \int_0^t ds e^{(i\delta - \gamma_{all})(t-s)} \left(\langle \sigma^+ \sigma^- (s) \rangle K(t-s) - \langle a^\dagger a(s) \rangle K^*(t-s) \right) \quad (\text{D.124})$$

D.3 Cavity efficiency

D.3.1 Emission and absorption spectra

From the works of Mahan [206, chap. 4.3.4] and Krummeheur [172, chap. 4.3.4], one can show that :

$$S^{abs}(\omega) = 2Re \left[\int_0^\infty dt e^{i(\omega - \omega_X)t} e^{-\frac{\gamma + \gamma^*}{2}t} K(t) \right] \quad (\text{D.125})$$

For the emission spectrum, by using the ZPL mirror symmetry, one gets a similar expression by replacing $K(t)$ by its complex conjugate :

$$S^{emi}(\omega) = 2Re \left[\int_0^\infty dt e^{i(\omega - \omega_X)t} e^{-\frac{\gamma + \gamma^*}{2}t} K^*(t) \right] \quad (\text{D.126})$$

D.3.2 Laplace transforms

Introduction

Let's use Laplace transform to go further :

$$F(s) = \int_0^\infty e^{-st} f(t) dt \quad (\text{D.127})$$

$$F^*(s^*) = \int_0^\infty e^{-st} f^*(t) dt \quad (\text{D.128})$$

We recall for the convolution two functions f and g that :

$$\mathcal{L} \left(\int_0^t ds f(s) g(t-s) \right) = \mathcal{L}(f) \mathcal{L}(g) \quad (\text{D.129})$$

Application for $K(t)$

Let's note $Q(\lambda) = \mathcal{L}(K)$. Then :

$$\mathcal{L}(e^{(i\delta - \gamma_{all})(t-s)} K(t-s)) = \int_0^\infty dt e^{-\lambda t} e^{(i\delta - \gamma_{all})t} K(t) \quad (\text{D.130})$$

$$= \int_0^\infty dt e^{-(\lambda - i\delta + \gamma_{all})t} K(t) \quad (\text{D.131})$$

$$= Q(\lambda + \gamma_{all} - i\delta) \quad (\text{D.132})$$

Appendix D. Cavity efficiency with phonon coupling

For the complex conjugate, we have :

$$\mathcal{L}(e^{(i\delta-\gamma_{all})(t-s)} K^*(t-s)) = \int_0^\infty dt e^{-\lambda t} e^{(i\delta-\gamma_{all})t} K^*(t) \quad (\text{D.133})$$

$$= \int_0^\infty dt e^{-(\lambda-i\delta+\gamma_{all})t} K^*(t) \quad (\text{D.134})$$

$$= Q^*(\lambda + \gamma_{all} + i\delta) \quad (\text{D.135})$$

Thus :

$$\mathcal{L}(e^{i\delta t} \langle e^{\Omega(t)} a \sigma^+ \rangle) = g \left(\mathcal{L}(\langle \sigma^+ \sigma^-(s) \rangle) Q(\lambda + \gamma_{all} - i\delta) - \mathcal{L}(\langle a^\dagger a(s) \rangle) Q^*(\lambda + \gamma_{all} + i\delta) \right) \quad (\text{D.136})$$

Now, let's define the Lorentzian function S_{cav} which represents the empty spectrum of the cavity :

$$\mathcal{L}_{cav}(\omega) = \frac{1}{1 + \left(\frac{2\omega}{\kappa}\right)^2} \quad (\text{D.137})$$

Let's compute its convolution with the absorption spectrum :

$$(S^{abs} * \mathcal{L}_{cav})(\omega) = \int_{-\infty}^\infty dx S^{abs}(\omega - x) S_{cav}(x) \quad (\text{D.138})$$

$$\propto \int_{-\infty}^\infty dx \text{Re} \left[\int_0^\infty dt e^{i(\omega-\omega_X-x)t} e^{-\frac{\gamma+\gamma^*}{2}t} K(t) \right] \mathcal{L}_{cav}(x) \quad (\text{D.139})$$

$$\propto \text{Re} \left[\int_0^\infty dt e^{-\frac{\gamma+\gamma^*}{2}t} K(t) \left(\int_{-\infty}^\infty dx e^{i(\omega-\omega_X-x)t} \mathcal{L}_{cav}(x) \right) \right] \quad (\text{D.140})$$

$$\propto \text{Re} \left[\int_0^\infty dt e^{-\frac{\gamma+\gamma^*}{2}t} K(t) \left(e^{i(\omega-\omega_X-\kappa/2)t} \right) \right] \quad (\text{D.141})$$

$$\propto \text{Re} \left[\int_0^\infty dt K(t) e^{i(\omega-\omega_X)t} e^{-\gamma_{all}t} \right] \quad (\text{D.142})$$

Let's define the cavity modified absorption and emission spectra :

$$\tilde{S}^{abs}(\omega) = \frac{(S^{abs} * \mathcal{L}_{cav})(\omega)}{\int \mathcal{L}_{cav}(\omega) d\omega} \quad (\text{D.143})$$

$$\tilde{S}^{emi}(\omega) = \frac{(S^{emi} * \mathcal{L}_{cav})(\omega)}{\int \mathcal{L}_{cav}(\omega) d\omega} \quad (\text{D.144})$$

We have (s is the coefficient of proportionality) :

$$\tilde{S}^{abs}(\omega) = 2\text{Re} [Q(\gamma_{all} - i\delta)] \quad (\text{D.145})$$

$$\tilde{S}^{emi}(\omega) = 2Re [Q^*(\gamma_{all} + i\delta)] \quad (D.146)$$

Expression of the cavity efficiency

We recall the population evolutions :

$$\begin{cases} \frac{d\langle a^\dagger a \rangle}{dt} &= ge^{i\delta t} \langle e^{\Omega_I(t)} a \sigma^+ \rangle + ge^{-i\delta t} \langle e^{-\Omega_I(t)} a^\dagger \sigma^- \rangle - \kappa \langle a^\dagger a \rangle \\ \frac{d\langle \sigma^+ \sigma^- \rangle}{dt} &= -ge^{i\delta t} \langle e^{\Omega_I(t)} a \sigma^+ \rangle - ge^{-i\delta t} \langle e^{-\Omega_I(t)} a^\dagger \sigma^- \rangle - \gamma \langle \sigma^+ \sigma^- \rangle \end{cases} \quad (D.147)$$

Let's apply a Laplace transform and set $\lambda = 0$. We note : $I = \int_0^\infty \langle \sigma^+ \sigma^- \rangle$ and we recall that $\int_0^\infty \langle a^\dagger a \rangle = \beta/\kappa$, where β is the efficiency :

$$\begin{cases} 0 &= 2g^2 Re \left(IQ(\gamma_{all} - i\delta) - \frac{\beta}{\kappa} Q^*(\gamma_{all} + i\delta) \right) - \beta \\ -1 &= -2g^2 Re \left(IQ(\gamma_{all} - i\delta) - \frac{\beta}{\kappa} Q^*(\gamma_{all} + i\delta) \right) - \gamma I \end{cases} \quad (D.148)$$

Let's inject the absorption and emission spectra :

$$Re(Q(\gamma_{all} - i\delta)) = Re(Q(\gamma_{all} - i(\omega_X - \omega_c))) \quad (D.149)$$

$$= Re \left[\int_0^\infty dt e^{i(\omega_X - \omega_c)t} e^{-\frac{\gamma + \gamma^* + \kappa}{2}t} K(t) \right] \quad (D.150)$$

$$= Re \left[\int_0^\infty dt e^{-i(\omega_X - \omega_c)t} e^{-\frac{\gamma + \gamma^* + \kappa}{2}t} K^*(t) \right] \quad (D.151)$$

$$= Re \left[\int_0^\infty dt e^{i(\omega_c - \omega_X)t} e^{-\frac{\gamma + \gamma^* + \kappa}{2}t} K^*(t) \right] \quad (D.152)$$

$$= \tilde{S}^{emi}(\omega_c)/2 \quad (D.153)$$

$$Re(Q^*(\gamma_{all} + i\delta)) = \tilde{S}^{abs}(\omega_c)/2 \quad (D.154)$$

$$\begin{cases} 0 &= g^2 \left(I \tilde{S}^{emi}(\omega_c) - \frac{\beta}{\kappa} \tilde{S}^{abs}(\omega_c) \right) - \beta \\ 1 &= g^2 \left(I \tilde{S}^{emi}(\omega_c) - \frac{\beta}{\kappa} \tilde{S}^{abs}(\omega_c) \right) + \gamma I \end{cases} \quad (D.155)$$

We obtain :

$$\beta = \frac{g^2 \tilde{S}^{emi}(\omega_c) \kappa}{g^2 \tilde{S}^{emi}(\omega_c) \kappa + g^2 \tilde{S}^{abs}(\omega_c) \gamma + \kappa \gamma} \quad (D.156)$$

And the final result is :

$$\beta = \frac{\tilde{S}^{emi}(\omega_c) \kappa}{\tilde{S}^{emi}(\omega_c) \kappa + \tilde{S}^{abs}(\omega_c) \gamma + \frac{\kappa \gamma}{g^2}} \quad (D.157)$$

French Summary

En 1905, Albert Einstein s'est attelé au problème de l'effet photoélectrique, qui concernait les échanges d'énergie discrets entre un champ électromagnétique et un métal [1]. Afin de comprendre ce phénomène, il a introduit l'idée que la lumière est composée de quanta d'énergie, par la suite appelés photons [2]. Le succès de sa théorie a ouvert la voie au développement de la mécanique quantique, et à ancré l'idée que la lumière ne pouvait être comprise que si elle était à la fois considéré comme une onde, et un ensemble de corpuscules.

En particulier, une source de photons uniques peut être définie comme une source émettant un flux de photons individuels. Ces photons ont une probabilité nulle d'être séparés par un retard nul, et la lumière produite est qualifiée de dégroupée. Une telle propriété ne peut être obtenue ou comprise avec des outils classiques. Dans les années 1960, la production de photons uniques a été réalisée en atténuant une source laser jusqu'à ce que la probabilité d'émettre deux photons à la fois devienne négligeable. Cependant, étant donné les statistiques poissoniennes de la lumière cohérente émise par les lasers, cette probabilité ne pouvait pas tomber à zéro. La première preuve expérimentale d'une lumière réellement anti-grappes a été obtenue avec des atomes de sodium à la fin des années 1970 [3], et a été suivi une décennie plus tard par des sources de photons uniques fiables [4, 5].

Depuis lors, le domaine de la génération de photons uniques a toujours été en développement, et plusieurs applications sont considérées. En particulier, les photons pourraient être utilisés comme qubits, c'est-à-dire des bits d'information pour la cryptographie quantique [6, 7]. Cette technique consiste en un moyen hautement sécurisé de transmettre l'information, protégée de l'espionnage par les lois de la mécanique quantique (en particulier l'impossibilité de mesurer sans changer le système et le théorème de non-clonage qui affirme que la copie des données quantiques est impossible). Néanmoins, en présence de plus d'un photon, la cryptographie quantique devient vulnérable, d'où l'importance d'une véritable source de photon unique.

Cependant, l'émission de photons un par un n'est pas la seule exigence pour une telle source. Elle doit également être à la demande, ce qui signifie que la génération de photons peut être déclenchée par des impulsions optiques ou électriques ; sa luminosité, définie comme la probabilité d'obtenir un photon pour chaque impulsion d'excitation devrait idéalement être un ; et les photons devraient être indiscernables [9, 10], ce qui signifie avoir le même paquet d'ondes. De plus, plusieurs propriétés pratiques sont recherchées, comme la possibilité d'émettre dans les bandes de télécommunications (1.3 μm et 1.55 μm), la capacité à travailler à température ambiante et la facilité d'intégration dans les dispositifs, en vue d'applications.

Cette dernière exigence a conduit les chercheurs à étudier les nano-émetteurs de matière condensée. Actuellement, la technologie la plus avancée est basée sur des émetteurs quasi zéro-dimensionnels appelés boîtes quantiques. Des sources à photons uniques brillantes, à la demande, avec un degré élevé d'indiscernabilité, ont maintenant été obtenues [11]. Mais les boîtes quantiques subissent trois inconvénients

majeurs : l'extraction compliquée des photons de la source, la difficulté à émettre à des longueurs d'onde de télécommunications [12], et à température ambiante.

Les nanotubes de carbone, sont un allotrope du carbone synthétisé en 1991 [13]. Ils se composent d'une couche d'atomes organisés dans un réseau en nid d'abeille enroulé en forme de tube, ayant un diamètre nanométrique et une longueur micrométrique. Les recherches sur ces structures quasi unidimensionnelles ont longtemps été confinées à leurs remarquables propriétés mécaniques (poids léger, haut module Young) et électroniques (métalliques ou semi-conducteurs, mobilité élevée) [14, 15]. Leur première étude optique a été réalisée une décennie plus tard, lorsque O'Connell et al. [16] ont réussi à isoler les nanotubes les uns des autres au moyen d'une encapsulation micellaire, afin d'empêcher ainsi l'extinction de la photoluminescence.

La géométrie des nanotubes de carbone peut être entièrement caractérisée par deux indices n et m , appelés indices chiraux. La plupart des propriétés électroniques et optiques des nanotubes de carbone peuvent être prédites à partir de ces indices. En particulier, certains nanotubes sont métalliques tandis que d'autres ont un écart d'énergie direct, inversement proportionnel à leur diamètre. La synthèse d'un nanotube de carbone d'une espèce donnée (c'est-à-dire avec des indices chiraux donnés), pour obtenir une énergie de transition donnée, est un champ de recherche propre. Actuellement, la plupart des processus de synthèse produisent une distribution d'espèces, mais les post-sélections peuvent apporter des puretés élevées [17]. Cependant, l'origine de la photoluminescence dans les nanotubes de carbone est complexe : les porteurs de charge sont confinés en raison de la géométrie quasi unidimensionnelle, conduisant à des excitons très stables, dominant l'émission jusqu'à température ambiante. [18]. La fonction d'onde excitonique déborde du tube et le rend très sensible à la permittivité diélectrique de son environnement [19]. En conséquence, l'énergie d'émission du nanotube de carbone ne peut pas être complètement comprise par ses indices chiraux, mais dépend fortement de son environnement local. De plus, Vialla et al. [20] ont montré que le spectre de photoluminescence était influencé par les interactions entre l'exciton et les phonons unidimensionnels se propageant le long de l'axe des nanotubes.

En 2008, Högele et al. [21] ont démontré qu'un seul nanotube de carbone pourrait émettre une lumière dégroupée à température cryogénique. Cependant, le mécanisme sous-jacent à ce phénomène reste flou. Il semble que les excitons multiples s'annihilent à un rythme rapide par les processus Auger [22, 23, 24] et que l'exciton restant est piégé autour d'un défaut dans le réseau de nanotubes, ou autour d'une charge dans son environnement [25, 26]. De fait, le contrôle des défauts dans les nanotubes a conduit récemment à la démonstration de l'anti-groupement à la fois dans les bandes de télécommunications et à température ambiante [27, 28].

Un autre atout des nanotubes de carbone est leur capacité à être contactés et excités électriquement, ce qui ouvre la voie à des sources à la demande intégrées [29, 30]. Néanmoins, trois inconvénients majeurs entravent leur développement : la difficulté d'obtenir un nanotube émettant à une longueur d'onde donnée (sélectivité de synthèse et sensibilité à l'environnement), leur spectre optique complexe et leur

efficacité quantique limitée, c'est-à-dire leur probabilité d'émission par impulsion d'excitation.

Dans ce travail, nous proposons d'associer un seul nanotube de carbone à une cavité de Fabry-Perot. Ce couplage est un outil puissant pour étudier la physique sous-jacente à la photoluminescence des nanotubes de carbone et pour renforcer leurs caractéristiques en tant qu'émetteurs à un seul photon. L'effet Purcell [31] consiste en une augmentation du taux d'émission spontanée et se traduit donc directement par une augmentation de l'efficacité de l'émetteur. Plus le volume de la cavité est petit, plus l'effet est fort. Cependant, le couplage d'une cavité à un seul émetteur nécessite une adaptation spatiale - c'est-à-dire le positionnement du mode cavité sur l'émetteur - et une adaptation spectrale - c'est-à-dire une même fréquence pour l'émission de nanotubes et le mode cavité. Les cavités monolithiques habituelles, développées pour les boîtes quantiques, sont inadéquates pour les nanotubes de carbone en raison de la dépendance de leur énergie d'émission sur leur environnement immédiat. En conséquence, le couplage d'un nanotube à de tels dispositifs repose sur le couplage aléatoire, avec des taux de succès non pertinents pour des applications [32].

En revanche, nous avons adapté une technologie flexible développée dans le domaine de la physique atomique [33]. Elle consiste en une micro-cavité ouverte formée entre un miroir situé au sommet d'une fibre optique et un miroir plan sur lequel sont dispersés des nanotubes de carbone à faible densité. La fibre elle-même est insérée dans une lentille mobile. De cette façon, un nanotube de carbone unique peut être étudié en espace libre par microscopie confocal et la fibre Fabry-Perot cavité peut être accordée de manière déterministe spatialement (mouvement latéral de la fibre) et spectrale (distance entre les miroirs) à l'émetteur.

La capacité d'étudier le même émetteur sans la cavité et pour différentes longueurs de cavité (différents couplages) donne un aperçu inestimable dans la naissance des effets de cavité de l'électro-dynamique quantique. Dans le régime de couplage faible, la cavité apporte un éclaircissement accru de la source de photon unique via l'effet Purcell. L'accordabilité de la cavité apporte également un moyen d'étudier l'effet d'alimentation de cavité prédit par Auffèves et al. [34, 35]. Les émetteurs de matière condensée usuels ont une largeur de raie plus étroite que la cavité dans laquelle ils sont incorporés. Au contraire ici, les nanotubes de carbone ont une largeur de raie d'au moins un ordre de grandeur plus grande. Dans ce cas, les caractéristiques spectrales de la lumière émise (énergie, largeur spectrale) reproduisent celles de la cavité, indépendamment de l'émetteur. Par conséquent, l'accord de la longueur de la cavité apporte une accordabilité spectrale de la source de photon unique.

Si le couplage surmonte les pertes du système, on atteint le régime de couplage fort. Dans ce cas, des particules mixtes lumière-matière, appelées polaritons, sont créées. La physique des polaritons dépend fortement de leur dimensionnalité. Les polaritons bidimensionnels ont donné la condensation de Bose-Einstein [217], ainsi que la génération de photons jumeaux [218], tandis que leurs homologues à zéro dimension sont étudiés pour les commutateurs optiques à un seul photon [219]. En raison de leur diamètre étroit (en dessous de 1 nm), et de leurs excitons fortement liés,

les nanotubes de carbone sont d'excellents candidats pour comprendre la physique unidimensionnelle des polaritons. Et inversement, les polaritons sont un outil pour mieux comprendre la diffusion et les propriétés de localisation des excitons dans les nanotubes de carbone.

Ce travail a été consacré au couplage d'un seul nanotube de carbone avec une cavité Fabry-Perot fibrée de faible volume afin d'augmenter le taux d'émission spontanée grâce à l'effet Purcell. Les nanotubes utilisés proviennent de solutions commerciales et ont été enveloppés dans PFO pour éviter la formation de fagots. Ils ont été déposés, avec une densité inférieure à un spot optique (limité par diffraction), sur un miroir diélectrique plan par centrifugation. Du polystyrène a été ajouté pour empêcher le clignotement, le vieillissement et diminuer la diffusion spectrale.

Un microscope confocal à balayage a été construit pour étudier la photoluminescence de ces nanotubes de carbone uniques à température cryogénique. Les observations - localisation spatiale, saturation, anisotropie de polarisation - sont cohérentes avec la littérature. Quand un nanotube de carbone est excité, plusieurs excitons (paires électron-trou fortement liées par le confinement unidimensionnel) sont formés et diffusent le long de l'axe des nanotubes. L'un est piégé sur un site localisé, en raison de défauts cristallins ou de charges dans le voisinage du tube, conduisant à l'émission de photons uniques.

Les études de photoluminescence et de diffusion spectrale tendent à confirmer que le spectre complexe des nanotubes de carbone, composé d'un pic Lorentzien et de deux ailes latérales, provient des interactions entre l'exciton localisé et un bain de phonons acoustiques se propageant le long de l'axe des nanotubes. Les ailes correspondent à l'émission d'un photon à une énergie inférieure (resp. plus élevée) plus l'émission (resp. l'absorption) d'un phonon. L'asymétrie correspond à un facteur de Boltzmann (à température cryogénique, l'absorption de phonons est défavorisée). Compte-tenu du caractère unidimensionnel des phonons, leur couplage à l'exciton devrait diverger à basse énergie, conduisant à un élargissement de la Ligne à Zéro Phonons. Cependant, les phonons à faible énergie sont supprimés, conduisant des largeurs de ligne aussi basses que 300 microeV.

Dans cette étude, l'efficacité des nanotubes de carbone en espace libre était comprise entre 1% et 5%, une gamme de valeurs incompatibles avec des applications. Par conséquent, nous avons décidé de coupler un seul nanotube à un résonateur. Dans ce cas, l'effet Purcell améliore l'efficacité de l'émetteur et canalise l'émission en cavité, ce qui facilite l'extraction de la lumière. Cependant, les cavités monolithiques couramment utilisées dans la matière condensée, conçues pour fonctionner à une longueur d'onde donnée, avec un émetteur à un endroit donné, sont mal adaptées aux nanotubes (la synthèse ne sélectionne pas complètement leurs caractéristiques spectrales). Les groupes qui ont essayé de faire correspondre au hasard et d'émetteur

avec un résonateur confissent des taux de réussite d'un sur des milliers [32] ...

Au contraire, notre approche consistait à construire une cavité spectralement et spatialement accordable. Les nanotubes ont été déposés sur un miroir, et le deuxième a été fabriqué au sommet d'une fibre optique. Au moyen d'une ablation au laser CO_2 , sa forme a été contrôlée avec précision : nous avons obtenu des dépressions concaves avec des rayons de courbures aussi faible que $10\ \mu\text{m}$, des profondeurs inférieures à $1.5\ \mu\text{m}$, conduisant à des volumes de mode effectifs inférieurs à $2\ \mu\text{m}^3$. La fibre a été insérée dans la lentille utilisée pour la microscopie confocale afin de faciliter le passage de l'espace libre à la cavité de manière reproductible et réversible : une fois un nanotube étudié en espace libre, la cavité est formée en amenant la fibre à l'emplacement de l'émetteur. L'adaptation spectrale est obtenue en ajustant la distance entre les deux miroirs. Ces cavités ont de nombreux atouts : volume en mode faible, facteurs de qualité jusqu'à 10^5 , adaptabilité à n'importe quel émetteur, possibilité de comparer le comportement du même émetteur avec et sans cavité, possibilité de changer le volume de mode par pas de $\lambda/2$; et l'émission peut être directement couplée à une fibre, ce qui est commode pour des applications.

Avec ces cavités, nous avons démontré des facteurs Purcell jusqu'à 120 pour les volumes de mode les plus faibles. Dans ce cas, 99% de la lumière émise est dirigée dans le mode cavité, et l'efficacité effective de la source atteint jusqu'à 50%, ce qui conduit à une brillance allant jusqu'à 10%. L'émission de photons uniques a été démontrée à la fois en espace libre et dans la cavité, avec une valeur typique de la fonction de corrélation du second ordre à zéro délai de 3.

En outre, cette émission de photon unique améliorée par effet Purcell est possible à la fois lorsque la cavité est en résonance avec la ZPL et lorsque la cavité était accordée vers l'aile phonon rouge ou bleue. Pour en tenir compte, nous avons développé un modèle sur l'effet de la cavité sur le couplage exciton-phonon. Nous avons montré que l'émission dans les ailes est renforcée par rapport à la ligne principale et que, si le couplage augmente, l'efficacité reste faible sur le côté bleu mais tend vers l'unité sur le côté rouge. Cela conduirait à une efficacité presque constante sur une plage spectrale plus de cent fois supérieure à la largeur spectrale de la cavité, ouvrant ainsi la voie au multiplexage.

Cette expérience a plusieurs perspectives. En termes d'applications, l'efficacité pourrait être augmentée en obtenant des nanotubes de carbone avec des largeurs spectrales inférieures et en réduisant le volume de la cavité (en réduisant par exemple la profondeur de la dépression concave). L'excitation électrique est déjà bien étudiée [29] et pourrait être mise en œuvre avec cette configuration pour un nanotube suspendu. Dans les bandes des télécoms, l'absorption de photon unique a été démontrée [27, 28]. Le passage à ces longueurs d'onde ne nécessiterait que le changement du diamètre des nanotubes utilisés. Aller à la température ambiante peut nécessiter des efforts supplémentaires. Bien que cela n'empêche pas le dégroupage [27], cela s'accompagne d'un élargissement de l'émission, et donc d'un effondrement du facteur Purcell.

Pour la cryptographie quantique, une figure de mérite encore à démontrer est

l'indiscernabilité. Dans l'espace libre, l'indiscernabilité, donnée par le rapport entre le taux d'émission spontanée et le déphasage total, est inférieure à 2%. Cependant, lorsqu'un nanotube est couplé à une cavité, cette dernière agit comme l'émetteur effectif, pompé par le premier de manière incohérente. Avec nos paramètres, l'indiscernabilité théorique, obtenue à partir des travaux de Grange et al. [205], serait de 25%. Contre intuitivement, cette valeur pourrait augmenter si les rapports κ/γ et g/γ diminuaient. Par exemple, le fait d'aller à la température ambiante, et donc d'élargir le spectre, pourrait améliorer significativement l'indiscernabilité.

Au-delà du régime de couplage faible, deux autres voies seraient intéressantes. La première serait laser à base de nanotubes uniques. Dans ce cas, la finesse de la cavité doit être augmentée afin de laisser le temps de stockage dépasser la durée de vie de l'émission spontanée. Plusieurs photons coexistent alors dans le mode cavité, conduisant à une émission stimulée.

Néanmoins, la perspective la plus intéressante repose sur le régime de couplage fort. Actuellement, le rapport entre le couplage et les pertes $g/(\gamma + \gamma^*) \sim 0.1$ tombe un ordre de grandeur trop bas. Cependant, au cours des derniers mois, plusieurs groupes ont démontré des signaux de photoluminescence de largeur spectrale $\hbar(\gamma + \gamma^*) < 50 \mu\text{eV}$, environ un ordre de grandeur inférieur à nos valeurs courantes. Avec de tels émetteurs, le couplage fort semble accessible, à condition que la largeur de la cavité reste inférieure à cette valeur, et mesurable si aucun artefact (tel que les vibrations) n'augmente la largeur spectrale de la cavité. Dans ce régime, l'échange d'énergie entre la cavité et le nanotube serait cohérent, conduisant à des quasi-particules mixtes lumière-matière appelées polaritons. Si ces particules sont déjà bien connues dans le cas des points quantiques, elles restent faiblement explorées dans leur forme unidimensionnelle. Les nanotubes de carbone sont donc d'excellents candidats pour explorer cette physique.

Pour conclure, nous espérons que ce travail a montré que les nanotubes de carbone ont leur propre place dans la recherche pour une source efficace à la demande de photon unique à température ambiante dans les longueurs d'onde des télécommunications. Un renforcement supplémentaire du couplage peut ouvrir la voie à la physique très riche des polaritons unidimensionnels. Et pour finir, la configuration originale présentée dans ce travail est extrêmement polyvalente et pourrait être utilisée pour coupler d'autres types d'émetteurs, comme les nano-diamants ou des molécules.

